Wrocław University of Technology
Centre of Advanced Materials and Nanotechnology

Materials Science-Poland

Vol. 27 • No. 4/1 • 2009

Oficyna Wydawnicza Politechniki Wrocławskiej

Materials Science-Poland is an interdisciplinary journal devoted to experimental and theoretical research into the synthesis, structure, properties and applications of materials.

Among the materials of interest are:

- glasses and ceramics
- sol-gel materials
- photoactive materials (including materials for nonlinear optics)
- laser materials
- photonic crystals
- semiconductor micro- and nanostructures
- piezo-, pyro- and ferroelectric materials
- high-T_c superconductors
- magnetic materials
- molecular materials (including polymers) for use in electronics and photonics
- novel solid phases
- other novel and unconventional materials

The broad spectrum of the areas of interest reflects the interdisciplinary nature of materials research. Papers covering the modelling of materials, their synthesis and characterisation, physicochemical aspects of their fabrication, properties and applications are welcome. In addition to regular papers, the journal features issues containing conference papers, as well as special issues on key topics in materials science.

Materials Science-Poland is published under the auspices of the Centre of Advanced Materials and Nanotechnology of the Wrocław University of Technology, in collaboration with the Institute of Low Temperatures and Structural Research of the Polish Academy of Sciences and the Wrocław University of Economics.

All accepted manuscripts are placed on the Web page of the journal and are available at the address: http://MaterialsScience.pwr.wroc.pl

All published papers are placed on the Web page of the journal and are **freely accessible** at the address: http://MaterialsScience.pwr.wroc.pl

Materials Science-Poland is abstracted/indexed in: Chemical Abstracts, Materials Science Citation Index, Science Citation Index Expanded, Scopus.

The Journal is supported by the State Committee for Scientific Research

Printed in Poland

Drukarnia Oficyny Wydawniczej Politechniki Wrocławskiej
Zam. nr 1103/2009.

Materials Science-Poland, *Vol. 27*, *No. 4/1*, *2009*

Interaction of Pb with hydrating alite paste XPS studies of surface products

W. NOCUŃ-WCZELIK*, M. NOCUŃ, G. ŁÓJ

University of Science and Technology AGH, Faculty of Materials Science and Ceramics,
30-059 Cracow, Al. Mickiewicza 30, Poland

A study into the effect of Pb-bearing compounds on hydration of cement has been carried out, using simplified cement models, including models for alite and gypsum. The kinetics of hydration of these compounds was evaluated by the calorimetry method. The microstructure has been characterized, and X-ray photoelectron spectroscopy was used to analyze thin layers of products formed on the surface of hydrating grains. Depending on the composition of the initial mixture and Pb-bearing compounds various effects were observed. When pure PbO was used as the additive, the reaction of alite with water was significantly accelerated but when the additive consisted of a mixture of PbO and gypsum, the alite/water reaction was retarded, as in the case of cement. As was found by the XPS studies, a part of Pb^{2+} ions enters the reaction with sulfate ions and the barrier of $PbSO_4$ which is poorly soluble is thus formed. Furthermore, lead introduced to the hydrated alite suspension is strongly bound by C–S–H, as can be derived from high binding energies of core electrons on Pb 4f orbitals.

Key words: alite; calorimetry; hydration; lead; XPS

1. Introduction

The interaction of cement paste/concrete mixtures with compounds containing heavy metals has been investigated for a long time [1–5]. Detailed studies focused on the immobilization (stabilization) of these materials in cement matrices [2–5]. Such interactions typically occur in waste products from the industrial manufacture of cement/concrete, for example with fly ash of various origins. Lead(II) oxide (PbO) is the most commonly occurring heavy metal impurity but other compounds such as sulfates, chlorides and nitrates also occur. As is well known, the latter compounds show better solubility in water than PbO.

Heavy metal compounds affect strongly the setting, hardening as well as the durability of cement paste/hardened material. As was reported over 30 years ago, small amounts of solid PbO or ZnO added to cement paste retard strongly the hydration process [1]. This effect has been attributed to the formation of an impermeable layer

* Corresponding author; e-mail: wiesia@uci.agh.edu.pl

of products – heavy metal hydroxides or other compounds produced as a result of C_3S hydration in the presence of these oxides. Calorimetric studies revealed a prolonged, dormant period with a "gap" of many hours between the first and the second heat evolution peaks [1]. The author [1] was of the opinion that full explanation of this serious retarding effect was not possible.

The retarding effect of Pb or other heavy metal compounds (salts) on hydration of cement was also proved in some later works [6, 7]. The hindering of the hydration process, depending on the additive content, was confirmed by calorimetric measurements. These results were compatible with delayed setting and hardening of cement mortars. However, for PbO content not exceeding 1–2 wt. % of cement, the data showed good conformity with the standard manufacturing requirements; the later strength results were even higher. There were no significant changes in water uptake or stability of volume.

The effect of heavy metals has been widely studied from the point of view of their immobilization in hardened cement matrix [2–4]. The researchers focused on studying the stabilization mechanism and leaching of heavy metals from various cement based materials. A very high degree of Pb immobilization was reported, as well as the formation of a highly disordered hydration product – calcium silicate hydrate (so-called C–S–H), in the presence of heavy metal compounds was found [3, 8–10].

It seems that the effect of PbO on cement/concrete hardening is principally attributed to the hydration of alite – the main constituent of cement but there are also some other aspects. The studies presented in this paper started on cements and were subsequently continued using alite samples. This is now common practice in research work [11]. Additionally, in previous works a close similarity was detected between the synthetic C–S–H phases and the cement pastes, used as immobilizing materials for heavy metals [8, 9].

2. Experimental

Synthetic alite was produced by repeated heating of analytically pure calcium carbonate and a silica gel mixture at 1450 °C. A small quantity of magnesium and aluminum hydroxides was added to facilitate the synthesis and to make the alite composition similar to those occurring in cements (MgO and Al_2O_3 contents – 0.3 and 0.5 wt. % of alite). The phase composition of final products was controlled by XRD. The sinter was subsequently ground in a laboratory ball mill to a Blaine specific surface of 3000±50 cm^2/g. The calcium sulfate dihydrate was also used as a component of the hydrating mixtures. In the experiments, the PbO additive was used (as it is the one most frequently occurring in wastes) or $Pb(NO_3)_2$ (easily soluble). PbO and $Pb(NO_3)_2$ were taken as materials of analytical purity.

Differential calorimetry was applied, similarly as in the case of cements, as a basic method of evaluating the hydration progress. The rate of heat evolution was monitored with a BMR type nonisothermal nonadiabatic calorimeter (constructed in the Institute of Physical Chemistry, Polish Academy of Sciences, Warsaw) on 5 g alite samples

mixed with water: the water-to-alite ratio was 0.5. The external (reference) temperature was 25 °C.

The experiments for the estimation of the composition of liquid phase were carried out on the suspension with excess water (w/s = 10). The suspensions were shaken and, after a time, filtered using a vacuum pump. The samples were collected after 10 min (i.e., at the beginning of the process when the dissolution occurs), 1 h (during the latent period, when the nuclei of products are formed), 10 h (when the formation of early hydrates is advanced, if there is no hindrance effect from admixtures) and 24 h (the formation of hydrates is generally completed if not seriously hindered).

Calcium, lead(II) and sulfate ion concentrations in the filtrate were determined by the ICP method. SEM and EDS studies (scanning electron microscope JEOL 5200 with the LINK ISIS equipment) were performed on the pieces of hydrated samples (soaked in acetone and dried). XRD studies were carried out on the powdered samples (ground and washed with acetone, before being finally dried).

In order to extract some information about the chemical composition of the products formed on the surface of the hydrating alite grains, the samples were specially prepared and were subjected to very sensitive X-Ray photoelectron studies (XPS) with an XPS spectrometer produced by VSW. The method is based on measuring the energy of photoelectrons (core electrons emitted from the internal atomic orbitals as a result of soft X-ray radiation in high vacuum, ca. 3×10^{-8} mbar; X-ray source characteristics: Al K_α, 200 W (10 kV, 20 mA), calibration on the C 1s peak position assuming 284.6 eV as a C–H peak position). These energies provide information concerning the chemical environment of analyzed atoms – the composition of the surface layer of molecular thickness. This method has not been applied frequently in the chemistry of cements. The data appertaining to alite hydration of short duration, based upon the XPS studies, were firstly reported by Ménétrier et al. [12]. One of the authors of the present work applied this method to investigate the products formed in alite paste hydrated with microsilica addition [13]. The analysis of the spectra related to alite hydrated in a Pb-containing environment was done using different databases with respect to Pb compounds; some measurements on the reference samples were also done. Special preparation of hydrating material consisted in the separation of coarse alite grains (>80 μm), their 24 h hydration in excess water (at water to alite ratio 10) and very careful washing with acetone on the 60 μm sieve, to remove smaller particles from the suspension.

3. Results and discussion

The sets of calorimetric curves are shown in Figs. 1–3. As is evident from the microcalorimetric curves, for PbO additive, the reaction of alite with water is accelerated (Fig. 1), while for lead nitrate the acceleration stage is retarded at higher concentrations but afterwards the process is more intense (Fig. 2).

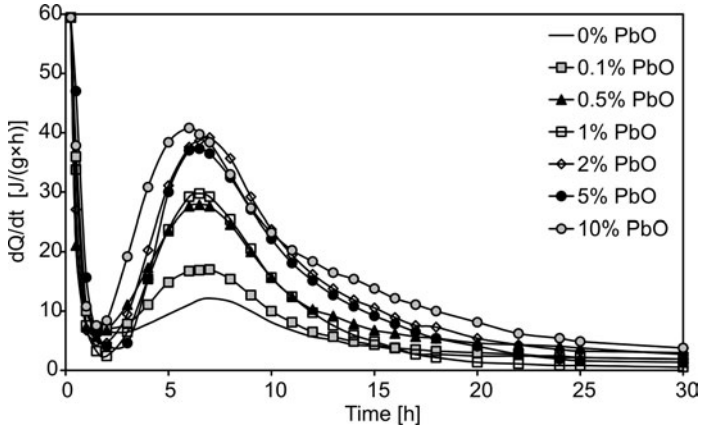

Fig. 1. Heat evolution during hydration of alite with PbO in water

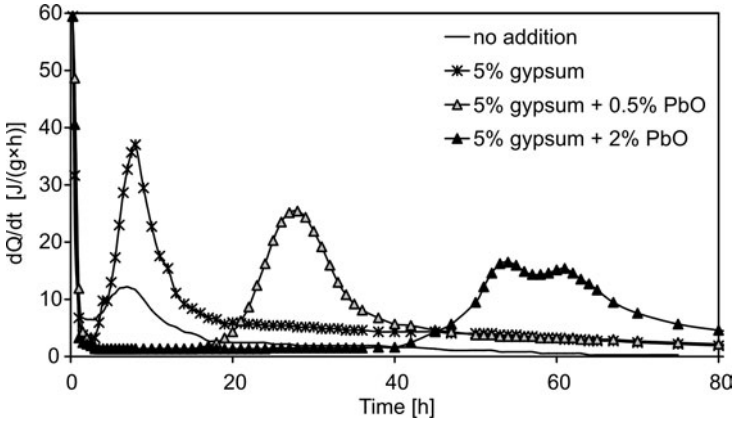

Fig. 2. Heat evolution during hydration of alite + gypsum +PbO

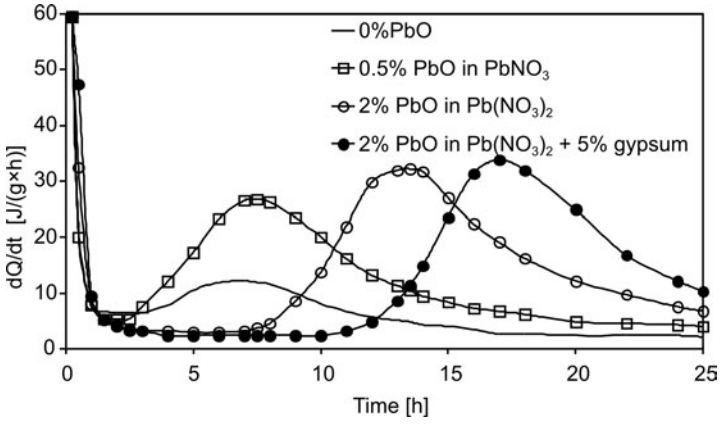

Fig. 3. Heat evolution during hydration of alite and alite + gypsum in $Pb(NO_3)_2$ solution

However, gypsum and PbO introduced simultaneously cause retardation of alite reaction with water, as well as some reduction of the height and modification of the shape of the main heat evolution peak (Fig. 3). This retarding effect is clearly lower in the lead nitrate solution (shorter induction period, Figs. 2 and 3). XRD studies did not reveal any new phases apart from C–S–H and gypsum.

Table 1. Binding energies (E_b) of core electrons and relative distribution of energies (*ED*) among particular bands/elements on the surface of hydrate alite grains from XPS measurements

Sample		O 1s			Si 2p		Ca 2p		Pb 4f		S 2p
Alite	E_b [eV]	533.2	531.6		102.0		351.9	348.5			
	ED [%]	55.2	17.6		4.3		6.4	16.4			
Alite hydrated	E_b [eV]	532.3	530.9		102.2	99.5	347.7	345.5			
	ED [%]	44.2	34.3		6.1	1.4	11.7	2.2			
Alite	E_b [eV]	532.7	531.4		102.6	100.6	348.0	347.2			170.2
+gypsum hydrated	*ED* [%]	62.6	23.9		4.4	0.9	18.1	4.6			5.1
Alite hydrated + PbO	E_b [eV]	531.5	530.9		102.7		348.2		140.1	138.5	
	ED [%]	73.2	5.9		8.1		11.5		0.9	0.4	
Alite + gypsum	E_b [eV]	533.0	531.5		103.5		348.9	347.3	140.4		168.0
+ PbO hydrated	*ED* [%]	51.4	24.5		8.5		9.6	1.7	1.5		1.9
Alite hydrated	E_b [eV]	532.5	530.0		102.8		348.3		140.0	138.8	
in $Pb(NO_3)$	*ED* [%]	70.6	6.2		8.1		13.7		0.9	0.5	
Alite +gypsum	E_b [eV]	532.7	531.4	529.7	103.0		348.4	346.5	140.2	138.6	168.5
hydrated in $Pb(NO_3)$	*ED* [%]	55.4	10.7	8.0	8.8		9.3	3.2	1.1	0.7	2.8

The treatment of the data produced as the results of XPS measurements was done with the aid of the XPSPEAK 4.1 program. The binding energies of core electron bonds on the atomic orbitals O 1s, Ca 2p, Pb 4f, S 2p were measured (Table 1) and subsequently compared to the database for XPS. As this database appeared to be insufficient for interpretation of XPS results for our disordered materials, the spectra recorded were identified and attributed to particular compounds based on other data occurring in the database and on the previous results. [13]. Some results were presented as a scheme of distribution of binding energies attributed to the core electrons on the O 1s and Ca 2p orbitals among the particular compounds occurring on the surface of hydrate alite grains (see Fig. 14)

The effect of PbO on the heat evolution during the reaction of alite with water differs from that observed in case of cement. PbO has no retarding influence on the neat alite paste (see Fig. 1). What is more – the substantial acceleration of alite hydration in the presence of PbO takes place, as is proved by an increase in the main heat evolution peak. Therefore one can conclude that the PbO hampering effect in cement paste, first reported many years ago [1], most probably should be attributed to the presence of components of cement other than silicates. In order to verify this assumption, 5% of gypsum was added to alite + PbO and the hindering effect similar to that observed for cement paste (see Fig. 3) appeared. The induction period increased with the amount of the additive. However, the hindering effect was less visible as the additive was intro-

duced in the form of lead nitrate solution (Fig. 2). When gypsum is not present in the mixture, the effect of lead in the form of soluble $Pb(NO_3)_2$ on alite hydration differs from that at PbO admixture (see Figs. 1 and 2). The calorimetric curve for the $Pb(NO_3)_2$ concentration, corresponding to 0.5% PbO, is almost identical, while at higher $Pb(NO_3)_2$ concentration, the prolonged induction period is followed by the accelerated reaction with a high dQ/dt peak. Obviously, one cannot exclude the nucleation effect of small PbO particles, however there are other factors involved.

The concentrations in the liquid phase shed some light on the process; however one should remember about the higher water-to-solid ratio, compared with the paste. From the solubility point of view there is no problem, because the solubility of the initial material and the hydration products is very low (calcium hydroxide and gypsum, considered as being highly soluble hydrated materials, exhibit solubility at the level of 1–2 g/dm^3). The excess of water and continuous agitation of the suspension may facilitate the dissolution and abrasion of an unstable gel-like product deposited on the hydrating grains. However, the results reflect the phenomena occurring in the hydrating systems and match well with the calorimetric data. Calcium concentrations in the alite suspensions with PbO after 10 min, 1 h 10 h and 24 h show no significant differences (Fig. 4).

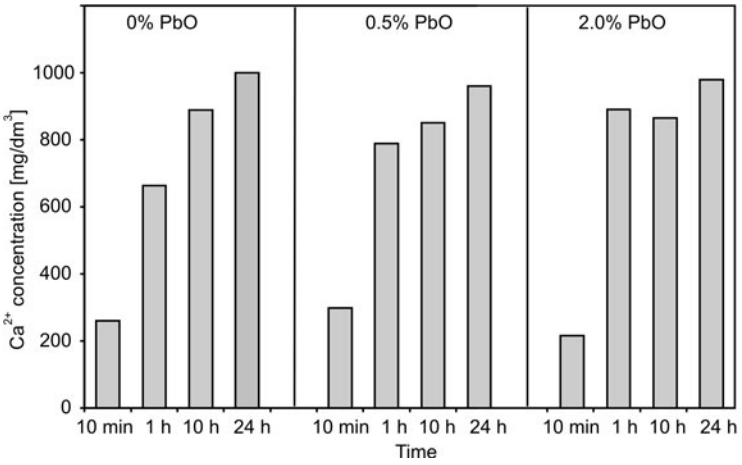

Fig. 4. Concentration of Ca^{2+} ions in the liquid phase during hydration of alite + PbO in water suspension (w/c = 10). Concentration of Ca^{2+} ions is not specially affected by the presence of PbO in the suspension. The saturation level with respect to calcium hydroxide is not attained

Upon addition of gypsum, the calcium concentration decreases when PbO is present in the suspension (Fig. 5). On the other hand, the lead ions in alite suspensions, which are effectively bound when introduced as 0.5% PbO, at 2% PbO, reveal higher concentrations. The maximum Pb ion concentration (fig. 6, after 10h) corresponds to ca. 30% of total PbO present in the suspension (70% is in the solid phase). This should be attributed to the effect of PbO transformation into the anionic complex [2], being the conse-

quence of the amphoteric character of lead. It seems also reasonable that after a superficial incorporation (or adsorption) of Pb into C–S–H the "excess" Pb ions remain in the alkaline liquid phase. In the gypsum-containing suspensions, the concentrations of Pb ions are negligible for 0.5% PbO addition. However for 2% PbO, the lead concentration increases but is much lower than in the absence of sulfate ions (see different scales in Figs. 6 and 7).

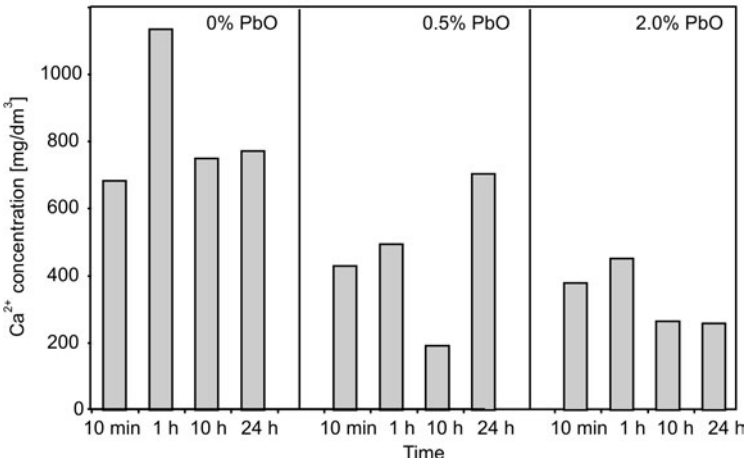

Fig. 5. Concentration of Ca^{2+} ions in the liquid phase during hydration of alite + gypsum + PbO in water suspension (w/c = 10). In the presence of gypsum and PbO, the concentration of Ca^{2+} ions is much lower than without gypsum. One should remember that the concentration of ions after a few hours corresponds to some intermediary situation between dissolution and precipitation from the liquid

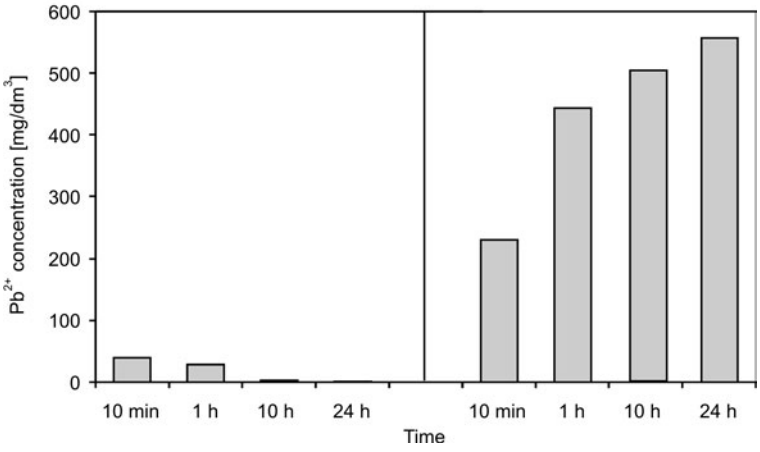

Fig. 6. Concentration of Pb^{2+} ions in the liquid phase during hydration of suspension of alite + PbO in water (w/c = 10). For a low PbO content, the there are hardly any Pb cations in the liquid phase (PbO consumption in the alkaline liquid – dissolution and precipitation). For a higher PbO content, the dissolution of PbO in alkaline suspension, followed by precipitation of Pb containing compounds takes place but there is always an excess of not precipitated Pb^{2+} ions

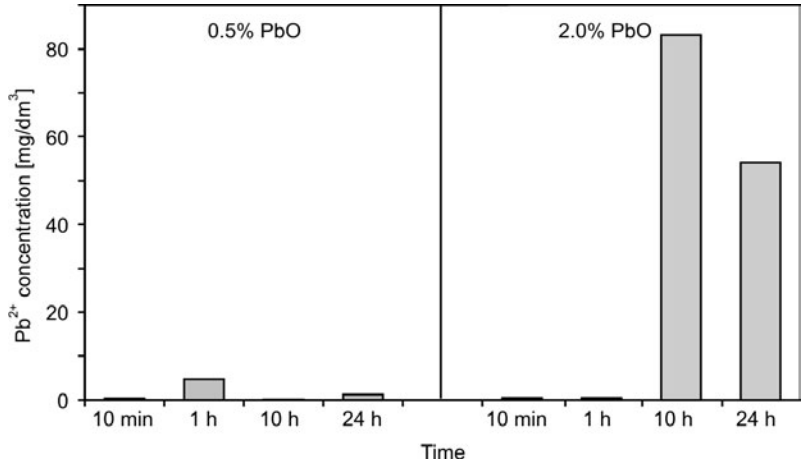

Fig. 7. Concentration of Pb^{2+} ions in the liquid phase during hydration of suspension of alite + PbO + gypsum in water suspension (w/c = 10) (note various scales in Figs. 6 and 7!). The concentration of Pb^{2+} ions is very low even for higher initial PbO content. The higher Pb contents for 2% PbO obtained after 10 h and 24 h reflect the instability of hydrating suspension and a competition between dissolution and precipitation of newly formed phases

The sulfate ion concentrations decrease systematically. The ions react with Ca and Pb ions and they also enter the C–S–H structure (SEM – EDS results), however their concentrations are higher after a time corresponding still to the induction period on the heat evolution curve for alite + gypsum + 2% PbO mixture.

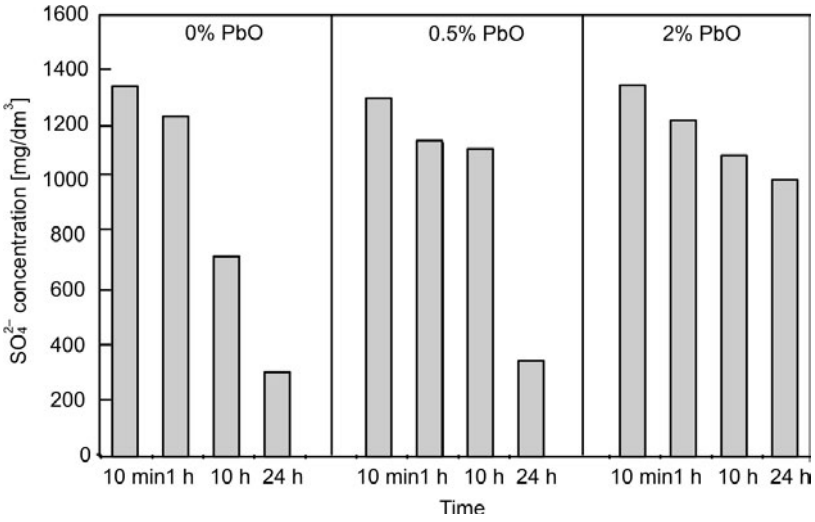

Fig. 8. Concentration of SO_4^{2-} ions in the liquid phase during hydration of suspension of alite + gypsum + PbO in water suspension (w/s = 10). Rather high concentration of sulfate ions at the beginning of the hydration further decreases upon time. It seems to be related to the calcium sulfate than to lead sulfate solubility

The retarding effect observed for the mixture of alite with gypsum, similar as in the case of portland cement paste, leads to the presumption that a part of Pb^{2+} ions enters the reaction with sulfate ions, and the barrier of poorly soluble $PbSO_4$ is thus formed. Sulfate ions in alite paste without any other additive cause acceleration of hydration. Gypsum dissolves relatively well, and it is present in the liquid phase, together with calcium ions (from gypsum and alite) being in an equilibrium (see Fig. 8). Subsequently an intense precipitation of calcium hydroxide and C–S–H takes place, as was confirmed by a very high heat evolution peak on the *dQ*/*dt* curve. One can presume that in the liquid phase of high concentration (water-to-solid ratio = 0.5) of complex composition in which, apart from calcium, silicate and sulfate ions, also lead ions appear, a new (pseudo)equilibrium can occur and the crystallization of $PbSO_4$ is possible; this phase can form a thin, impermeable membrane. The membrane collapses after a time. The crystallization of compounds more complex than simple sulfate cannot be excluded. High saturation of the liquid phase, numerous components, shortage of good analytical procedures of chemical composition determination give no possibility of obtaining a satisfactory set of data for verification of thermodynamic predictions indicating which phases might be potentially formed.

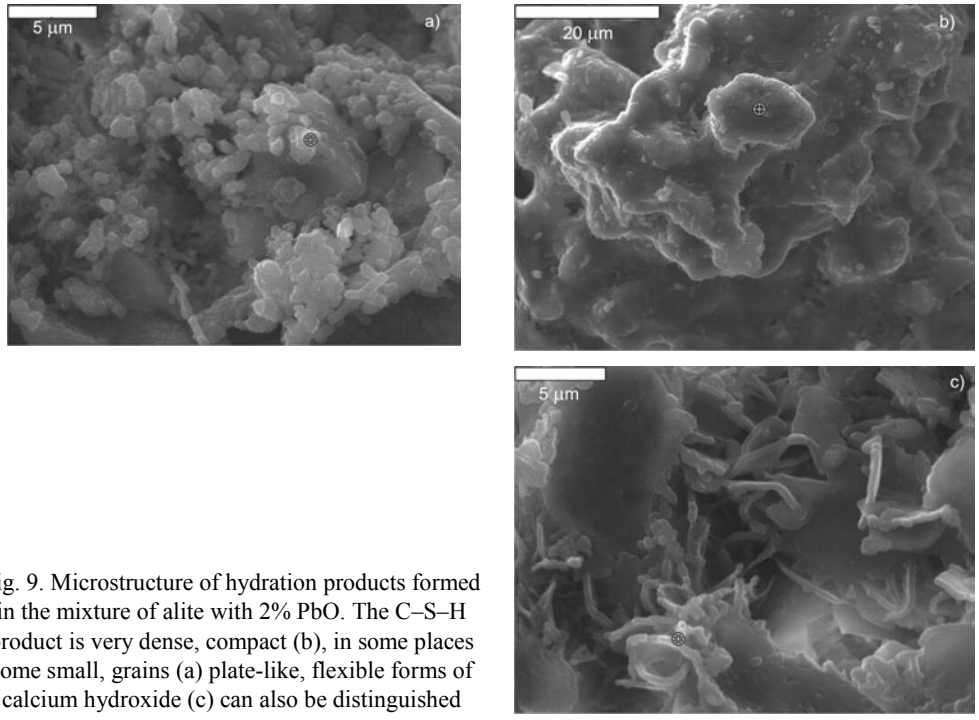

Fig. 9. Microstructure of hydration products formed in the mixture of alite with 2% PbO. The C–S–H product is very dense, compact (b), in some places some small, grains (a) plate-like, flexible forms of calcium hydroxide (c) can also be distinguished

A compact matrix of C–S–H phase, built up from very fine, well adherent particles, is the main component of alite pastes doped with Pb compounds (Figs. 9–13). In the areas of loose structure one can observe small, deformed portlandite platelets as

well as C–S–H short rods. In many analytical points in C–S–H particles Pb is easily detectable (Fig. 10).

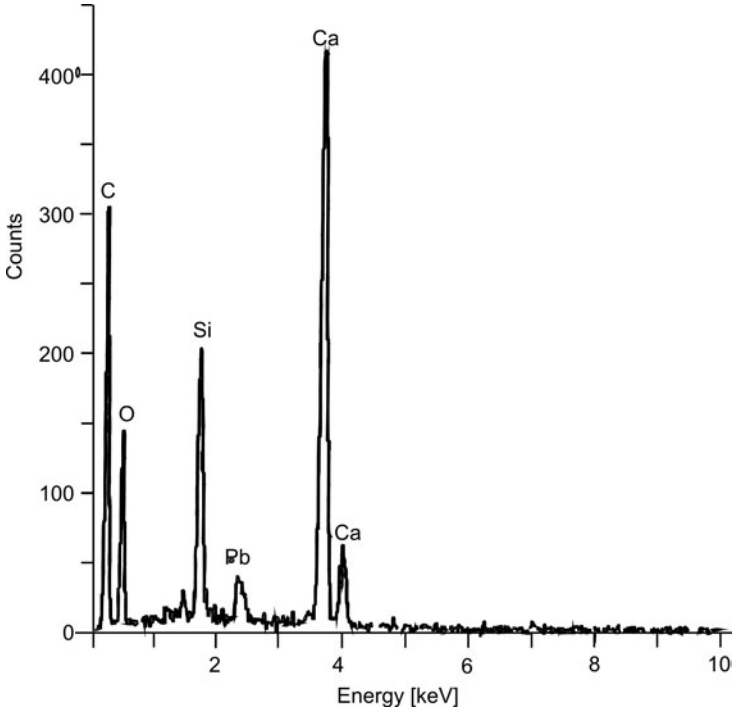

Fig. 10. EDS analysis in the spot shown in Fig. 9a. Pb is built up to the C–S–H

Because the attempt of detecting lead-containing phases by XRD failed (too low content or amorphous character), X-Ray electron spectroscopy was applied for the chemical analysis of the surfaces of hydrated grains. This method was adopted mainly to acquire additional information about the "binding state" of Pb with the alite hydrating surface. It was found that the binding energies of core electrons relating to the Pb 4f orbital (≥ 140 eV, in some cases splitting with some lower value) should be mainly attributed to the occurrence of lead in the form of $PbSO_4$; similar values are characteristic of Pb in complex organic compounds. It was also found that the binding energies of core electrons on the S 2p orbitals in the samples with Pb correspond to the sulfate ions bound in $PbSO_4$ (binding energies of core electrons 2p in sulfur atoms are lower in the case of gypsum; this has been also verified experimentally in this work). However, because there is a disproportion between the total energy values (surfaces of bands), showing the shortage of sulfate ions on the surfaces of hydrating alite grains to transform all the Pb ions into sulfate (in the samples with lead- and sulfate-bearing components), one can conclude that the part of Pb^{2+} is built in superficial parts of the C–S–H phase. In the samples with Pb compounds containing no sulfate, high energies of XPS spectra (≥ 140 eV) were also recorded.

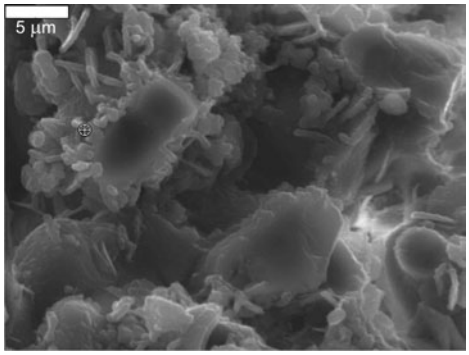

Fig. 11. SEM. Microstructure of hydration products formed in alite paste processed with $Pb(NO_3)_2$ solution (concentration corresponds to 2% PbO by mass of alite), similar to that produced with 2% PbO

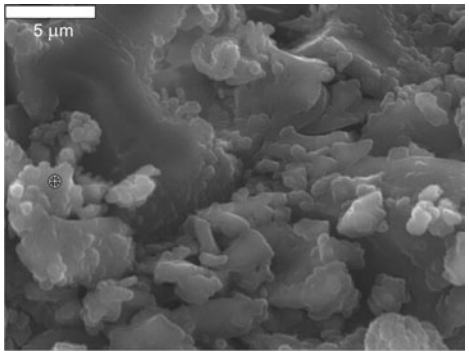

Fig. 12. SEM. Microstructure of hydration products formed in 95% alite + 5% gypsum mixture with 2% PbO. Massive, uniform C–S–H together with small, poorly separated grains

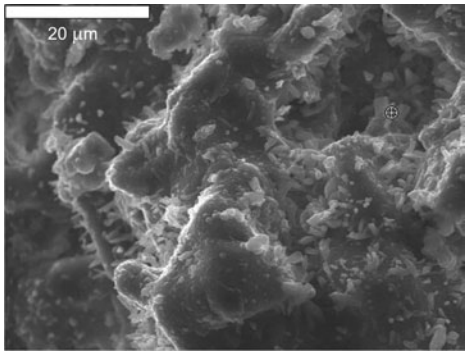

Fig. 13. Microstructure of products of hydration formed in the 95% alite + 5% gypsum mixture with 2% PbO (dense, compact, low porosity; similar as that in Fig. 9b)

XPS measurements provided other information regarding hydrating samples. XPS analysis of the surface of the alite sample exposed to water revealed the presence of C–S–H and calcium hydroxide in the layer that was only a few molecules thick. When alite is hydrated in the mixture with gypsum at excess water, a substantial part of C–S–H is replaced by a sulfate product – undoubtedly gypsum. With the addition of PbO to the hydrating suspension, there is no portlandite on the alite surface but the $PbO/Pb(OH)_2$ together with Pb incorporated to the C–S–H can be derived from distribution of oxygen. Addition of gypsum with PbO to the hydrating alite gives in turn C–S–H with strongly bound Pb (with energy $\geq$ 140 eV, as mentioned above). The formation of lead sulfate results from the presence of sulfate anion with binding energies of core electrons 2p in sulfur atoms attributed to sulfate anion in $PbSO_4$ (as discussed above). The composition of hydrated alite surface is modified also when the hydration takes place in the lead nitrate solution – Pb is then incorporated to the C–S–H phase, some amount of portlandite crystallizes. When gypsum is introduced to this mixture, one can find C–S–H modified by Pb, $PbSO_4$, as well as by some amount of $PbO/Pb(OH)_2$ and portlandite.

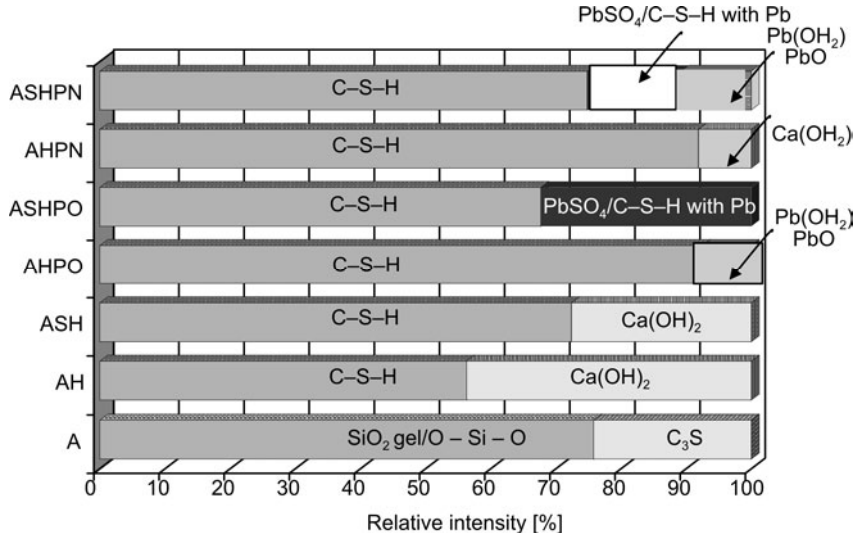

Fig. 14. Distribution of binding energies of core electrons on O 1s orbitals among particular compounds on the surface of hydrated alite grains, from XPS measurements (A – alite; H – hydration in water suspension, S – gypsum, PO – PbO, PN – $Pb(NO_3)_2$)

The spectrum of alite coarse grained surface in Pb^{2+} ions and gypsum containing suspension is complex. One should remember that alite was shaken with water (*w*/*s* = 10) and it could be the reason why only a part of $PbSO_4$ was precipitated on the surface of grains (this compound shows some solubility). It should be underlined that throughout all the measurements a strong bond is seen between Pb and a component of hydrated alite paste – mainly C–S–H. Therefore C–S–H in the experiments reported in the presented work acts as a Pb ion immobilizing environment. Recently in some reports the Ca–Pb–S–H formula appeared, as attributed to the C–S–H soaked with Pb ions; this combination has been fully described based on the microstructure and microprobe analysis [5].

4. Conclusions

PbO additive does not retard the hydration of alite as in cement paste. A significant acceleration of heat evolution and heat evolved value is observed with increasing PbO content. Upon the addition of gypsum to the alite paste, hydrated with PbO or $Pb(NO_3)_2$, the reaction becomes strongly retarded – a substantial elongation of the induction period takes place. In alite pastes hydrated with Pb-bearing compounds, there are no other phases, apart from alite and alite hydration products (C–S–H and portlandite), according to XRD analysis. The microstructure of alite pastes hydrated with Pb compounds shows the presence of compact, homogenous C–S–H (poorly distinguishable, highly adherent, small particles) with Pb bound to the surface. The

portlandite crystals are imperfect, with declination from a hexagonal shape. Lead introduced to the hydrated alite suspension is presumably incorporated into the C–S–H phase, as it can be derived from the high binding energies of core electrons on Pb 4f orbitals. The sulfate ions in Pb^{2+} containing hydrated suspension are combined in $PbSO_4$.

References

[1] LIEBER W., 5th International Symposium on the Chemistry of Cement, Tokyo, 2 (1968), 444.
[2] GLASSER F.P., *Immobilisation potential of cementitious materials*, [In:] *Environmental Aspects of Construction with Waste Material*, Elsevier, Amsterdam, 1994.
[3] NOCUŃ-WCZELIK W., MAŁOLEPSZY J., 10th International Congress on the Chemistry of Cement, Goeteborg, 4 (1997), 4iv043.
[4] TAMAS F.D., CSETENYI L., TROTTHART J., Cem. Concr. Res., 22 (1992), 399.
[5] LEE D., SWABRICK G., WAITE T.D., Cem. Concr. Res., 35 (2005), 1027.
[6] NOCUŃ-WCZELIK W., MAŁOLEPSZY J., Thermochim. Acta, 269/270, (1995), 613.
[7] NOCUŃ-WCZELIK W., ŁÓJ G., 11th International Congress on the Chemistry of Cements, Durban (2003), 1803.
[8] NOCUŃ-WCZELIK W., TRYBALSKA B., RAKOWSKA A., Polish Ceramic Bull., 46 (1994), 289.
[9] NOCUŃ-WCZELIK W., *Structure and properties of hydrated calcium silicates*, Polish Academy of Sciences, Committee of Ceramics, Cracow, Poland, 1999.
[10] RIGO E., GIES H., KRUG M., MISKIEWICZ K., STADE H., WIEKER W., Zement-Kalk-Gips, 53 (2000), 414.
[11] KURDOWSKI W., NOCUŃ-WCZELIK W., Cem. Concr. Res., 13 (1983), 341.
[12] MÉNÉTRIER D., JAWED I., SUN T.S., SKALNY J., Cem. Concr. Res., 9 (1979), 473.
[13] NOCUŃ-WCZELIK W., 12th Int. Congr. on X-Ray Optics and Microanalysis, Cracow, Poland, 2 (1989), 811.

Received 4 April 2008
Revised 7 April 2008

Materials Science-Poland, *Vol. 27*, *No. 4/1*, *2009*

High temperature impedance spectroscopy study of non-stoichiometric bismuth zinc niobate pyrochlore

K. B. TAN[1*], C. C. KHAW[2], C. K. LEE[3], Z. ZAINAL[1], Y. P. TAN[1], H. SHAARI[1]

[1]Faculty of Science, Universiti Putra Malaysia, 43400 Serdang, Selangor, Malaysia

[2]Faculty of Engineering and Science, Universiti Tunku Abdul Rahman, 53300 Kuala Lumpur, Malaysia

[3]Academic Science Malaysia, 902-4 Jalan Tun Ismail, 50480 Kuala Lumpur, Malaysia

Single phase non-stoichiometric bismuth zinc niobate, $Bi_3Zn_{1.84}Nb_3O_{13.84}$ was prepared by a conventional solid state method. The sample was refined and fully indexed on the cubic system, space group *Fd*3*m*, $Z = 4$ with $a = 10.5579(4)$ Å. Electrical characterisation was performed using an ac impedance analyser over the temperature range of 25–850 °C and frequency range of 5 Hz–3 MHz. Typical dielectric response was observed in $Bi_3Zn_{1.84}Nb_3O_{13.84}$ with high relative permittivity, low dielectric loss and negative temperature coefficient of capacitance, with the values of 147, 0.002 and –396 ppm/°C, at 100 kHz at ambient temperature, respectively. The material is highly resistive, with the conductivity of 10^{-21} $ohm^{-1}\cdot cm^{-1}$ and a high activation energy of ~1.59 eV.

Key words: *activation energy; bismuth zinc niobate; dielectric response; impedance spectroscopy; pyrochlore*

1. Introduction

Due to its excellent properties, advanced ceramics have been used in a wide range of industrial applications such as electrical and electronic components, superconductors, catalyst and automobile components [1–3]. The study of advanced ceramic materials involves many disciplines, including chemistry, physics, mechanical engineering, materials science and metallurgy. Both electroceramics and structural ceramics are classified as advanced ceramics, and they have different applications. Applications of electroceramics involve electrical and magnetic properties, whereas applications of structural ceramics mainly rely on their mechanical behaviour [4].

One of the promising candidates in electroceramics is bismuth pyrochlore [5]. Pure bismuth oxides are highly reactive, volatile and thermally unstable with poly-

*Corresponding author, e-mail: tankb@science.upm.edu.my

morphic transitions in which monoclinic α-Bi_2O_3 transforms to a defect fluorite δ-Bi_2O_3 above 729 °C, and then followed by the formation of two metastable phases, tetragonal β-Bi_2O_3 and body-centred cubic γ-Bi_2O_3, while cooling down [6]. However, bismuth derivatives are suitable and cost effective for various commercial applications, particularly in microwave and radio frequency applications, due to their low firing temperatures This follows the trend of miniaturisation with passive integration using multilayer ceramic technology whereby active or passive components are laminated and co-fired at low temperatures. In general, pyrochlore materials have the formula $A_2B_2O_7$, indicating the existence of two different crystallographic sites, namely a relatively larger 8- coordinate A site and a smaller 6-coordinate B site within the structure. These sites are commonly occupied by a combination of A^{3+} and B^{4+} cations, A^{2+} and B^{5+} cations or other combinations with a required average mixed valency [7]. By far the most extensively studied Bi-based dielectrics are the cubic pyrochlore $Bi_{3/2}ZnNb_{3/2}O_7$ ($k' = 150$, $t_k = -400$ ppm/°C) and the monoclinic zirconolite phase ($k' = 80$, $t_k = 200$ ppm/°C). Their permittivities have temperature dependencies of opposite signs. Consequently, the two dielectrics are considered to be a good pair to obtain new dielectrics with good temperature dependences by combining them.

An "ideal" composition for a pyrochlore phase in the Bi_2O_3–ZnO–Nb_2O_5 (BZN) system could be $Bi_3Zn_2Nb_3O_{14}$, referred to as P, in which the expectation is that a part of Zn and all Bi would be disordered over the large, 8-coordinate A sites; the remainder of Zn, together with Nb, would be disordered over the octahedral B-sites. However, it has been shown that the material of composition $Bi_3Zn_2Nb_3O_{14}$ contains excessive ZnO as a second phase and lies outside the BZN subsolidus solid solution area [9–13]. The pure phase composition was confirmed to be ZnO deficient by electron probe microanalysis and a combination study of electron, neutron and X-ray diffraction.

Since the 1990's many of the fundamental aspects of BZN materials have been clarified. However, there are inconsistencies in the literature regarding the characterisation of BZN materials, particularly electric permittivities of multiphase samples from various researchers are scattered in the range of 80–120 [9–13]. Preliminary electrical studies on Bi_2O_3–ZnO–Nb_2O_5 ternary system indicate that these materials are highly insulating and their conductivities are not likely to be determined at temperatures below 500 °C. However, it is possible to measure permittivities at high frequencies at ambient temperatures and above. An overall objective of electrical characterisation is to investigate the effects of composition and temperature on the bulk permittivity, i.e. variation of bulk permittivity with composition and whether the permittivity varies, positively or negatively with temperature. Investigation of various possible sources of error and variations in permittivity measurements are therefore indispensable before a firm conclusion can be drawn in correlating permittivity with density, sintering temperature and electrodes. The electrical data were collected on samples whose sintering conditions have been optimised with respect to the capacitance value, bismuth loss and pellet density. The focus of this paper is on the high

temperature electrical behaviour of optimised $Bi_3Zn_{1.84}Nb_3O_{13.84}$ via a systematic impedance spectroscopy study.

2. Experimental

Cubic pyrochlore $Bi_3Zn_{1.84}Nb_3O_{13.84}$ was prepared via conventional solid state reactions using Bi_2O_3 (Alfa Aesar, 99.99 %), ZnO (Alfa Aesar, 99.99 %), and Nb_2O_5 (Alfa Aesar, 99.99 %) as starting materials. ZnO and Nb_2O_5 were dried at 600 °C while Bi_2O_3 was dried at 300 °C for 3 h prior to weighing. Stoichiometric quantities of the oxides were weighted and mixed with sufficient volume of acetone in an agate mortar to ensure the homogeneity of the mixture. The resulting powder was transferred into a gold boat and pre-fired at 700 °C for 24 h (below Bi_2O_3 melting point of ca. 825 °C) in a Carbolite muffle furnace. Subsequently, the mixture was fired at temperatures of 800 °C and 950 °C for 24 h with intermediate regrinding. The phase purity of the sample was examined at room temperature by X-ray diffraction using a Shimadzu X-ray powder diffractometer XRD-6000 equipped with a diffracted-beam graphite monochromator, with CuK_α radiation (1.5418×10^{-10} m). Pellets of a single phase sample were prepared using a stainless steel die measuring 8 mm in diameter. A sufficient amount of powder was added, cold pressed uniaxially, and sintered at 1050 °C in order to increase the mechanical strength and to reduce the intergranular resistance in the pellets. Gold paste (Engelhard) was smeared and hardened onto parallel faces of the ceramics. The pellets with gold electrodes attached were placed on a conductivity jig and inserted in a horizontal tube furnace. The pellets were characterised using an ac Hewlett Packard LF HP4192A impedance analyser over the frequency range from 5 Hz to 1.3×10^7 Hz with the applied voltage of 100 mV. Conductivity measurements were carried out over the temperature range of 28–850 °C on heating and cooling cycles at each 50 °C interval. The samples were allowed to equilibrate at each temperature for 30 min prior to measurement. Most measurements were made in air, and, if necessary, in oxygen free nitrogen (OFN) at the flow rate of 80 cm^3/min for reducing atmosphere study. The nitrogen gas was supplied to the sealed tube furnace for 1 h in order to create an equilibrated nitrogen atmosphere prior to measurement.

3. Results and discussion

The electrical properties of optimised $Bi_3Zn_{1.84}Nb_3O_{13.84}$ pellets with the density of ca. 90 % sintered at 1050 °C were determined by ac impedance spectroscopy over the frequency range of 5 Hz–13 MHz in air. The measured impedance data are represented in the Nyquist form with a typical complex plane plot (Z'' vs. Z'). The impedance is normalised by the geometric factor and represented in the form of the dependence $\rho^* = Z^*(S/d) = \rho' + j\rho''$ where ρ^* is the complex resistivity and S/d is the geometric factor. The parameters S and d represent the area and the separation of the electrodes

[14, 15]. Perfect semicircles are only observed in the Cole–Cole plots of cubic pyrochlore $Bi_3Zn_{1.84}Nb_3O_{13.84}$ above 550 °C (Fig. 1).

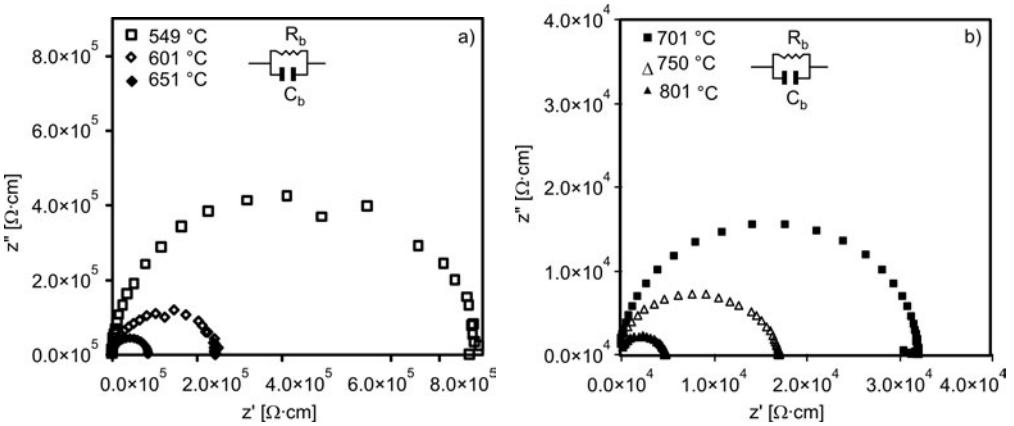

Fig. 1. Cole–Cole plots of $Bi_3Zn_{1.84}Nb_3O_{13.84}$ at various temperatures

The impedance data can be represented by the equivalent circuit shown in the inset of Fig. 1. The circuit consists of parallel R and C elements of the bulk material and the total impedance Z^* for the circuit is given by:

$$Z^* = \frac{1}{j\omega C + \frac{1}{R}} = \frac{R}{1 + j\omega CR} = Z' - jZ'' \tag{1}$$

An associated capacitance of 1.19×10^{-11} F·cm^{-1} (after correction for jig) is obtained at 549 °C and this corresponds to the bulk properties of the material. The corresponding bulk resistivities, R_b from ca. 8.3×10^5 to ca. 2×10^3 Ω·cm over the temperature range 550–850 °C are obtained from the intercept on the real part of the impedance. This could be associated with the increase in thermally activated drift mobility of electric charge carriers according to the hopping conduction mechanism. In addition, the resistivity falls as the temperature increases, because the probability of carriers being promoted into the conduction band, or being transferred from one defect to another is governed by thermal fluctuations which are described by the Boltzmann statistics [16]. On the other hand, higher dielectric polarisation may result in higher electric permittivities and higher losses as the temperature increases [17].

For a highly resistive material, the Nyquist diagram is not completely defined as the data fitting may lead to a gross error. Hence, the capacitance and permittivity value can be extracted based on the electrical response in a high frequency range of 10^5–10^7 Hz using the equation $-Z'' = 1/(jC_b 2\pi f)$ where Z'' is the imaginary part of impedance, j is the operator $(-1)^{1/2}$ and ω is the angular frequency. The capacitance C_b of the bulk material can be determined from the slope of the plot $-Z''$ vs. $1/2\pi f$. A bulk capacitance of 1.19×10^{-11} F·cm^{-1} (after correction for the stray capacitance from the empty

jig) is obtained for $Bi_3Zn_{1.84}Nb_3O_{13.84}$ at 549 °C (Fig. 2) which agrees reasonably well with that obtained from the Cole–Cole plot ($\omega RC_b = 1$).

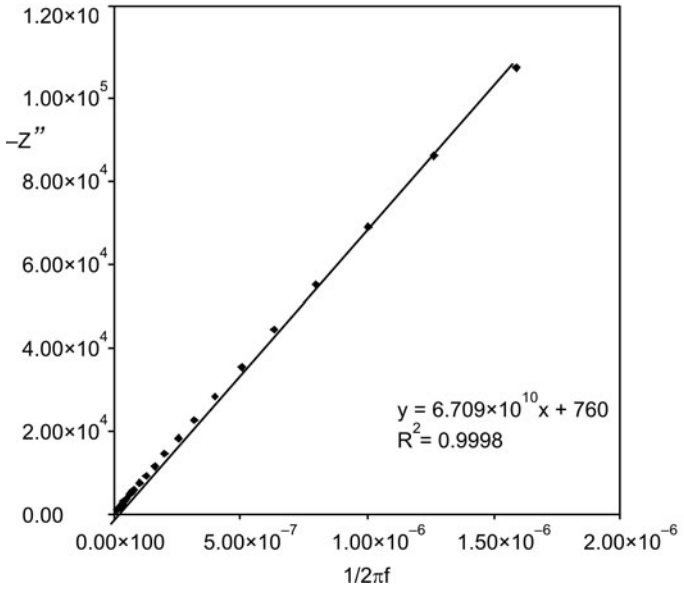

Fig. 2. Imaginary part of impedance, Z'', in function of the reciprocal angular frequency, at 549 °C

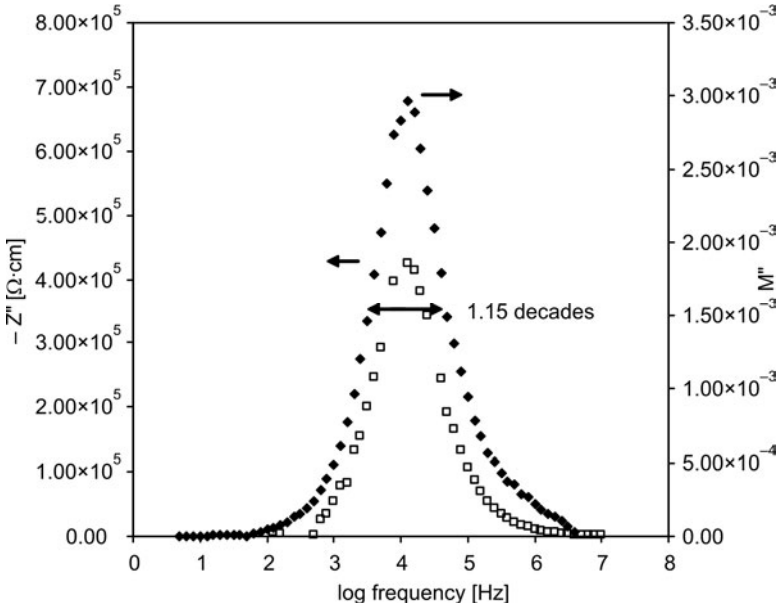

Fig. 3. Combined Z'' and M'' spectroscopic plots for cubic pyrochlore $Bi_3Zn_{1.84}Nb_3O_{13.84}$ at 549 °C

The impedance data of the material are further examined using the combined spectroscopic plots of imaginary components of the complex impedance, Z'' and electric modulus, M''. The frequency maxima of Z'' and M'' should be coincident, and the full width at a half maximum (FWHM) should be equal to 1.14 decade for an ideal Debye response representing bulk properties. There appears to be no grain boundary effect as two overlapping peaks with the FWHM value of ca. 1.15 decades are obtained (Fig. 3), indicating that the material is homogeneous.

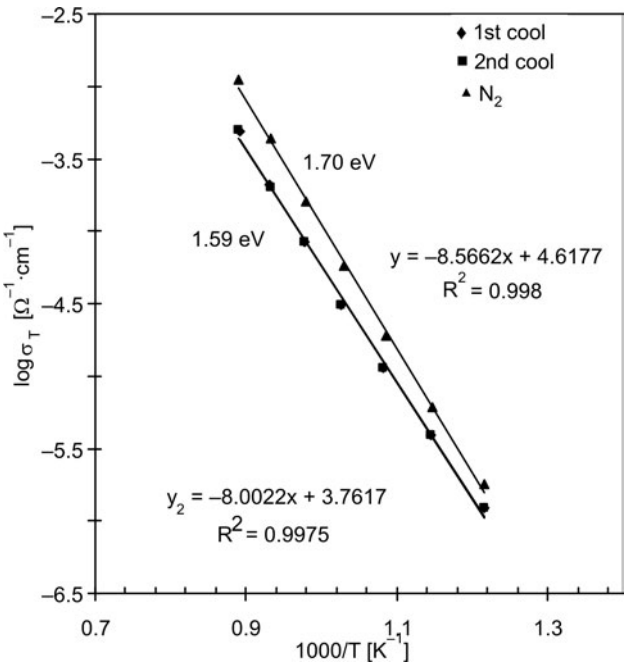

Fig. 4. Conductivity Arrhenius plots of cubic pyrochlore, $Bi_3Zn_{1.84}Nb_3O_{13.84}$

Figure 4 shows the electrical conductivity of the material in function of temperature. The Arrhenius law is applied in order to correlate the observed behaviour with a general dependence, $\sigma = \sigma_0 \exp(-E_a/kT)$ where σ_0 represents the pre-exponential factor, E_a is the apparent activation energy of the conduction process, k is Boltzmann's constant and T is absolute temperature. The conductivity data are reproducible and reversible in heat–cool cycles with a high activation energy of of 1.59 eV. Usually, high activation energy is required for the occurrence of a hopping type electronic mechanism, especially with the presence of defects of the oxygen vacancy in the pyrochlore structure [14, 15]. The conductivity at room temperature is determined by the data extrapolation. Cubic pyrochlore, $Bi_3Zn_{1.84}Nb_3O_{13.84}$, exhibits the conductivity of an order lower than that of bismuth zinc antimonite (BZS) with the value of $10^{-21}\ \Omega^{-1}\cdot cm^{-1}$ at room temperature. The high resistivity of Bi based pyrochlores has been noted in literature and these materials are mainly used for dielectric applications [18].

Oxides are susceptible to oxygen loss with creation of anion vacancies and associated reduction at high temperatures, especially under reducing atmosphere where a process, $2O^{2-} \rightarrow O_2 + 4e^-$ takes place. In a nitrogen atmosphere, $Bi_3Zn_{1.84}Nb_3O_{13.84}$ exhibits n-type conduction with higher conductivity and the activation energy of 1.70 eV (Fig. 4). This may be considered as evidence that cation disordered pyrochlores (A ↔ B exchange) exhibit a high level of intrinsic oxygen Frenkel disorder (48*f* → 8*b*). It was suggested by Clayton et al. [19] that $Bi_3Zn_2Nb_3O_{14}$ pyrochlore disclosed a n- to p-type behaviour in function of temperature and partial pressure of oxygen. The p-type conductivity dominated at high pO_2, under oxidizing conditions and n-type conductivity dominated at low pO_2 with considerable ionic contribution to the conductivity, due to the presence of the shallow minimum in conductivity measurements.

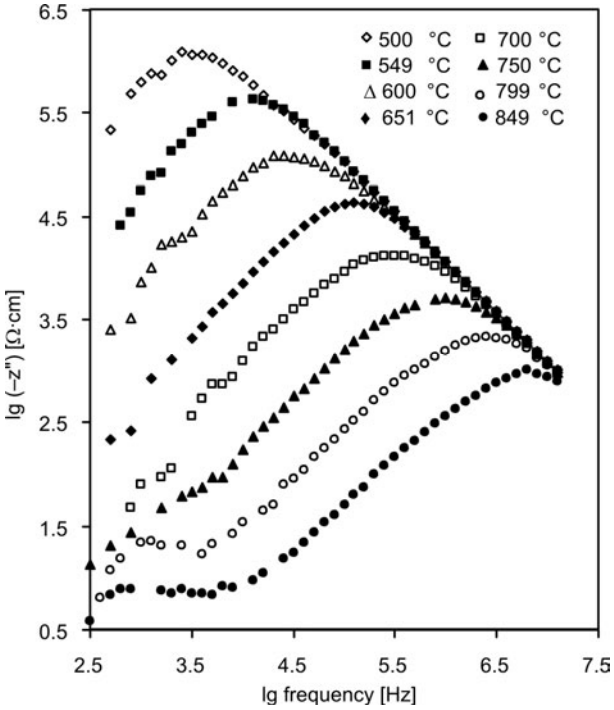

Fig. 5. Imaginary part of impedance in function of frequency for cubic pyrochlore, $Bi_3Zn_{1.84}Nb_3O_{13.84}$ at various temperatures

A dispersion of imaginary impedance, Z'' in function of frequency is shown in Fig. 5. The maxima of the curves shift towards a higher frequency region as the measuring temperature increases; this indicates the presence of a polarisation process in the dielectric material. Peak frequencies in Fig. 5 are used in an Arrhenius plot (peak frequency type) to show its dependence on temperature. Figure 6 shows the evolution of the peak frequency that follows the Arrhenius law with an apparent activation energy

of 1.55 eV. This value is in good agreement with the activation energy, previously calculated from the conductivity Arrhenius plot, i.e. 1.59 eV. This suggests strongly that the electrical behaviour of cubic pyrochlore $Bi_3Zn_{1.84}Nb_3O_{13.84}$ is influenced by the polarisation phenomenon in the crystalline lattice and that the conduction mechanism is of the hopping type [14, 15].

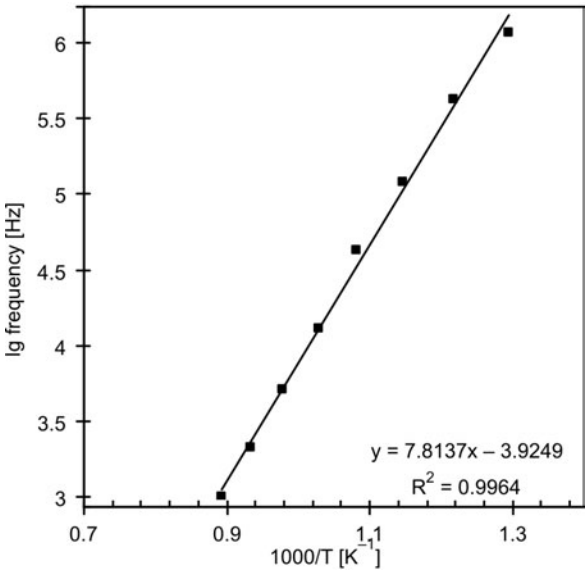

Fig. 6. Arrhenius plot for the peak frequency, lg(–Z'') of cubic pyrochlore, $Bi_3Zn_{1.84}Nb_3O_{13.84}$

The electric modulus is inversely proportional to the capacitance C. The peak heights of the modulus plots (Fig. 7) are independent of temperature, indicating that $Bi_3Zn_{1.84}Nb_3O_{13.84}$ does not exhibit ferroelectric properties in the temperature range under study. Similarly, the dielectric relaxation behaviour of ideal BZN cubic pyrochlore, $Bi_3Zn_2Nb_3O_{14}$, has been studied and it was suggested to be neither a dipolar glass nor a relaxor ferroelectric [20]. The complex dielectric response of $Bi_3Zn_2Nb_3O_{14}$ between 100 Hz and 100 kHz revealed a dielectric relaxation below the polar phonon frequencies. Relaxation at room temperature was observed at the frequency of 10^8 Hz, and the high frequency limit of relaxation frequencies was nearly temperature independent. The relaxation was postulated to be associated with hopping of disordered Bi and Zn atoms at A sites (each of the A atoms occupy one of 6 equivalent, closely spaced positions) and hopping of O′ atoms among 12 sites [20].

The complex electric permittivity ε^* can be expressed as a complex number

$$\varepsilon^* = \varepsilon'(\omega) - j\varepsilon''(\omega) \tag{2}$$

where ε′ and ε″ are the real and imaginary parts of the complex permittivity. Figure 8 illustrates the relative permittivity of $Bi_3Zn_{1.84}Nb_3O_{13.84}$ in function of frequency. High

dispersion characteristics in the curves at frequencies lower than 1 kHz could be attributed to the dielectric material behaviour where the conduction mechanism of a hopping type is present [14, 15]. This is probably due to atomic defects in cubic pyrochlores where intrinsic oxygen vacancies are present.

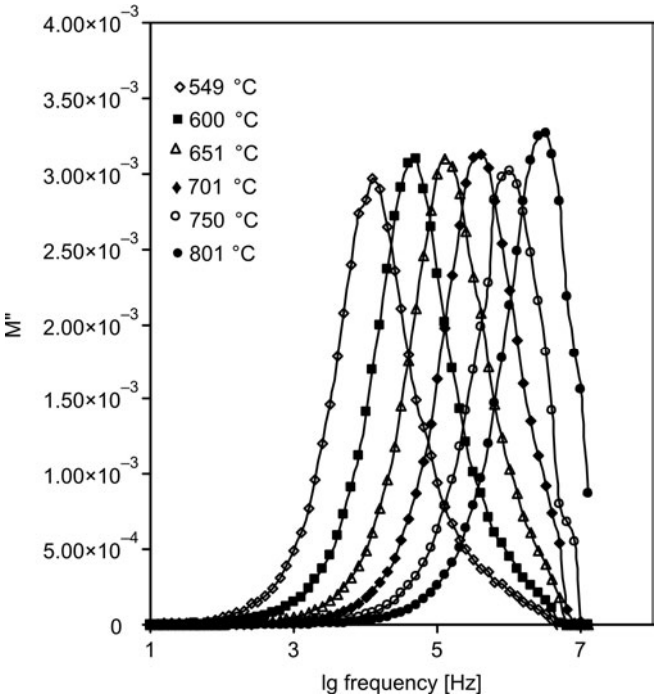

Fig. 7. Imaginary part of the electrical modulus in function of frequency

On the other hand, permittivity depends on the concentration of defects and the extent to which the internal field is raised above the applied field. Occurrence of a continuous flow of current rather than a limited oscillation between sites is noted to be due to high concentration of defects and/or high probability of hopping events. This contribution to the permittivity is small while the resistivity remains at a sufficiently high level for the dielectric of practical interest [16]. The degree of dispersion decreases as the frequency increases. In the frequency range of $10–10^3$ kHz, a frequency-independent response is observed over the entire temperature range studied (Fig. 8). This may be attributed to the inherent characteristic of dielectric materials as the oscillating system cannot follow the resonant frequency or jumping frequency ω_r in an applied field.

Figure 9 illustrates the real part of complex permittivity in function of temperature at several frequencies. The decline in permittivity in the temperature range of 25–400 °C (100–1000 kHz) indicates a negative temperature coefficient of permittivity of ca. 396 ppm/°C which is comparable to the reported value –400 ppm/°C [21, 22].

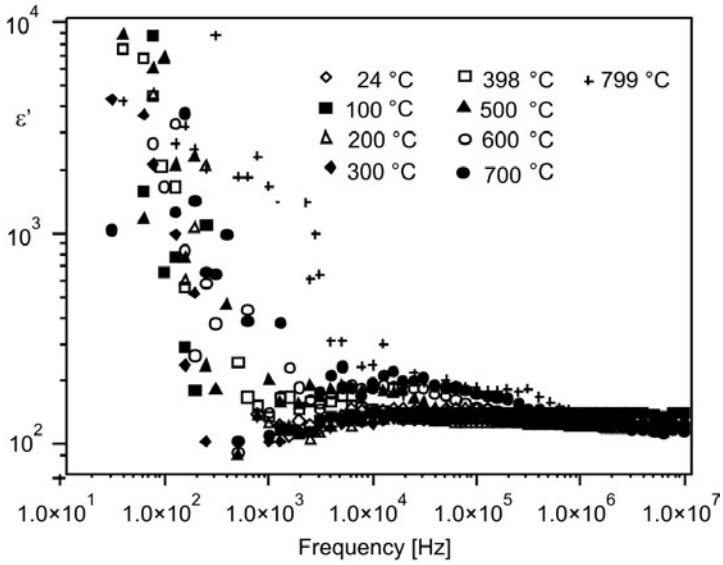

Fig. 8. Permittivity, ε′ in function of frequency at various temperatures

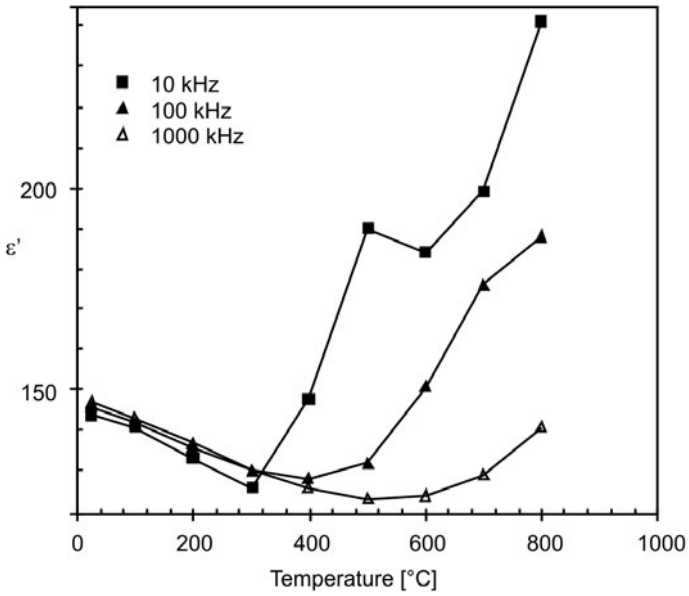

Fig. 9. Real part of complex permittivity in function of temperature at several frequencies

The dielectric loss can be expressed as

$$\tan\delta = \frac{\varepsilon''(\omega)}{\varepsilon'(\omega)} \tag{3}$$

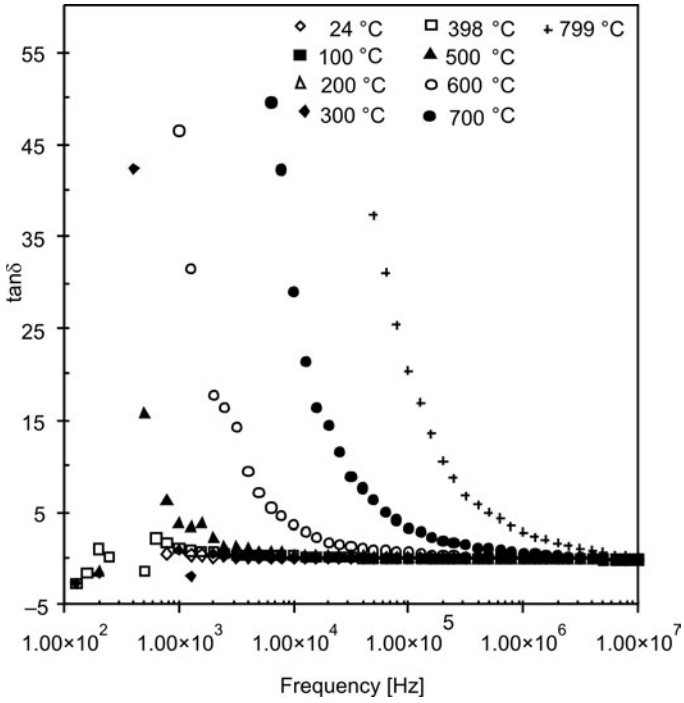

Fig. 10. Dielectric losses, tanδ, in function of frequency at several temperatures

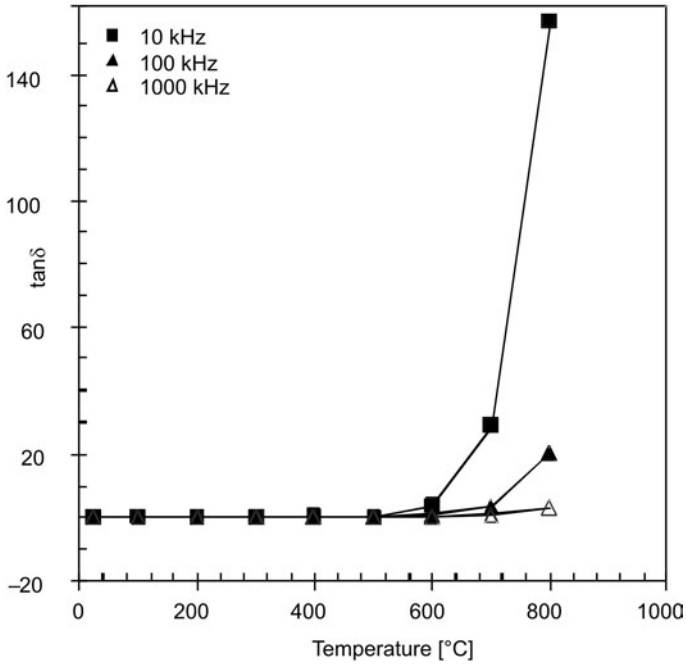

Fig. 11. Dielectric losses, tanδ, in function of temperature at several frequencies

A dense and pore free structure is a prerequisite for a low loss dielectric, as the pores may take up moisture which results in a higher dielectric loss, particularly if soluble ions are leached from the solid phase. The dielectric losses at various temperatures are shown in Fig. 10. All curves display a similar frequency independent behaviour below 500 °C. Above 500 °C, an appreciable increase in the dielectric losses is observed. Dielectric losses are strongly dependent on frequencies, i.e. lower loss is observed at higher frequencies (Fig. 11). The behaviour below 500 °C could be associated with the non-frequency dependence of dielectric loss (above kilohertz region) of BZN cubic pyrochlore with hopping conduction mechanism mentioned earlier. High dielectric loss at low frequencies is possibly due to time availability for the displacement of defects. Energy is lost through the movement of the screening charge (adjustment of surrounding ions relative to their state when the defect is absent) against the applied field. The ratio of energy lost, W_L, to energy stored, W_S, in each hopping transition is represented by $W_L/W_S = (1 - \xi)/\xi$ where ξ is the restraint of screening imposed by the lattice [16]. On the other hand, increase in temperature above 500 °C may increase the number of thermally activated charge carriers (defects) and this will lead to displacement of defects. $Bi_3Zn_{1.84}Nb_3O_{13.84}$ possesses the highest value of the relative permittivity and the lowest value of the dielectric loss in comparison with two analogous systems, $Bi_3Zn_2M_3O_{14}$, (M = Ta and Sb). There is a decrease in the relative permittivity and increase in the dielectric loss passing from the Nb system to the Sb one with the values from ca. 148 to 48 and from ca. 0.002 to 0.006, respectively [22–24]. This could be associated with the substitution of less polarisable Sb^{5+} or Ta^{5+} cations.

4. Conclusion

The cubic pyrochlore, $Bi_3Zn_{1.84}Nb_3O_{13.84}$ exhibits a typical dielectric behaviour in the frequency and temperature ranges studied. High dispersion of permittivity and high dielectric loss at low frequencies and frequency-independent permittivity and dielectric loss at high frequencies (> 100 kHz) with much lower permittivity and dielectric loss are observed. These phenomena could be attributed to the dielectric behaviour of the material, where the conduction mechanism of a hopping type is present. In general, the sample is highly resistive with a high activation energy of ca. 1.59 eV; a high relative permittivity value, 147 and low dielectric loss, 0.002, making it a potential material to be applied in multilayer ceramic capacitors (MLCC).

Acknowledgements

Financial support from the Ministry of Science, Technology and Innovation (MOSTI) is gratefully acknowledged. Special thanks are extended to Prof. A. R. West for his constructive suggestions and comments on impedance study.

References

[1] HEYWANG W., THOMANN H., *Positive Temperature Coefficient Resistors*, [In:] B.C.H Steele (Ed.), *Electronic Ceramics*, Elsevier, London, 1991, p. 29.
[2] RAO C.N.R., GOPALAKRISHNAN J., *New Direction in Solid State Chemistry*, 2nd Ed., Cambridge University Press, Cambridge, 1997.
[3] MUKTHA B., DARRIET J., GIRIDHAR MADRAS., GURU ROW T.N., J. Solid State Chem., 179 (2006), 3919.
[4] SEGAL D.L., *Powders for Electronic*, [In:] B.C.H. Steele (Ed.), *Electronic Ceramics*, Elsevier, London, 1991, p. 185.
[5] CANN D.P., RANDALL C.A., SHROUT T.R., Solid State Commun., 100 (1996), 529.
[6] ZHOU W., J. Solid State Chem., 101 (1992), 1.
[7] SUBRAMANIAM M.A., ARAVAMUDAN G., SUBBA RAO G.V., Progr. Solid State Chem., 15 (1983), 55.
[8] VALANT M., SURUROV J. Am. Ceram. Soc., 88 (2005), 2540.
[9] NINO J.C., LANAGAN M.T., RANDALL C.A., J. Mater. Res., 16 (2001), 1460.
[10] WITHERS R.L., WELBERRY T.R., LARSSON A-K., LIU Y., NOREN L., RUNDLOF H., BRINK F.J., J. Solid State Chem., 177 (2004), 231.
[11] TAN K.B., LEE C.K., ZAINAL Z., MILES G.C., WEST A.R., J. Mater. Chem., 15 (2005), 3501.
[12] VANDERAH T.A., LEVIN I., LUFASO M.W., Eur. J. Inorg. Chem., (2005), 2895.
[13] LEVIN I., AMOS T.G., VANDERAH T.A., RANDALL C.A., LANAGAN M.T., J. Solid State Chem., 168 (2002), 69.
[14] NOBRE M.A.L., LANFREDI S., Mater. Lett., 47 (2001), 362.
[15] NOBRE M.A.L., LANFREDI S., Appl. Phys. Lett., 81 (2002), 451.
[16] HERBERT J.M., *Ceramics Dielectrics and Capacitors*, [In:] D.S. Campbell (Ed.), *The Properties of Dielectrics*, Gordon and Breach Science Publishers, Amsterdam, 1985, p. 9.
[17] DU H.L., YAO X., WANG H., Ferroelectrics, 262 (2001), 89.
[18] RANDALL C.A., NINO J.C., BAKER A., YOUN H-J., HITOMI A., THAYER R., EDGE L.E., SOGABE T., ANDERSON T.D., SHROUT T.R., TROLIER-MCKINSTRY S., LANAGAN M.T., Am. Ceram. Soc. Bull., (2003), 9101.
[19] CLAYTON J., TAKAMURA H., METZ R., TULLER H.L., WUENSCH B.J., J. Electroceramics, 7 (2001), 113.
[20] KAMBA S., POROKHONSKY V., PASHKIN A., BOVTUN V., PETZELT J. Phys. Rev. B., 66 (2002), 054106.
[21] NINO J.C., LANAGAN M.T., RANDALL C.A., J. Applied. Phys., 89 (2001), 4512.
[22] WANG X.L., WANG H., YAO X., J. Am. Ceram. Soc., 80 (1997), 2745.
[23] YOUN H.J., SOGABE T., RANDALL C.A., SHROUT T.P., LANAGAN M.T., J. Am. Ceram. Soc., 84 (2001), 2557.
[24] DU H.L., YAO X., Mater. Electr., 15 (2004), 13.

Received 12 May 2008
Revised 31 October 2008

Materials Science-Poland, *Vol. 27*, *No. 4/1*, *2009*

Surfactant-assisted synthesis and characterization of hydroxyapatite nanorods under hydrothermal conditions

M. SALARIAN[1*], M. SOLATI-HASHJIN[2], S. SARA SHAFIEI[2], A. GOUDARZI[2], R. SALARIAN[3], A. NEMATI[4]

[1]School of Engineering, School of Materials Engineering, Tehran Science and Research Branch, Islamic Azad University, Tehran, Iran

[2]Biomedical Engineering Faculty, Amirkabir University of Technology, Tehran, Iran

[3]Maziar University, School of Engineering, Mazandaran, Noor, Iran

[4]School of Materials Science and Engineering, Sharif University of Technology, Tehran, Iran

Hydroxyapatite (HAp) nanorods with uniform morphology and controllable size were successfully synthesized by precipitating $Ca(NO_3)_2{\cdot}4H_2O$ and $(NH_4)_2HPO_4$ in the presence of cetyltrimethylammonium bromide (CTAB) and polyethylene glycol 400 (PEG 400) as cationic surfactant and non-ionic co-surfactant, respectively, under hydrothermal conditions. The effect of hydrothermal temperature on the composition, morphology and size of HAp particles was studied using X-ray diffraction (XRD), Fourier transform infrared spectrometry (FTIR) and scanning electron microscopy (SEM). Results revealed that the morphology and size of HAp particles can be effectively controlled by the presence of CTAB and PEG surfactants. In addition, the temperature of the hydrothermal treatment plays an important role in controlling the morphology and size of HAp particles. The aspect ratio of rod-like particles increases with the increase in the hydrothermal temperature. Moreover, the crystallinity of HAp powders increases with the increase in the hydrothermal temperature. The template action of CTAB and the co-template action of PEG 400 used to regulate the nucleation and crystal growth are also discussed.

Key words: *nanorods; hydroxyapatite; surfactant; morphology*

1. Introduction

Hydroxyapatite ($Ca_{10}(PO_4)_6(OH)_2$, HAp) nanoparticles have been of great interest because their mineral components are similar to human hard tissues [1–3]. Synthetic

[*]Corresponding author, e-mail: mehrnazsalarian@gmail.com

HAp has excellent biocompatibility and bioactivity, thus it is used in the reconstruction of damaged bone or teeth [4, 5]. The principal limitation in its clinical use as a load bearing implant is its mechanical brittleness. Generally, the fracture strength and fracture toughness of ceramic materials are effectively improved by dispersing rod-like crystals and thin filaments into the bulk materials. Thus, HAp rod-like crystals and whiskers do appear to be useful as materials for improving the mechanical properties of synthetic biomaterials, etc. [6–8].

It is well-known that the strength of ceramic fibres and whiskers is size-dependent. As the diameter or length decrease, the strength of ceramic fibres and whiskers increases. Moreover, their physical properties such as fracture toughness and fracture strength depend on the crystal structure, composition and sizes [9].

HAp can be synthesized by many chemical processing routes such as solid state reaction [3, 10], coprecipitation and hydrothermal technique [11, 12]. Solid state reactions usually give stoichiometric and well-crystallized products but they require relatively high temperatures and long heat-treatment times. Moreover, the sintering capacity of such powders is usually low and ultimately results in inferior mechanical properties of the sintered matrices [8, 12]. In the case of coprecipitation, nanometer size powders can be prepared. However, their crystallinity and Ca/P ratio depend mainly upon the preparation conditions and are in many cases lower than for well-crystallized stoichiometric HAp. The hydrothermal technique usually results in HAp powders with a high degree of crystallinity and the Ca/P ratio close to the stoichiometric value [8, 12]. However, the obtained powders have typical agglomeration and their size distribution is relatively wide. Therefore, the size distribution of HAp powders cannot be well controlled using the normal hydrothermal method [12]. A newly developed hydrothermal technique that is used to synthesize nanopowders, nanorods and nanoneedles [1, 8, 13] is the surfactant-assisted hydrothermal method. This method inhibits the excess agglomeration of the particles, since the surfactants can adsorb on the surface of particles. In addition, the surfactants can serve as a versatile “soft” template for the synthesis of 1 D nanostructured materials [8, 14]. Furthermore, the hydrothermal treatment can effectively increase the crystallinity of the product [8].

In this study, hydroxyapatite nanorods with uniform morphology and controllable size have been successfully synthesized in the presence of cetyltrimethylammonium bromide (CTAB) acting as a soft template and polyethylene glycol 400 (PEG 400) acting as a co-template. Also, the effect of hydrothermal temperature on the composition, morphology and size of hydroxyapatite particles is investigated.

2. Experimental

Materials and methods. The starting materials used in this study were calcium nitrate tetrahydrate ($Ca(NO_3)_2{\cdot}4H_2O$) (Merck Prolabo 22 384.298), diammonium hydrogen phosphate ($(NH_4)_2HPO_4$) (Merck Prolabo 21 306.293), cetyltrimethylammonium bromide (CTAB) (Merck 102342) and polyethylene glycol (PEG 400) (Merck

807485). All chemicals were of analytical grade. The Ca/P molar ratio was equal to 1.67 (stoichiometric ratio of HAp).

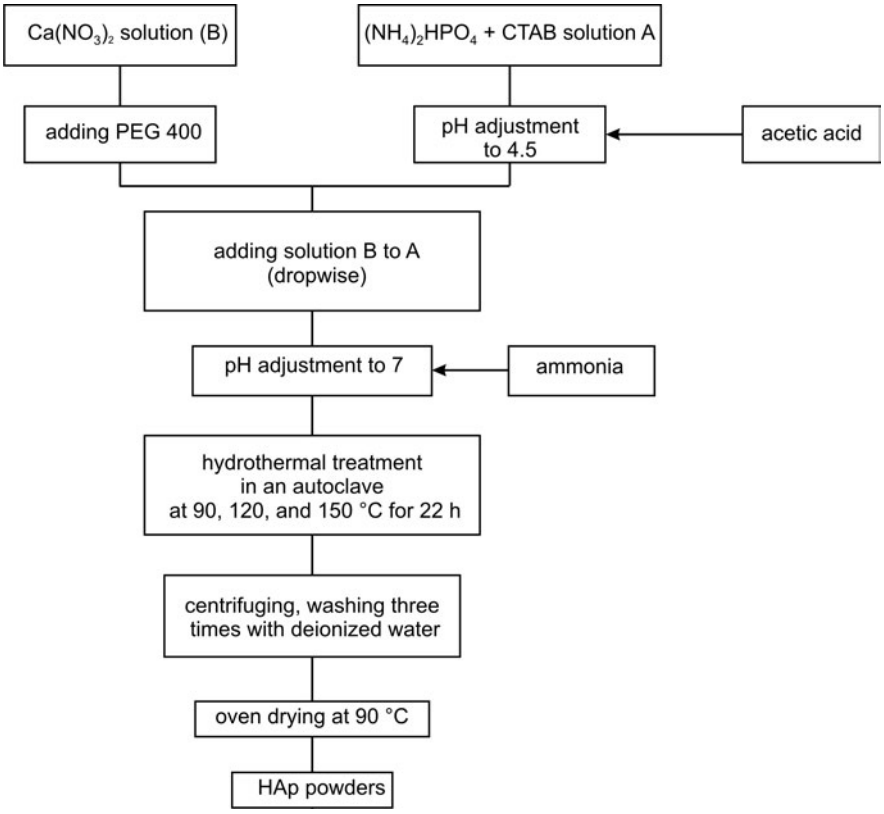

Fig. 1. The process flowchart for synthesis of HAp nanorods

The general procedure was the following: 0.03 mole of $(NH_4)_2HPO_4$ and 0.021 mole of CTAB were dissolved in 125 ml of deionized water. The solution was stirred for 30 min with a magnetic stirrer to ensure that the cooperative interaction and self-assembly process were completed. Then the pH value was adjusted to 4.5 by adding pure acetic acid. After that, 0.05 mole of $Ca(NO_3)_2{\cdot}4H_2O$ was dissolved in 175 ml of deionized water and 50 ml of PEG 400 was simultaneously added to the solution under constant stirring for 30 min. Then the mixed solution of $Ca(NO_3)_2{\cdot}4H_2O$ and PEG 400 were added to the latter dropwise under continuous magnetic stirring in air. pH of the solution was adjusted to 7 using ammonia. The final milky suspension was transferred to a stainless steel autoclave, sealed tightly and hydrothermally treated in an oven at 90, 120 and 150 °C for 22 h. The resulting precipitates were separated from the suspension by centrifuging, washed three times with deionized water to remove the residual CTAB and PEG 400, and then oven dried at 90 °C for 22 h to yield white powders. The flowchart for HAp nanorod synthesis is shown in Fig. 1.

Characterization. The crystallographic structural analysis was carried out by X-ray diffraction (XRD) method using a D4 Bruker powder diffractometer with monochromatic CuK_α radiation (λ = 1.5406 Å) over the 2θ range of 10–70° at a scan rate of 1deg/min in the Guinier geometry. The operational voltage and the current were 40 kV and 30 mA, respectively. Fourier transform infrared (FT-IR) spectroscopy (Bruker IFS 48) was used to identify the functional groups. The potassium bromide (KBr) disk technique was used for the analysis, using 2 mg of HAp powders compacted under hydraulic pressure with 200 mg of KBr . The spectrum was recorded in the 4000–400 cm^{-1} region with 2 cm^{-1} resolution averaging 100 scans.

The morphology and size of HAp particles were investigated by a XL30 Philips scanning electron microscopy (SEM). The powders for SEM analysis were prepared by sprinkling the dried HAp onto one side of a double adhesive tape, which was stuck to an aluminum stub. The stub was then gold coated using EMITECH K450X (England) to a thickness of 20-30 nm and examined with an accelerating voltage of 20 kV.

3. Results

Typical XRD patterns of the HAp samples obtained at 90, 120 and 150 °C are shown in Fig. 2. Phase identification of the synthesized powders was accomplished by comparing the experimental XRD patterns with the database compiled by the Joint Committee on Powder Diffraction Standards (JCPDS), namely the following card numbers: 9-432 for HAp, 9-169 for whitlockite (β-$Ca_3(PO_4)_2$) and 9-80 for monetite ($CaHPO_4$). In general, the XRD patterns exhibit characteristic peaks of HAp but some differences may be observed. The XRD pattern of the HAp powder obtained at 150 °C (Fig. 2, curve A) contains sharp peaks which can be perfectly matched to crystalline HAp with no additional peaks, while those obtained at 120 °C and 90 °C (curves B and C) contain some peaks corresponding to whitlockite and monetite structures. At 150 °C, no impurity other than HAp is detected by the XRD, which indicates that the product is monophase of HAp. Thus we may conclude that HAp powders do not crystallize completely below 150 °C.

There is also a sign of directional growth in the XRD patterns. In a standard HAp pattern, the intensity of diffracted X-rays corresponding to the (211) and (002) planes are assumed to be 100 and 40 units, respectively, thus the ratio $I_{(211)}/I_{(002)}$ is equal to 2.5. In HAp powder synthesized at 150 °C, the diffraction peak corresponding to (002) is sharp, and its relative intensity is far greater than the standard value (I_{211}/I_{002} = 1.85). This indicates that the (002) surface is more fully grown in this sample; in other words, HAp nanorods are oriented to grow along the *c* axis. For the HAp samples obtained at 120 °C and 90 °C, the $I_{(211)}/I_{(002)}$ ratios are 2.1 and 2.2, respectively. The results indicate that in all samples, the longitudinal direction of rod-like HAps is [002], and the directional growth along the *c* axis is more prominent in HAp powders synthesized at 150 °C as will be seen in the SEM photographs.

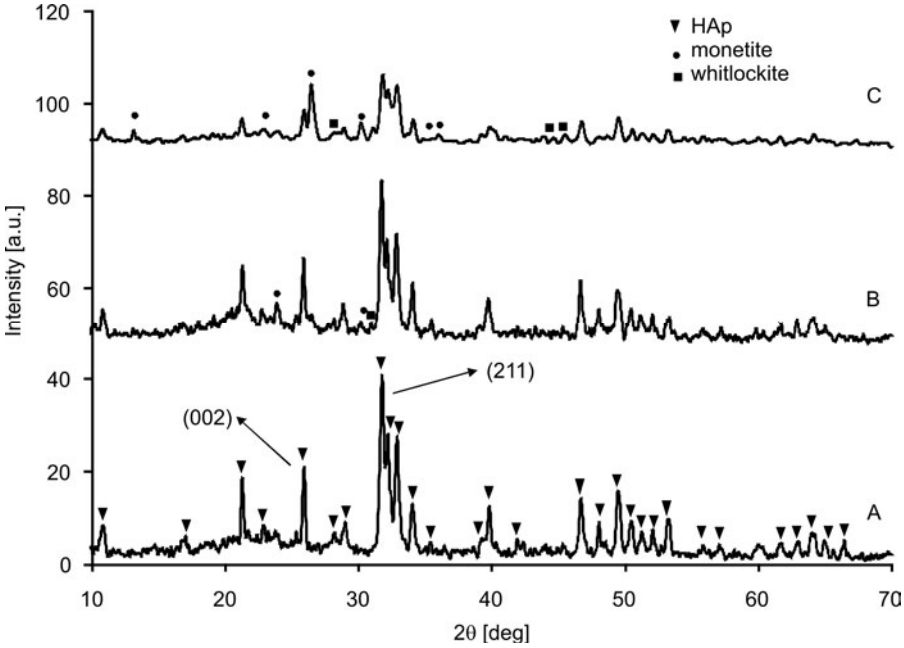

Fig. 2. Typical XRD patterns of HAp powders obtained at: 150 °C (A), 120 °C (B) and 90 °C (C)

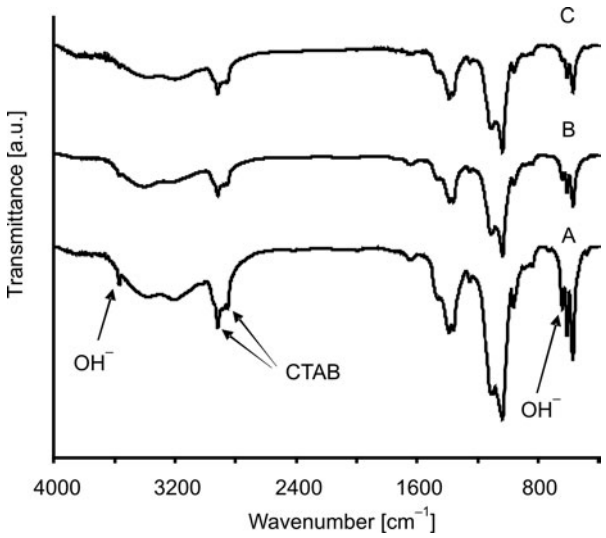

Fig. 3. Typical FTIR spectra of HAp powders obtained at: 150 °C (A), 120 °C (B) and 90 °C (C)

Figure 3 shows typical FTIR absorption spectra of the HAp samples synthesized at 90, 120 and 150 °C. In general, the FTIR spectra of all samples display the same profile. In all these HAp powders, absorption peaks at 1460, 882 and 670 cm^{-1} are as-

signed to carbonate ions [15, 16] which reveal that a certain level of carbonate substitution takes place in these samples, although this is not shown by the XRD phase analysis. The carbonate ions may come from a reaction between atmospheric carbon dioxide and solution during the synthesis process. The C–H stretching vibration bands appearing at 2851 and 2916 cm^{-1} are attributed to residual CTAB [9, 17] which show that the organic surfactant has not been completely washed away and remains in the obtained samples.

By a simple heat treatment (1 h at 450 °C), the residual organic materials will be removed. The characteristic bands for PO_4^{3-} appeared at 471.2 (υ_2 PO_4^{3-} [18]), 565 and 602.7 (υ_4 PO_4^{3-} [19]), 962 (υ_1 PO_4^{3-} [5, 19]), 1031 and 1095 (υ_3 PO_4^{3-} [20]), and 1248 cm^{-1} (P–O stretching vibration of PO_4^{3-} [21]). The band at 1382 cm^{-1} is assigned to the N–O stretching mode of NO_3^- [22]. A broad band at 1633 and 3197 cm^{-1} corresponds to adsorbed water [9, 23], while the broad band at 3401 cm^{-1} may come from the H_2O lattice because this band exists in the range of 3550–3200 cm^{-1} for hydrated H_2O [9]. The medium band at 1355 is attributed to OH in-plane bend [9]. Two medium sharp peaks at 633 and 3570 cm^{-1} attributed to vibrational [24] and structural OH^- [20, 23] modes are better visible and sharper in the HAp sample obtained at 150 °C (Fig. 3, curve A) compared with the product obtained at 120 °C (Fig. 3, curve B), whereas for powders synthesized at 90 °C they are relatively indistinct (Fig. 3, curve C) which indicates a lower crystallinity of the product obtained at lower hydrothermal temperatures. Overall, it could be deduced that the crystallinity of the obtained powders increases with the increase in the hydrothermal temperature.

To screen the influence of surfactants on the morphology and size of HAp particles, the synthesis process was conducted with and without CTAB and PEG 400. Figure 4 shows the SEM micrographs of the sample synthesized at 150 °C in the absence of CTAB and PEG 400 and those obtained at 90, 120 and 150 °C in the presence of CTAB and PEG 400. As shown in the Fig. 4a, in the absence of both CTAB and PEG 400, the HAp particles are spherical with the diameter of about 50–80 nm. On the other hand, from the SEM photographs of HAp powders synthesized at 150 °C in the presence of both surfactants (Fig. 4b), the HAp particles have uniform, long, rod-like morphology with the typical diameter of about 50–80 nm and the average aspect ratio of about 16–20. For the HAp sample obtained at 120 °C (Fig. 4c), the rod-like particles with the mean particle size of about 80–120 nm in diameter and the aspect ratio of about 8–10 are clearly observed, but they are aggregated. At 90 °C, the product shows a plate-like structure and rod-like particles with the aspect ratio of about 6 and crystal diameter of about 100–120 nm, randomly distributed in the sample shown in Fig. 4d. HAp particles obtained at 150 °C are much thinner and longer; besides, nanorods have a more uniform size distribution, and are much more separated from each other compared with HAp samples obtained at 120 °C and 90 °C. Thus, we can conclude that the hydrothermal temperature plays a key role in the control of the crystal morphology and the crystal size.

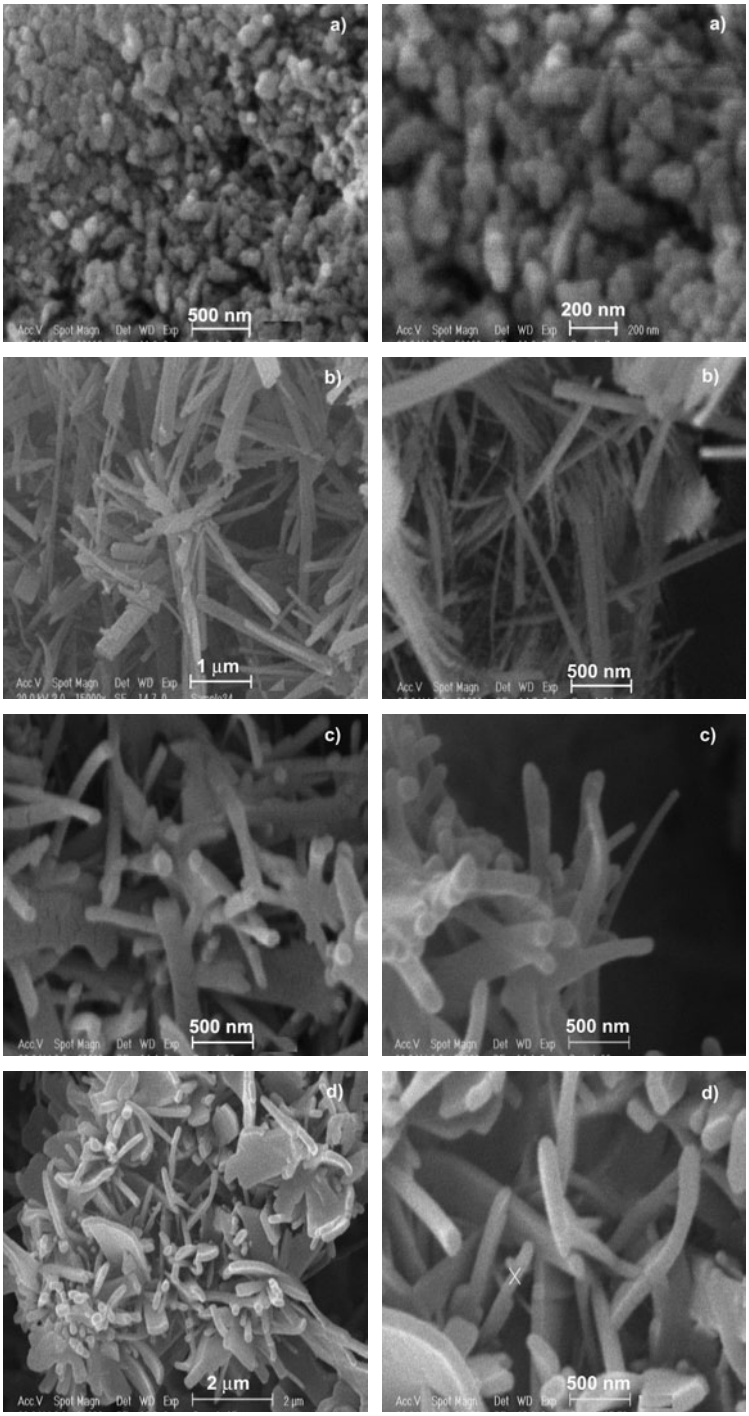

Fig. 4. Typical SEM photographs of the HAp powders obtained at 150 °C in the absence of CTAB and PEG 400 (a), in the presence of CTAB and PEG 400 at 150 °C (b), 120 °C (c), 90 °C (d)

4. Discussion

High temperature and high pressure of hydrothermal treatment could have two effects on the final products. Firstly, they might cause some fibres to aggregate, but the interaction between the aggregates would be so weak that they would tend to dissolve in the aqueous system. Secondly, they might raise the solubility of HAp to some extent and accelerate the dissolution and crystallization process. Also, the hydrothermal treatment can effectively increase the crystallinity of the product [8, 25].

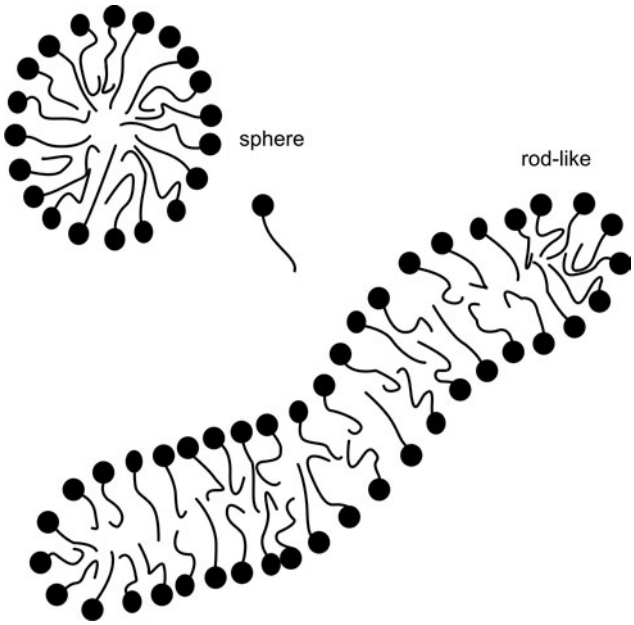

Fig. 5. The transition from a spherical micelle to a long rod- or thread-like micelle at high enough concentrations

The effect of CTAB on the HAp crystallization system is thought to act as a soft template [5, 8, 9], resulting in epitaxial growth of the product [5]. CTAB is a cationic surfactant and its critical micelle concentration (CMC) is 0.03% (0.9–1.0 mM) [9, 26]. Above the CMC, a transition from spherical micelles to rod-like micelles occurs and the size of micelles increases as the CTAB concentration increases, eventually resulting in long, flexible, thread-like micelles [27], as shown in Fig. 5. Micellar growth can be considered to arise from two mechanisms. In one mechanism, there is an internal driving force causing the formation of large aggregates with a different geometry. In the other mechanism, micellar growth is induced by intermicelle repulsions allowing a better packing of the micelles. This will occur at high concentrations, when the micelles come in direct, close contact. In our system, with the CTAB concentration of 0.168 M, micellar growth could easily result in long rod-like micelles. In an aqueous system, the CTAB would ionize completely and result in a cation with a tetrahedral

structure. Meanwhile, the phosphate anion has also a tetrahedral structure [5, 9]. Because of the complementary relationship between the charge and the stereochemistry, a process called molecule recognition could be realized at the inorganic/organic interface [28]. Thus, in that case, CTAB could be well incorporated in the phosphate anion [5]. When Ca^{2+} solution is added to PO_4^{3-} solution, $Ca_9(PO_4)_6$ clusters tend to form on the rod-shaped micellar surface, due to the conformation compatibility between the identical, hexagonal shapes of the micelles and the $Ca_9(PO_4)_6$ clusters. During the hydrothermal stage, CTAB–HAp complexes are formed and they coalesce to form nanorod structures. The micelles act as nucleating sites for the growth of HAp crystals [29, 30].

Particle formation is a very complex process, involving nucleation, growth, coagulation and flocculation. Addition of PEG can affect the nucleation during the crystallization process. After nucleation, PEG can influence particle growth, coagulation and flocculation [25]. Among common water soluble polymers, PEG is one of the most flexible polymers in an aqueous medium because of the flexible ether linkages in its backbone and the absence of bulky side groups. Thus, it is sterically less hindered in the aqueous medium [31, 32]. PEG can modify or control the surfaces of the nanometer crystals. In addition, PEG is a non-ionic surfactant able to form long chain structures in aqueous solution [9], and therefore it acts as a co-template. It has been reported that the PEG molecule has the ability to chelate Ca^{2+} [33, 34]; therefore, PEG –OH can attract Ca^{2+} released from $Ca(NO_3)_2{\cdot}4H_2O$ to form the bond of PEG–O–Ca^{2+}–O–PEG, then PEG–O–Ca^{2+}–O–PEG reacts with the PO_4^{3-} released from $(NH_4)_2HPO_4$ to produce HAp crystal nuclei [33]. Moreover, the most important role of the surfactant is to inhibit the excess aggregation of CTAB micelles, because the surfactant could absorb on the surface of particles. As a result of their adsorption, an electrical double layer develops on the surfaces of solids or liquids. Adsorbed surfactant layers may involve micellar type structures and induce the formation of long, rod-like micelles. Therefore, we can reasonably assume that the template and co-template action endow the surfactants with the capability to control the crystallization and growth processes.

5. Conclusions

The morphology and size of hydroxyapatite crystals can be controlled by the presence of CTAB surfactant and PEG 400 cosurfactant under hydrothermal conditions.

The temperature of hydrothermal treatment plays a key role in the control of the morphology and size of the HAp crystal.

The high crystallization and homogeneity in the size distribution and the shape of the product obtained at 150 °C are attributed to the hydrothermal treatment and the soft template of the surfactants. The longitudinal direction of nanorods is [002], as confirmed by the XRD pattern of the samples.

The FTIR analysis proved that the products are carbonated apatite, although it was not shown by the XRD analysis. Since CHAp is known to be a better biomaterial than pure HAp, due to the similarity to the composition of biological apatite [23], the HAp powders obtained in this study are expected to show excellent bioactivity.

Using HAp nanorods as raw materials is an effective way to obtain dense bioceramics with good mechanical properties. Therefore, the obtained HAp nanorods may be used as strength-enhancing additives for the preparation of HAp ceramics or biocompatible nanocomposites with improved mechanical properties.

Acknowledgements

The authors express their gratitude to Prof. F. Moztarzadeh for supplying the necessary equipment.

References

[1] SUN Y., GUO G., WANG Z., GUO H., Ceram. Int., 32 (2006), 951.
[2] HENCH L.L., J. Am. Ceram. Soc., 74 (1991), 1487.
[3] ELLIOTT J.C., *Structure and Chemistry of the Apatites and Other Calcium Orthophosphates*, Elsevier, Amsterdam, 1994.
[4] GROOT K.D., *Bioceramics of Calcium Phosphate*, CRC PRESS, Boca Raton, 1983.
[5] WANG Y., ZHANG S., WEI K., ZHAO N., CHEN J., WANG X., Mater. Lett., 60 (2006), 1484.
[6] MIZUTANI Y., UCHIDA S., FUJISHIRO Y., SATO T., Brit. Ceram. T., 97 (1998), 105.
[7] YASZEMSKI M.J., PAYNE R.G., HAYES W.C., LANDER R., MIKOS A.G., Biomaterials, 17 (1996), 175.
[8] LIN K., CHANG J., CHENG R., RUAN M., Mater. Lett., 61 (2007), 1683.
[9] LIU Y., HOU D., WANG G., Mater. Chem. Phys., 86 (2004), 69.
[10] MURUGAN R., RAMAKRISHNA S., Comp. Sci. Technol., 65 (2005) 2385.
[11] NARASARAJU T.S.B., PHEBE D.E., J. Mater. Sci., 31 (1996), 1.
[12] BYRAPPA K., *Handbook of Hydrothermal Technology*, William Andrew Publishing, LLC/Noyes Publications, New Jersey, 2001.
[13] YAN L., LI Y., DENG Z., ZHUANG J., SUN X., Int. J. Inorganic Mater., 3 (2001), 633.
[14] MELDRUM F.C., KOTOV N.A., FENDLER J.H., J. Phys. Chem., 98 (1994), 4506.
[15] LIU J.B., YE X.Y., WANG H., ZHU M.K., WANG B., YAN H., Ceram. Int., 29, (2003), 629.
[16] ZAPANTA L.R., Nature, 403 (1965), 206.
[17] KANDORI K., HORIGAMI N., YASUKAWA A., ISHIKAWA T., J. Am. Ceram. Soc., 80 (1997), 1157.
[18] FOWLER B.O., *Structural Properties of Hydroxyapatites and Related Compounds*, MD, Gaithersburg, 1968.
[19] HE Q.J., HUANG Z.L., Cryst. Res. Technol., 42 (2007), 460.
[20] PANDA R.N., HSIEH M.F., CHUNG R.J., CHIN T.S., J. Phys. Chem. Solids, 64 (2003), 193.
[21] BLAKESLEE K.C., CONDRATE R.A., J. Am. Ceram. Soc., 54 (1971), 559.
[22] ANEE T.K., ASHOK M., PALANICHAMY M., NARAYANA KALKURA S., Mater. Chem. Phys., 80 (2003), 725.
[23] CHENG Z.H., YASUKAWA A., KANDORI K., ISHIKAWA T., J. Chem. Soc. Faraday Trans., 94 (1998), 1501.
[24] LIAO C., LIN F., CHEN K., SUN J., Biomaterials, 20 (1999), 1807.
[25] ZHANG F., ZHOU Z., YANG S., MAO L., CHEN H., YU X., Mater. Lett., 59 (2005), 1422.
[26] DELSANNTI M., MOUSSAID A., MUNCH J.P., J. Colloid Interf. Sci., 157 (1993), 285.
[27] HAN S.H., HOU W.G., DANG W.X., XU J., HU J.F., LI D.Q., Mater. Lett., 57 (2003), 4520.
[28] SHIH W., WANG M., HON M., J. Cryst. Growth, 275 (2005), 2339.

[29] XIONG Y.J., XIE Y., YANG J., ZHONG R., WU C.Z., DU G.A., J. Mater. Chem., 12 (2002), 3712.
[30] YAO J., TJANDRA W., CHEN Y.Z., TAM K.C., MA J., SOH V., J. Mater. Chem., 13 (2003) 3053.
[31] WANG P., TAN K.L., KANG E.T., J. Biomat. Sci. Polym. E., 11 (2000), 169.
[32] KIM B.S., HRKACH J.S., LANGER R., Biomaterials, 21 (2000), 259.
[33] QIU C., XIAO X., LIU R., Ceram. Int., 30 (2007), 980.
[34] HOSSAING S.F.A., HUBBELL J.A., Biomaterials, 15 (1994), 921.

Received 14 May 2008
Revised 12 November 2008

Materials Science-Poland, *Vol. 27*, *No. 4/1*, *2009*

On the synthesis and properties of bulk ternary Cr_2AlC ceramics

W.B ZHOU[1, 2*], B.C. MEI[2], J.Q. ZHU[1]

[1]School of Materials Science and Engineering, Wuhan University of Technology, Wuhan 430070, P.R. China

[2]State Key Laboratory of Advanced Technology for Materials Synthesis and Processing, Wuhan University of Technology, Wuhan 430070, P.R. China

Dense bulk Cr_2AlC was synthesized by hot-pressing of Cr, Cr_3C_2 and Al powders as starting materials. The phase composition was determined by X-ray diffraction (XRD), the microstructures of the samples were observed with a scanning electron microscope (SEM) and thermal, electrical as well as the mechanical properties at and above room temperature were determined. The results showed that Cr_2AlC grains have columnar and plate-like shapes, and that it is a good electrical and thermal conductor.

Key words: *ceramics; chromium aluminum carbide; hot-pressing*

1. Introduction

Layered ternary carbide Cr_2AlC has received considerable attention because of an unusual combination of good properties which makes it a candidate for many high temperature applications [1]. Like metals, it is an excellent electrical and thermal conductor, easily machinable, plastic, relatively soft, and not susceptible to thermal shock at higher temperatures. Like ceramics, it is oxidation resistant, refractory and has a high tensile strength, a high melting point and good thermal stability. Due to these unique properties, it is expected to have applications in various fields such as a substitute for machinable ceramics, kiln furniture, heat exchangers, and so on.

Even though Cr_2AlC has so many excellent properties, it has not received much attention until recent years, because it is difficult to synthesize bulk samples of Cr_2AlC with high purity. Schuster et al. [2] synthesized Cr_2AlC power by sintering Cr, Al and C powder through arc melting, then the sample was sealed in an evacuated quartz tube, annealed at temperatures between 600 and 1200 °C (170–500 h), and quenched in water. This method is limited to laboratory scale by its low efficiency. Recently, Manoun et al. [3] have successfully fabricated single-phase, fully dense, polycrystal-

*Corresponding author, e-mail: jsyczwb@hotmail.com

line samples of Cr_2AlC by reactive HIPing of Cr, Al and graphite powders. However, the preparation process was very complicated. Tian et al. [4] obtained bulk Cr_2AlC by hot pressing of Cr, Al and C powders at 1350 °C for 1 h, together with a small amount of Cr_7C_3. Further increase in temperature or extension of dwell time did not change the phase assemblage in an obvious way. More recently, Lin et al. [5] also have successfully fabricated single phase bulk Cr_2AlC through a solid–liquid (S–L) reaction by sintering Cr, Al and C powders at 1400 °C and 1350 °C for 60 min and 30 min, respectively. The relative density of the sample is 95% of the theoretical value.

In our previous work, we successfully obtained high purity Ti_3SiC_2 and Ti_3AlC_2 using TiC, instead of Ti and C as raw materials [6, 7]. Thus in the present research, we fabricated bulk Cr_2AlC by hot-pressing of Cr, Cr_3C_2 and Al powders. Additionally, the mechanical properties, thermal and electrical properties of the obtained Cr_2AlC sample were also investigated.

2. Experimental

High purity powders of Cr (99.9% pure, 4.3 μm), Al (99.8% pure, 12.8 μm) and Cr_3C_2 (99.8%, 5.5 μm) were used as raw materials. They were mixed in ethanol for 24 h and then compacted uniaxially under the pressure of 20 MPa in a graphite mold pre-sprayed with a layer of BN. The compacted mixture was first heated in an Ar atmosphere at the rate of 5 °C/min from room temperature to 600 °C, under the pressure of 10 MPa. Then it was heated up to and maintained at a temperature of 1350 °C for 2h, at which time the pressure was gradually increased to 30 MPa. Finally, the sample was cooled down to room temperature. Before examination, the surfaces of the sintered samples were machined to remove the layer contaminated by the carbon sheet, using a fine grit high speed diamond wheel.

The sintered sample was polished and the density was measured by the Archimedes principle. Powders were drilled from the bulk of the samples for X-ray diffraction (XRD) characterization. The phase identification was made by XRD using a rotating anode X-ray diffractor (Model D/MAX-RB, RIGAKU Corporation, Japan). Scans were made with Cu K_α radiation (40 kV and 50 mA) at the rate of 1deg/min, using a step of 0.02°. The XRD data was refined for the lattice parameters by the Rietveld analysis. Pure silicon was added as an internal standard. The microstructures of the samples were investigated by the energy dispersive spectroscopy (EDS) method via scanning electron micrographs (SEM) (Model JSM-5610LV, JEOL Ltd., Japan). The microhardness was measured with a Leitz Microhardness Tester (Leitz Wetzlar, Germany) at 1 N with the loading time of 30 s. The hardness was calculated by averaging at least 10 measurements. Three-point bending tests were performed to measure flexural strength and fracture toughness (K_{IC}). The dimensions of the specimens subjected to flexural strength testing were 3×4×36 mm^3 and the crosshead speed was 0.5 mm/min. K_{IC} was measured by the single-edge notch beam (SENB) method with specimen dimensions of 4×8×36 mm^3. A notch 4 mm long and ca. 0.15 mm wide was

made by the electrical discharge method. The notch root radius was about 0.15 mm. The crosshead speed for fracture toughness testing was 0.05 mm/min. The thermal diffusivity α and heat capacity C_p were directly measured by a thermal constants measuring instrument (Sinku-Riko Model TC-7000) using the laser flash method. The thermal conductivity λ was calculated from the following equation:

$$\lambda = dC_p\alpha \tag{1}$$

where is the density (kg/m^3) of the sample, C_p its heat capacity (J/(kg·K)) and α – the coefficient of temperature conductivity (m^2/s).

The thermal expansion of the bulk polycrystalline samples was measured in air from room temperature to 1300 °C with a dilatometer. Electrical conductivity was measured using the four-probe method, from room temperature to 600 °C in vacuum. The Seebeck coefficient in vacuum was evaluated to 600 °C.

3. Results and discussions

3.1. Synthesis and microstructure of Cr_2AlC

Compared with the elemental chromium and chromium carbide, the melting point of aluminum is relatively low (ca. 933 K), so the weight loss of aluminum in the starting composition will inevitably occur, especially at elevated temperatures. Tian et al. [8] investigated Al content phase assemblage of Cr_2AlC and found that when the amount of additive Al is equal to or greater than 20 at. %, the Cr_2AlC phase becomes the only phase appearing in the final sample. Thus in the present research, samples initially having the molar ratio Cr: Al: C=2: 1.2: 1 were investigated.

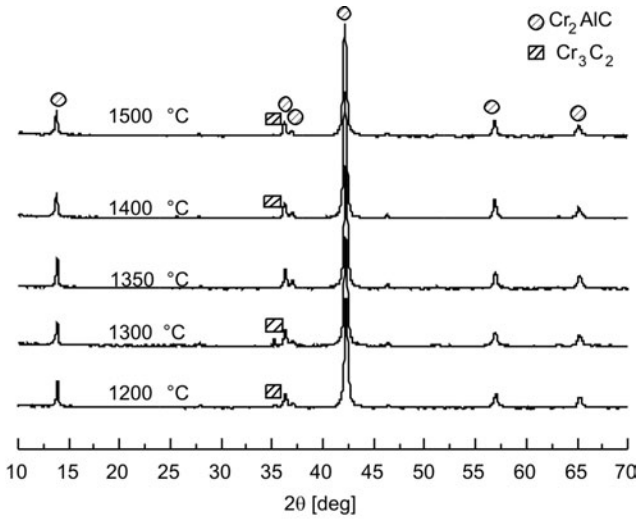

Fig. 1. X-ray diffraction patterns of the products sintered at various temperatures

Figure 1 shows the X-ray diffraction patterns of the products sintered at various temperatures from 1200 °C to 1500 °C. Between 1200 °C and 1300 °C, the main phase was Cr_2AlC, Cr_3C_2 phase was also found. When sintered at 1350 °C, no phase but Cr_2AlC was identified by X-ray diffraction, which indicated that the products were of high-purity. When the temperature was increased to 1400–1500 °C, the Cr_3C_2 peak appeared again, which indicated that Cr_2AlC could decompose into Cr_3C_2 and Al when the sintering temperature exceeded 1400 °C. The measured lattice parameters of sample (c) a = 0.2858±0.0002 nm and c = 1.2808±0.0002 nm were very close to those reported by other authors [2, 5].

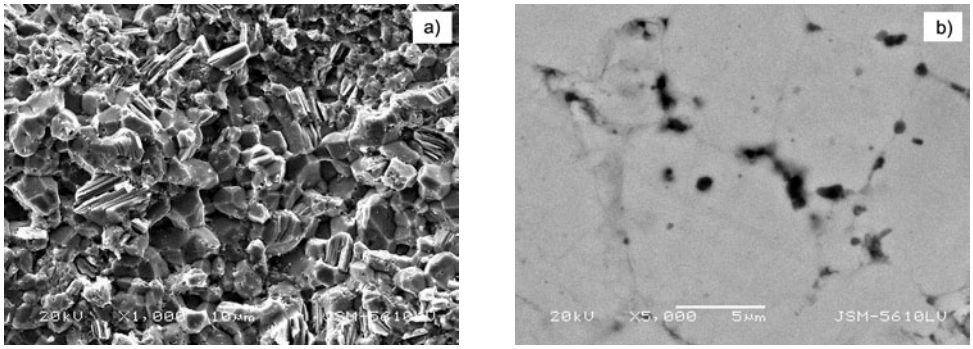

Fig. 2. SEM micrograph of the fracture surface for Cr_2AlC (a) and a typical BSE micrograph of the polished surface of Cr_2AlC (b)

Figure 2 shows the SEM micrograph of the fractured faces of samples sintered at 1350 °C for 2 h. The grains with the layered feature characteristic of Cr_2AlC can be clearly seen in the sample. The average grain size of Cr_2AlC is about 10 μm. A typical SEM micrograph, taken with back-scattered electron imaging, of the polished sample is shown in Fig. 2b. Some dark phases exist in the sample. Energy dispersive spectroscopy (EDS) analysis revealed that they were Cr_3C_2 phase. Cr_3C_2 phase could not be detected in the XRD spectrum due to its low content.

3.2. Mechanical properties of Cr_2AlC

The measured density of bulk material sintered at 1350 °C was 5200 kg/m^3, i.e. 99.4% of the theoretical value (5229 kg/m^3). The fracture toughness of Cr_2AlC is 5.8 MPa·m$^{1/2}$, being slightly lower than that of Ti_3AlC_2 and Ti_3SiC_2 but is still higher than that of conventional ceramics such as Al_2O_3, SiC, TiB_2, etc. The flexural strength of Cr_2AlC is 498 MPa, which is higher than that of Ti_3AlC_2 and Ti_3SiC_2. The compressive strength of the obtained sample was 627 MPa, which was lower than the value reported by Tian et al. Vickers indentation hardness was tested on the polished polycrystalline Cr_2AlC surface. The very highly polished surface of the sample showed metallic lustre. The measured Vickers hardness of Cr_2AlC sample was

5.2 GPa, which was similar to other reported values. More importantly, the material had the same machinability as that of graphite. It could easily be machined with ordinary mechanical machining tools, and holes could readily be drilled by using common steel drills, without adding lubricants.

3.3. Thermal and electrical properties

The average thermal expansion coefficient of the sample in the range 25–1300 °C was $1.31\times10^{-5}\,K^{-1}$, equal to that reported by Tian et al. [9] but a little higher than that of that Ti_3AlC_2 ($9.0\times10^{-6}\,K^{-1}$) [10].

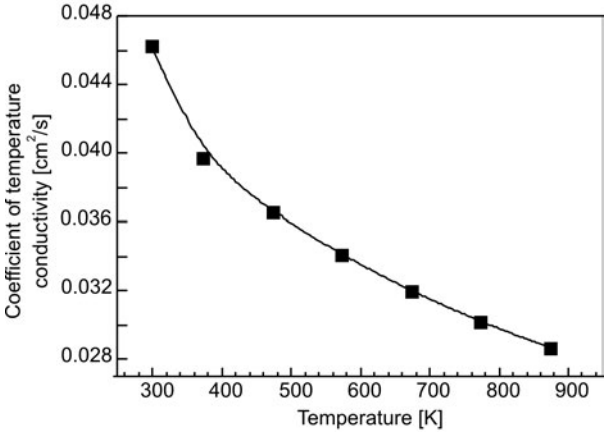

Fig. 3. Temperature dependence of the coefficient of temperature conductiity of Cr_2AlC

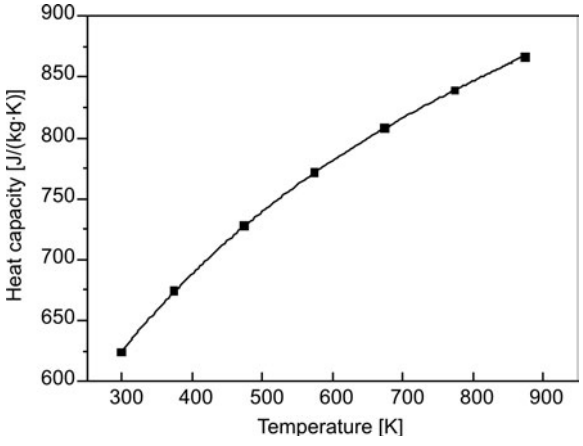

Fig. 4. Temperature dependence of the specific heat capacity of Cr_2AlC

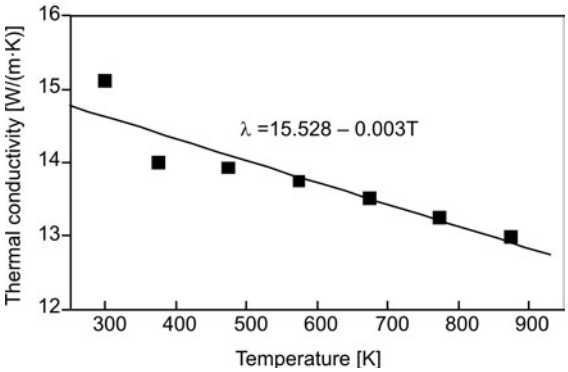

Fig. 5. Temperature dependence of the thermal conductivity of Cr_2AlC

The coefficient of temperature conductivity of each sample was determined in the range 25–600 °C. It decreased with the increase in temperature, as shown in Fig. 3. The specific heat capacity 624 J/(kg·K) of the sample obtained from Fig. 4 is higher than that of Ti_2AlC (581 J/(kg·K)) [11], and Cr_2AlC (590 J/(Kg·K)) [9].

The thermal conductivities of the sample λ between 25 °C and 600 °C can be calculated from Eq. (1). The thermal conductivity decreases slightly with the increase in temperature, as shown in Fig. 5. The least-squares fit of the data is shown as a straight solid line in Fig. 5.

The thermal conductivity of the sample in the range of 200-400 °C is from 13.84 W/(m·K) to 13.52 W/(m·K), which is lower than that of Cr_2AlC sample reported by Tian et al. [9]. The difference between the results of the two works is not clearly understood. It is probably due to the difference in particle sizes and impurities in the final samples.

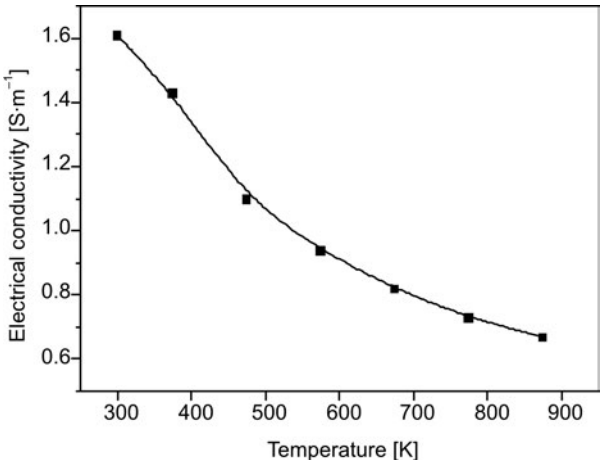

Fig. 6. Temperature dependence of the electrical conductivity of Cr_2AlC

The temperature dependence of the electrical conductivity of the Cr_2AlC sample is shown in Fig. 6 in the range 25–600 °C. The electrical conductivity of the sample decreases with the increase in temperature. At room temperature, the Cr_2AlC had an electrical conductivity of 1.6×10^6 $S\cdot m^{-1}$, which is lower than that of Ti_3SiC_2 and Ti_3AlC_2.

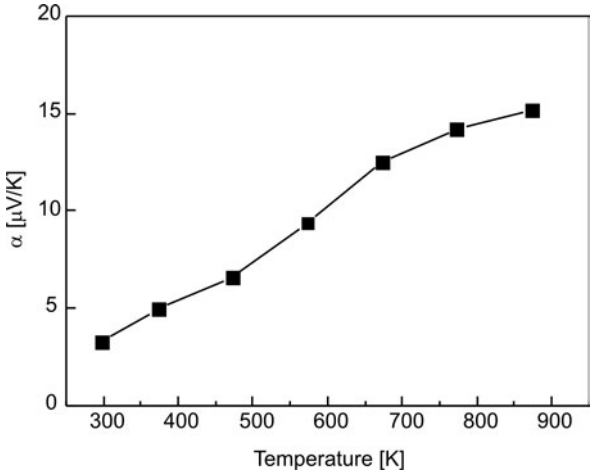

Fig. 7. Temperature dependence of the Seebeck coefficient of the Cr_2AlC sample

Figure 7 shows the Seebeck coefficient of Cr_2AlC in function of temperature. It changes in the range from 3.3 to 15.2 μV/K between room temperature and 873 K. This small positive value of the Seebeck coefficient and the metallic conductivity suggest that Cr_2AlC, similarly as Ti_3SiC_2 [12], is a semi-metal with hole carriers.

4. Conclusions

Dense polycrystalline Cr_2AlC can be obtained by hot pressing of the Cr, Al and Cr_3C_2 powders. A slight excess of Al is beneficial to synthesis of Cr_2AlC. The optimum temperature is 1350 °C. Cr_2AlC grains have an obvious, layered nature.

The flexural strength, fracture toughness and compressive strength of the obtained sample were 498 MPa, 5.8 $MPa\cdot m^{1/2}$ and 627 MPa, respectively. It had the Vickers hardness of 5.2 GPa and could be easily machined by using ordinary mechanical machining tools.

The coefficient of thermal expansion of Cr_2AlC is 1.3×10^{-5} K^{-1} in the range 25 –1200 °C. The temperature coefficients of thermal conductivity and electrical conductivity decrease upon increase of temperature. The heat capacity of Cr_2AlC increases from 624 J/9kg·K) to 867 J/(kg·K) over the range of 25–600°C.

The Seebeck coefficient changed from 3.3 to 15.2 μV/K between room temperature and 873 K. These small positive values of the Seebeck coefficient suggest that Cr2AlC is semi-metallic with hole carriers.

Acknowledgements

The authors are grateful for the support given by the National Natural Science Foundation of China under Contracts No. 50572080, No. 20771088 and Doctoral Foundation of Wuhan University of Technology (No.471-38650142).

References

[1] BARSOUM M.W., Prog. Solid. St. Chem., 28 (2000), 201.
[2] BOUCHAIB M., Phys. Rev. B., 73 (2006), 024110.
[3] SCHUSTER J.C., NOWOTNY H., VACCARO C., J. Solid St. Chem., 32 (1980), 213.
[4] TIAN W.B., WANG P.L., KAN Y.M., ZHANG G.J., LI Y.X., YAN D.S., Mater. Sci. Eng. A., 3 (2007), 229.
[5] LIN Z.J., ZHOU Y.C., LI M.S.,WANG J.Y., Z. Metall., 6 (2005), 291.
[6] ZHU J.Q., MEI B.C., LIU J., XU X.W., J. Mater. Sci. Lett., 22 (2003), 1111.
[7] ZHOU W.B., MEI B.C., ZHU J.Q., Mater. Lett., 59 (2005), 1547.
[8] TIAN W.B., WANG P.L., ZHANG G.J., KAN Y.M., LI Y.X., YAN D.S., Mater. Sci. Eng. A., 454–455 (2007), 132.
[9] TIAN W.B., WANG P.L., ZHANG G.J., KAN Y.M.,LI Y.X., YAN D.S., Scripta Mater., 54 (2006), 841.
[10] TZENOV N.V., BARSOUM M.W., J. Am. Ceram. Soc., 3 (2000), 825.
[11] BARSOUM, M.W., SALAMA I., EL-RAGHY T., GOLCZEWSKI J., PORTER W.D., WANG H., SEIFERT H.J., ALDINGER F., Metall. Mater. Trans. A, Phys. Metall. Mater. Sci., 33 (2002), 2775.
[12] GAO N.F., MIYAMOTO Y., ZHANG D., J. Mater. Sci. Lett., 34 (1999), 4385.

Received 23 May 2008
Revised 26 February 2009

Materials Science-Poland, *Vol. 27*, *No. 4/1*, *2009*

Preparation and characterization of La- and Ni-doped magnetite nanoparticles

J. MA[1], Y. JI[2*], M. TIAN[1]

[1]Zhongyuan University of Technology, Zhengzhou 450007, P. R. China

[2]Key Laboratory of Textile Science and Technology, Ministry of Education, Donghua University, Shanghai, P.R. China 201620

La- and Ni-doped Fe_3O_4 nanocomposite particles with a high saturation magnetization were prepared by a homogeneous precipitation method in aqueous solutions. The obtained nanoparticles were characterized by X-ray diffraction (XRD), transmission electron microscopy (TEM), inductively-coupled plasma atomic emission spectroscopy (ICPAES) and vibrating sample magnetometry (VSM). The results showed the diameters of La- or Ni-doped Fe_3O_4 composite particles to be in the range of 10–25 nm. The specific saturation magnetization of La- or Ni-doped Fe_3O_4 was considerably higher than that of pure Fe_3O_4 nanoparticles. The nanocomposite particles exhibited superparamagnetic behaviour.

Key words: magnetic material; nanocomposite; superparamagnetism; doped Fe_3O_4

1. Introduction

The superparamagnetic nanometer scale composites, with its special properties, have been widely applied in the fields of aviation and spaceflight, electronic, chemical and machinery industries, energy production and metallurgy, environmental protection and medical treatment [1–3]. Fe_3O_4 nanoparticles are one of several widely used magnetofluids, its saturation magnetization however, is generally insufficient to meet the requirements of some technical applications. Many research groups have proved that the magnetic performance of ferromagnetic nanoparticles, in particular Fe_3O_4, could be improved by doping them with rare earth or transition metal elements [4–9]. In this paper, superparamagnetic La- or Ni-doped Fe_3O_4 nanoparticles were prepared by a new method of homogeneous precipitation in aqueous solutions. The synthesized composite particles exhibited superparamagnetic behaviour and the specific saturated magnetization was highly improved.

*Corresponding author, e-mail: jiyali@dhu.edu.cn

2. Experimental

Materials. Lanthanum oxide of purity not lower than 99.9 wt. % was used. Other reagents were of analytical grade used without further purification, including ferric chloride hexahydrate ($FeCl_3 \cdot 6H_2O$), iron chloride ($FeCl_2 \cdot 4H_2O$), sodium dodecylbenzene sulfonate (NaDS), ammonium hydroxide ($NH_3 \cdot H_2O$), absolute ethanol, acetone and methanol.

Preparation of La- or Ni-doped Fe_3O_4 nanoparticles. An appropriate NaDS aqueous solution was placed in a 250 cm^3, four-necked round-bottom flask equipped with a condenser, a nitrogen gas inlet, and a mechanical stirrer. Then, a mixture of $FeCl_3 \cdot 6H_2O$ and $FeCl_2 \cdot 4H_2O$ (molar ratio 2:1) in deionized water and a selected amount of lanthanum oxide in HCl solution (or $NiCl_2$ in deionized water) were added into the flask. The mixture was stirred under nitrogen atmosphere for 30 min, followed by the addition of 1.5 mol/dm^3 $NH_3 \cdot H_2O$ aqueous solution until pH equaled 9. The reaction was allowed to run for 2 h at this pH level. After that, the mixture was aged at 80 °C for 40 min. Finally, the composite nanoparticles were obtained by purification repeatedly using magnetic field separation, and propanone and deionized water washing.

Characterization. The morphologies of the resulting composites were examined with a Hitachi H-800 transmission electron microscope. X-ray diffraction diagrams were recorded on a RD/MAX-RC diffractometer using Cu K_α radiation (λ = 1.5406 Å). The contents of Fe and La were measured with an IRIS Advantage 1000 inductively-coupled plasma atomic emission spectrometer (ICPAES) produced by the Thermo Jarrell Ash. The magnetization measurements were performed at room temperature using a Lakeshore 7400 vibrating sample magnetometer.

3. Results and discussion

3.1. Structure and morphology

In Table 1, the results of elemental analysis are given determined by ICPAES measurements, showing that Fe_3O_4 was successfully doped by La or Ni using the method of homogenous precipitation in aqueous solution.

Table 1. Results of elemental analysis of La- or Ni-doped Fe_3O_4

Fe_3O_4	Element	Contents [wt. %]
La doped	Fe	62.9±0.5
	La	3.5±0.5
Ni doped	Fe	64.5±0.5
	Ni	2.3±0.5

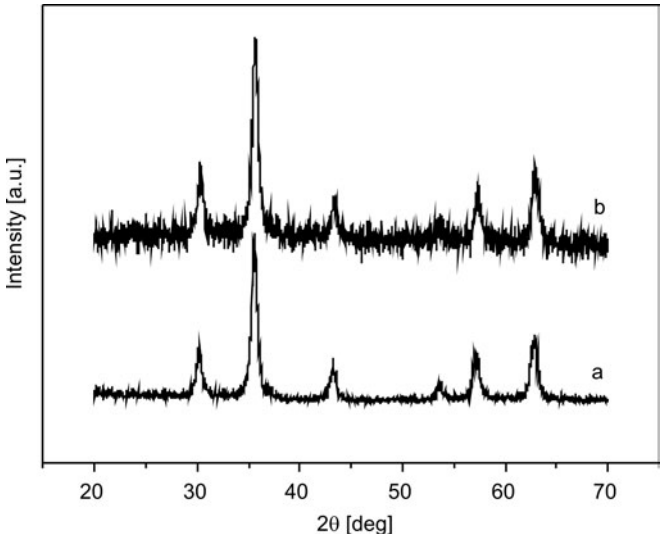

Fig. 1. XRD patterns of Fe_3O_4 (a) and La-doped Fe_3O_4 (b)

Figure 1 shows XRD patterns of Fe_3O_4 and La-doped Fe_3O_4 nanoparticles. The main peaks at 2θ in the pattern of La-doped Fe_3O_4 are 35.54, 43.18, 57.24 and 62.24°, similarly as in the standard Fe_3O_4, indicating that La-doped Fe_3O_4 nanoparticles mainly contain Fe_3O_4 crystal phase. The lattice constants (a) of the standard bulk Fe_3O_4 and the Fe_3O_4 nanocrystals estimated from XRD spectra are given in Table 2. The lattice constant for La-doped Fe_3O_4 nanoparticles is higher compared to that in pure Fe_3O_4 nanoparticles, suggesting that La well incorporated into the magnetite lattice and results in the expansion of the crystal cell. However, the measured La and Fe weight contents (Table 1) in the synthesized products suggest that they are far too nonstoichiometric to sustain the magnetite lattice. Thus, our La doped sample most probably contains La oxide, but is of too small volume to be observed in the XRD pattern.

Table 2. The calculated lattice constants in Fe_3O_4

Sample	Lattice constant a [Å]
Standard bulk Fe_3O_4	8.3960
Undoped Fe_3O_4 nanoparticles	8.3573
La-doped Fe_3O_4 nanoparticles	8.3710
Ni-doped Fe_3O_4 nanoparticles	8.3125

A typical XRD diffraction profile of Ni-doped Fe_3O_4 particles is given in Fig. 2. Compared with JCPDS 19-0629 of standard Fe_3O_4, the main peaks at 2θ = 30.3, 35.8, 43.22, 57.46 and 63.04° are attributed to the diffractions of the (020), (311), (400),

(511) and (440) planes of Fe_3O_4 magnetic particles, indicating the resulting composites contain Fe_3O_4 crystals.

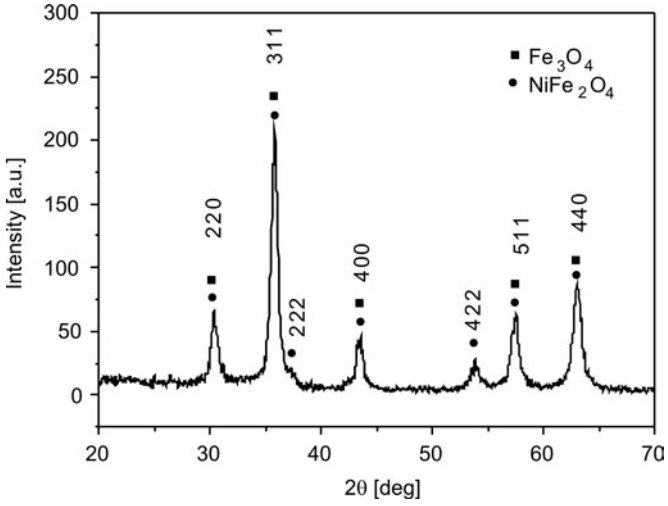

Fig. 2. XRD pattern of Ni-doped Fe_3O_4 particle

Furthermore, the lattice constant *a* for Ni-doped Fe_3O_4 nanoparticles (Table 2) is somewhat smaller in comparison with that for pure Fe_3O_4 nanoparticles, suggesting that Ni is also incorporated into magnetite lattice, resulting in the shrinkage of crystal cell. Similar to La-doped Fe_3O_4, some oxygen is also probably present in Ni oxide. According to the appearance of the diffraction peaks of the (222) and (422) planes and JCPDS10-0325 of $NiFe_2O_4$ crystals, it is concluded that the resulting Ni-doped Fe_3O_4 particles may contain $NiFe_2O_4$ crystals, although characteristic diffraction peaks of $NiFe_2O_4$ may overlap.

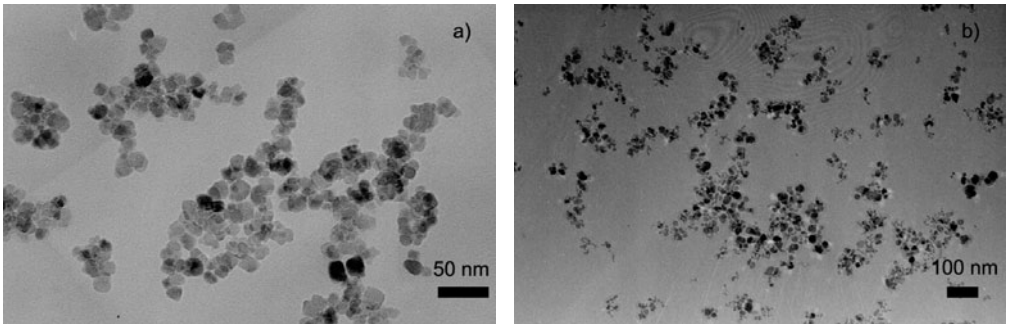

Fig. 3. TEM of La-doped Fe_3O_4 nanoparticle (a) and Ni-doped Fe_3O_4 nanoparticle (b)

The morphologies of the resulting La- or Ni-doped Fe_3O_4 composites are shown in Fig. 3. The size of the nanoparticles is in the range of 10–25 nm. Some of them form multiparticle aggregates, presumably due to the magnetic dipolar interparticle interaction.

3.2. Magnetic properties

Dependences of magnetizations of Fe_3O_4, La-doped Fe_3O_4 and Ni-doped Fe_3O_4 on the applied magnetic field at room temperature are shown in Fig. 4. The specific saturation magnetization of our Fe_3O_4 nanocrystals is 76.12 emu/g, which is somewhat smaller than that of the bulk magnetite (92 emu/g) [10]. The difference in the magnetization value between the bulk examined nanoparticles might be attributed to the small particle size effect [11].

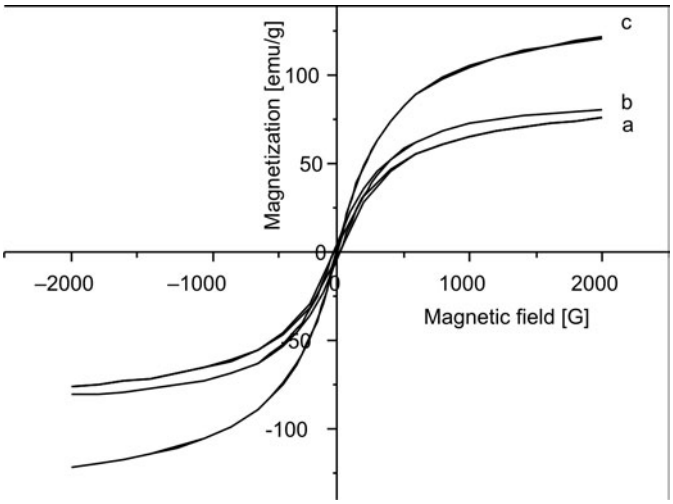

Fig. 4. Hysteresis loops of Fe_3O_4 and La or Ni-doped Fe_3O_4:
a) Fe_3O_4; b) La-doped Fe_3O_4; c) Ni-doped Fe_3O_4

Conversely, the specific saturation magnetization of Ni doped Fe_3O_4 is 121.78 emu/g, being much higher than the standard value (92 emu/g) and that of pure Fe_3O_4 nanoparticles. It can be established from the surface effects that the magnetization would increase as the surface anisotropy decreases [9, 12]. The impurity $NiFe_2O_4$, for which the magnetocrystalline anisotropy constant is lower than that of Fe_3O_4 [8], may preferentially be localized on the surface of Ni doped magnetite nanocrystal, thus, resulting in the increase of saturation magnetization. The saturation magnetization of La-doped Fe_3O_4 is 80.97 emu/g, higher than that of the Fe_3O_4 nanocrystals, but smaller than the standard value. The corresponding coercive forces of the doped composites are nearly 0 Oe and no hysteresis effects occur, which is typical of superparamagnetic materials.

4. Conclusions

Fe_3O_4 and La- or Ni-doped Fe_3O_4 nanocomposites were prepared by the chemical coprecipitation method in aqueous solution. The results show that the particle diame-

ters of La- or Ni-doped Fe_3O_4 are in the range of 10–25 nm. The specific saturation magnetization of Fe_3O_4 is 76.12 emu/g. The specific saturation magnetizations of La- or Ni-doped Fe_3O_4, being 80.97 and 121.78 emu/g, respectively, are considerably higher than that of pure Fe_3O_4 nanoparticles synthesized by the authors and those doped composites exhibit superparamagnetic behaviour.

Acknowledgements

This work was supported by the *111 Project*, B07024.

References

[1] GOMEZ-ROMERO P., Adv. Mater., 13 (2001), 163.
[2] MA J. M. , WANG Y., NIU J. S., SHEN X. Y., J. Macromol. Sci. B, 45 (2006), 533.
[3] SOHN B. H., COHEN R. E., PAPAEFTHYMIOU G. C., J. Magn. Magn. Mater., 182 (1998), 216.
[4] WANG J. P., HAO X. F., LIN M. F., LIU J. F., XING X. R., MENG J., J. Chin. Rare Earth Soc., 24 (2006), 461.
[5] ZHANG P. P., HAN C. H., CHENG J. P., CHEN X. G., YE Y., Chin. J. Inorg. Chem., 24 (2008), 307.
[6] GUO X. Y., YAN X. R., CUI X. L., WANG J. P., BAI T., Chin. J. Inorg. Chem., 20 (2004), 910.
[7] MOHAPATRAA M., PANDEYB B., UPADHYAYB C., ANANDA S., DASA R. P., VERMA H. C., J. Mag. Magn. Mat., 295 (2005), 44.
[8] LELIS M. F. F., FABRIS J. D., MUSSEL W. N., TAKEUCHI A. Y., J. Mat. Res., 6 (2003), 145.
[9] WESSELINOWA J. M., APOSTOLOVA I., J. Phys.: Condens. Matter, 19 (2007), 406235.
[10] ZAITSEV V. S., FILIMONOV D. S., PRESNYAKOV I. A., GAMBINO R. J., CHU B. J., Colloid Interface Sci., 212 (1999), 49.
[11] SAWATZKY G. A., VAN DER WOUDE F., MORRISH A. H., Phys. Rev., 187 (1969), 747.
[12] WESSELINOWA J. M., APOSTOLOVA I., J. Phys.: Condens. Matter, 19 (2007), 216208.

Received 19 June 2008
Revised 24 April 2009

Materials Science-Poland, *Vol. 27*, *No. 4/1*, *2009*

Structure and characterization of copper(II) perchlorate with diethyl(pyridin-2-ylmethyl) phosphonate (2-pmpe) ligand: $[Cu(2\text{-pmpe})_2(ClO_4)_2]$

B. ŻUROWSKA[1*], A. BIAŁOŃSKA[1], J. OCHOCKI[2]

[1]Faculty of Chemistry, University of Wroclaw, Joliot-Curie 14, 50-383 Wrocław, Poland

[2]Department of Bioinorganic Chemistry, Faculty of Pharmacy, Muszyńskiego 1, Medical University, 90-151 Łódź, Poland

Copper(II) mononuclear compound $[Cu(2\text{-pmpe})_2(ClO_4)_2]$ (2-pmpe = diethyl(pyridin-2-ylmethyl) phosphonate was synthesized and studied. Examination of the crystal structure by the X-ray diffraction method revealed two crystallographically unrelated molecules, $[Cu(1)(2\text{-pmpe})_2(ClO_4)_2]$ (**1**) and $[Cu(2)(2\text{-pmpe})_2(ClO_4)_2]$ (**2**) in an asymmetric part of the unit cell. The geometry about the Cu(**1**) and Cu(**2**) chromophores shows elongated octahedra, resulting from the didentate N,O-bonded two chelate 2-pmpe ligands and two coordinated perchlorate ions around the Cu(II) cations (CuN_2O_4 chromophore). Similarly to **1**, molecules **2** are linked to each other by weak C–H···O hydrogen bonds and π···π stacking interactions. Additionally, both **1** and **2** molecules are linked to each other through weak C–H···O hydrogen bonds and C–H···π contacts, resulting in a 3D polymeric network arrangement. Magnetic data indicate a very weak intermolecular exchange interaction between copper(II) ions ($zJ' = -0.20$ cm^{-1}) transmitted through non-covalent interactions in the crystal lattice. The spectral properties are in accordance with the structural and magnetic data.

Key words: *copper(II); phosphonic acid ester; crystal structure, spectroscopy; magnetism*

1. Introduction

Structure and bond properties of copper(II) complexes have been of constant interest in inorganic chemistry and biochemistry [1, 2] similarly as various ligand phosphonate derivatives due to their broad spectrum of biological properties. In recent years, much attention has been focused on the synthesis of phosphonate and phosphate esters of N-heterocyclic systems (pyridine or quinoline) and their platinum(II) and palladium(II) complexes, because of their potential applications [3] and significant

*Corresponding author, e-mail: zurowska@chem.uni.wroc.pl

antitumor activity [4–15]. Recently, we have demonstrated a high reactivity of these phosphonate with transition metal ions [16–23]. Our interest has also been focused on the magnetic properties of these compounds because it may allow the estimation of the strength of the magnetic coupling between magnetic centres through intramolecular covalent and/or intermolecular non-covalent interactions.

Studies of very weak non-covalent intermolecular interactions are of fundamental importance for further development of inorganic supramolecular chemistry and the prediction of crystal structures. These contacts generate or have an influence on interesting supramolecular properties such as electrical, optical and magnetic ones, and play a major role in the functioning of biological macromolecules [24–27].

The present paper is a continuation of our earlier investigation on the coordination properties of the N-heterocyclic phosphonate diesters including structural, spectroscopic and magnetic properties of obtained species.

It is worth mentioning that the interaction of the (pyridin-2-ylmethyl)phosphonate and (quinolin-2-ylmethyl)phosphonate diesters (2-pmpe and 2-qmpe, respectively) with some copper(II) and cobalt(II) salts leads to copper–picolinate or copper– and cobalt–quinaldinate systems through the oxidative decomposition of these ligands with cleavage of the C–P bond [22, 28].

In this work, the crystal structure of the mononuclear copper(II) compound with diethyl(pyridin-2-ylmethyl)phosphonate ligand (2-pmpe) was investigated (Fig. 1), having the formula $[Cu(2\text{-pmpe})_2(ClO_4)_2]$. Spectroscopic and magnetic properties are presented with reference to the crystal structure.

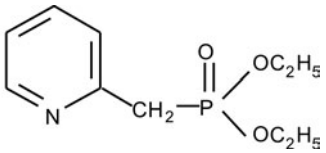

Fig. 1. Molecule of the diethyl(pyridin-2-ylmethyl) phosphonate (2-pmpe) ligand

2. Experimental

Synthesis of the $Cu(2\text{-pmpe})_2(ClO_4)_2]$ complex[*]. The diethyl(pyridin-2-ylmethyl) phosphonate (2-pmpe) ligand was obtained according to procedure described in detail elsewhere [17]. The perchlorate complex was synthesized by dissolving the hydrated copper(II) perchlorate (1 mmol) in ethanol (10 cm^3) and adding dropwise under stirring to the solution of the ligand (2 mmol) in ethanol (20 cm^3). The crystalline blue product was obtained by slow evaporation of the solvent at room temperature.

[*]Although no problem was encountered in this work, perchlorate salts containing organic ligands are potentially explosive. They should be prepared in small quantities and handled with care.

Anal. calcd. for $C_{20}H_{32}Cl_2CuN_2O_{14}P_2$: C, 33.32; H, 4.48; N, 3.89; Cu, 8.82. Found: C, 33.55; H, 4.56; N, 3.69; Cu, 8.63 %.

Physical measurements. Metal content was determined using a Carl Zeiss Jena atomic absorption spectrophotometer and an ARL model 3410 ICP spectrometer. Elemental analyses were carried out using a Perkin-Elmer elemental analyzer 2400CHN. Solid-state electronic spectrum (28000–4000 cm^{-1}) was performed on a Cary 500 spectrophotometer. Solid state EPR spectra were recorded at room temperature and at 77 K on a Bruker ESP 300E spectrometer operating at X-band, equipped with a Bruker NMR gaussmeter ER 0.35 M and a Hewlett Packard microwave frequency counter HP 5350B. Magnetic measurements were carried out with a Quantum Design SQUID magnetometer (type MPMSXL-5). The measurements were recorded in a magnetic field of 0.5 T in the temperature range 1.8-300K. Corrections for diamagnetic contributions are based on subtracting the sample holder signal and estimating the contribution χ_D from the Pascal constants [29]. The effective magnetic moments were calculated from $\mu_{eff} = 2.83(\chi_M T)^{1/2}$ using temperature-independent paramagnetism of 60×10^{-6} $cm^3\cdot mol^{-1}$ for Cu(II) ion [30].

Determination of the crystal structure of [Cu(2-pmpe)$_2$(ClO$_4$)$_2$]. X-ray data were collected on a Kuma KM4CCD diffractometer (Mo K_α radiation, λ = 0.71073 Å). X-ray data were collected at 100 K using an Oxford Cryosystem device. Data reduction and analysis were carried out with the CrysAlice 'RED' program [31]. The space group was determined using the XPREP program. The structure was determined by direct methods using the XS program and refined using all the F^2 data, as implemented by the XL program [32]. Non-hydrogen atoms were refined with anisotropic displacement parameters. All H atoms were placed at calculated positions. Before the last cycle of refinement, all H atoms were fixed and were allowed to ride on their parent atoms.

3. Results and discussion

3.1. Description of the structure of [Cu(2-pmpe)$_2$(ClO$_4$)$_2$]

Two crystallographically unrelated molecules, [Cu(1)(2-pmpe)$_2$(ClO$_4$)$_2$] (**1**) and [Cu(1)(2-pmpe)$_2$(ClO$_4$)$_2$ (**2**), exist in the asymmetric part of the unit cell (Fig. 2). The Cu(**1**) and Cu(**2**) copper ions are located in a special position. The crystallographic parameters are summarized in Table 1. The selected bond lengths and angles are listed in Table 2.

Diethyl(pyridin-2-ylmethyl)phosphonate (2-pmpe) ligands acting as a didentate bonding, chelate to the Cu(**1**) and Cu(**2**) atoms through the pyridyl nitrogen and the phosphoryl oxygen atoms resulting in six-membered rings. The P=O group is arranged in a *trans* position. The O atoms of the perchlorate anions complete a distorted octahedral surrounding of Cu(**1**) and Cu(**2**) atoms. As presented in Table 2, the Cu-N and Cu–O bond length between the Cu atoms and the 2-pmpe ligands are shorter than

Cu–O bonds between Cu atoms and perchlorate anions. It causes a significant distortion of the coordination polyhedron around the Cu(**1**) and Cu(**2**) ions (CuN_2O_4 chromophore). In the crystal under investigation, the Cu–O (coordinated perchlorate) distances (2.482(3) and 2.433(3) Å) are longer than the Cu–O (coordinated perchlorate) distances found in crystals of related Cu(II) compounds with N-heterocyclic phosphate ligand (2.409 (**2**) Å) [33].

Table 1. Crystal data and structure refinement for $[Cu(2\text{-pmpe})_2(ClO_4)_2]$

Empirical formula	$C_{20}H_{32}Cl_2CuN_2O_{14}P_2$	D_c, $Mg \cdot m^{-3}$	1.680
Formula weight	720.86	Absorption coefficient, mm^{-1}	1.137
Temperature, K	100(**2**)	$F(000)$	742
Wavelength, Å	0.71073	Crystal size, mm	0.26 x 0.11 x 0.09
Crystal system	triclinic	θ range for data collection, deg	3.11 - 27.00
Space group	$P\bar{1}$	Ranges of h, k, l	–10=>10, –14=>14, –19=>18
a, Å	8.442(3)	Reflections collected	15969
b, Å	11.158(3)	Independent reflections, R_{int}	6220 (0.0759)
c, Å	15.248(4)	Completeness to 2θ = 54.00	99.7%
α, deg	87.30(3)	Absorption correction	analytical
β, deg	84.23(3)	Data/parameters	6220/373
γ, deg	86.35(3)	Goodness-of-fit, F^2	1.151
Volume, $Å^3$	1424.9(7)	Final R/wR indices, $I>2\sigma I$	0.0723/0.1028
Z	2	Largest diff. peak/hole, $e \cdot Å^{-3}$	0.429/–0.484

Table 2. Bond lengths (Å) and angles (°) for $[Cu(2\text{-pmpe})_2(ClO_4)_2]$

Molecule (**1**)	Molecule (**2**)
Cu(**1**)–N(1) 1.952(3)	Cu(**2**)–O(1A) 1.966(3)
Cu(**1**)–N(1) 2.058(3)	Cu(**2**)–N(1A) 2.060(4)
Cu(**1**)–O(11) 2.482(3)	Cu(**2**)–O(21) 2.433(3)
P(1)–N(1) 1.499(3)	P(1A)–O(1A) 1.493(3)
P(1)–O(3) 1.546(3)	P(1A)–O(3A) 1.554(3)
P(1)–N(1) 1.558(3)	P(1A)–O(2A) 1.564(3)
N(1)–P(1)–O(3) 115.50(17)	O(1A)–P(1A)–O(3A) 114.90(18)
N(1)–P(1)–N(1) 111.94(16)	O(1A)–P(1A)–O(2A) 113.05(18)
O(3)–P(1)–N(1) 105.98(18)	O(3A)–P(1A)–O(2A) 103.93(17)
N(1)–P(1)–C(7) 110.7(**2**)	O(1A)–P(1A)–C(7A) 109.84(19)
O(3)–P(1)–C(7) 102.59(19)	O(3A)–P(1A)–C(7A) 104.9(**2**)
N(1)–P(1)–C(7) 109.64(19)	O(2A)–P(1A)–C(7A) 109.74(19)
N(1)–Cu(**1**)–N(1)^{i} 88.06(13)	O(1A)–Cu(**2**)–N(1A)^{ii} 86.90(13)
N(1)–Cu(**1**)–N(1) 91.94(13)	O(1A)–Cu(**2**)–N(1A) 93.10(13)
N(1)–Cu(**1**)–O(11) 95.59(11)	O(1A)–Cu(**2**)–O(21) 97.79(12)
N(1)–Cu(**1**)–O(11) 90.55(12)	N(1A)–Cu(**2**)–O(21) 88.24(13)
N(1)–Cu(**1**)–O(11)^{ii} 84.41(11)	O(1A)–Cu(**2**)–O(21)^{ii} 82.21(12)
N(1)–Cu(**1**)–O(11)^{ii} 89.45(12)	N(1A)–Cu(**2**)–O(21)^{ii} 91.76(13)

Symmetry transformations used to generate equivalent atoms: (i) $-x+2,-y,-z+1$, (ii) $-x+1,-y+1,-z$

The P(1)-N(1) and P(1A)-O(1A) bond lengths of the phosphoryl P=O group of both crystallographically unrelated ligands are equal to 1.499(3) and 1.493(3) Å, respectively, and are smaller than the P–O bond lengths of the phosphonate groups (Table 2). Analysis of the geometric parameters indicates that the environment of the P(1) and P(1A) atoms is distorted tetrahedral i.e. the angles deviate from the ideal value of 109.5^o, observed for other phosphonate diesters [34].

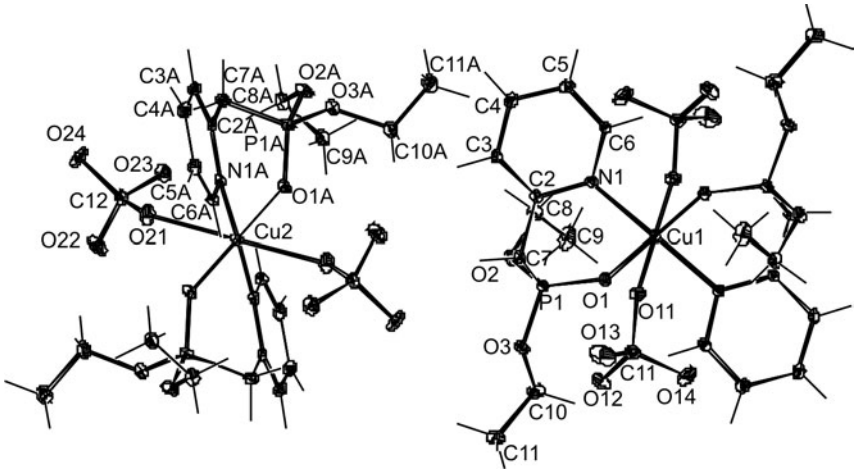

Fig. 2. Relative orientation of the molecules **1** and **2** in the crystal of [Cu(2-pmpe)$_2$(ClO$_4$)$_2$] showing the atomic numbering. Symmetry codes are given in Table 2

Crystalographically unrelated molecules, [Cu(1)(2-pmpe)$_2$(ClO$_4$)$_2$] (**1**) and [Cu(2)(2-pmpe)$_2$(ClO$_4$)$_2$] (**2**) are linked by π···π interaction, formed between pyridyl rings, resulting in ribbons extended in the [100] direction. The ribbons are stabilized by C–H···O hydrogen bonds formed between the aromatic C–H group of the pyridine rings and coordinated perchlorate oxygens [C(4)–H(4)···O(11)^{iii} and C(4A)-H(4A)···O(21)^{vi}] (symmetry codes are given in Table 3). The ribbons are linked to each other by C–H···O hydrogen bonds and C–H···π contacts. Additionally, the molecules **1** and **2** are stabilized by intramolecular C–H···O hydrogen bonds (Table 3).

Table 3. Geometry of the hydrogen bonds [Å] and contacts for [Cu(2-pmpe)$_2$(ClO$_4$)$_2$] [deg]

D–H···A	d(D-H)	d(H···A)	d(D···A)	<(DHA)
1	2	3	4	5
Interactions for molecule (**1**)				
Intra				
C(7)–H(7B)···O(11)	0.99	2.54	3.286(6)	132
C(6)–H(6)···O(12)^{i}	0.95	2.57	3.338(5)	138
Inter				
C(4)–H(4)···O(11)^{iii}	0.95	2.45	3.274(6)	144

Table 3 continued

1	*2*	3	4	5
Interactions for molecule (**2**)				
Intra C(8A)–H(8D)···O(23)	0.99	2.33	3.318(6)	174
Inter C(4A)–H(4A)···O(21)^{vi}	0.95	2.61	3.354(6)	136
Interactions between (**1**) and (**2**) molecules				
C(3)–H(3)···O(22)^{ii}	0.95	2.64	3.463(6)	146
C(7)–H(7A)···O(22)^{ii}	0.99	2.54	3.472(6)	157
C(11)–H(11A)···O(23)^{vii}	0.98	2.55	3.314(6)	134
C(5)–H(5)···O(2A)^{viii}	0.95	2.54	3.434(6)	156
C(9)–H(9B)···CP2^{ix}	0.98	3.02	3.919(6)	153
Interactions between (**2**) and (**1**) molecules				
C(10A)–H(10C)···O(13)^{v}	0.99	2.57	3.342(6)	134
C(7A)–H(7C)···O(12)^{iv}	0.99	2.28	3.251(6)	167

S*y*mmetr*y* transformations used to generate equivalent atoms: (i) –*x*+2, –*y*, –*z*+1; (ii) –*x*+1, –*y*+1, –*z*; (iii) –*x*+1, –*y*, –*z*+1; (iv) *x*–1, *y*+1, *z* (v) *x*, *y*+1, *z* (vi) –*x*, –*y*+1, –*z* (vii) –*x*+2, –*y*+1, –*z*; (viii) –*x*+1, –*y*+1, –*z*+1; (ix) *x*+1, *y*, *z*.

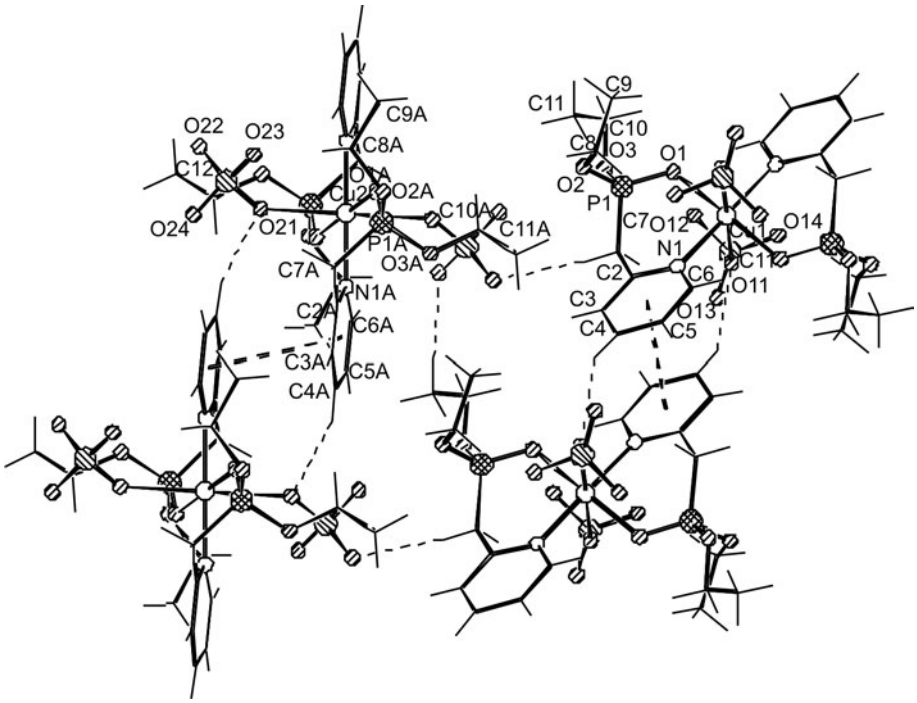

Fig. 3. Arrangement of the molecules **1** and **2** in the crystal of $[Cu(2\text{-pmpe})_2(ClO_4)_2]$ and their linkage through weak C–H···O hydrogen bonds and π–π interactions (dashed lines). Other hydrogen contacts linked to the molecules **1** and **2** are listed in Table 3

The dihedral angle between planes defined by N(1), N(1), N(1)^i, N(1)^i and N(1A), O(1A), N(1A)^{ii}O(1A)^{ii} atoms is equal to 67.68°. Arrangement of the molecules **1** and **2** in the crystal of [Cu (2-pmpe)$_2$(ClO$_4$)$_2$] is shown in Fig. 3. The C–H···O hydrogen bonds, C–H···π contacts and π···π interactions, given in detail in Tables 3 and 4 stabilize the structure and give rise to a three-dimensional (3D) network. Crystal packing of the molecules **1** and **2** is shown in Fig. 4.

Table 4. π···π interactions [Å] and [deg]

	Cp·Cp	Interplanar angle	Cp (perp)	Slippage
Cp1···Cp1^i	3.628	0.00(20)	3.486(3)	1.01
Cp2···Cp2^v	3.798	0.00(22)	3.637(3)	1.09

Symmetry transformations used to generate equivalent atoms: (i) –*x*+2, –*y*, –*z*+1, (v) *x*, *y*+1, *z*; Cp1 – centroid of N(1) C(2) C(3) C(4) C(5) C(6) ring; Cp2 – centroid of N(1A) C(2A) C(3A) C(4A) C(5A) C(6A) ring.

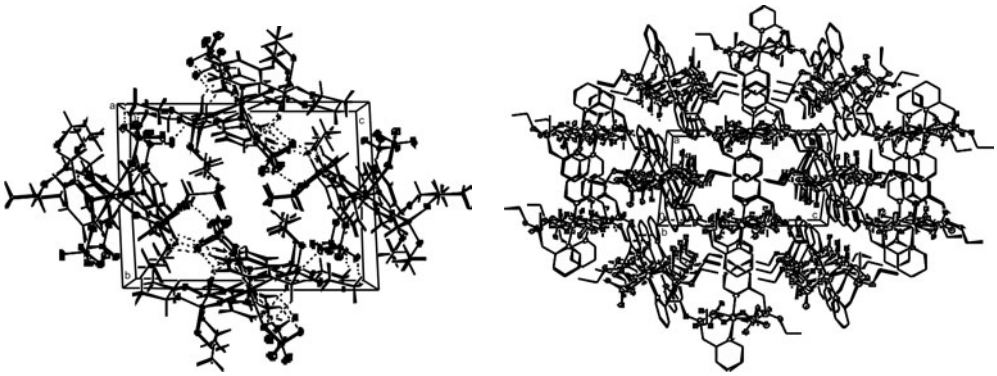

Fig. 4. Crystal packing of the molecules **1** (left) and **2** (right) in the crystal of [Cu(2-pmpe)$_2$(ClO$_4$)$_2$] viewed down the *a*-axis and *b*-axis, respectively. The C–H···O hydrogen bonds are shown with dashed lines

The shortest intermolecular metal–metal separations for Cu(1)···Cu(1)^{ix} and Cu(2)···Cu(2)^{ix} (*ix* = 1+*x*, *y*, *z*) are of 8.442(3) Å. For Cu(1)···Cu(2), Cu(1)···Cu(2)^{ix} and Cu(1)···Cu(2)^{x} (*x* = *x*, *y*, 1–*z*), these separations are: 10.322(4), 9.979(4) and 10,080(4) Å, respectively.

3.2. Spectroscopic properties

In the infrared spectrum of the compound studied, the bands corresponding to the stretching modes of the pyridine ν(C=C) and ν(C=N) observed at 1589, 1570 cm^{-1} for the free ligand are shifted to the higher frequencies in the complex (1610, 1571 cm^{-1}). The characteristic out-of-plane and in-plane deformation bands of the 2-substituted

pyridine ring (405 and 602 cm^{-1}, respectively) are also shifted to higher frequencies (416 and 616 cm^{-1}, respectively), suggesting coordination of the pyridyl nitrogen atom. The band at 967 cm^{-1} associated with a pyridine ring breathing mode is characteristically shifted to higher energy (972 cm^{-1}) on coordination.

A very strong band at 1250 cm^{-1}, which corresponds to the P=O stretching frequencies of the free ligand in the spectrum of the title compound, is shifted towards lower frequencies by 75 cm^{-1}, indicating the coordination of the phosphoryl oxygen atom to the metal ion and suggests, that 2-pmpe acts as a N,O-bonded chelate ligand. For monodentate coordination of 2-pmpe through the oxygen atom a shift about 20–30 cm^{-1} is observed [21]. The strong non-splitting absorption band of uncoordinated perchlorate anion at about 1110 cm^{-1} in the IR spectrum of $[Cu(2\text{-pmpe})_2(ClO_4)_2]$ is distinctly split to two components, observed at around 1090 and 1120 cm^{-1}. Also a strong absorption band characteristic of uncoordinated perchlorate ion, centred at 620 cm^{-1} is significantly split (610 and 628 cm^{-1}) in the spectrum of the compound. These features indicate unidentate coordination of the perchlorate group [34–36]. The far-IR region of the compounds reveals one band at ca. 270 cm^{-1} attributed to the ν(M–N) stretching vibration.

A broad asymmetric band centred at 14 800 cm^{-1} with a shoulder of ca. 12 700 cm^{-1} observed in the ligand field spectrum is characteristic of tetragonally distorted octahedral complexes [37], consistent with the structural analysis.

3.3. Magnetic properties

The EPR X-band powder spectrum of the copper compound is of the axial type with g values of $g_{\|} = 2.28_6$ and $g_{\perp} = 2.06_6$ at room temperature. The spectrum is independent of temperature. The $g_{\|}$ value is in agreement with that observed for CuN_2O_4 chromophore [38]. The spectrum of copper(II) compound in a frozen solution of ethanol was also recorded. This spectrum shows g values similar to the g values of the powder spectra, which indicates that the complex is stable in solution.

It is well known that weak non-covalent interactions not only stabilize crystal structure, but may also provide pathways for magnetic superexchange. Since the above analysis of the structure of the Cu(II) compound indicates that small but not negligible intermolecular magnetic exchange interaction cannot be excluded, we performed a magnetic study of this compound.

The magnetic properties of the compound, represented in the form of $\chi_{Cu}T$ and $1/\chi_{Cu}$ vs. temperature plots in the 1.8–300 K temperature range, are shown in Fig. 5 (χ_{Cu} is the molar magnetic susceptibility per Cu(II) ions). The effective magnetic moment μ_{eff} at room temperature (μ_{eff} =1.93 μ_B, $\chi_M T$ = 0.466 $cm^3 \cdot mol^{-1} \cdot K$) is within the usually observed range of experimental values for complexes in the octahedral configuration [39, 40]. At 1.8 K, the effective magnetic moment μ_{eff} is equal to 1.83μ_B ($\chi_M T$ = 0.418 $cm^3 \cdot mol^{-1} \cdot K$). The best fit values of the Curie (C) and Weiss (θ) constants, obtained from the equation $\chi_M = (C/(T-\theta)]$ within the measured temperature

region, are equal to 0.460 cm^3·K·mol^{-1} and –1.44 K, respectively. The negative Weiss constant (θ)suggests the possibility of a very weak magnetic interaction between magnetic centres via the non-covalent bond system in the crystal lattice at lower temperatures.

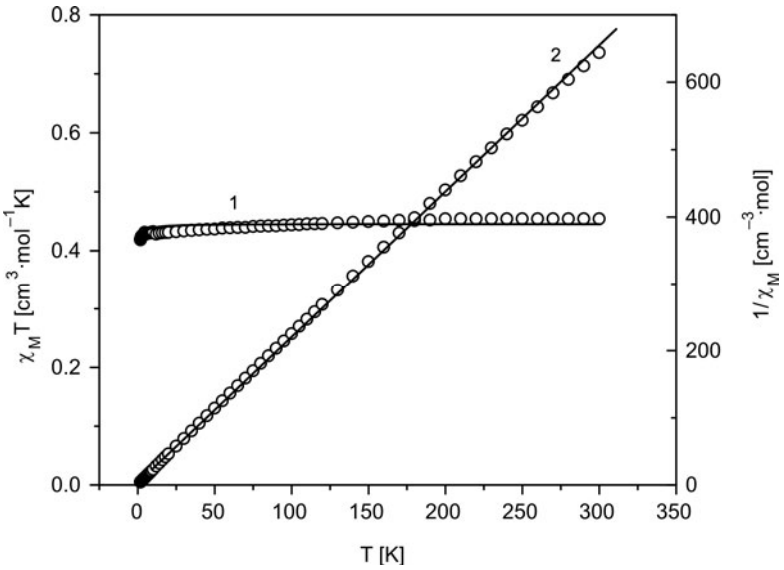

Fig. 5. Temperature dependences of $\chi_{Cu}T$ (1) and $1/\chi_{Cu}$ (2) for [Cu(2-pmpe)$_2$(ClO$_4$)$_2$]. Solid lines correspond to the best theoretical fit (see text)

Therefore, in order to evaluate the intermolecular interactions of the magnetic centre of the [Cu(2-pmpe)$_2$(ClO$_4$)$_2$] compound, a molecular exchange field model was used [41]:

$$\chi_M = \frac{N\beta^2 g^2}{3kT} S(S+1) \tag{1}$$

$$\chi_M^{\text{corr}} = \frac{\chi_M}{1 - \frac{2zJ'}{N\beta^2 g^2}\chi_M} \tag{2}$$

where χ_M is the equation for the magnetic susceptibility of paramagnetic centre, χ_M^{corr} is the measured experimental susceptibility, zJ' is the intermolecular exchange parameter, z is the number of nearest neighbours. In the frame of this model, the best fit parameters obtained by the least squares fit are the following: $zJ' = -0.21$ cm^{-1}, $g = 2.18$ with the value of $R = 6.87 \cdot 10^{-6}$, where R is the agreement factor, defined as

$$R = \sqrt{\frac{\sum_i \frac{\left(\chi_i^{\exp} - \chi_i^{\text{calc}}\right)^2}{\left(\chi_i^{\exp}\right)^2}}{\sum_i \frac{1}{\left(\chi_i^{\exp}\right)^2}}}$$

The temperature dependence of the experimental and calculated values of $\chi_M T$ of the Cu(II) compound is shown Fig. 5.

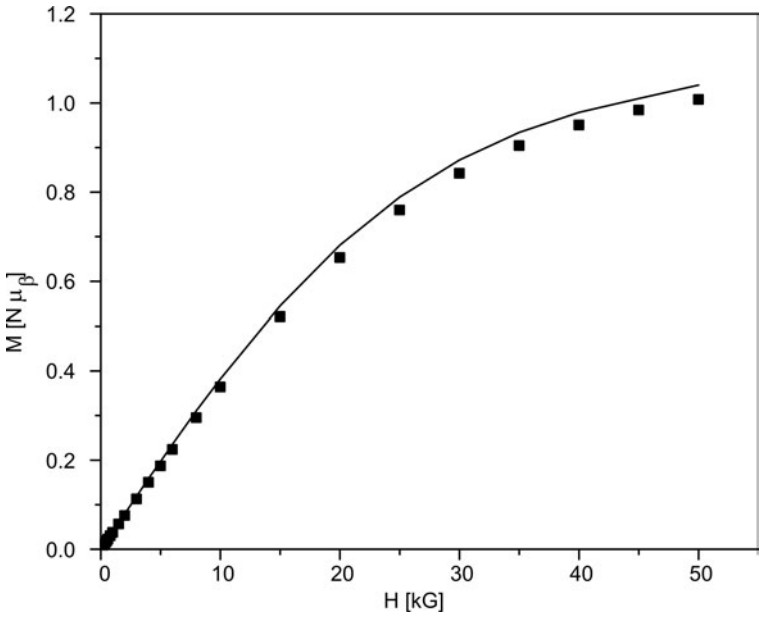

Fig. 6. Molar magnetization in function of the magnetic field, experimental (■).
The solid line represents the Brillouin function, assuming $g = 2.18$ (the value of the fit)

The molar magnetization M of the studied compound was measured in function of the applied magnetic field H at 2 K (Fig. 6). The magnetization ($M/N\mu_\beta$) per Cu(II) ion at 5 kGs (5 T) tending to one electron is close to that expected for an isolated Cu(II) ion (1 $N\mu_\beta$). At intermediate fields, the experimentally determined data points lie below the theoretical curve, indicating a weak antiferromagnetic coupling between the copper(II) ions.

4. Conclusions

The reaction of copper(II) perchlorate with diethyl(pyridin-2-ylmethylphosphonate) ligand 2-pmpe leads to crystallization of the $[Cu(2\text{-pmpe})_2(ClO_4)_2]$ complex.

There are two crystallographically unrelated [Cu(2-pmpe)$_2$(ClO$_4$)$_2$] molecules in an asymmetric part of the unit cell. The crystal structure is stabilized by weak C–H···O, C–H···π and π···π interactions, resulting in an extensive, three-dimensional network.

Differences between copper(II) and cobalt(II) perchlorate complexes with N-heterocyclic phosphonate or N-heterocyclic phosphate ligands are worth mentioning. While perchlorate anions are coordinated in the Cu(II) complexes, they are uncoordinated in the Co(II) complexes, and water molecules are coordinated to Co(II) ions [19, 42].

In conjugation with structural studies, the magnetic properties of the title compound were investigated. A small value of zJ' is compatible with the expected limit $|J'| < 0.5$ cm^{-1} for exchange interactions between the copper(II) ions transmitted through weak intermolecular noncovalent interactions.

Finally, it is worth mentioning that the studied compound is stable in solution when exposed to air. According to our earlier observation [22, 28], the didentate coordination of the 2-pmpe ligand stabilizes the complex preventing oxidative cleavage of C–P bond of the ligand and carboxylate compound formation*.

Acknowledgement

The work was supported by the by the Polish Ministry of Science and Higher Education (Grant No. N405 303236) (J. O.) and by Grants Nos. 503-3016-2 and 502-13-777 (J. O.).

References

[1] MURPHY B.P., HATHAWAY B.J., Coord. Chem. Rev., 63 (1993), 124.
[2] HATHAWAY B.J., [In:] G. Wilkinson, R.D. Gillard, J.A. McCleverty (Eds.), *Comprehensive Coordination Chemistry*, Vol. 5, Pergamon Press, Oxford, 1987, p. 553.
[3] KALINOWSKA U., CHĘCIŃSKA L., WAŁECKA M., ERXLEBEN A., LIPPERT B., OCHOCKI J., Inorg. Chim. Acta, 358 (2005), 2464.
[4] ARANOWSKA K., GRACZYK J., CHĘCIŃSKA L., PAKULSKA W., OCHOCKI J., Pharmazie, 61 (2006), 457.
[5] ZIĘBA R., MALINOWSKA K., WIEWIÓROWSKI M., GRACZYK J., Acta Pol. Pharm., 57 (2000), 136.
[6] CHĘCIŃSKA L., WAŁECKA M., OCHOCKI J., ARANOWSKA K., Acta Cryst., E59 (2003) m350.
[7] BRZEZIŃSKA-BŁASZCZYK E., MIŃCIKIEWICZ M., OCHOCKI J., Eur. J. Pharmacol., 155 (1996), 298.
[8] KOSTKA B., OCHOCKI J., Pharmazie, 51 (1996), 990.
[9] KAJMAN-BRONŻEWSKA L., OCHOCKI J., Pharmazie, 198 (1997), 52.
[10] ZHAO G., LIN H., YU P., SU H., ZHU S., SU X., CHEN Y., J. Inorg. Biochem., 145 (1999), 73.
[11] IAKOVIDOU Z., PAPAGEORGIOU A., DEMERTZIS M.A., MIOGLOU E., MOURELATOS D., KOTSLS A., NATH YADAV P., KOVALA-DEMERTZI D., Anti-Cancer Drugs, 12 (2001), 65.
[12] ĆURIĆ M., TUŠEK-BOŽIC L., VIKIĆ-TOPIĆ D., STARCIA V., FURLANI A., BALZARINI J., DE CLERCQ E., J. Inorg. Biochem., 63 (1996), 125.
[13] TUŠEK-BOŽIĆ L., ĆURIĆ M., BALZARINI J., DE CLERCQ E., Nucleos, Nucleot., 14 (1995), 777.
[14] TUŠEK-BOŽIĆ L., MATIJAŠIĆ J., BOCELLI G., SGARBOTTO P., FURLANI A., SCARIA V., PAPAIOANNOU A., Inorg. Chim. Acta, 185 (1991), 229.

---

*Crystallographic data for the structure have been deposited with the Cambridge Crystallographic Data Centre, CCDC-685325. Copies of the data can be obtained free of charge on application to the Director, CCDC, 12 Union Road, Cambridge CB2 1EZ, UK (Fax: int.code +(1223)336-033, e-mail for inquiry: fileserv@ccdc.cam.ac.uk).

[15] TUŠEK-BOŽIĆ L., MATIJAŠIĆ J., BOCELLI G., CALESTANI G., FURLANI A., STARCIA V., PAPAIOANNOU A., J. Chem. Soc., Dalton Trans., (1991), 195.
[16] OCHOCKI J., ŻUROWSKA B., MROZIŃSKI J., REEDIJK J., Proc. III Symp. on Inorganic Biochemistry and Molecular Biophysics, and VI Int. Scientific School on Biological Macromolecules, Wrocław –Karpacz, Wrocław 1991, 212.
[17] OCHOCKI J., KOSTKA K., ŻUROWSKA B., MROZIŃSKI J., GAŁDECKA E., GAŁDECKI Z., REEDIJK J., J. Chem. Soc. Dalton Trans., (1992), 2955.
[18] OCHOCKI J., ŻUROWSKA B., MROZIŃSKI J., KOOIJMAN H., SPEK A.L., REEDIJK J., Eur. J. Inorg. Chem., (1998), 169.
[19] ŻUROWSKA B., MROZIŃSKI J., CIUNIK Z., OCHOCKI J., J. Mol. Struct., 79 (2006), 98.
[20] ŻUROWSKA B., MROZIŃSKI J., CIUNIK Z., OCHOCKI J., J. Mol. Struct., 843 (2007), 26.
[21] ŻUROWSKA B., MROZIŃSKI J., OCHOCKI J., Mater. Sci.-Poland, 25 (2007), 1063.
[22] ŻUROWSKA B., OCHOCKI J., MROZIŃSKI J., CIUNIK Z., REEDIJK J., Inorg. Chim. Acta, 357 (2004), 755.
[23] ŻUROWSKA B., ŚLEPOKURA K., LIS T., OCHOCKI. J., Inorg. Chim. Acta, 362 (2008), 733
[24] JEFFREY G.A., SAENGE W., *Hydrogen Bonding in Biological Structures*, Springer, Berlin, 1991; JEFFREY G.A., *An Introduction to Hydrogen Bonding*; Oxford, New York, 1997; ROESKY H.W., ANDRUH M., Coord. Chem. Rev., 91 (2003), 236.
[25] FISHER B.E., SIGEL H., J. Am Chem. Soc., 102 (1980), 2998; SUGIMORI T., SHIBAKAWA K., MASUDA H., ODANI A., YAMAUCHI O., Inorg. Chem., 32 (1993), 4951; COSTA-FILHO A.J., MUNTE C.E., BARBERATO C., CASTELLANO E.E., MATTIOLI M.P.D., CALVO R., NASCIMENTO O.R., Inorg. Chem., 38 (1999), 4413; JANIAK CH., J. Chem. Soc. Dalton Trans., (2000), 3885.
[26] ZARIĆ S.D., POPOIĆ D.M., KNAPP E-W., Chem. Eur. J., 6 (2000), 3935; ZARIĆ S.D., Chem. Phys. Lett., 77 (1999), 311; PERUTZ M.F., PHILOS M.F.. Trans. R. Soc. A, 105 (1997), 345; MILČIĆ M., ZARIĆ S.D., Eur. J. Inorg. Chem., (2001), 2143.
[27] BRILL A.S., *Transition Metals in Biochemistry*; Springer, Berlin, 1977; LIPPARD S.J., BERG J.M., *Principles of Bioinorganic Chemistry*, University Science Books; Mill Valley, CA, 1994.
[28] ŻUROWSKA B., BRZUSZKIEWICZ A., Polyhedron, 27 (2008), 1623.
[29] KÖNIG E., *Magnetic Properties of Coordination and Organometallic Transition Metal Compounds*, Springer, Berlin, 1966.
[30] CARLIN R.L., *Magnetochemistry*, Springer, Heidelberg, 1986.
[31] CrysAlis 'RED', Oxford Diffraction (Poland), Wroclaw, 2001, 2003.
[32] SHELXTL-NT [version 5.1], Bruker AXS Inc., Madison, WI, 1999.
[33] ŻUROWSKA B., KALINOWSKA-LIS U., BRZUSZKIEWICZ A., OCHOCKI J., Inorg. Chim. Acta, 362 (2008), 1435.
[34] NAKAMOTO K., *Infrared and Raman Spectra of Inorganic and Coordination Compounds*, Wiley, New York, 1978.
[35] HATHAWAY B. J., UNDERHILL A. E., J. Chem. Soc., (1961) 3091.
[36] LEWIS D.L., ESTES E.D., HODGSON D.J., J. Cryst. Mol. Struct., 67 (1975), 5.
[37] LEVER A.B.P., *Inorganic Electronic Spectroscopy*, Elsevier, Amsterdam, 1986.
[38] HATHAWAY B.J., BILLING D.E., Coord. Chem. Rev., 143 (1970), 5.
[39] MABBS F.E., MACHIN D.J., *Magnetism of Transition Metal Complexes*, Chapman and Hall, London, 1973.
[40] FIGGIS B.N., LEWIS J., Prog. Inorg. Chem., 37 (1964), 6.
[41] SMART J.S., *Effective Field Theories of Magnetism*, W.P. Saunders Comp., Philadelphia, 1966, p. 24.
[42] ŻUROWSKA B., KALINOWSKA-LIS U., BIAŁOŃSKA A., OCHOCKI J., J. Mol. Struct., 889 (2008), 98.

Received 20 June 2008
Revised 16 Septemberr 2008

Materials Science-Poland, *Vol. 27*, *No. 4/1*, *2009*

Coordination properties of the diethyl (pyridin-3-ylmethyl)phosphonate ligand (3-pmpe) with nitrate transition metal salts

B. ŻUROWSKA[1*], A. KOTYŃSKI[2], J. OCHOCKI[2]

[1]Faculty of Chemistry, University of Wrocław, Joloit-Curie 14, 50-383 Wrocław, Poland

[2]Department of Bioinorganic Chemistry, Faculty of Pharmacy, Muszyńskiego 1 Medical University, 90-151 Łódź, Poland

A new series of nitrate transition metal complexes containing diethyl(pyridin-3-ylmethyl)phosphonate (3-pmpe) as a ligand, having a general formula $[M(3\text{-pmpe})_2(H_2O)_2](NO_3)_2$ (M = Cu, Co and Ni) and $[Zn(3\text{-pmpe})_2](NO_3)_2$ were prepared. The complexes were identified and characterized by the elemental analysis, spectroscopic and magnetic studies. Ligands containing two donor atoms, heterocyclic nitrogen and phosphoryl oxygen atoms bind in a bidentate bridging manner *via* the pyridine nitrogen and the phosphoryl oxygen atoms. The magnetic behaviour in the temperature range 1.8–300 K) of the Cu(II), Ni(II), Co(II) complexes as well as their spectroscopic properties suggest polymeric structure of all complexes and the existence of a weak antiferromagnetic exchange coupling between paramagnetic centres inside the dibridged linear chains $[M(3\text{-pmpe})_2M]_n$.

Key words: *N,O ligand; transition metal complexes; spectroscopy; magnetism*

1. Introduction

Ligand species, including some organophosphorus compounds containing phosphonic acids and their esters, derivatives of the pyridine or quinoline and their metal complexes exhibit significant biological and pharmacological activity. These compounds might be considered as analogues of naturally occurring phosphates. During recent years, much attention has been focused on the synthesis of N-heterocyclic phosphonates and their platinum(II) and palladium(II) complexes, because of their potential applications [1] and significant antitumor properties [2–13]. The present paper is a continuation of our earlier investigation of the reactivity of these N,O donor

*Corresponding author, e-mail: zurowska@ chem.uni.wroc.pl

ligands with transition metal ions [14–21], i.e. diethyl(pyridin-2-ylmethyl)-, (pyridin-4-ylmethyl)- and (quinolin-2-ylmethyl)phosphonate ligands (2-pmpe, 4-pmpe and 2-qmpe, respectively). The coordination compounds with these ligands were investigated with regard to their spectral and magnetic properties which provide a chemical base for their biological activity. The crystal structure of the representative compounds, i.e. $[Co(2\text{-}pmpe)_2Cl_2]$ [14], $[Co(2\text{-}pmpe)_2(H_2O)_2](ClO_4)_2$ [15], $[Cu(2\text{-}pmpe)_2(ClO_4)_2]$ [16], $[Cd_4(2\text{-}pmpe)_4Cl_8]$ [17] (with N,O-bonded chelate ligand) and $[Co(4\text{-}pmpe)_2(H_2O)_2](ClO_4)_2{\cdot}2H_2O$ (with N,O-bridging ligand) [18] as well as $[M(2\text{-}qmpe)_4(H_2O)_2](ClO_4)_2$ (with O-bonded ligand), where M = Ni, Mn [19] was determined. We found recently that the interaction of 2-pmpe and 2-qmpe with some copper(II) and cobalt(II) salts leads to an unusual oxidative decomposition of the ligands [21, 22]. In this reaction, cleavage of C–P bond occurs and copper–pikolinate, copper– and cobalt–quinaldinate systems are produced.

Recently, we have reported the coordination properties of the 3-pmpe ligand (Fig. 1) with zinc(II) chloride [23]. IR and X-ray analyses show that in the reaction of $ZnCl_2$ with 3-pmpe in methanol, three crystalline polymorphs were found: $[Zn(3\text{-}pmpe)Cl_2]_2$ (**1**) and $[Zn(3\text{-}pmpe)Cl_2]_n$ (**2** and **3**). In **1**, Zn(II) ions are doubly bridged by the 3-pmpe ligand, resulting in the formation of dinuclear species. In polymeric compounds **2** and **3**, Zn(II) ions are singly bridged by the 3-pmpe, resulting in the formation of one-dimensional chains.

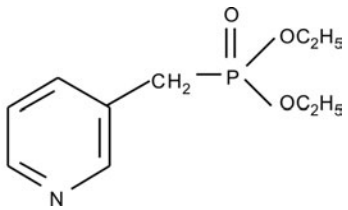

Fig. 1. Schematic drawing of diethyl(pyridin-3-yl)methylphosphonate ligand (3-pmpe)

Here we extend our studies to the synthesis and characterization of nitrate compounds for the purpose of studying the coordination behaviour of the diethyl(pyridin-3-ylmethyl)phosphonate (3-pmpe), stoichiometries and geometrical features of the resulting species. Additionally, our interest is the study of the stability of the metal(II) compounds in solution. Unfortunately, we have not succeeded in preparing the complex crystals suitable for the X-ray studies. The physicochemical properties of the compounds and their possible structures are discussed based on their spectral (infrared, ligand field and EPR spectra) and magnetic features.

2. Experimental

General comments and physical measurements. Starting materials and solvents for the synthesis were obtained commercially and used as-received. Metal content was

determined using a Carl Zeiss Jena atomic absorption spectrophotometer. Elemental analyses were carried out using a Perkin-Elmer elemental analyzer 2400CHN. Infrared spectra (100–4000 cm^{-1}) were recorded on a Bruker IFS 113v spectrophotometer using KBr pellets, and solid state electronic spectra (4000–28 000 cm^{-1}) were performed on a Cary 500 spectrophotometer. ^{1}H and ^{31}P NMR spectra were recorded on a Varian Mercury-300 spectrometer operating at a frequency 300 MHz. Chemical shifts were reported using a standard (δ) notation in ppm with respect to TMS (1%) as an internal standard and H_3PO_4 (85%) as an external standard. The EPR spectra of powder samples were recorded (at 295 and 77 K) on a Bruker ESP 300E spectrometer operating at X-band and equipped with a Bruker NMR. Magnetic measurements of polycrystalline samples were carried out with a Quantum Design SQUID magnetometer (MPMSXL-5 type). The measurements were recorded in a magnetic field of 0.5 T over the temperature range 1.8–300 K. The correction for diamagnetism of the experimental susceptibility was based on subtracting the sample-holder signal and estimating the contribution χ_D from Pascal constants [24]. The effective magnetic moments were calculated from $\mu_{eff} = 2.83(\chi_M T)^{1/2}$, using the temperature-independent paramagnetism of 60×10^{-6} $cm^3\cdot mol^{-1}$ for Cu (**1**), of 220×10^{-6} $cm^3\cdot mol^{-1}$ for Ni (**2**), and of 150×10^{-6} $cm^3\cdot mol^{-1}$ for Co (**3**) [25].

*Synthesis of the ligand***.** Diethyl(pyridin-3-ylmethylphosphonate (3-pmpe) was prepared according to the procedure described in detail elsewhere [23].

^{1}H-NMR (300 MHz, $CDCl_3$): δ = 1.26 (t, 6H, $^{3}J_{HH}$ = 6.9, 2 CH_3), 3.15 (d, 2H, $^{2}J_{HP}$ = 21.6; py-CH_2P), 4.06 (dq, 4H, $^{3}J_{HH}$ = 6.9; 2 $POCH_2$), 7.24-7.29 (m, 1H, (py) H-C5), 7.67-7.72 (m, 1H, (py) H-C4), 8.43-8.51 (m, 2H, (py) H-C2, H-C6); ^{31}P-NMR (300 MHz, $CDCl_3$): δ = 25.16; IR (film) ν_{max} (cm^{-1}): (py-ring) 1570 (m), 1550(w), (P = O) 1265 (vs), (P–O–C) 1050–1025(vs); (vs – very strong, m – medium, w – weak).

Synthesis of the complexes. The nitrate complexes were prepared by dissolving the appropriate quantity of hydrated metal nitrate (1 mmol) in ethanol (10 cm^3) and adding to a solution of the ligand (3 mmol) in ethanol (20 cm^3). The resulting solutions were filtered off, and left to evaporate slowly at room temperature. Blue (**1**) green (**2**), pink (**3**) and white (**4**) the Cu(II), Ni(II) Co(II) and Zn(II) compounds were obtained.

[Zn(3-pmpe)$_2$](NO$_3$)$_2$. ^{1}H-NMR (300 MHz, $CDCl_3$): δ = 1.26 (t, 6H, $^{3}J_{HH}$ = 6.9, 2 CH_3), 3.38 (d, 2H, $^{2}J_{HP}$ = 21.8; py-CH_2P), 3.94 (dq, 4H, $^{3}J_{HH}$ = 6.9; 2 $POCH_2$), 7.27 (m, 1H, (py) H-C5), 7.74 (m, 1H, (py) H-C4), 8.67 (m, 2H, (py) H-C2, H-C6).

Anal. Found (**1**): C, 29.27; H, 5.92; N, 8.22; Cu, 9.32; Calc. for [$C_{20}H_{40}N_4P_2O_{14}Cu$ (**1**): C, 30.36; H, 6.34; N, 8.41; Cu, 9.15 %

Anal. Found (**2**): C, 35.47; H, 5.96; N, 8.27; Ni, 8.67; Calc. for [$C_{20}H_{40}N_4P_2O_{14}Ni$) (**2**): C, 35.67; H, 5.50; N, 8.51; Ni 8.45 %

Anal. Found (**3**): C, 35.46; H, 5.96; N, 8.27; Co, 8.70; Calc. for [$C_{20}H_{40}N_4P_2O_{14}Co$] (**3**); C, 35.75; H, 6.05; N, 8.54; Co 8.23 %

Anal. Found (**4**): C, 37.07; H, 5.61; N, 8.65; Zn, 10.09; Calc. for [$C_{20}H_{36}N_4P_2O_{12}Zn$] (**3**); C, 37.25; H, 5.48; N, 8.50; Zn 10.48 %

3. Results and discussion

The stoichiometry of the investigated complexes was established from the elemental analysis and metal determination. The analytical and spectroscopic results (see below) demonstrated that 3-pmpe is a ligand able to form coordination compounds with M(II) nitrate salts having the M(II) to ligand molar ratio 1:2 of the following stoichiometries: $[M(3\text{-pmpe})_2(H_2O)_2](NO_3)_2$, M = Cu (**1**), Ni (**2**), Co (**3**) and $[Zn(3\text{-pmpe})_2](NO_3)_2$ (**4**)]. The compounds are stable in solution when exposed to air.

3.1. Infrared and ligand field spectra

The selected infrared spectral bands are shown in Table 1.

Table 1. Selected infrared spectroscopic frequencies (cm^{-1}) of the metal complexes with 3-pmpe

Compound	ν(C = C) ν(C = N)	ν(P = O)	δ(PO–C)	ν(P–OC)	δ(C = N)[a]	δ(C = N)[b]	ν(M–N)
3-pmpe	1633w[c] 1592w 1576m	1250vs 1240sh	1163w 1133vw	1054vs 1027vs	600w	400w	
Cu (**1**)	1609s 1584m	1226vs 1197vs	1162m	1050vs 1021vs	613w	417w	278w
Ni (**2**)	1607m 1571m-w	1214vs 1191vs	1167m-w 1142w	1041vs 1024vs	610w	419w	278w
Co (**3**)	1607m 1584w	1228vs 1190vs	1162w 1141w	1048vs 1024vs	611w	413w	278vw
Zn (**4**)	1582m 1609w	1200vs 1215vs	1163w 1140w	1040vs 1025vs	611w	418w	270w

[a]In-plane pyridine ring deformation.
[b]Out-of-plane pyridine ring deformation.
[c]Abbreviations: v = very, s = strong, m = medium, w = weak, sh = shoulder.

The IR spectra of all the complexes are different in their line shapes and relative intensities, indicating that there is no isomorphism within these groups of compounds. In the infrared spectra of the complexes studied, the bands due to the stretching modes of the pyridine ν(C = C) and ν(C = N) observed in the region 1600–1500 cm^{-1} are not shifted appreciably, whereas the characteristic out-of-plane and in-plane deformation bands of the 3-substituted pyridine ring are shifted to higher frequencies, suggesting coordination of the pyridyl nitrogen donor atom (Table 1). The band at 967 cm^{-1} is associated with a pyridine ring breathing mode of vibration, and is characteristically shifted to higher energy on coordination. Thus, the band observed at 976, 975, 974 and 970 cm^{-1} for **1**, **2**, **3** and **4** compounds, respectively, indicates the coordination of pyridine residues. The very strong band at 1250 cm^{-1} which corresponds to the P=O

stretching frequencies of the free ligand in the spectra of the all complexes, is shifted towards lower frequencies, indicating the coordination of the phosphoryl oxygen to the metal ion. Other ligand bands characteristic of the phosphonate moiety, δ(PO-C) at 1130–1170 cm^{-1} and ν(P–OC) at 1030–1050 cm^{-1}, do not show any significant shifts upon the formation of the M(II) complex. The far IR region of all the compounds shows one band attributed to the ν(M–N) stretching vibration.

The infrared spectra of all the studied compounds show a very strong band at 1384 cm^{-1}, characteristic of an ionic nitrate [26, 27]. The presence of water molecules in the compounds is deduced from the elemental analysis and the IR spectrum [27]. The strong band at about 3420–3440 cm^{-1}, corresponding to ν(OH) stretching mode, is observed in the IR spectra of the Cu(II), Ni(II) and Co(II) compounds. These bands indicate the presence of coordinated water molecules in the hydrogen bonds [28]. The IR spectrum of the Zn(II) compound shows the absence of all vibrations which might be attributed to the presence of water molecules.

The ligand field spectrum of the Cu(II) compound shows a broad asymmetric band centred at 15 200 cm^{-1}, associated with the $^2E \rightarrow {}^2T_{1g}$ transition in the O_h symmetry. Ligand field spectra of the Ni(II) and Co(II) compounds have the typical representative features of divalent metal ions having high spin in an octahedral environment [29]. The ligand field spectrum of the Ni(II) complex exhibits three spin-allowed bands in O_h symmetry (25 575, 14 925, 8620 cm^{-1}), which, in order of decreasing energy, are assigned to the, $^3A_{2g} \rightarrow {}^3T_{1g}(F)$ and $^3A_{2g} \rightarrow {}^3T_{2g}$ transition. The spin-forbidden absorption at about 13 590 cm^{-1} is observed as a shoulder. For the Co(II) complex, spin-allowed bands in O_h symmetry at 21 280 (sh), 19 340 and 8330 cm^{-1} are observed, corresponding to the $^4T_{1g}(F) \rightarrow {}^4T_{1g}(P)$, $^4T_{1g}(F) \rightarrow {}^4A_{2g}$ and $^4T_{1g}(F) \rightarrow {}^4T_{2g}$, respectively. Asymmetric band for Cu(II) and in the near IR region for Ni(II) and Co(II) compounds show that the metal ions are in an octahedral, tetragonally distorted environment. The calculated [30, 31] spectrochemical parameters D_q and B for Ni (860, 975 cm^{-1}, respectively) and for Co (910, 830 cm^{-1}, respectively) indicate that the nickel and cobalt compounds according to the literature [30, 31] are not isomorphous. Relative high values of the parameter *B* might reflect the deviation from the octahedral geometry.

3.2. EPR and magnetic properties

The EPR spectrum of the Cu(II) compound is of an axial type, with *g* values at room temperature of $g_{||} = 2.24_7$ and $g_{\perp} = 2.08_5$. The spectrum is independent of temperature. The EPR spectrum of the Co(II) compound shows no lines at room temperature, but does show one broad line at 77 K, with $g \approx 3.90$. The Ni(II) compound does not exhibit an X-band spectrum.

The magnetic behaviour of the **1**–**3** complexes is shown in Fig. 2 in the form of the plot $\chi_M T$ vs. T (χ_M being the magnetic susceptibility per mole of the metal atoms).

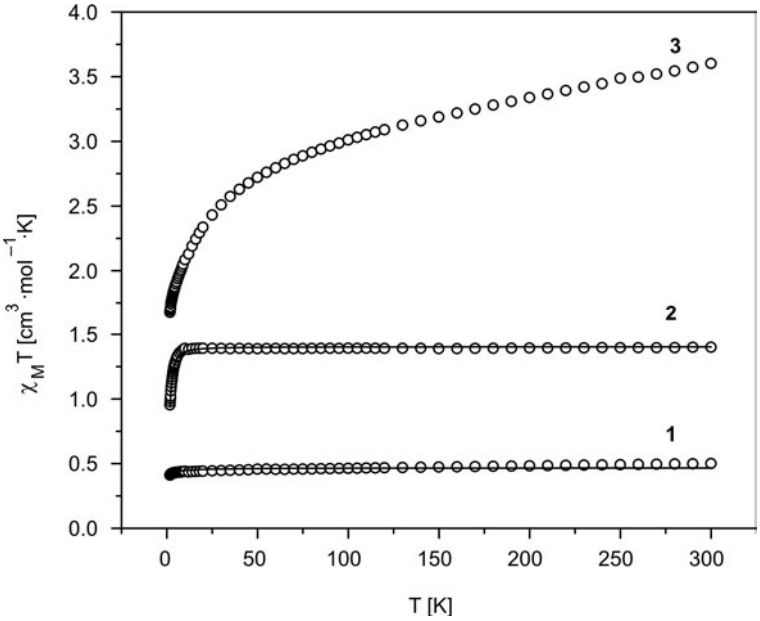

Fig. 2. Plot of $\chi_M T$ versus T for $[Cu(3\text{-pmpe})_2(H_2O)_2](NO_3)_2$ (1), $[Ni(3\text{-pmpe})_2(H_2O)_2](NO_3)_2$ (2) and $[Co(3\text{-pmpe})_2(H_2O)_2](NO_3)_2$ (3). Solid lines correspond to the best theoretical fit (see text)

The effective magnetic moments at room temperature for the Cu(II) ($\mu_{eff} = 2.00\mu_B$), Ni(II) ($\mu_{eff} = 3.35\mu_B$) and the Co(II) ($\mu_{eff} = 5.37\mu_B$) complexes are within the usually observed range of experimental values for the complexes in octahedral configuration [32]. The negative value of the Weiss constant (θ), obtained from the equation $\chi_M = [C/(T - \theta)]$ within the measured temperature region, equal to –0.47 K for the Cu(II) compound, may suggest the possibility of a very weak magnetic interaction between magnetic centres. The value of the Weiss constant (θ) for the Ni(II) compound is –1.40 K. Since the zero-field splitting parameters of isolated Ni(II) ions are usually large and lie in the range 4–8 cm^{-1} [33, 34], the decrease of $\chi_M T$ at lower temperatures observed for the nickel(II) compound (Fig. 2) can be explained by weak antiferromagnetic interactions and/or zero-field splitting effects [34]. The Co(II) compound behaves as a Curie–Weiss paramagnet, at temperatures above 100 K. The negative Weiss constant of –24.8 K obtained in the range 100–300 K is due to the effect of spin coupling, resulting in a gradual transformation of an isotropic $s = 3/2$ at high temperature to an anisotropic $s_{eff} = 1/2$ at low temperature. Because the value of the Weiss constant of –24.8 K differs from that expected for an isolated Co(II) ion with a spin-orbit coupling of –170 cm^{-1}, i.e. –20 K [35], antiferromagnetic exchange interaction between cobalt ions is also expected.

The analytical results and spectroscopic data suggest that two 3-pmpe ligands act as N,O-bridges between metal centres, thus the complexes may be expressed as coordination polymers having the general formula $\{[M(3\text{-pmpe})_2(H_2O)_2](NO_3)_2\}_n$ (M = Cu, Ni, Co) and $\{[Zn(3\text{-pmpe})_2](NO_3)_2\}_n$ (Fig. 3).

The occurrence of intrachain exchange interactions cannot be excluded if the proposed structure is valid. Consequently, we examined the magnetic behaviour of both the Cu(II) and the Ni(II) compounds. Lack of a model for a 3/2 chain system precludes theoretical analysis of the magnetic data of the Co(II) compound.

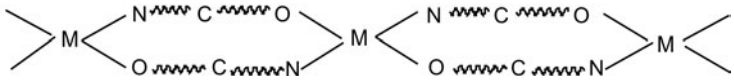

Fig. 3. Scheme of the proposed structure, showing the coordination of 3-pmpe ligand

In order to analyse the magnetic behaviour of the Cu(II) compound, a uniform $S = 1/2$ infinite chain model with Eq. (1) derived by Bonner and Fisher [36, 37] has been used:

$$\chi_{Cu} = \frac{Ng^2\beta^2}{kT} \times \frac{0.25 + 0.14995x + 0.30094x^2}{1 + 1.9862x + 0.68854x^2 + 6.0626x^3} \tag{1}$$

where $x = |J|/kT$ and the other parameters have their usual meanings. Assuming this model, the best-fit parameters obtained for the Cu(II) compound by the least-squares fit are the following: $J = -0.43$ cm^{-1}, $g = 2.13$ with the value of $R = 1.17 \cdot 10^{-4}$, where R is the correlation factor, defined as

$$R = \sqrt{\frac{\sum_i \frac{\left(\chi_i^{\text{exp}} - \chi_i^{\text{calc}}\right)^2}{\left(\chi_i^{\text{exp}}\right)^2}}{\sum_i \frac{1}{\left(\chi_i^{\text{exp}}\right)^2}}}$$

Experimental magnetic data for the Ni(II) compound were fitted to the Ising chain model [38]. The best fit parameters obtained by the least squares fit are as follows: $J = -0.23$ cm^{-1}, $D = 2.46$ cm^{-1}, $R = 8.85 \times 10^{-5}$. The satisfactory results for the Cu(II) and Ni(II) compounds shown in Fig. 3 confirm their polymeric chain structure and indicate very weak antiferromagnetic exchange interaction between magnetic centres inside the dibridged linear chain. Lack of a single crystal study precludes interpretation of the obtained values of exchange parameters J but suggests that metal–metal distance must be large, leading to observed only very weak antiferromagnetic coupling.

4. Summary

The results described in the present paper have shown that nitrate complexes of Cu(II), Ni(II), Co(II) with 3-pmpe ligand are six-coordinate, formed by two N,O-

bridging 3-pmpe ligand and two water molecules (MN_2O_4 chromophore). The Zn(II) compound is four coordinated (ZnN_2O_2 chromophore). The nitrate ions in the all compounds are ionic. In light of the analytical, spectroscopic and magnetic data (for paramagnetic centres), the investigated compounds may be represented as polymeric chains having the general formula $\{[M(3\text{-pmpe})_2(H_2O)_2](NO_3)_2\}_n$ (M = Cu, Ni, Co) and $\{[Zn(3\text{-pmpe})_2](NO_3)_2\}_n$. The magnetic behaviour of the complexes is explained by very weak magnetic exchange between paramagnetic centres (Cu, Ni and Co) inside the chains.

In summary, in the 3-pmpe ligand, a sterically unfavourable position of the pyridine nitrogen and phosphonate oxygen atoms leads to dimeric [23] and polymeric compounds as presented in Ref. [23], and in this paper, in which ligand acts as an N,O bridge to the metal ions. It is worth mentioning that 3-pmpe ligand reacts with chloride metal(II) ions and $ZnCl_2$ in molar ratios of 1:1 and 1:2 [23], but with metal(II) nitrate it reacts in a 1:2 molar ratio.

Acknowledgements

This work was supported by the Polish Ministry of Science and Higher Education (Grant No. N N405 303236) (J.O), and by Grant No. 502-13-700 (A.K.) and 502-13-777 (J.O.) of the Medical University of Łódź (Statute fund No. 503-3016-2).

References

[1] KALINOWSKA U., CHĘCIŃSKA L., MAŁECKA M., ERXLEBEN A., LIPPERT B., OCHOCKI J., Inorg. Chim. Acta, 358 (2005), 2464.
[2] ARANOWSKA K., GRACZYK J., CHĘCIŃSKA L., PAKULSKA W., OCHOCKI J., Pharmazie, 61 (2006), 5.
[3] ZIĘBA R., MALINOWSKA K., WIEWIÓROWSKI M., GRACZYK J., Acta Pol. Pharm., 57 (2000), 136.
[4] CHĘCIŃSKA L., MAŁECKA M., OCHOCKI J., ARANOWSKA K.,. Acta Cryst., E59 (2003), m350.
[5] BRZEZIŃSKA-BŁASZCZYK E., MIŃCIKIEWICZ M., OCHOCKI J., Eur. J. Pharmacol., 298 (1996), 155.
[6] KOSTKA B., OCHOCKI J., Pharmazie, 51 (1996), 990.
[7] KAJMAN-BRONŻEWSKA L., OCHOCKI J., Pharmazie, 52 (1997), 198.
[8] ZHAO G., LIN H., YU P., SU H., ZHU S., SU X., CHEN Y., J. Inorg. Biochem., 73 (1999), 145.
[9] IAKOVIDOU Z., PAPAGEORGIOU A., DEMERTZIS M.A., MIOGLOU E., MOURELATOS D., KOTSLS A., NATH YADAV P., KOVALA-DEMERTZI D., Anti-Cancer Drugs, 12 (2001), 65.
[10] ĆURIĆ M., TUŠEK-BOŽIC L., VIKIĆ-TOPIĆ D., STARCIA V., FURTANI A., BALZARINI J., DE CLERCQ E., J. Inorg. Biochem., 63 (1996), 125.
[11] TUŠEK-BOŽIĆ L., ĆURIĆ M., BALZARINI J., DE CLERCQ E., Nucleos, Nucleot. 14 (1995), 777.
[12] TUŠEK-BOŽIĆ L., MATIJAŠIĆ J., BOCELLI G., SGARBOTTO P., FURLANI A., SCARIA V., PAPAIOANNOU A., Inorg. Chim. Acta, 185 (1991), 229.
[13] TUŠEK-BOŽIĆ L., MATIJAŠIĆ J., BOCELLI G., CALESTANI G., FURLANI A., STARCIA V., PAPAIOANNOU A., J. Chem. Soc., Dalton Trans., (1991), 195.
[14] OCHOCKI J., ŻUROWSKA B., MROZIŃSKI J., REEDIJK J., Proc. III Symp. on Inorganic Biochemistry and Molecular Biophysics, VI Int. Scientific School on Biological Macromolecules, Wrocław–Karpacz, 1991, 212.
[15] ŻUROWSKA B., MROZIŃSKI J., CIUNIK Z., OCHOCKI J., J. Mol. Struct., 791 (2006), 98.
[16] ŻUROWSKA B., BIAŁOŃSKA A., OCHOCKI J., Mater. Sci.-Poland, 27 (2009), 987.
[17] ŻUROWSKA B., MROZIŃSKI J., CIUNIK Z., OCHOCKI J., J. Mol. Struct., 834 (2007), 26.

[18] OCHOCKI J., KOSTKA K., ŻUROWSKA B., MROZIŃSKI J., GAŁDECKA E., GAŁDECKI Z., REEDIJK J., J. Chem. Soc. Dalton Trans., (1992), 2955.
[19] OCHOCKI J., ŻUROWSKA B., MROZIŃSKI J., KOOIJMAN H., SPEK A.L., REEDIJK J., Eur. J. Inorg. Chem., (1998), 169.
[20] ŻUROWSKA B., MROZIŃSKI J., OCHOCKI J., Mater. Sci.-Poland, 25 (2007), 1063.
[21] ŻUROWSKA B., OCHOCKI J., MROZIŃSKI J., CIUNIK Z., REEDIJK J., Inorg. Chim. Acta, 357 (2004), 755.
[22] ŻUROWSKA B., BRZUSZKIEWICZ A., POLYHEDRON, 27 (2008), 1623.
[23] ŻUROWSKA B., ŚLEPOKURA K., LIS T., OCHOCKI J., Inorg. Chim. Acta, 362 (2008), 733
[24] KÖNIG E., *Magnetic Properties of Coordination and Organometallic Transition Metal Compounds*, Springer, Berlin, 1966.
[25] CARLIN R.L., *Magnetochemistry*, Springer, Berlin, 1986.
[26] CURTIS N.F., CURTIS N.F., Inorg. Chem. 4 (1965), 804.
[27] NAKAMOTO K., *Infrared and Raman Spectra of Inorganic and Coordination Compounds*, Wiley, New York, 1986.
[28] YOUNGAME S. CHAICHIT N., KONGSAEREE P., VAN ALBADA G.A., REEDIJK J., Inorg. Chim. Acta, 324 (2001), 232.
[29] LEVER A.B.P., *Inorganic Electronic Spectroscopy*, Elsevier, Amsterdam, 1986.
[30] REEDIJK J, VAN LEEUWEN P.W.N.M, GROENEVELD W.L., Recl. Trav. Chim. Pays Bas, 87 (1968), 129.
[31] REEDIJK J., DRIESSEN W.L., GROENEVELD W.L., Recl. Trav. Chim. Pays Bas, 88 (1969), 1095.
[32] FIGGIS F.N., LEVIS J., Progress Inorg. Chem., 6 (1964), 37.
[33] GINSBERG A.P., MARTIN R.L., BROOKES R.W., SHERWOOD R.C., Inorg. Chem. 11 (1972), 2884.
[34] BOCA R., Coord. Chem. Rev., 248 (2004), 757.
[35] MABBS F.E., MACHIN D.J., *Magnetism and Transition Metal Complexes*, Chapman and Hall, London, 1973.
[36] HALL J.W.A., Ph.D. Dissertation, University of North Carolina, 1977.
[37] BONNER J.C., FISHER M.E., Phys. Rev., A 135, (1964), 640.
[38] O'BRIEN S., GAURA R.M., LANDEE C.P., WILLETT R.D., Solid State Commun., 39 (1981), 1333.

Received 30 June 2008
Revised 28 August 2008

Materials Science-Poland, *Vol. 27*, *No. 4/1*, *2009*

Blue shift of photoluminescence of Al_2O_3–morin nanocomposites

X. LIU[1*], Q. WANG[2], Y. LI[1], Y. GUO[1]

[1]College of Science, Civil Aviation University of China, Tianjin 300300, China

[2]Department of Student Affairs, Civil Aviation University of China, Tianjin 300300, China

Using $AlCl_3$ and ammonia as starting materials, Al_2O_3 nanoparticles were fabricated by the chemical precipitation method. Morin was chemically bound on the surface of Al_2O_3 nanoparticles by the ultrasonic method, and the Al_2O_3–morin fluorescent nanocomposite was obtained. Because of interaction between the morin molecules and the surface atoms of Al_2O_3 nanoparticles, a blue-shift of the photoluminescence was observed for the nanocomposites compared with that of morin.

Key words: *nanocomposite; ultrasonic method; morin; photoluminescence blue shift*

1. Introduction

Aluminum oxides are most commonly used as adsorbents, catalysts and catalyst supports [1]. At the same time, the preparation and properties of Al_2O_3 nanomaterials have been extensively investigated [2–5]. Nanocomposite materials have also been very thoroughly investigated, as they can be widely used in the field of luminescence [6, 7], sensors [8] and catalysts [9], etc. A large amount of dangling bonds and vacancies on the surface of nanoparticles makes it possible to prepare, by surface reaction, nanocomposite materials with excellent properties. For example, ZrO_2–morin nanocomposites were successfully fabricated by a simple heat refluxing method and a photoluminescence enhancement phenomenon was observed [10].

At the same time, morin, as a kind of O,O-donating chelating regent, is most frequently used as an analytical reagent, especially as a fluorescent reagent [11]. It is only weakly fluorescent by itself but forms highly fluorescent complexes with Al^{3+}, thus it is a very sensitive reagent for the fluorometric determination of aluminum: its sensitivity limit is of the order of several parts per billion [12, 13]. In addition, the Al_2O_3 composites [14–16] have also been widely investigated. To our best knowledge, there have been no reports on Al_2O_3 / morin nanocomposites till now.

*Corresponding author, e-mail: xl_liu@cauc.edu.cn

In this paper, Al_2O_3 nanoparticles were synthesized by the chemical precipitation method, using $AlCl_3$ and ammonia as starting materials. Furthermore, the nanoparticles were used as the precursors for synthesizing Al_2O_3–morin nanocomposite fluorescent materials by the ultrasonic irradiation method.

2. Experimental

Materials. The starting materials are $AlCl_3$ (A.R.), ammonia (25–28%, A.R.), deionized water, anhydrous ethanol and morin (Scheme 1). The material was purchased from E. Merck, Darmstadt.

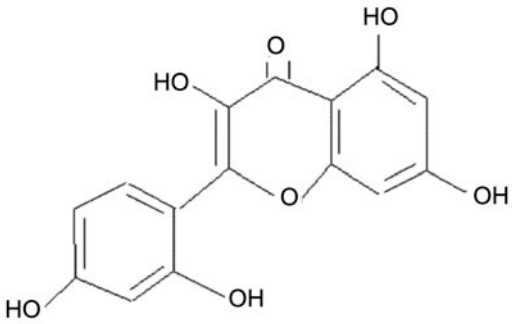

Scheme 1. The structure of the morin molecule

Synthesis of Al_2O_3 nanoparticles. Under vigorous stirring, $AlCl_3$ solution (0.5 mol/dm^3) and ammonia were added slowly to a 500 cm^3 beaker with 100 cm^3 deionized water, and pH was fixed at 8. After continuous stirring for 1 h, a precipitate was obtained which was then filtered and washed with deionized water and five times with alcohol. The obtained powder was dried in an oven at 120 °C for 3 h. Finally, the product was heated at 1100 °C for 3 h, and white nanoparticle Al_2O_3 was obtained.

Synthesis of Al_2O_3–morin nanocomposites. Four aliquots of 2.0 g Al_2O_3 nanoparticles were firstly added to four beakers, and then mixed with 50 cm^3 morin alcohol solutions of various concentrations: 1×10^{-5}, 1×10^{-4}, 5×10^{-4} and 1×10^{-3} mol/dm^3. All samples were ultrasonically treated at 50 °C for 8 h. Thus obtained aqueous Al_2O_3 –morin nanocomposites were filtered for several times with alcohol to remove the excessive morin molecules. Finally, the nanocomposites were dried in an oven for 6 h at 50 °C

Characterization. The photoluminescence spectra of the samples were obtained with a WGY-10 fluorescent spectrometer. The morphology of the samples was tested using a JEM-100CX II transmission electron microscope (TEM) with an accelerating voltage of 150 kV. Fourier transform infrared spectroscopy (FTIR) measurements of the samples were collected on an Avata330 spectrometer with a spectral resolution of 4 cm^{-1}. The samples were mixed with KBr, for which the weight ratio of sample to

KBr was 1:100, and pressed into pellets for characterization. All measurements were carried out at room temperature.

3. Results and discussion

The TEM photograph of the synthesized Al_2O_3 nanoparticles is shown in Fig. 1. It was found that the size of the Al_2O_3 nanoparticles was distributed uniformly the average particle size being ca. 20 nm. The XRD pattern of the Al_2O_3 nanoparticles is shown in Fig. 2. All the sharp peaks in the figure can be assigned to Al_2O_3.

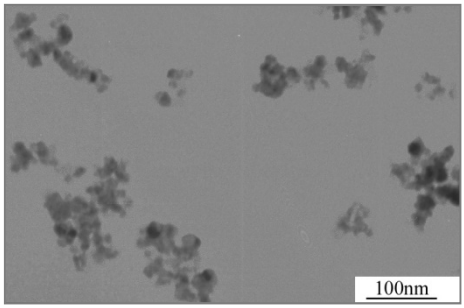

Fig. 1. TEM photograph of Al_2O_3 nanoparticles

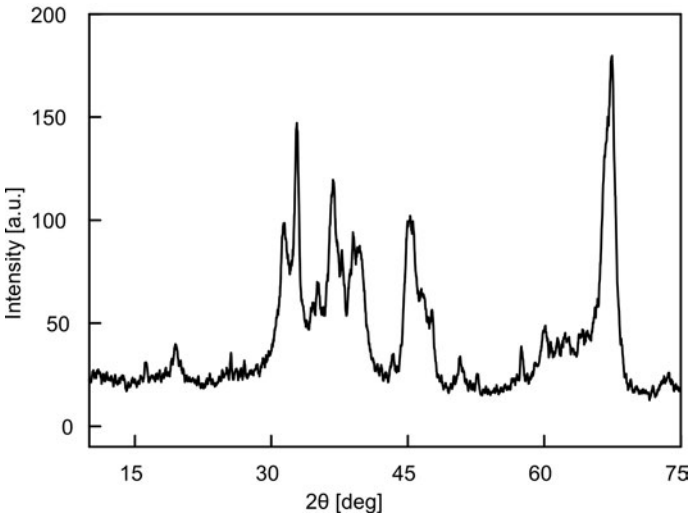

Fig. 2. XRD pattern of Al_2O_3 nanoparticles

Figure 3 shows the FTIR spectra of the nanocomposite, morin and Al_2O_3 nanoparticles in the range of 1680 cm^{-1} to 1160 cm^{-1}. In this figure, the major absorption peaks of Al_2O_3 nanoparticles are located at 1627 and 1398 cm^{-1} (curve a), while the peaks at 1652, 1509 and 1247 cm^{-1} in curve c can be attributed to the stretch vibration mode of C=O in the =C=O group, the vibration of C=C in benzene rings, and the

asymmetric stretching vibration of C–O–C, respectively. The peaks at 1204 and 1174 cm^{-1} have been assigned to the stretching vibration of C–O in 1, 2, 3, 4, 5 ≡C–OH group. The other peaks at 1607, 1573, 1469, 1450 cm^{-1} originate from the vibration of the C=C bond in benzene rings, and those at 1353, 1328 and 1309 cm^{-1} are attributed to the vibration of OH groups [17]. It can seen that the peaks at 1353 cm^{-1} (O–H), 1247 cm^{-1} (C–O–C) and 1174 cm^{-1} (C–O in 1, 2, 3, 4, 5 ≡C–OH group), which originate from the absorption of morin, shift to 1367, 1238 and 1183 cm^{-1}, respectively, in the nanocomposites. This result indicates that complex bonds may form between Al atom of Al_2O_3 nanoparticles and the O atom of ≡C–OH and –C–O–C– groups [18, 19], thus the corresponding FTIR absorption peaks change.

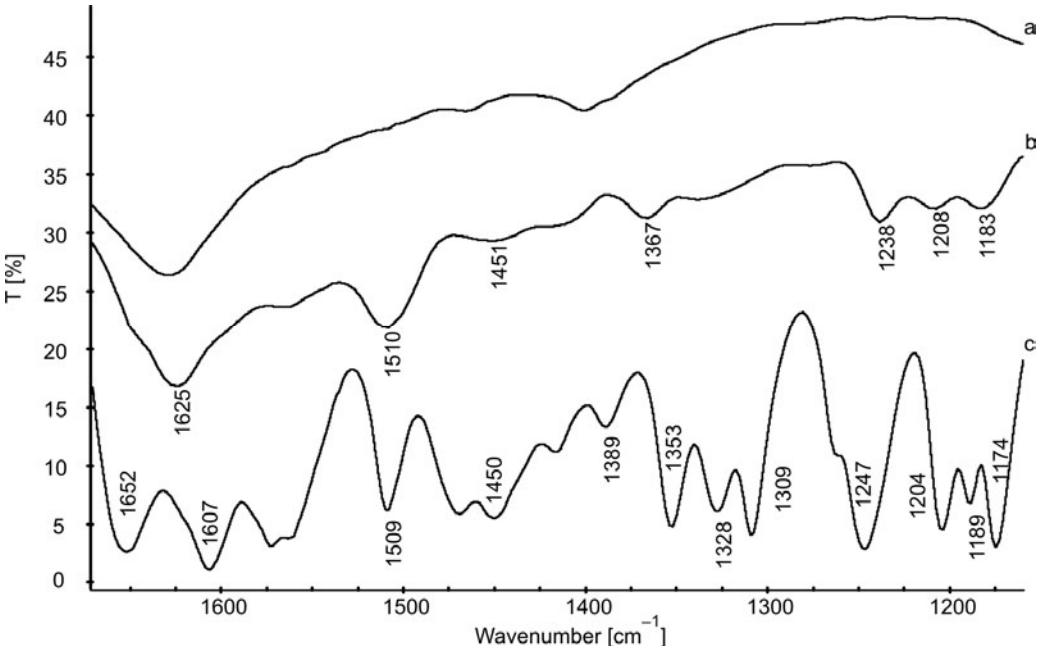

Fig. 3. FTIR spectra of samples: a) Al_2O_3 nanoparticle, b) the nanocomposite and c) morin

Figures 4 and 5 show the photoluminescence (PL) spectra of morin solution and the nanocomposites under the excitation of 430 nm. From Figure 5, it is clear that as the morin concentration increases, the PL intensity increases at first and subsequently decreases. At the same time, the peak positions show a red shift from 516 to 524 nm. At low concentrations, morin molecules can be sufficiently dispersed on the surface of Al_2O_3 nanoparticles. With the increase in the morin concentration, more and more morin molecules contribute to the PL intensity. On the other hand, if too many morin molecules are adsorbed on the surface of Al_2O_3 nanoparticles, they will combine with each other, and dimers or aggregates will be formed. As a result, the energy band gap of the molecules decreases and the interaction between electrons and phonons in-

creases [20], and this phenomenon directly causes a red shift of the peak wavelength and the decrease in the PL intensity.

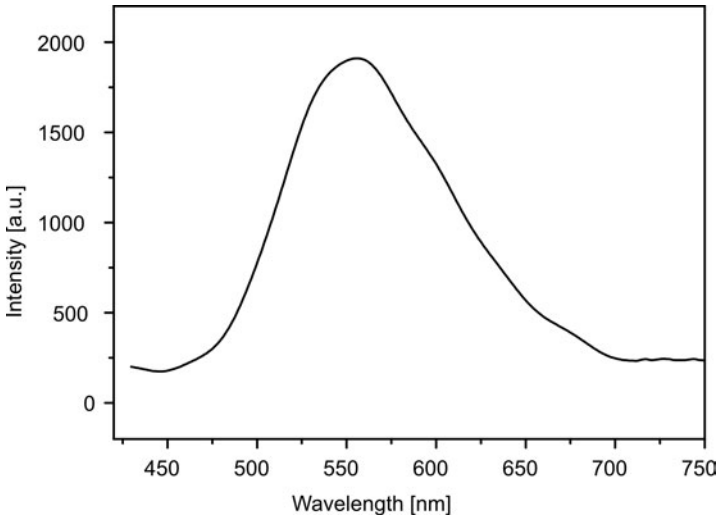

Fig. 4. Photoluminescence spectrum of morin solution (1.0×10^{-3} mol/dm^3)

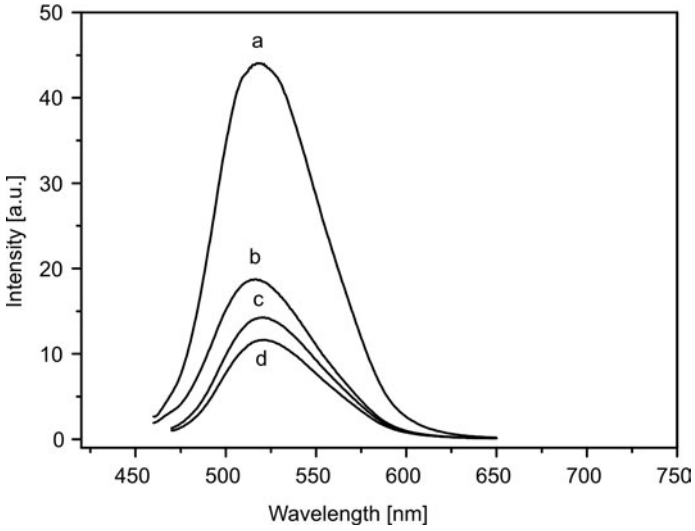

Fig. 5. Photoluminescence spectra of Al_2O_3–morin nanocomposites:
a)1.0×10^{-4} mol/dm^3, b) 1.0×10^{-5} mol/dm^3, c) 5.0×10^{-4} mol/dm^3 and d) 1.0×10^{-3} mol/dm^3

In addition, by comparing Figs. 4 and 5 it is visible that the peak of the naocomposite at 516 nm shows a blue shift of 40 nm with respect to that (556 nm) of morin particles. It is well known that the luminescence of a dye depends strongly on its concentration in solution. The PL intensity becomes weaker when the molecules become too concentrated. In other words, the more the dye molecules are dispersed, the more effi-

cient the luminescence. From the above results, it is known that the morin molecules are adsorbed on the surface of Al_2O_3 nanoparticles, thus the interaction between the morin molecules decreases and a good dispersion of dye molecules is obtained. As a result, a blue shift of the peak wavelength of the nanocomposites is observed [20].

4. Conclusions

Al_2O_3 nanoparticles were synthesized by a chemical precipitation method, using $AlCl_3$ and ammonia as starting materials. Using the synthesized Al_2O_3 nanoparticles as the precursor, Al_2O_3–morin nanocomposite fluorescent materials were synthesized by the ultrasonic method. A blue shift of 40 nm of the PL peak was observed in the nanocomposites with respect to that of morin.

Acknowledgement

This project is jointly supported by the Natural Science Foundation of Tianjin (Contract No. 09JCYBJC04200) and the Science Foundation of CAUC (05qd06q).

References

[1] LEE H.C., KIM H.J., CHUNG S.H., LEE K.H., LEE H.C., LEE J.S., J. Am. Chem. Soc., 125 (2003), 2882.
[2] PATHAL L.C., SINGH T.B., DAS S., VERMA A.K., RAMACHANDRARAO P., Mater. Lett., 57 (2002), 3063.
[3] ZHOU J., DENG S.Z., CHEN J., SHE J.C., XU N.S., Chem. Phys. Lett., 365 (2002), 505.
[4] HUANG C., WANG J., HUANG C., Mater. Lett., 59 (2005), 3746.
[5] ZHANG Y., LIU J., HE R, ZHANG Q., ZHANG X., Chem. Phys. Lett., 360 (2002), 579.
[6] YI T., TANCREZ N., CLÉMENT R., LEDOUX-RAK I., ZYSS J., J. Lumin., 110 (2004), 389.
[7] LIU X., CUI D., WANG Q., XU H., LI M., J. Mater. Sci., 40 (2005), 1111.
[8] LU Z., TANG Y., Mater. Chem. Phys., 92 (2005), 5.
[9] YANG H., SHI R., ZHANG K., HU Y., TANG A., LI X., J. Alloys Comp., 398 (2005) , 200.
[10] LIU X., LI Y., WANG X., Mater. Lett., 60 (2006), 1943.
[11] SHEN Y., JIA R., LUO H., CHEN X., XUE D., HU Z., Spectrochim. Acta Part A, 60 (2004), 1007.
[12] FRITZ III W., Anal. Chem., 33 (1961), 1360.
[13] SAARL L.A., SELTZ W.R., Anal. Chem., 55 (1983), 667.
[14] KERKWIJK B., MULDER E., VERWEIJ H., Adv. Eng. Mater., 1 (1999), 69.
[15] GONG H., YIN Y., WANG X., LIU Y., Mater. Res. Bull., 39 (2004), 513.
[16] YKONG.-M., BAE C.-J., LEE S.-H., KIM H.-W., KIM H.-E., Biomaterials, 26 (2005), 605.
[17] XIE X., Applications of infrared spectroscopy in organic chemistry and drug chemistry, Beijing, Science Press, 1987, P41-330 (in Chinese).
[18] SONG Z., WANG S., LI L., Spectrosc. Spect. Anal., 15 (1995), 75.
[19] ZHANG Q., WANG L.F., LI.Q.K., Chin. J. Inorg. Chem., 18 (2002), 107.
[20] HASHIMATO K., HIRAMOTO M., SAKATA T., Chem. Phys. Lett., 148 (1988), 215.

Received 4 July 2008
Revised 18 April 2009

Materials Science-Poland, *Vol. 27*, *No. 4/1*, *2009*

The effect of hydrothermal temperature on the synthesis of monoclinic bismuth vanadate powders

A. ZHANG*, J. ZHANG

College of Sciences, North China University of Technology, Beijing 100144, P.R. China

Pure phase monoclinic bismuth vanadate powders of a nanosized diameter were synthesized by the hydrothermal method and characterized using XRD, TEM, DRS, Raman and FTIR techniques. The results revealed that the hydrothermal conditions (16 h at 140–240 °C) are favourable for the formation of monoclinic bismuth vanadate powders. They also indicated that if samples are prepared by the route described in this paper, an increase in the grain size and a gradual decrease of the band gap occur as the hydrothermal temperature increases.

Key words: *bismuth vanadate; hydrothermal method; hydrothermal temperature*

1. Introduction

The photocatalytic degradation of organic and inorganic pollutants involves reactions that offer much promise for the solution of urgent environmental issues that confront mankind today. Great progress has been made in the research and application of these reactions, mostly with semiconductors under UV light irradiation [1, 2]. Presently, developing visible light responsive photocatalysts is the most important research direction in this field, because the utilization of visible light, which accounts for more than half of the solar spectrum, is significant. However, most of the photocatalysts developed thus far have wide band gaps, and can therefore utilize only a very small portion of sunlight. Only a limited number of photocatalysts absorbing visible light have been discovered so far [3, 4].

Bismuth vanadate ($BiVO_4$) has recently attracted considerable attention for its strong photocatalytic effect on water splitting and pollutant degradation under visible light irradiation [5–7]. There are three crystalline phases reported for synthetic $BiVO_4$, namely the monoclinic scheelite type, the tetragonal sheelite-type and the tetragonal zircon type and the photocatalytic properties are strongly influenced by its crystal

*Corresponding author, e-mail: a.p.zhangg@gmail.com)

phase. The phase transition between monoclinic scheelite structure and tetragonal scheelite structure of $BiVO_4$ reversibly occurs at about 255 °C, whereas the irreversible transition from tetragonal zircon structure to monoclinic $BiVO_4$ occurs after heat treatment at 400–500 °C and cooling to room temperature [8].

Since the first fabrication of crystalline $BiVO_4$, several methods have been reported for the preparation of $BiVO_4$ such as solid state reaction, the sol–gel method, the hydrothermal method, coprecipitation, metalorganic decomposition, etc. Hydrothermal synthesis, a soft chemical process depending upon many factors such as the hydrothermal treatment, pH, temperature and duration of synthesis, etc., can be used to fabricate materials with various morphologies and photocatalytic properties [9–12]. This study reports on a hydrothermal route for the synthesis of pure phase monoclinic $BiVO_4$ powders. For comparison, various temperatures were used, and all samples were characterized by X-ray diffraction (XRD), transmission electron microscopy (TEM), diffuse reflectance spectra (DRS), Raman and FTIR techniques.

2. Experimental

Materials and process. Bismuth nitrate pentahydrate ($Bi(NO_3)_3 \cdot 5H_2O$, analytical grade) and ammonium metavanadate (NH_4VO_3, analytical grade) from Beijing Chemical Company were used as received without further purification. All other chemicals used in the experiments were also analytical grade reagents, and deionized water was used for preparation of solutions.

In a typical preparation process, 0.02 mol $Bi(NO_3)_3 \cdot 5H_2O$ and 0.02 mol NH_4VO_3 were dissolved in 20 cm^3 of 65% (w/w) HNO_3 and 20 cm^3 6 M NaOH solutions separately, and each stirred for 2 h at room temperature. After that, these two mixtures were mixed together and stirred for about 1 h to get a stable, salmon-pink, homogeneous mixture. Then, the mixture was sealed in a 50 cm^3 Teflon-lined stainless autoclave, and allowed to heat for 16 h at hydrothermal temperatures ranging from 140 to 240 °C under autogenous pressure in an oven. Finally, the precipitate was filtered, washed three times with distilled water, and dried in vacuum at 80 °C for 12 h.

Characterization. X-ray powder diffraction (XRD, Beijing Purkinjl General Instrument Co. LTD, model XD-3; accelerating voltage 36 kV, applied current 30 mA) patterns were recorded in the region of 2θ from 17° to 55° using $CuKi_\alpha$ radiation (λ = 0.15418 nm) with a step scan of 4.0 deg/min at room temperature using a counter diffractometer (graphite monochromator, proportional counter). The morphologies and particle sizes of samples were examined by transmission electron microscopy (TEM, Hitachi Model H-7500; accelerating voltage 80 kV). Before placement onto Cu netting for TEM preparation, the samples were all dispersed in anhydrous ethanol: water 1: 1 solution (V/V) and treated in ultrasonic cleaner for each about 2 min. The Raman spectra were recorded by a microprobe Raman system (Renishaw H13325 spectrophotometer) with a holographic notch filter and a CCD detector, and the excitation at 514.5 nm (12 MW at the head) from an Ar ion laser. All the samples were oriented on

the stageof an Olympus BHSM microscope, equipped with 15× and 50× objectives, and recorded at the resolution of 2 cm^{-1} in the range from 150 to 1000 cm^{-1}. The FTIR spectra were recorded at RT using a Perkin-Elmer spectrometer (model Gx) with Spectrum Gx software Kit (Issue B). All the FTIR transmittance spectra of samples that had been pressed into KBr pellets were collected in the wave number range from 400 to 1800 cm^{-1} using the KBr beam splitter. Optical absorption spectra of the samples were obtained on a doubled-beam UV-visible spectrophotometer (model YU-1901, Beijing Purkinjl General Instrument Co. LTD) equipped with an integrating sphere. UV-vis diffuse reflectance spectra (DRS) of $BiVO_4$ were recorded by using $BaSO_4$ as a reference, and were converted from reflection to absorbance by the Kubelka–Munk method [13].

3. Results and discussion

3.1. XRD results of $BiVO_4$ powders

Figure 1 shows the XRD patterns of samples prepared for 16 h at various hydrothermal temperatures. It is clear that these diffraction peaks are all in good agreement with the standard Joint Committee on Powder Diffraction Standards (JCPDS) card No. 14-0688, which is assigned to monoclinic $BiVO_4$. No impurity peaks were observed in any of these XRD patterns.

The results indicate that the hydrothermal conditions imposed (hydrothermal synthesis for 16 h over a wide range of temperatures) are favourable for the formation of monoclinic scheelite $BiVO_4$.

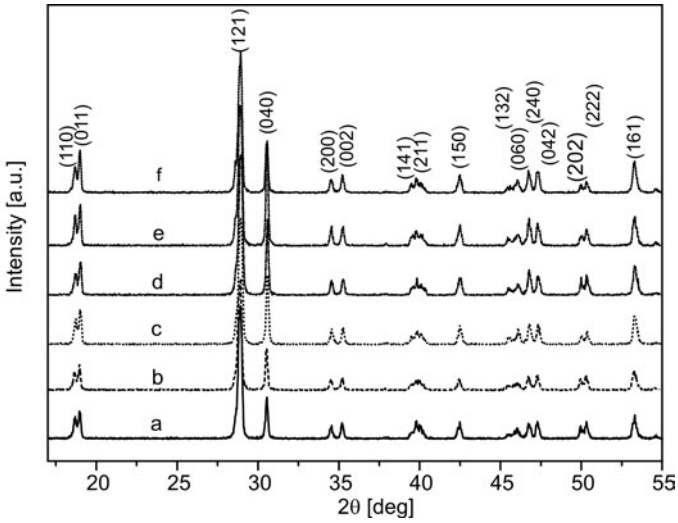

Fig. 1. XRD patterns of $BiVO_4$ prepared at various hydrothermal temperatures T [°C]: a) 140, b) 160, c) 180, d) 200, e) 220, f) 240

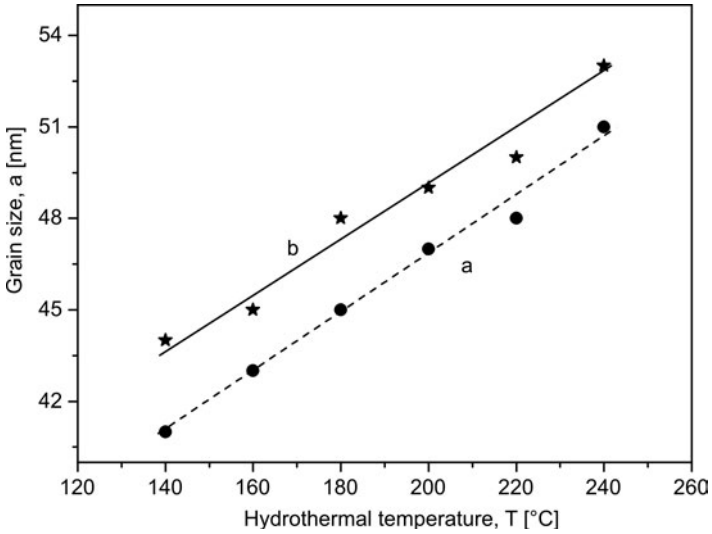

Fig. 2. The dependence of the grain size on the hydrothermal temperature:
a) calculated from the Scherrer formula with XRD results,
b) calculated according to the statistical analysis of large number (100–150)
of particles from TEM pictures

The crystalline size of these powders was estimated from the Scherrer formula [14]

$$D = \frac{K\lambda}{\sqrt{\beta_s^2 - \beta_e^2}\cos\theta} \tag{1}$$

where D is the crystal size, K is usually taken as 0.89 [5, 12, 14]; λ is the wavelength of the X-ray radiation (0.15418 nm); β_s and β_e are the peak widths at half-maximum height of the sample and the equipment broadening, respectively; $2\theta = 30.55°$ as for monoclinic $BiVO_4$ [5, 12]. As a result, the crystal sizes of samples were evaluated as 41, 43, 45, 47, 48, 51 nm for samples (a) to (f) respectively, showing a clear growth trend, as can be seen from line *a* in Fig. 2.

3.2. TEM results for $BiVO_4$ powders

Figure 3 shows TEM images of $BiVO_4$ powders and their relative abundance of particles prepared at various temperatures. It shows that all primary particles with nanosized diameters were relatively similar in size and were almost spherical. Particle sizes and their relative abundance were estimated according to the statistical tests for a large number (100–150) of particles, and the average diameters of particles were measured as 44, 45, 48, 49, 50, 53 nm in Fig. 3af, respectively. It revealed that phase-pure monoclinic $BiVO_4$ with nanosized diameter can be synthesized effectively by the hydrothermal method.

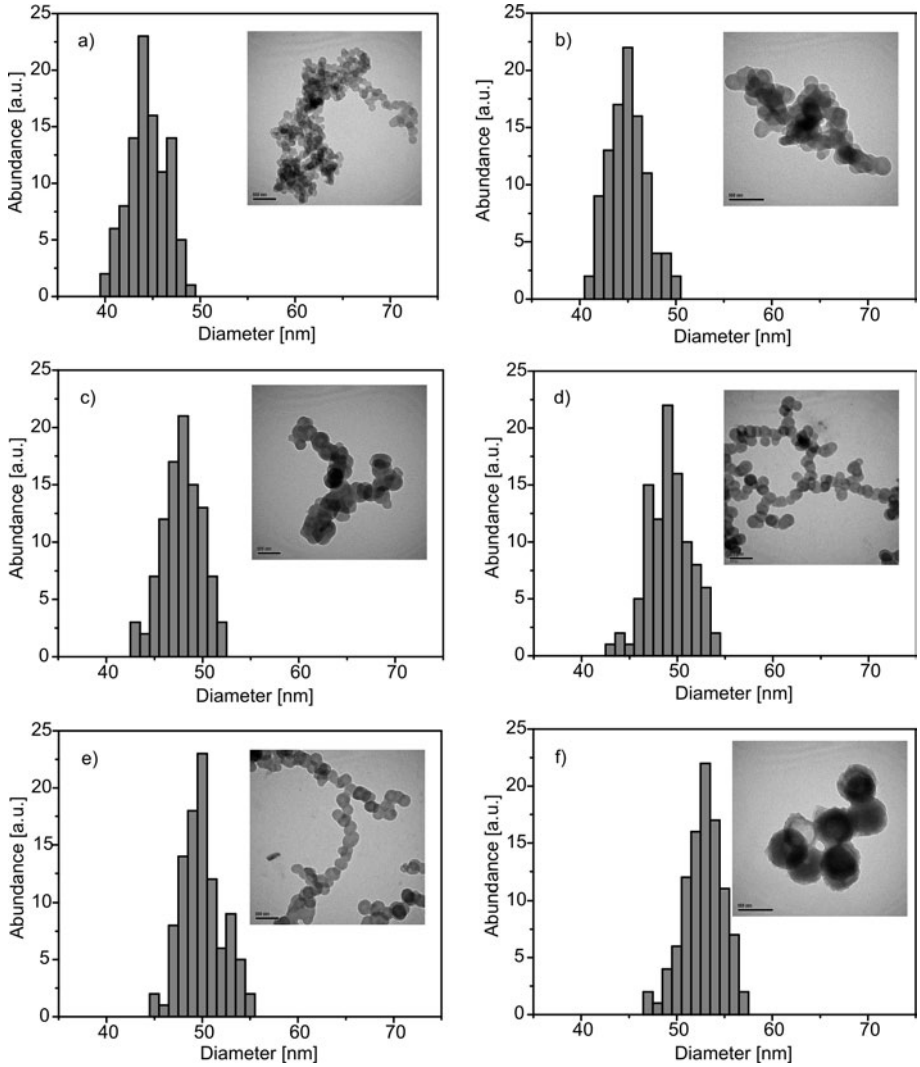

Fig. 3. TEM images of $BiVO_4$ and their relative abundance of grain size fabricated at various hydrothermal temperatures, T [°C]: a) 140, b) 160, c) 180, d) 200, e) 220, f) 240

It is clearly seen from TEM data that linear-chain aggregations of particles occur. These aggregations might be formed by the sintering of nanosized particles in the long duration process of synthesis, because many single nanoparticles were also observed. Furthermore, the $BiVO_4$ sample prepared at low temperature has even more particle aggregation (Fig. 3a), and each aggregation looks agglomeration-like, with an asymmetrical shape measuring about ten times the particle size. When prepared at high temperature, samples with a nearly spherical form are obtained (Fig. 3f) and the average particle size is greater than that obtained at low temperature, showing a growth trend as a function of increasing temperature, as seen in Fig. 2, line b. It is

interesting that the average particle size and the associated, temperature-dependent growth trend are in good agreement with their expected values according to the Scherrer equation based on XRD patterns; furthermore, some of the larger particle sizes observed in TEM pictures may be attributed to minor anomalies in the implementation of experiments

3.3. Raman and FTIR results for $BiVO_4$ powders

The Raman spectra of the 150–1000 cm^{-1} region of samples are shown in Fig. 4a. The results of the band component analysis [15, 16] of Raman and IR spectra of sam

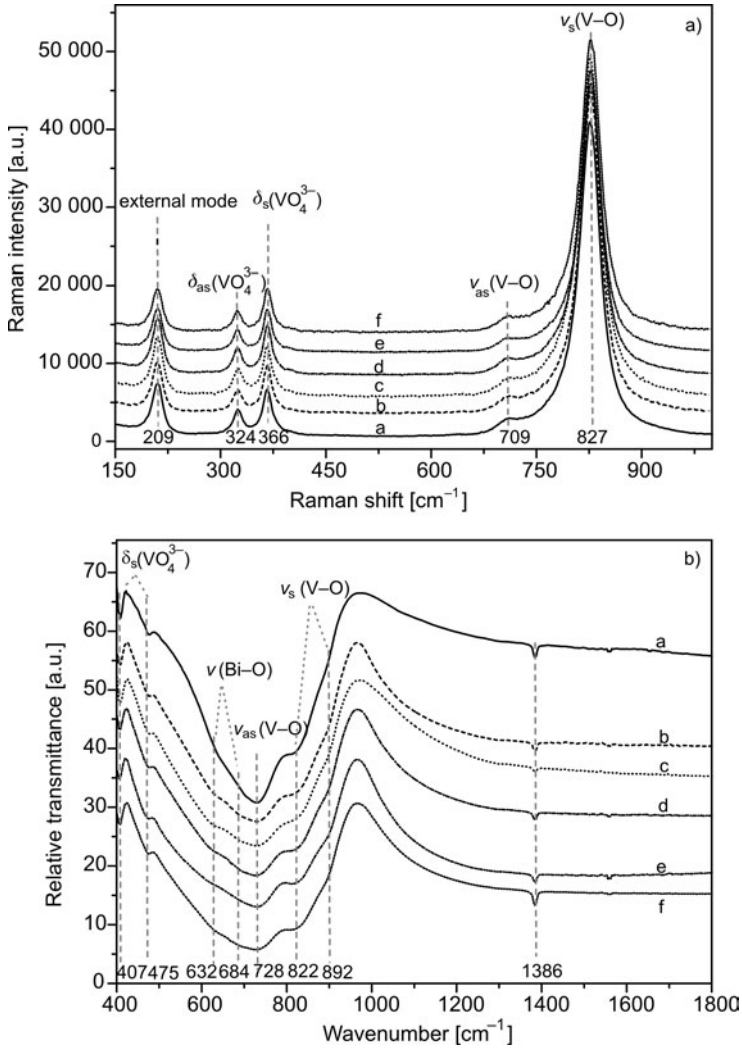

Fig. 4. Raman (a) and FTIR (b) spectra of $BiVO_4$ fabricated at various hydrothermal temperatures, T [°C]: a) 140, b) 160, c) 180, d) 200, e) 220, f) 240

ples are also marked in Fig. 4. It showed the same feature, namely that each spectrum was dominated by an intense Raman band at 827 cm^{-1} assigned to ν_s(V–O), and with a weak shoulder at about 709 cm^{-1} assigned to ν_{as}(V–O). The $\delta_s(VO_4^{3-})$ and $\delta_{as}(VO_4^{3-})$ modes are at 366 and 324 cm^{-1}, respectively, and external modes (rotation/translation) occur at 209 cm^{-1}. Figure 4b shows FTIR spectra of recorded samples, ranging from 400 to 1200 cm^{-1} at RT. All the samples are mainly characterized by a broad and strong IR band near 728 cm^{-1} with shoulders at 892, 822, 684 and 632 cm^{-1}. One weak CO_3^{-} derived band is observed at 1386 cm^{-1}, which might be due to the adsorption of atmospheric carbon dioxide during the experiments [15, 17]. It reveals that all the samples exhibited the same monoclinic scheelite structure, although their particle diameters and particle morphologies increased in a continuous manner as the hydrothermal temperature increased from 140 to 240 °C.

3.4. DRS results of $BiVO_4$ powders

It is well known that the electronic structure of the semiconductor usually plays a crucial role in its photocatalytic activity [14, 18]. DFT calculations of the electronic structure [19] showed that the valence band (VB) of $BiVO_4$ is composed of hybridized Bi 6s and O 2p orbitals, whereas the conduction band (CB) is composed of V 3d orbitals; and the hybridization of the Bi 6s and O 2p orbital may enhance the migration of photo-excited holes, which is beneficial to photocatalytic oxidation of organic pollutants [5, 7, 20].

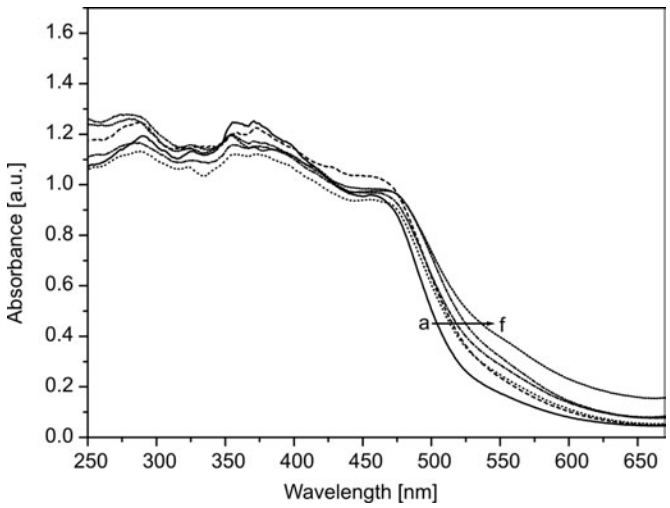

Fig. 5. DRS spectra of $BiVO_4$ fabricated at various hydrothermal temperatures, T [°C]: a) 140, b) 160, c) 180, d) 200, e) 220, f) 240

Figure 5 shows the DRS of $BiVO_4$ prepared hydrothermally at various temperatures. It was found that all samples showed strong absorption in the visible light re-

gion, in addition to that in the UV region, which is the characteristic absorption profile of monoclinic scheelite $BiVO_4$. The steep gradients of spectra indicated that the visible light absorption is due to the band-gap transition, and the prolonged absorption tail, up to about 650 nm, should result from the crystal defects that form when $BiVO_4$ grows [5, 9]. The absorption edges of samples shift to red, from about 530 to 590 nm, as the hydrothermal temperature increases, which indicates different band gaps of the samples. As in a crystalline semiconductor, the band gaps can be calculated from the following equation [12, 21],

$$\alpha h\nu = A\left(h\upsilon - E_g\right)^{n/2} \tag{2}$$

where α, ν, E_g and A are the absorption coefficient, incident light frequency, band gap and a constant, respectively. Among them, n depends on the characteristics of the transition in a semiconductor, i.e., direct transition (n = 1) or indirect transition (n = 4). For $BiVO_4$, n is taken as 1 [12, 15]. The band gap energy for the $BiVO_4$ can be thus estimated from a plot $(\alpha h\nu)^2$ versus photon energy ($h\nu$), as can be seen from Fig. 6.

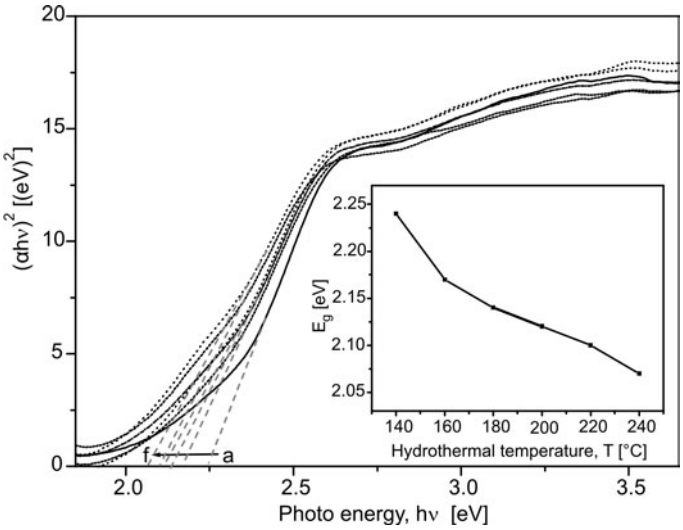

Fig. 6. Plots of the $(\alpha h\nu)^2$ versus photo energy ($h\nu$) for $BiVO_4$ powders fabricated at various hydrothermal temperatures, T [°C]: a) 140, b) 160, c) 180, d) 200, e) 220, f) 240

The intercept of the tangent to the x axis will give a good approximation of the band gap for $BiVO_4$. Thus the E_g of $BiVO_4$ can be estimated about 2.24, 2.17, 2.14, 2.12, 2.10 and 2.07 eV for samples (a)–(f) respectively, showing a decreasing trend, as can be seen in the inset of Fig. 6. These data clearly demonstrate that the electronic structures of $BiVO_4$ were changed by the temperature used in the hydrothermal synthesis. It proves that the variations in the hydrothermal temperature led to different degrees of aggregation and changes of grain size, which therefore resulted in the samples having different electronic structures.

4. Conclusion

Highly crystallized monoclinic $BiVO_4$ crystals with nanosized diameters were synthesized hydrothermally and characterized by XRD, TEM, DRS, Raman and FTIR techniques. From XRD and TEM data, the grain size was observed to increase when the hydrothermal temperature increased from 140 to 240 °C. DRS results indicated that samples prepared at higher hydrothermal temperatures may consist of larger particles with less aggregation, and thus lead to a smaller band gap.

Acknowledgement

We acknowledge the financial support of the Scientific Research Foundation of North China University of Technology and the Natural Science Foundation of Beijing. Professor Y. Fang (Capital Normal University, P.R. China) and Miss Q. Cheng (Beijing Purkinjl General Instrument Co. LTD, P.R. China) are also thanked for conducting tests and for helpful discussions regarding this manuscript.

Reference

[1] FUJISIMA A., HONDA K., Nature, 37 (1972), 238.
[2] FUJISHIMA A., RAO T.N., TRYK D.A., J. Photochem. Photobiol. C, 1 (2000), 1.
[3] KUDO A., UEDA K., KATO H., MIKAMI I., Catal. Lett., 53 (1998), 229.
[4] KOHTAIN S., HIRO J., YAMAMOTO N., KUDO A., TOKUMURA K., NAKAGAKI R., Catal. Commum., 6 (2005), 185.
[5] YU J.Q., KUDO A., Adv. Funct. Mater., 16 (2006), 2163.
[6] KOHTANI S., KOSHIKO M., KUDO A., Appl. Catal. B: Environ., 46 (2003), 573.
[7] TUCKS A., BECK H.P., Dyes Pigments, 72 (2007), 163.
[8] KUDO A., OMORI K., KATO H., J. Am. Chem. Soc., 121 (1999), 11459.
[9] YAO W.F., YE J.H., Chem. Phys. Lett., 450 (2008), 370.
[10] ZHOU L., WANG W.Z., XU H.L., Cryst. Growth Des., 8 (2008), 728.
[11] ZHANG L., CHEN D.R., JIAO S.X., J. Phys. Chem. B, 110 (2006), 2668.
[12] ZHANG X., AI Z.H., JIA F.L., ZHANG L.Z., FAN X.X., ZOU Z.G., Mater. Chem. Phys., 103 (2007), 162.
[13] KUBELKA P., MUNK F.E., BEITRAG O.F., Z. Tech. Phys., 12 (1931), 593.
[14] WELLER M.T., *Inorganic Materials Chemistry*, Oxford University Press, London, 1994.
[15] LIU J.B., WANG H., WANG S., YAN H., Mater. Sci. Eng. B, 104 (2003), 36.
[16] GOTIĆ M., MUSIĆ S., IVANDA M., ŠOUFEK M., POPOVIĆ S., J. Mol. Struct., 744–747 (2005), 535.
[17] GALEMBECK A., ALVES O.L., J. Mater. Sci., 37 (2002), 1923.
[18] FU H., PAN C., YAO W., ZHU Y., J. Phys. Chem. B, 109 (2005), 22432.
[19] OSHIKIRI M., BOERO M., YE J., ZOU Z., KIDO G., J. Chem. Phys., 117 (2002), 7313.
[20] TANG J., ZOU Z.G., YE J.H., Angew. Chem. Int. Edit., 43 (2004), 4463.
[21] BUTLER M.A., J. Appl. Phys., 48 (1977), 1914.

Received 4 July 2008
Revised 3 October 2008

Materials Science-Poland, *Vol. 27*, *No. 4/1*, *2009*

Rapid synthesis of Nd:YAG nanopowder by microwave flash combustion

R. CHOUDHARY*, K. LAISHRAM, R. K. GUPTA

Chemistry Division, Laser Science and Technology Centre, DRDO, Metcalfe House, Delhi-110054, India

Nd:YAG nanopowders were successfully synthesized by a novel approach using rapid microwave drying of sol. Citrate nitrate sol was treated in a microwave oven for a few minutes. The as-prepared precursor was calcined at 900 °C for 2 h. Characterization was done by thermogravimetric analysis, Fourier transform infrared spectroscopy, X-Ray diffraction (XRD) and transmission electron microscopy (TEM). XRD showed the formation of phase pure polycrystalline YAG. The particle size was found to be 24 nm (estimated from Scherrer's equation). TEM indicated that the particle size was in the 24–70 nm range. Nd^{3+} doping was confirmed by SEM–EDX. Nd:YAG nanopowder synthesized by this method was of low agglomeration and the particles were spherical in shape.

Key words: *microwave-flash combustion; Nd:YAG; nanopowder; transparent ceramics*

1. Introduction

Yttrium aluminum garnet, $Y_3Al_5O_{12}$ (YAG), is a well-known inorganic compound with excellent chemical, physical and optical properties. The usual applications of nanosized YAG doped with lanthanide ions include phosphors and laser active media [1]. Recent investigations indicate that Nd:YAG polycrystalline ceramics based on the sintering of nanopowders are one of the most promising materials for solid state lasers [2–6]. There are several methods to produce Nd:YAG nanopowder such as the sol-gel method [7, 8], co-precipitation [9, 10], spray pyrolysis [11] and the combustion [12, 13] technique. Microwave assisted processing is an area of recent research into the rapid and controlled synthesis of homogeneous nanopowders which have low sintering temperature, high density and an improved microstructure for the fabrication of transparent ceramics [14]. It has been claimed that this route can produce materials with superior properties compared with those fabricated by conventional methods [15].

*Corresponding author, e-mail address: mann_rekha@lastec.drdo.in

In a microwave combustion process, since the heating takes place at the molecular level, such a process is likely to produce less agglomerated powders than those reported for other materials [16] In this paper, we report on the synthesis of Nd:YAG nanopowders by the microwave induced combustion reaction. Microwave initiated combustion has several advantages, such as rapid heating and enhanced reaction kinetics [17].

2. Experimental

Aluminum nitrate, $Al(NO_3)_3 \cdot 9H_2O$ (99.9% purity Alfa Aesar), yttrium nitrate, $Y(NO_3)_3 \cdot 6H_2O$ (99.9% purity Alfa Aesar), neodymium nitrate, Nd $(NO_3)_3 \cdot 6H_2O$ (99.9% purity Alfa Aesar) and citric acid anhydrous (99.5% purity Alfa Aesar) were used as-provided to prepare Nd:Y:Al in the molar ratio of 0.06:2.94:5. This was subsequently dissolved in water so as to achieve a total solid content of 60%, after the addition of citric acid. Water for preparing the solutions was purified using a Millipore Elix 10 purifier. The nitrate–citrate sol was sonicated for 2 h at 80 °C in an ultrasonic bath having the frequency of 40 kHz (Scheme 1). pH was then adjusted to ca. 1 by passing dilute gaseous ammonia. The sol was transferred into an alumina crucible. Drying was carried out using a 2.45 GHz domestic microwave oven at 900 W, till combustion took place. Combusted powder was calcined at 900 °C for 2 h in an oxygen rich atmosphere, maintained by passing oxygen gas (3 dm^3/min). The heating rate, from room temperature to 900 °C, was maintained at 10 °C/min using a Eurotherm 2604 microprocessor controlled temperature programmer.

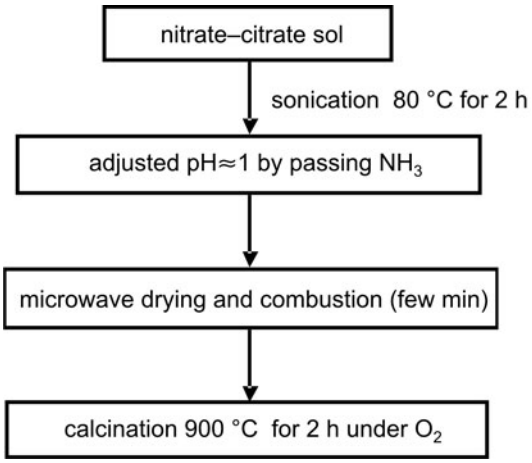

Scheme 1

TG/DTA of combusted powder was carried out in air at the heating rate of 10 °C/min from room temperature to 1300 °C, on a Perkin Elmer Diamond simultaneous TGA/DTA system. FTIR spectra were recorded with a FTIR Spectrometer (Bruker, model Vector 22) using KBr pellets. XRD was carried out using a Philips X-ray dif-

fractometer, PW 3020 in the 2θ range from 15° to 80°, keeping a step size of 0.02. Particle size was calculated using Scherrer's equation [18]:

$$p = \frac{0.9\lambda}{(\beta^2_{\text{sample}} - \beta^2_{\text{inst}})^{1/2} \cos\theta} \tag{1}$$

where p is the crystallite diameter, λ = 1.54056 Å, θ is the diffraction angle, β_{sample} is the full width at half maximum (FWHM) of the diffraction peak and β_{inst} is a characteristic parameter of the instrument. Nd^{3+} doping was confirmed by EDX using a scanning electron microscope (Zeiss Evo Series 50). The particle size and the morphology of the crystalline powder was characterized by Transmission Electron Microscope (FEI Philips Morgagni 268D, AC Voltage 100kV having a magnification factor of up to 280,000)

3. Results and discussion

The thermal analysis of microwave combusted precursor of Nd:YAG powder is shown in Fig. 1. The first weight loss, for temperatures of up to 200 °C, is due to the dehydration of adsorbed moisture. Weight loss for temperatures between 350 to 550 °C is due to the loss of organic residues, in the form of carbon dioxide, and the decomposition of nitrates. A total weight loss of ~62% was observed for temperatures of up to 550 °C. An exothermic peak at ~ 934 °C, along with small weight loss, is due to the crystallization of YAG. X-ray diffraction shows that under isothermal heat treatment conditions the crystalline phase appears even at a much lower temperature [19, 20].

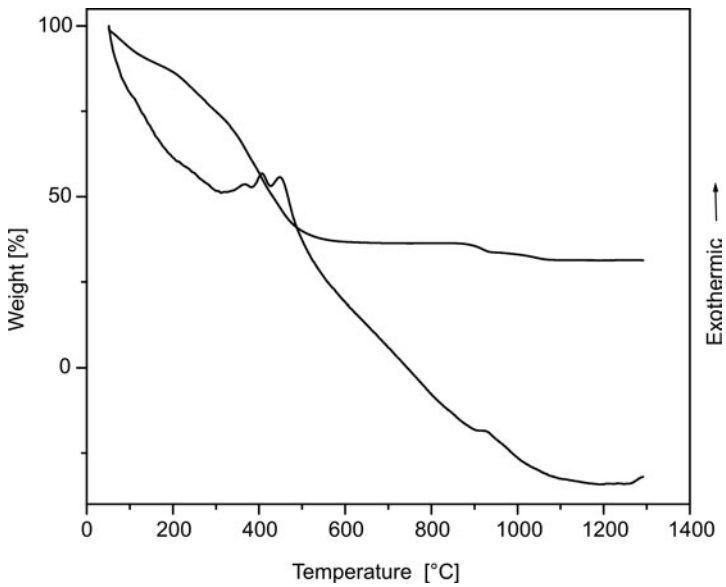

Fig. 1. TGA and DTA curves of Nd:YAG precursor powder by the microwave flash combustion technique

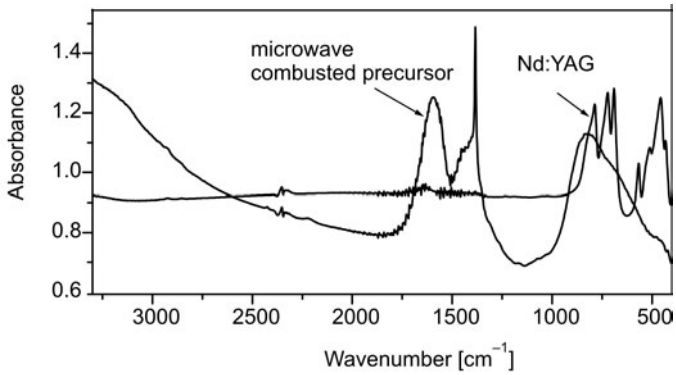

Fig. 2. FTIR of microwave combusted precursor and Nd:YAG powders

FTIR spectra in Fig. 2 show a band at ca. 2350 cm^{-1}, which belongs to carbon dioxide from the atmosphere. The inequalities in the path length in the spectrometer result in an imperfect subtraction of sample and reference beams, and thus the peak attributed to atmospheric carbon dioxide appears in the spectrum [21, 22]. The broad band in the region of 900–450 cm^{-1} in a precursor is replaced by several bands. The FTIR spectrum of the microwave combusted and calcined powder Nd:YAG exhibited well defined peaks at 787, 722 and 690 cm^{-1}, due to stretching vibrations of the Al–O bond in tetrahedral sites, and absorption peaks at 566, 511, 457 and 432 cm^{-1} associated with stretching of the Al–O bond in octahedral sites of the garnet structure. The peaks matched with the reported data for a well crystallized YAG [23, 24].

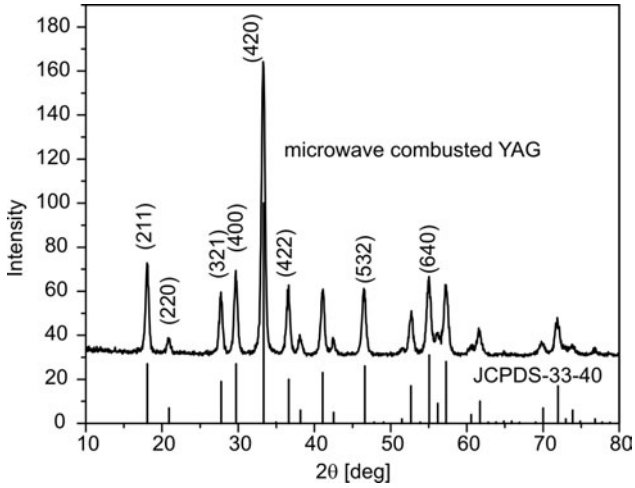

Fig. 3. XRD pattern of nanocrystalline Nd:YAG powder calcined at 900 °C for 2 h under oxygen atmosphere

The peaks observed in the XRD pattern for the powder calcined at 900 °C for 2 h in an O_2 atmosphere are shown in Fig. 3. XRD peaks were indexed in terms of the

garnet structure, according to standard JCPDS 33-40. The main peak is centred at 2θ = 33.35° and corresponds to a crystal plane with Miller indices of [420] characteristic of YAG [24]. The average primary particle size, calculated from Scherrer's equation, was 24 nm. The cell parameter calculated by the least square method was found to be 12.026 Å for microwave synthesized Nd:YAG, indicating partial substitution of Y^{3+} sites with Nd^{3+} cations [21, 26]. The cell parameters reported in JCPDS for YAG (cubic) crystals is 12.010 Å [27].

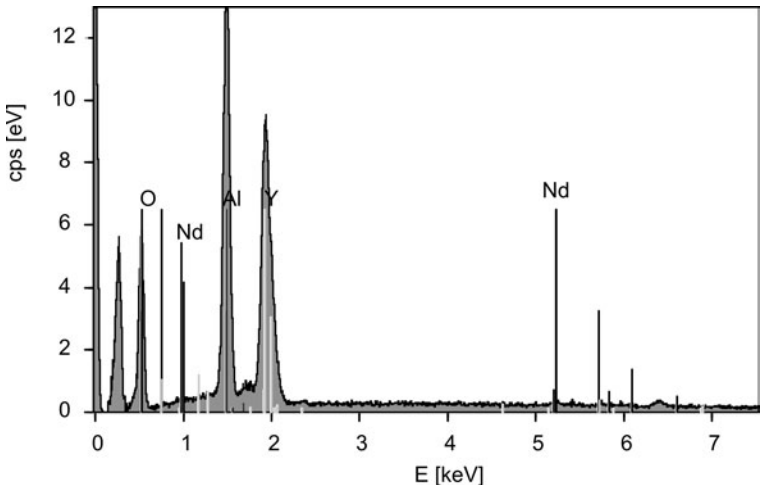

Fig. 4. EDX spectra of calcined Nd:YAG powder

EDX powder spectra in Fig. 4 confirmed the doping of Nd^{3+} ions. Peaks of all constituent elements Y, Al, Nd and O are observed in the EDX spectrum of Nd:YAG nanopowders.

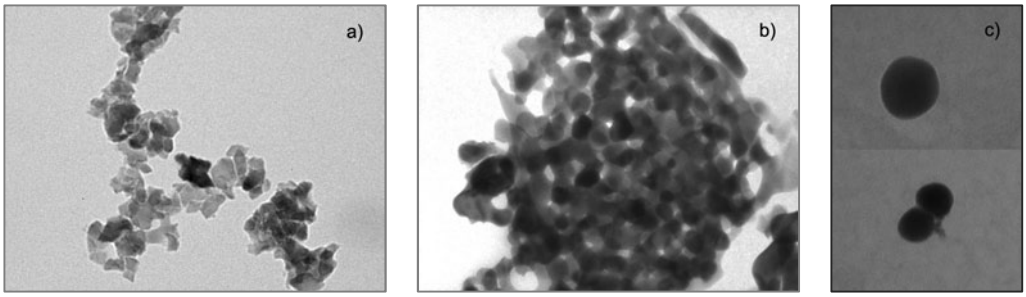

Fig. 5. TEM images of Nd:YAG powder synthesized by:
a) conventional sol-gel method and b), c) using microwave heating

The TEM micrographs of Nd:YAG powder calcined at 900 °C for 2 h in an oxygen atmosphere are shown in Fig. 5. The particle size was observed in the range of 24–70 nm. The shape of the particles was spherical and regular compared with that of

particles prepared by the conventional, but otherwise similar, sol-gel process (Fig. 5). Particles were found to be separate and less agglomerated. Microwave assisted synthesis mostly yields less agglomerated powder [14]. Such regular shaped spherical nano-sized powders with lesser agglomeration are considered highly sinterable for transparent ceramics [1].

4. Conclusions

Single phase nanocrystalline Nd:YAG powder was synthesized by rapid microwave drying and combustion of nitrate–citrate sol, followed by calcination at 900 °C for 2 h in an oxygen atmosphere. Particle size was found to be 24 nm by XRD. The cell parameter was calculated to be 12.026 Å and SEM-EDX indicates Nd doping.

TEM shows the spherical morphology of nano-sized powders in the range of 24–70 nm, with little agglomeration, indicating higher sinterability.

Microwave processing of sol leads to a fine-grained product in short processing time which makes this process attractive and interesting.

Acknowledgements

The authors wish to express their sincere thanks to Dr. Anil Kumar, Director of the Laser Science and Technology Centre, Delhi, for his constant inspiration and encouragement of this work. The authors thank the Characterization Division of the Solid State Physics Laboratory, CFEES Delhi and IIT Delhi, for providing us with timely characterization.

References

[1] CAPONETTI E., MARTINO D.C., SALADINO M.L., Langmuir, 23 (2007), 3947.
[2] SEKITA M., HANEDA H., YANAGITANI T., SHIRASAKI S., J. Appl. Phys., 67 (1990), 453.
[3] PAKUTINSKIENE I., MATHUR S., SHEN H., KUDABIENE G., JASAITIS D., KAREIVA A., Mater. Sci. (Medziagotyra)., 9 (2003), 374.
[4] HRENIAK D., STRĘK W., MAZUR P., Mater. Sci., 20 (2002), 39.
[5] IKESUE A., Opt. Mater., 19 (2002), 183.
[6] MAH T-II, PARTHASARTHY T.A., LEE H.D., J. Ceram. Proc. Res., 5 (2004), 369.
[7] CHUNG B-J., PARK J-Y., SIM S-M., J. Ceram. Proc. Res., 4 (2003), 145.
[8] DE LA ROSA E., DIAZ-TORRES L.A., SALAS P., ARREDONDO A., MONTOYA J.A., ANGELES C., RODRIGUEZ R.A., Opt. Mater., 27 (2005), 1793.
[9] LI X., LI Q., WANG J., YANG S., LIU H., Opt. Mater., 29 (2007), 528.
[10] CAPONETI E., SALADINO M.L., SERRA F., ENZO S., J. Mater. Sci., 42 (2007), 4418.
[11] DEVI P.S., LI Y., MARGOLIS J., PARISE J.B., SAMPATH S., HERMAN H., HANSON J.C., J. Mater. Res., 17 (2002), 2846.
[12] COSTA A.L., ESPOSITO L., MEDRI V., BELLOSI A., Adv. Eng. Mater., 9 (2007), 307.
[13] GUO X., DEVI P.S., RAVI B.G., PARISE J.B., SAMPATH S., HANSON J.C., J. Mater. Chem., 14 (2004), 1288.
[14] MANGALARAJA R.V., RAMAM K.V.S., RAVI J., CAMURRI C.P., Mater. Sci.-Poland., 25 (2007), 1075.
[15] MUNIR Z.A., Am. Ceram. Soc. Bull., 67 (1988), 342.
[16] SUBRAMANIAN V., BURKE W.W., HONGWEI Z., BINGQING W., J. Phys. Chem., 112 (2008), 4550.
[17] RAMESH D.P., MARY F., DINESH K.A., RUSTUM R., J. Am. Ceram. Soc., 85 (2002), 117.

[18] CULITY B.D., STOCK S.R., *Elements of X-Ray Diffraction*, 2nd Ed., Addison-Wesley, MA, 1978.
[19] CINIBULK M.K., J. Am. Ceram. Soc., 83 (2000), 1276.
[20] WANG S., XU Y., LU P., XU C., CAO W., Mater. Sci. Eng., B 127 (2006), 203.
[21] LELECKAITE A., KAREIVA A., Opt. Mater., 26 (2004), 123.
[22] HARWOOD L.M., MOODY C.J., PERCY J.M., *Experimental Organic Chemistry – Standard and Microscale*, Blackwell Publishing, London, 1999.
[23] PANNEER S.M., SUBANNA G.N., RAO K.J., J. Mat. Res., 16 (2001), 2776.
[24] VAIDHYANATHAN B., BINNER J.G.P., J. Mater. Sci., 41 (2006), 5954.
[25] PEREIRA P.F.S., CAIUT J.M.A., RIBEIRO S.J.L., MESSADDEQ Y., KATIA J.C., LUCAS A.R., MOLINA E.F., NASSAR E.J., J. Lumin., 126 (2007), 378.
[26] CAPONETTI E., ENZO S., LASIO B., SALADINO M.L., Opt. Mater., 29 (2007), 1240.
[27] KAITHWAS N., DESHMUKH M., KAR S., DAVE M., LALLA N.P., RYU H., BARTWAL K.S., Cryst. Res. Technol., 42 (10) (2007), 991.

Received 17 October 2008
Revised 5 December 2008

Materials Science-Poland, *Vol. 27*, *No. 4/1*, *2009*

Non-stoichiometric boron carbide synthesized in moderate temperature conditions

G. SUN[1*], Y. W. LI[2], Q. K. HU[1], Q. H. WU[1], D. L. YU[3]

[1]Institue of Materials Science and Engineering, Henan Polytechnic University, Jiaozuo 454000, China

[2]Department of Chemistry and Physics, Henan Polytechnic University, Jiaozuo 454000, China

[3]State Key Laboratory of Metastable Materials Science and Technology, Yanshan University, Qinhuangdao, 066004, China

Non-stoichiometric boron carbide was successfully synthesized through a chemical synthetic route by using tribromide and carbon tetrachloride as reactants and metal sodium as co-reductant at 700 °C. The synthesized sample was characterized by X-ray powder diffraction, transmission selected area electron diffraction, electronic energy loss spectra (EELS) and scanning electron microscopy. The results of the analysis revealed that the synthesized boron carbide crystals have rhombohedral structure and equiaxial morphology. Results of the EELS analysis indicate that the compositions of the synthesized boron carbide are not uniform, the carbon content can range from 9 at. % to 11 at. %.

Key words: *non-stoichiometric boron carbide; chemical synthesis; X-ray diffraction; electron energy loss spectroscopy*

1. Introduction

Boron carbide is an important non-metallic material possessing many excellent properties such as high melting point, high elastic modulus, high hardness, high corrosion and oxidation resistance. These properties make boron carbide suitable for high performance applications such as armour plating, nozzles, bearings and cutting tools [1–4]. Boron carbide can be also used as a neutron absorber and shielding material in nuclear plants due to a high neutron reactivity and high neutron absorption cross section of ^{10}B [5].

Boron carbide has a rhombohedral structure in which B_{12} icosahedra are linked by direct covalent bonds and 3-atom intericosahedral chains along the main diagonal of

*Corresponding author, e-mail: mcsunguang@tom.com

the rhombohedron. Boron carbide is not a stoichiometric compound, the carbon content can range from ca. 8 at. % (the boron-rich limit) to about 20 at. % (the carbon-rich limit) [6]. This large range of the B/C ratio implies that the carbon atoms substitute, to various extents, boron atoms within intericosahedral chains and the icosahedra, and the structure of boron carbide still keeps a single phase throughout the entire range [7].

Traditionally, boron carbide can be synthesized by chemical reactions including carbothermal reduction of boron oxide (B_2O_3), boric acid (H_3BO_3), borax ($Na_2B_4O_7$) etc., as well as by the direct combination of boron and carbon [3]. Other routes for the synthesis of boron carbide powder are the magnesiothermal reduction of B_2O_3 in the presence of carbon at 1000–1200 °C [3, 8] the reduction of BCl_3 by CH_4 at 1500 °C with laser [9] and the carbothermal reduction of boric acid–citric acid gel precursor [10]. The industrial method for the production of boron carbide is carbothermal reduction of boric acid at above 2000 °C [11]. To our knowledge, these methods are carried out at high temperature (higher than 1000 °C). Recently, some high melting point materials have been successfully synthesized under low temperature synthesis conditions, such as diamond [12], c-BN [13] and boron carbide [14]. The stoichiometric rod-like B_4C crystals were obtained at low temperature (450 °C) through a co-reduction route by using boron tribromide (BBr_3) and carbon tetrachloride (CCl_4) [15]. Because boron carbide is a non-stoichiometric compound, in principle, it is easier to obtain the crystals whose compositions deviate from B_4C. In this paper, we report a moderate temperature synthesis route for non-stoichiometric boron carbide by using BBr_3 and CCl_4 as reactants in the presence of metal sodium as co-reductant.

2. Experimental

The synthesis was were carried out in a glove box, which was filled with Ar gas. 10 cm^3 of CCl_4 and 5 cm^3 BBr_3 were put into a 50 cm^3 stainless steel autoclave. 13 g of sodium was also used as a co-reductant. No catalyst was needed in this procedure. The autoclave was sealed and heated to 700 °C at the heating rate of 70 °C/h and kept for 20 h before being cooled to room temperature naturally. The dark precipitate was collected and washed with distilled water three times. Dilute hydrochloride acid was used, in order to remove some metal impurity. Then, the precipitate was boiled with mixed acid (H_2SO_4: HNO_3 = 3:1) to remove the created carbon and washed 3 times with distilled water. After being dried under vacuum at 100 °C for about 4 h, a black powder was obtained. The whole reaction process for the synthesis of boron carbide can be formulated as follows

$$4BBr_3 + CCl_4 + 16Na \xrightarrow{700\,^{\circ}C} B_4C_{1-x} + 4NaCl + 12NaBr + xC$$

The final product was characterized using X-ray powder diffraction (XRD) and transmission electron microscopy (TEM, JEM-2010) to confirm the formation of the boron carbide phase. XRD spectra were obtained on a Rigaku Dmax-2000PC X-ray

diffractometer with Ni filtered Cu K_α radiation at the scanning rate of 5 deg/min. An electron energy loss spectrometer (EELS, Gatan-ENFINA-776) was employed to determine the chemical composition of the individual crystal in the synthesized powder in the TEM. The crystal size and morphology of the synthesized powders was investigated using scanning electron microscopy (SEM, KYKY-2800).

3. Results and discussion

XRD was used to check the structure of the synthesized sample. In its XRD spectrum (Fig. 1), all the reflection peaks correspond to rhombohedral boron carbide. The lattice parameters determined from XRD are a = 5.621 Å and c = 12.11 Å (due to the symmetrical relationship between the rhombohedral structure and the hexagonal structure, the lattice parameters of the rhombohedral lattice can also be given for the hexagonal lattice), both of which being slightly higher than the reported values of the standard B_4C (PCPDF 35-0789: a = 5.600 Å, c = 12.08 Å) and the synthesized B_4C in ref. [15] (a = 5.604 Å, c = 12.09 Å), and slightly smaller than the reported values of the standard $B_{13}C_2$ (PCPDF 26-0233: a = 5.617 Å, c = 12.09 Å).

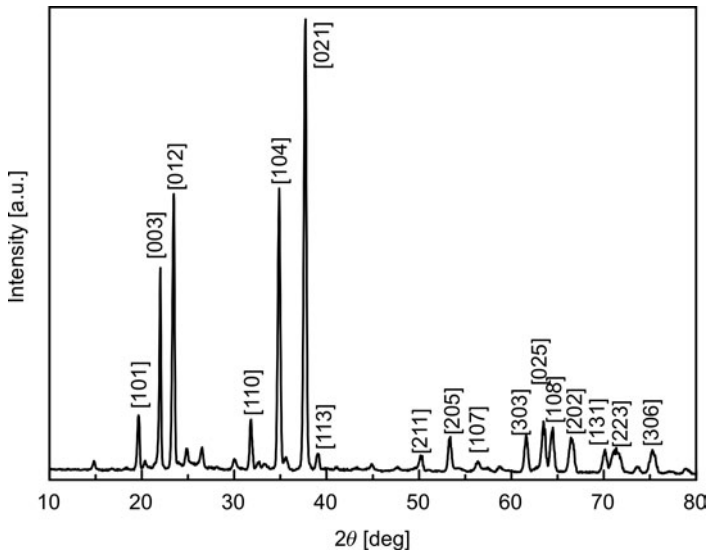

Fig. 1. XRD spectrum of the synthesized sample

In order to further determine the crystal structure and chemical composition of the obtained sample, SAED and parallel EELS measurements were performed on the synthesized crystals. Figure 2 shows typical SAED patterns of a synthesized rhombohedral boron carbide crystal along the <111> and <4 $\bar{3}$ 1> axes. From the clear spots appearing in Fig. 2, it can be seen that the synthesized boron carbide has high crystallinity. Figure 3 shows the corresponding EELS spectrum of the boron carbide crystal

shown in Fig. 2. In Figure 3, the characteristic K-shell ionization edges of elemental boron (188.4 eV) and carbon (284.8 eV) are observed, and no traces of other elements such as chlorine, bromine or sodium, are detected, suggesting that the synthesized boron carbide crystals contain no major impurities.

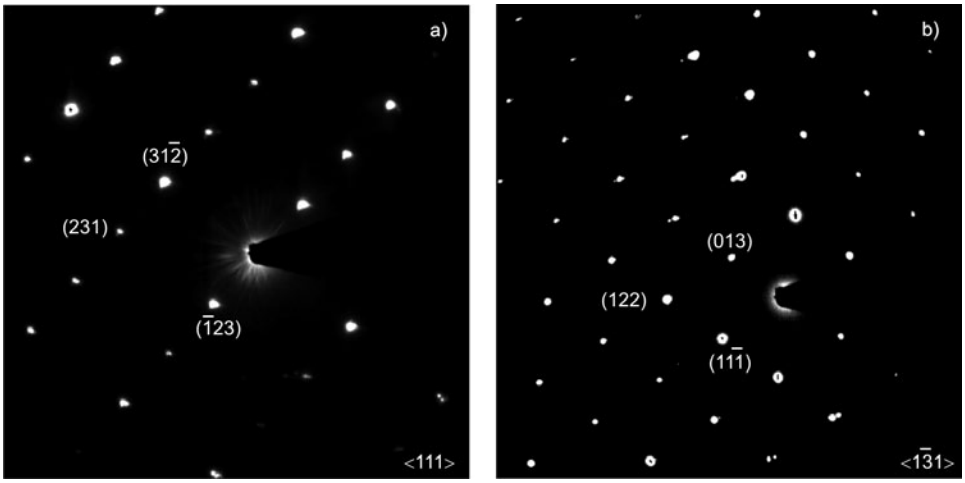

Fig. 2. SAED patterns of a rhombohedral boron carbide crystal in: a) <111> axis and in b) < 4$\bar{3}$1 > axis

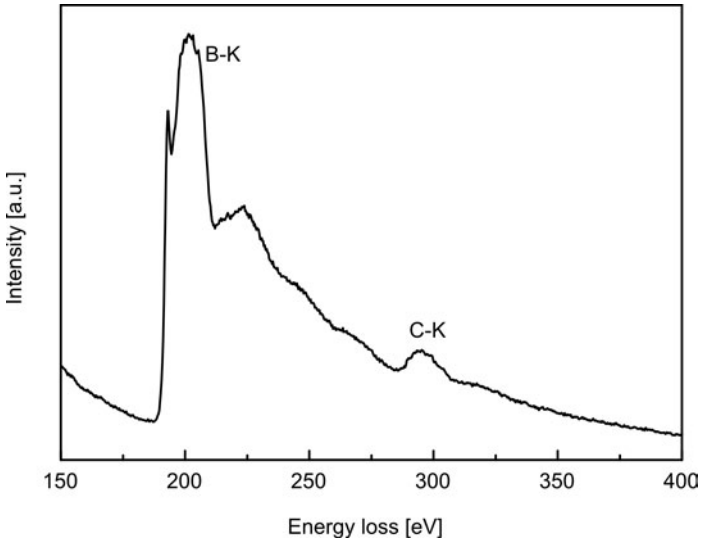

Fig. 3. The EELS spectrum taken from the crystal corresponding to Fig. 2, exhibiting characteristic K-shell ionization edges of boron at 188 eV and carbon at 284 eV with the carbon contents 10.7 at. %

From the background-subtracted EELS spectra of Fig. 3, the atomic percents of the boron carbide crystal have been quantified by using the usual hydrogenic cross-

sections. The quantified result reveals that the contents of B and C in the synthesized boron carbide crystal are 89.3 at. % and 10.7 at. %, respectively. Further EELS measurements were performed on more than 30 various crystals selected randomly in the sample to determine their compositions. It was found that the carbon contents of the synthesized boron carbide crystals are not uniform, and range between 9 at. % to 11 at. %. Thus, it can be expressed as B_4C_{1-x} ($0.5 < x < 0.6$). Such carbon contents are obviously different from those in crystals synthesized at 450 °C [14].

The different experimental results may imply that through such a reaction procedure, a higher reaction temperature (700 °C) favours the formation of the non-stoichiometric B_4C_{1-x} ($0.5 < x < 0.6$), but not the stoichiometric B_4C. It is well known that boron carbide it is a non-stoichiometric compound, whose carbon content can range from 8at. %-20at. %. Generally, since the atomic radius of carbon (0.91 Å) is smaller than that of boron (1.17 Å), different carbon contents in rhombohedral boron carbide will result in slight changes of the lattice parameters. In other words, with the increased of carbon content in the rhombohedral boron carbide crystals, the dimensions of the unit cell will be slightly shrunk (see the comparison of the lattice parameters between B_4C, $B_{13}C_2$ and the synthesized boron carbide sample shown in Table 1). That is why the lattice parameters of the synthesized rhombohedral boron carbide are slightly larger than that of the standard B_4C and the as-prepared B_4C in ref. [15].

Table 1. Lattice parameters of B_4C, $B_{13}C_2$ and boron carbide synthesized in the present paper

Boron carbide	Carbon content [at. %]	Lattice parameters [Å]	
		a	*c*
B_4C_{1-x} ($0.5< x <0.6$) synthesized in this work	9–11	5.621	12.11
$B_{13}C_2$, PCPDF 26-0233	13.3	5.617	12.09
B_4C, PCPDF 35-0789	20	5.600	12.08
B_4C, synthesized in ref. [15]		5.604	12.09

It should be noted that besides the reaction temperature, the reaction pressure may also play an important role in the formation of boron carbide with various carbon content. At the beginning of the reaction, the pressure should be relatively high, due to the evaporation of BBr_3 and CCl_4. Based on the ideal gas law, we estimate that the initial pressure in the autoclave is about 24 MPa. As the reaction proceeds, CCl_4 and BBr_3 are consumed gradually by sodium, thus the pressure should gradually become lower. At the end of the reaction, the pressure should reach a minimum. The changes in pressure may be a reason for the different carbon contents in the formed boron carbide crystals.

In order to determine the size and the morphology of the synthesized boron carbide crystals, SEM measurements were performed. Figure 4 shows the SEM image of the synthesized boron carbide crystals. The crystal size of the synthesized boron carbide is between 5 and 30 μm and its morphology is nearly equiaxial. In our samples,

we did not find any rod-like crystals as described in the Ref. [15]. This implies that the reaction temperature may play an important role in the morphology of boron carbide. In other words, the lower reaction temperature (450 °C) is favourable to the formation of rod-like boron carbide, whereas the higher reaction temperature (700 °C) is favourable to the formation of equiaxial boron carbide.

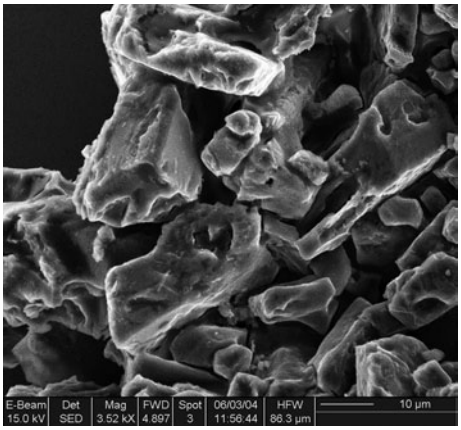

Fig. 4. SEM image of the synthesized boron carbide crystals

4. Conclusions

Highly crystalline non-stoichiometric boron carbide crystals were successfully synthesized through a facile co-reduction synthetic route by using CCl_4 and BBr_3 as reactants and metal Na as co-reductant at 700 °C. The carbon content of the synthesized boron carbide crystals ranges from 9 at. % to 11at. %. The size of the synthesized boron carbide crystals is between 5 and 30 μm and their morphology is nearly equiaxial. Due to a simple process and cheap carbon resource (CCl_4) such a co-reduction method may also be used to synthesize other carbides, for example the attractive carbon nitride and boron carbon nitride compounds.

Acknowledgements

The authors acknowledge financial support of NSFC (Grant No. 50225207, 50342033 and 50372055).

References

[1] WOOD C., EMIN D., Phys. Rev. B., 29 (1984), 4582.
[2] BOUGOIN M., THEVENOT F., J. Mater. Sci., 22 (1987), 109.
[3] SPOHN M.T., Am. Ceram. Soc. Bull., 72 (1993), 88.
[4] SCHWETZ K.A., SIGL L.S., PFAU L., J. Solid State Chem., 133 (1997), 68.
[5] THEVENOT F., J. Eur. Ceram. Soc., 6 (1990), 205.
[6] BOUCHACOURT M., THEVENOT F., J. Less-Common Met.,82 (1981), 219.

[7] CONDE O., SILVESTRE A.J., OLIVERIRA J.C., Surf. Coat. Technol., 125 (2000), 141.
[8] THEVENOT F., [In:] *Advanced Ceramics, Key Engineering Materials*, Vols. 56, 57, C. Ganguly, S.K Roy, P.R. Roy (Eds.), TransTech, Zurich, 1991, 59.
[9] KNUDSEN A.K., [In:] *Ceramic Powder Science, Advances in Ceramics*, Vol. 21, G.L. Messing, K.S. Mazdiyasni, J.W. Mccauley, R.A. Haber (Eds.), Amer. Ceram. Soc., Westerville, OH, 1987, 237.
[10] SINHA A., MAHATA T., SHARMA B.P., J. Nucl. Mater., 301 (2002), 165.
[11] SCOTT J.J., US Pat. No.3161471, 1964.
[12] XIE Y., QIAN Y.T., WANG W.Z., ZHANG S.Y., ZHANG Y.H., Science, 272 (1996), 1417.
[13] FU Q., CAO C.B., ZHU H.S., Chem. Phys. Lett., 314 (1999), 223.
[14] MONDAL S., BANTHIA A.K., J. Eur. Ceram. Soc., 25 (2005), 287.
[15] SHI L., GU Y.L., CHEN L.Y., QIAN Y.T., YANG Z.H., MA J.H., Solid State Commun., 128 (2003), 5.

Received 25 July 2008
Revised 29 April 2009

Materials Science-Poland, *Vol. 27*, *No.4/1*, *2009*

Acoustical investigations of uranium chalcogenides

R. K. SINGH[1*], K. K. PANDEY[2], M.P. SINGH[1], R. P. SINGH[1]

[1]Department of Physics, Banaras Hindu University, Varanasi-221005, India.

[2]Department of Physics, H.C.P.G. College, Varanasi-221001, India.

Ultrasonic attenuation due to phonon–phonon interaction and thermoelastic loss was evaluated in uranium chalcogenides viz. UX, X= S, Se, Te in fcc phase in the temperature range 50–600 K for longitudinal and shear waves along the <100>, <110> and <111> directions of propagation. Electrostatic and Born–Mayer repulsive potentials were used to obtain second and third order elastic constants, taking the nearest neighbour distance and hardness parameter as the input data. Second and third order elastic constants (obtained at various temperatures) were used to obtain the Gruneisen parameters and non-linearity or anisotropy parameters, which in turn were used to evaluate the ultrasonic attenuation coefficient over the frequency square due to phonon–phonon interaction, $(\alpha/f^2)_{p-p}$ in the Akhiezer regime. It has been found that at lower temperatures α/f^2 increases rapidly with temperature, and at higher temperatures the rate of increase becomes small. Contribution to the total attenuation due to thermoelastic loss is negligible in comparison with that of phonon–phonon interaction, i.e. a major part of the energy from the sound wave is removed, due to interaction of acoustic phonons with thermal phonons (lattice vibrations).

Key words: *elastic constants; ultrasonic attenuation; nonlinearity coupling constants*

1. Introduction

Uranium monochalcogenides with uranium in a trivalent state under atmospheric pressure exhibit metallic conductivities. Uranium compounds, besides their important use in reactor technology, possess other interesting and also controversial properties [1–5]. Hence, they have attracted the attention of both experimental and theoretical solid state physicists. These chalcogenides (UX, X = S, Se, Te) show ferromagnetic ordering [6–9].

Ultrasonic attenuation studies have been made in different types of solids viz. dielectric, mixed dielectric, semiconducting and metallic substances at room temperature as well as at higher temperatures. There may be different reasons for the attenuation of ultrasonic waves propagating through solids (crystalline or amorphous). These

[*]Corresponding author email: rksingh_17@rediffmail.com

important factors for sound attenuation are electron–phonon interaction, phonon –phonon interaction, thermoelastic loss and loss due to screw and edge dislocations. Phonon–phonon interaction is the principal reason of ultrasonic attenuation at higher temperatures viz. 100 K and above, in all types of solids, i.e. metallic, semiconducting and dielectric. In solids, a small contribution (2–5%) of the total attenuation coefficient occurs due to thermoelastic loss, i.e. due to heat transfer from compressed to rarefied parts of the materials due to strain caused by sound waves [10–12].

Sound attenuation studies offer the possibility to detect and characterize microstructural properties as well as flaws in materials, controlling material behaviour, based on physical mechanisms, to predict the future performance of the material. Structural inhomogeneities, elastic parameters, non-linearity parameters are strongly connected with frequency or temperature dependences of ultrasonic attenuation mechanisms [12–15].

The present paper deals with temperature variation of ultrasonic attenuation due to p–p interaction in the 50–600 K range, and along the <100>, <110> and <111> crystallographic directions of propagation for longitudinal and shear waves and for shear waves polarized along various directions.

2. Theory

2.1. Theory of second and third order elastic constants

Second and third order elastic constants (SOEC and TOEC), C_{ij}^0 and C_{ijk}^0 at 0 K have been obtained using the electrostatic and Born–Mayer potentials and following Brugger's [16] definition of elastic constants. According to Brugger's definition, the *n*th order elastic constant is defined as

$$C_{ijklmn....} = \left(\frac{\partial u}{\partial \varepsilon_{ij} \partial \varepsilon_{kl} \partial \varepsilon_{mn} ...} \right) \tag{1}$$

where u is the crystal free energy density and ε_{ij} is the strain tensor. In Voigt notation C_{IJK} replaces $C_{ijklmn...}$ in which $ij \rightarrow I\ldots$, etc. For cubic crystals, (uranium chalcogenides have fcc structure) three independent SOEC (C_{11}, C_{12}, C_{44}) and six independent TOEC (C_{111}, C_{112}, C_{144}, C_{166}, C_{456}, C_{123}) occur. Using the theory discussed in [17], SOEC and TOEC at 0 K viz. C_{ij}^0, C_{ijk}^0 obtained are given as

$$C_{11}^0 = -1.56933 \frac{z^2 e^2}{r_0^4} + \frac{1}{q r_0} \left(\frac{1}{r_0} + \frac{1}{q} \right) Q(r_1) + \frac{2}{q r_0} \left(\frac{1}{\sqrt{2} r_0} + \frac{1}{q} \right) Q(r_2)$$

$$C_{12}^0 = C_{44}^0 = 0.344778\frac{z^2e^2}{r_0^4} + \frac{1}{qr_0}\left(\frac{1}{\sqrt{2}r_0} + \frac{1}{q}\right)Q(r_2)$$

$$C_{111}^0 = 10.26390\frac{z^2e^2}{r_0^4} - \left(\frac{3}{qr_0^2} + \frac{3}{q^2r_0} + \frac{1}{q^3}\right)Q(r_1) - \left(\frac{3}{\sqrt{2}r_0^2q} + \frac{3}{q^2r_0} + \frac{\sqrt{2}}{q^3}\right)Q(r_2)$$

$$C_{112}^0 = C_{166}^0 = 1.209625\ \frac{z^2e^2}{r_0^4} + \left(\frac{3}{2\sqrt{2}r_0^2q} + \frac{3}{q^2r_0} + \frac{\sqrt{2}}{q^3}\right)Q(r_2)$$

$$C_{123}^0 = C_{144}^0 = C_{456}^0 = 1.20862\ \frac{z^2e^2}{r_0^4} - \left(\frac{3}{2\sqrt{2}r_0^2q} + \frac{3}{2q^2r_0} + \frac{1}{\sqrt{2}q^3}\right)Q(r_2)$$

$$Q(r_1) = A\exp\left(-\frac{r_0}{q}\right), \qquad Q(r_2) = A\exp\left(-\frac{r_0\sqrt{2}}{q}\right)$$

Where z, A, r, q are the valence constant, pre-exponential constant, nearest neighbour distance and the hardness parameter, respectively

According to lattice dynamics developed by Ludwig et al. [18, 19], the temperature dependences of SOEC and TOEC can be obtained by adding a vibrational contribution to the elastic constants, SOEC and TOEC at any temperature are given by,

$$C_{ij}(T) = C_{ij}^0 + C_{ij}^{\text{vib}} \tag{2}$$

and

$$C_{ijk}(T) = C_{ijk}^0 + C_{ijk}^{\text{vib}} \tag{3}$$

where C_{ij}^{vib} and C_{ijk}^{vib} are vibrational contributions to elastic constants, where

$$C_{11}^{\text{vib}} = f^{1,1}G_1^2 + f^2G_2, \qquad C_{12}^{\text{vib}} = f^{1,1}G_1^2 + f^2G_{1,1}, \qquad C_{44}^{\text{vib}} = f^2G_{1,1}$$

$$C_{111}^{\text{vib}} = f^{1,1,1}G_1^3 + 3f^{2,1}G_2G_1 + f^3G_3$$

$$C_{112}^{\text{vib}} = f^{1,1,1}G_1^3 + f^{2,1}(2G_{1,1} + G_2)G_1 + f^3G_{2,1}$$

$$C_{123}^{\text{vib}} = f^{1,1,1}G_1^3 + 3f^{2,1}G_1G_{1,1} + f^3G_{1,1,1}$$

$$C_{144}^{\text{vib}} = f^{2,1}G_1G_{1,1} + f^3G_{1,1,1}$$

$$C_{456}^{\text{vib}} = f^3G_{1,1}, \qquad C_{166}^{\text{vib}} = f^{2,1}G_1G_{1,1} + f^3G_{2,1}$$

where

$$G_3 = 2Q(r_1)\left(30 + 30q_0 + 9{q_0}^2 - {q_0}^3 - {q_0}^4\right)H + 2G_{2,1}$$

$$G_{2,1} = Q(r_2)\left(15\sqrt{2} + 15q_0 + \frac{9}{\sqrt{2}{q_0}^2} - {q_0}^3 - \sqrt{2}{q_0}^4\right)H$$

$$G_2 = 2Q(r_0)\left(-6 - 6q_0 - {q_0}^2 + {q_0}^3\right)H + 2G_{1,1}$$

$$G_{1,1} = Q(r_2)\left(-3\sqrt{2} - 6\sqrt{2}q_0 - \sqrt{2}{q_0}^2 + 2{q_0}^3\right)H$$

$$G_1 = 2Q(r_0)\left(2 + 2q_0 - {q_0}^2\right) + Q(r_2)\left(\sqrt{2} + 2q_0 - \sqrt{2}{q_0}^2\right)H$$

where

$$Q(r_1) = A\exp\left(-\frac{r_0}{q}\right), \qquad Q(r_2) = A\exp\left(-\frac{r_0\sqrt{2}}{q}\right)$$

$$f^2 = f^3 = \left(\frac{\hbar w_0}{8{r_0}^3}\right)\coth X$$

$$f^{1,1} = f^{2,1} = -\left(\frac{1}{2{r_0}^3}\right)\left(\frac{\hbar w_0}{48}\right)\left(\frac{X}{\sin \mathrm{h}^2 X}\right) + \coth X$$

$$f^{1,1,1} = \left(\frac{\hbar w_0}{384{r_0}^3}\right)\left(\left(\frac{\hbar w_0}{kT}\right)^2\left(\frac{\mathrm{ctgh}X}{6\sinh^2 X}\right) + \frac{X}{\sinh^2 X} + \coth X\right)$$

$$X = \left(\frac{\hbar w_0}{2kT}\right)$$

$$H = \left[\left(\frac{r_0}{q-2}\right)Q(r_1) + 2\left(\frac{r_0}{q} - \sqrt{2}\right)Q(r_2)\right]^{-1}$$

where ω_0 is the angular frequency of the acoustic wave.

2.2. Theory of sound attenuation

In the Akhiezer regime ($\omega\tau_{th} << 1$), a sound wave passing through a solid can be attenuated by two processes [20]. First, if the wave is longitudinal, periodic contractions and dilations in the solid induce a temperature wave via thermal expansion. En-

ergy is dissipated by heat conduction between regions of different temperatures. This is called thermoelastic loss. Secondly, dissipation occurs as the gas of thermal phonons tries to reach an equilibrium characterized by a local (sound wave induced) strain. This is the internal friction mechanism.

The physical basis for obtaining the attenuation coefficient is that the elastic constants contributed by the thermal phonons relax [21]. The phonon contribution to the unrelaxed elastic constants is evaluated by taking into consideration the change in energy of the thermal phonons due to applied instantaneous strain. The frequency of each mode ν_i is changed by

$$\frac{\partial \nu_i}{\nu_i} = -\gamma_i^j S_j$$

where γ_i^j is the generalised Gruneisen parameter and S_j is the instantaneous strain. It is assumed that all phonons of a given direction of propagation and polarization have equal change in frequency. Then phonons of the *i*th branch and the *j*th mode undergo a change in temperature T

$$\frac{\Delta T_i}{T_0} = -\gamma_i^j S_j$$

A relaxed elastic constant is obtained after there is phonon–phonon coupling among various branches and ΔT_i relax to a common temperature change ΔT, given by

$$\frac{\Delta T}{T} = -\left\langle \gamma_i^j \right\rangle S_j$$

where $\left\langle \gamma_i^j \right\rangle$ is the average value of γ_i^j. Thermal relaxation time [22, 23] is given by the following equation

$$\tau = \tau_s = \frac{\tau_l}{2} = \frac{3K}{C_v < V >^2} \tag{4}$$

where K is the thermal conductivity, C_v is the specific heat per unit volume and $<V>$ is the Debye average velocity.

According to Mason and Batemann, SOEC and TOEC (which are measure of anharmonicity of the crystal) are related by the Gruneisen parameter γ_i^j and hence by the nonlinearity parameter D. Ultrasonic attenuation due to phonon–phonon interaction in the Akhiezer regime ($\omega\tau << 1$) is given by [22, 23]

$$\left(\frac{\alpha}{f^2}\right)_{p-p} = \frac{2\pi^2 D E_0 \tau}{3\rho V^3} \tag{5}$$

where the non-linearity coupling constant D is given by

$$D = 9\left\langle \left(\gamma_i^j\right)^2 \right\rangle - \frac{3\left\langle \gamma_i^j \right\rangle^2 C_v T}{E_0} \tag{6}$$

Here $\left\langle \left(\gamma_i^j\right)^2 \right\rangle$ and $\left\langle \gamma_i^j \right\rangle^2$ are the square average and the average square Gruneisen parameters, V is the sound wave velocity for longitudinal waves (V_L) and for shear waves (V_S), E_0 is the lattice energy density, and ρ is the density.

The Debye average velocity is given by [22, 23]

$$\frac{3}{\left(< V >\right)^3} = \frac{1}{V_L^3} + \frac{2}{V_S^3} \tag{7}$$

Ultrasonic attenuation due to thermoelastic loss is given by [22, 23]

$$\left(\frac{\alpha}{f^2}\right)_{th} = \frac{4\pi^2 \left\langle \gamma_i^j \right\rangle^2 kT}{2\rho V_L^5} \tag{8}$$

This type of attenuation occurs for the longitudinal wave only because in shear wave propagation, the volume remains unaltered and there is no heating effect, which makes this contribution nil.

Dislocation damping due to screw and edge dislocations also produces appreciable loss, due to phonon–phonon interaction. Dislocation damping is measured in terms of viscous drag coefficients. Viscous drag coefficients due to screw and edge dislocations are given by [13]

$$B_{\text{screw}} = 0.071\eta \tag{9a}$$

$$B_{\text{edge}} = \frac{0.053\eta}{\left(1-\sigma^2\right)} + \frac{0.0079}{\left(1-\sigma^2\right)\frac{\mu}{\phi}\theta} \tag{9b}$$

where

$$\theta = \varepsilon_L - \frac{4}{3}\varepsilon_S, \qquad \varepsilon_L = \frac{E_0 \Sigma_L \tau_L}{3}, \qquad \varepsilon_S = \frac{E_0 \Sigma_S \tau_S}{3}$$

$$\phi = \frac{C_{11} + 2C_{12}}{3}, \qquad \mu = \frac{C_{11} - C_{12} + C_{44}}{3}, \qquad \sigma = \frac{C_{12}}{\frac{C_{11} + C_{12}}{3}}$$

here ϕ, μ, ε, σ, θ are the bulk modulus, shear modulus, phonon viscosity, Poisson's ratio and compressional viscosity, respectively.

3. Results and discussion

The second and third order elastic constants (SOEC and TOEC) at various temperatures have been calculated by taking two basic parameters, the nearest neighbour distance using lattice constants, $r = (a/\sqrt{2})$ [24] and the hardness parameter, q (equal to 0.278 Å, 0.395 Å, 0.198 Å for US, USe and UTe, respectively). The calculated values of the second and third order elastic constants are given in Tables 1 and 2.

Table 1. C_{ij} (10^{10} N/m^2) at 300 K for uranium chalcogenides

Compound	C_{11}	C_{12}	C_{44}
US	11.84 11.9 [24] 30.5 ± 1.5 [27] 24.5 ± 1.4 [25] 30.17 ± 0.39 [26]	1.25 3.9 [24] – 0.4 ±0.7 [25] 1.32±0.73 [5]	1.47 5.5 [24] 1.72±0.05 [27] 2.1 ± 0.1 [25] 1.69 ± 0.019 [2]
USe	5.96 6.0 [24] 19.4 ± 1.4 [4]	1.24 0.4 [24] 0.0 ± 0.7 [4]	1.35 2.2 [24] 1.6 ± 0.1 [4]
UTe	14.26 0.20 [24] 14.9 ± 0.3 [4] 14.34 ± 0.36 [26]	0.51 0.002 [24] −2.0 ± 0.4 [4] –	0.92 1.90 [24] 1.13 ± 0.04 [4] 1.20 ± 0.02 [26]

Table 2. C_{ijk} (10^{10} N/m^2) at 300 K for uranium chalcogenides

Compound	C_{111}	C_{112}	C_{123}	C_{144}	C_{166}	C_{456}
US	–245.33	–4.26	0.71	2.77	–5.52	2.76
USe	–102.03	–4.97	1.66	2.34	–5.42	2.33
UTe	–400.29	–0.12	–4.06	1.78	–3.21	1.78
LiF	–6.75	–2.60	1.01	1.01	–2.80	0.96
Ref. [17]	–5.97	–2.61	0.91	0.97	–2.64	0.88

The SOEC values were compared with experimental values obtained by other authors who performed the neutron scattering experiment [4, 25], ultrasonic experiment [26, 27] and theoretical approaches [24]. There is agreement between the evaluated and the experimental values of the second order elastic constants. However, the value of C_{11} for US agrees with the theoretical value but differs appreciably from the experimental one. There is also disagreement between the theoretical and experimental values of SOEM for some of the compounds studied, but this may be because we have derived our expressions assuming that the overlap repulsion is significant only up to the level of next nearest neighbours. Furthermore, other approaches for obtaining elastic moduli can be used at one temperature only, while our approach is simple and can

be used for obtaining the temperature dependence of the elastic constants over a wide temperature range. Our approach is very simple, involves only two basic parameters; the nearest neighbour distance (r) and the hardness parameter (q). The TOEM values have not been compared due to the unavailability of data in the literature. But, in order to justify our approach for the calculation of TOEM values, we have evaluated third order elastic constants for fcc structured LiF [17]. The values which were obtained by adopting present approach are in close agreement with the available values (Table 2).

The thermal energy density, E_0, and the specific heat per unit volume, C_v, are calculated in function of the Debye temperature, θ_D (138.7 K, 138.7 K and 114.8 K for US, USe and UTe, respectively [28]) using a table [29, 30] of physical constants: this was the primary input data used to obtain the average square, square average Gruneisen parameters, non-linearity coupling constants (D_l and D_s) and ultrasonic attenuation along different crystallographic directions. The evaluated values of the nonlinearity coupling constants D_l and D_s for US, USe and UTe at 300 K are given in Table 3. It is clear from Table 3 that the values of D_l and D_s increase with temperature up to 400 K and then decrease at higher temperatures (i.e., anharmonicity of the crystal first increases and then decreases, since the nonlinearity coupling constant is the measure of anharmonicity of the crystal).

Table 3. Acoustic coupling constants (D_l and D_s) for longitudinal and shear waves along various directions of propagation for uranium chalcogenides at 300 K

Compound	<100>		<110>			<111>		
	D_l	D_s	D_l	D_s^*	D_s^{**}	D_l	D_s^+	D_s^{++}
US	64.32	0.782	55.83	2.32	146.32	1667.54	75.08	282.35
USe	37.73	1.294	33.86	8.14	85.37	406.85	43.61	72.22
UTe	153.98	0.779	137.51	6.34	356.52	8699.84	184.21	2036.79

* – polarization along [100], ** – polarization along [001], + polarization along [110], ++ polarization along [$\bar{1}$10].

Temperature variation of ultrasonic attenuation due to phonon–phonon interaction for longitudinal and shear waves viz. $(\alpha/f^2)_l$ and $(\alpha/f^2)_s$ along different crystallographic directions of propagation and polarization are shown in Figs. 1, 2. It can be seen from the figures that the temperature variation of $(\alpha/f^2)_l$ has a similar profile along all the directions of propagation for longitudinal and shear waves. $(\alpha/f^2)_l$ and $(\alpha/f^2)_s$ increase with temperature and the rate of their increase for longitudinal waves is higher compared with shear waves. This might be due to the higher rate of interaction of acoustical and thermal phonons. The values of $(\alpha/f^2)_l$ and $(\alpha/f^2)_s$ are larger along the <111> direction of propagation in comparison with the <100> and <110> direction of propagation. This may be attributed to larger anharmonicity along the <111> direction of propagation. Furthermore, as the molecular weight increases in a given chalcogenide series, $(\alpha/f^2)_{th}$ is found to increase along a given direction of propagation at a particular temperature for longitudinal (or shear) waves.

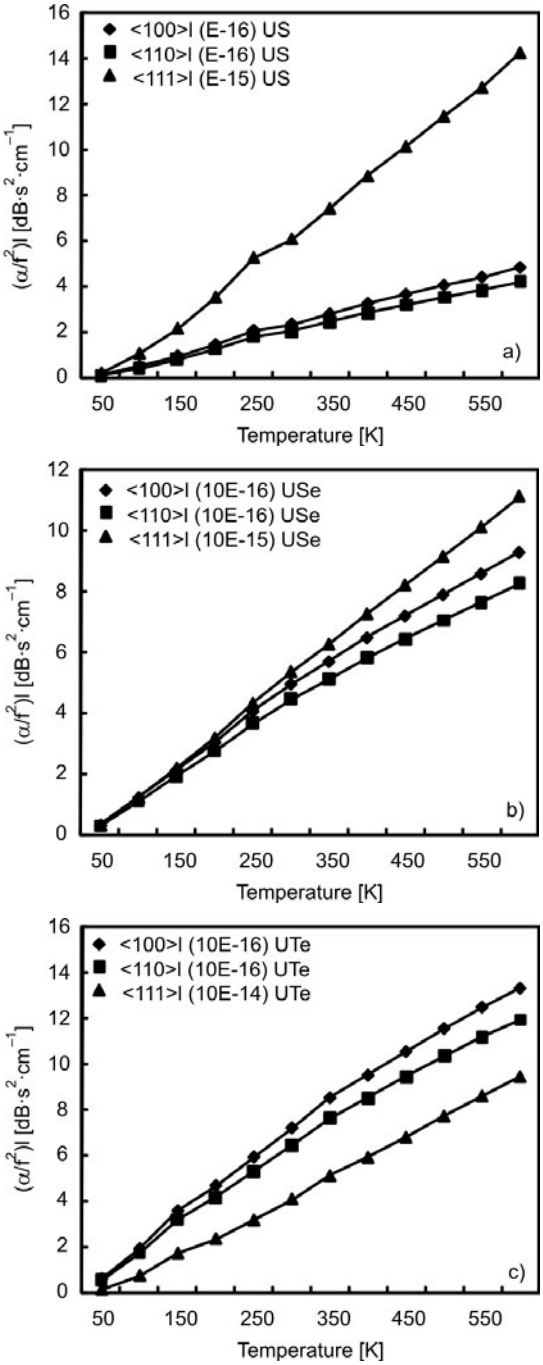

Fig. 1. Temperature dependence of ultrasonic attenuation due to phonon–phonon interaction for a longitudinal wave along various directions of propagation for: a) US, b) USe, c) UTe

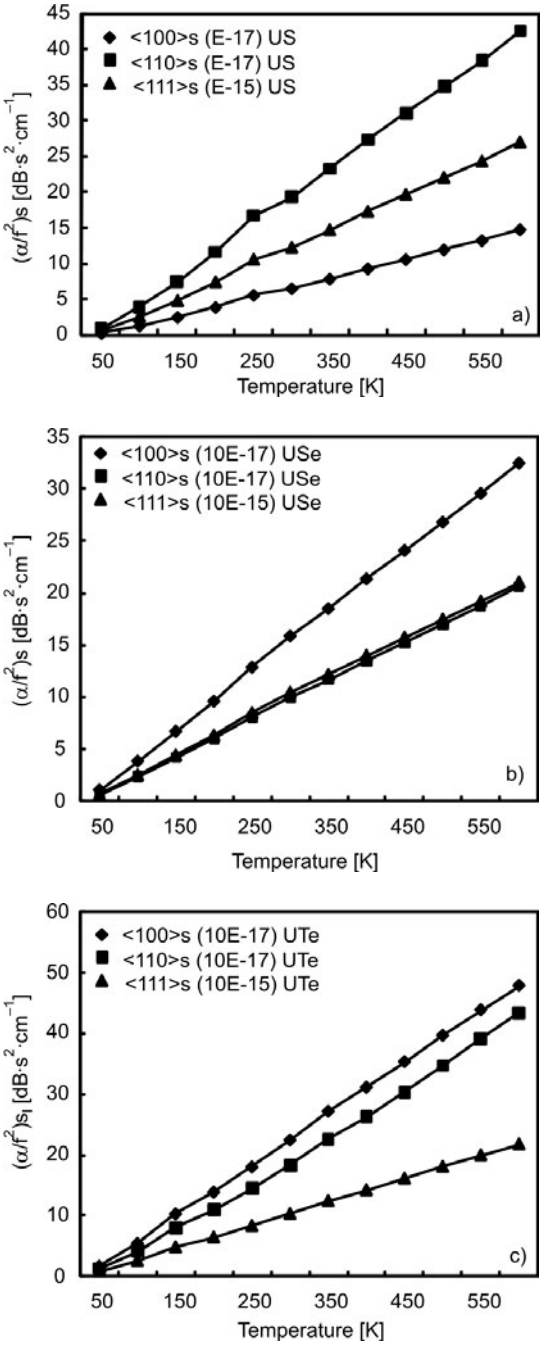

Fig. 2. Temperature dependence of the ultrasonic attenuation due to phonon–phonon interaction for a shear wave along various directions of propagation for: a) US, b) USe, c) UTe

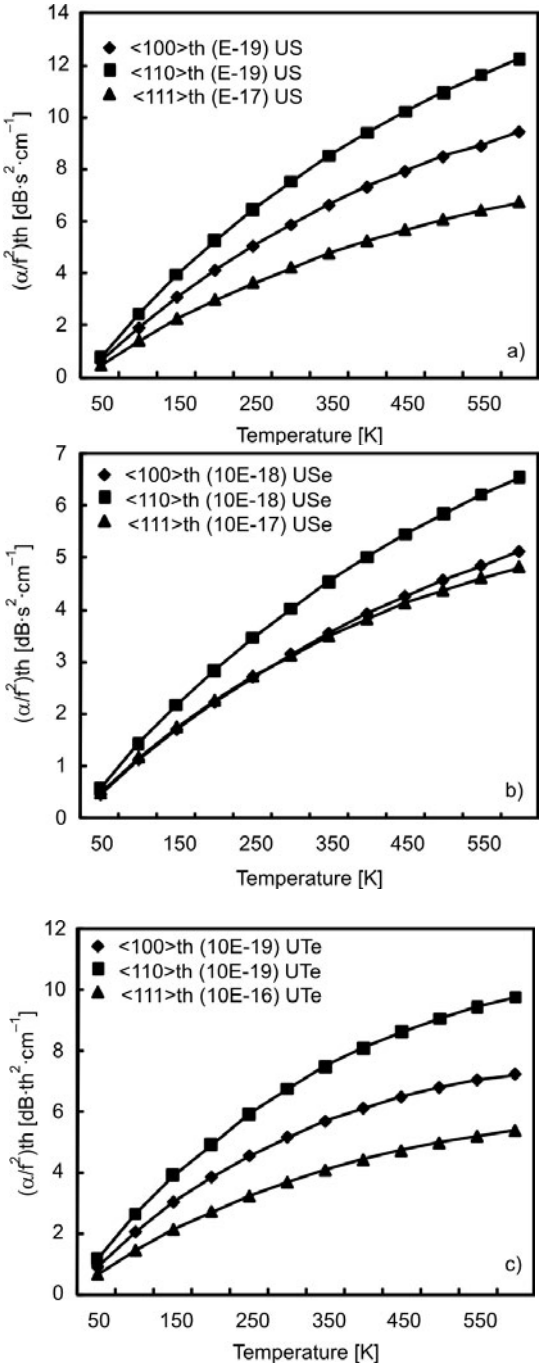

Fig. 3. Temperature dependence of the ultrasonic attenuation due to thermoelastic loss for longitudinal wave along various directions of propagation for: a) US, b) USe, c) UTe

Temperature dependences of ultrasonic attenuation due to thermoelastic loss viz. $(\alpha/f)_{th}$ along various directions are shown in Fig. 3. It can be seen that $(\alpha/f)_{th}$ also increases with temperature. It results from Figs. 1–3 it that ultrasonic attenuation over the frequency square due to thermoelastic loss $(\alpha/f)_{th}$ is of the order of 10^{-17}–10^{-19} dB·s^2·cm^{-1} and is negligible in comparison with attenuation due to phonon–phonon interaction, which is of the order of 10^{-15}–10^{-17} dB·s^2·cm^{-1}, i.e. attenuation due to thermoelastic loss is about 1% of the attenuation due to phonon–phonon interaction. Hence the total attenuation is predominantly due to ultrasonic attenuation .

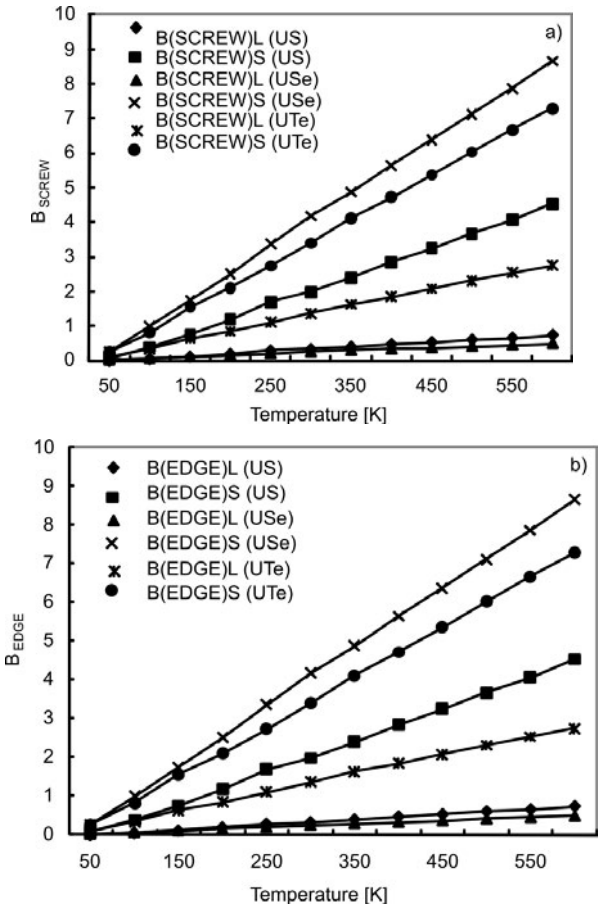

Fig. 4. Temperature dependence of the coefficient of viscosity for a longitudinal wave (cp) and shear wave (mp) due to: a) screw, b) edge dislocation along various directions of propagation

The viscous drag coefficients (B_{SCREW} and B_{EDGE}) were calculated using, Eqs. 9. The temperature dependences of viscous drag due to screw and edge dislocations for longitudinal and shear waves are shown in Figs. 4a, b, respectively. Clearly these parameters increase as the temperature increases.

Acknowledgements

One of the authors (R.K. Singh) gratefully acknowledges financial support from the University Grants Commission, New Delhi.

References

[1] OLSEN J.S., STENSTRUP S., GERWARD L., BENDICT V., SPIRLET J.C., RECTT G.D.J., Less Common. Met., 98 (1984), 291.
[2] VAN DOORN C.F., DU PLESSIS P. DE V., Magn. J. Magn. Magn. Mater., 5, (1977), 164,
[3] OLSEN J.S., GEWARD L., BENEDICT V., J. Appl. Cryst., 18 (1985), 37.
[4] JACKMAN J.A., HOLDEN T.M., BUYERS W.J.L., DU PLESSIS P. DE V., VOGT O., GEMOSSAR G., Phys. Rev. B, 33 (1986), 7144.
[5] LANDER G.H., STIFLING W.G., ROSSAT-MIGNOD J.M., HAGEN M., VOGT O., Phys. Rev. B, 41 (1990), 6899.
[6] BENEDICT U., J. Alloys Comp., 223 (1995), 216.
[7] LEGER J.M., OKI K., ROSSAT- MIGNOD J., J. Phys. C: Solid State Phys., 17 (1984). 4935.
[8] HOLDEN T.M., BUYERS W.J.L., SVENSSEN E.C., JACKMAN J.A., MURRAY A.F., VOGT O., DU PLESSIS P. DE V., J. Appl. Phys., 53 (1982), 1967.
[9] SCHOENES J., FRICK B., VOGT O., Phys. Rev B., 30 (1984), 6578.
[10] PANDEY D.K., SINGH D., YADAV R.R., Appl. Acoust., 68 (2007), 766.
[11] SINGH R.K., SINGH R.P., SINGH M.P., SRIVASTAVA P.C., J. Phys. Condens. Matter, 20 (2008), 345227.
[12] SINGH R.K., SINGH R.P., SINGH M.P., CHAURASIA S.K., Acta Phys. Polon. A, 115 (2009), 624.
[13] SINGH R.K., SINGH R.P., SINGH M.P., Physica B, 404 (2009), 95.
[14] SINGH R.K., SINGH R.P., SINGH M.P., CHAURASIA S.K., Acoust. Phys., 55 (2009), 186.
[15] SINGH R.K., SINGH R.P., SINGH M.P., Acoust. Soc. Am., Proc. Meetings on Acoustics, 4 (2008), 045006.
[16] BRUGGER K., Phys. Rev. A, 133 (1964), 1611.
[17] GHATE P.B., Phys. Rev. B, 139 (1965), A1666.
[18] LEIBFRIED G., HANN H., J. Phys., 150 (1958), 497.
[19] MORI S., HIKI Y., J. Phys. Soc. Japan, 45 (1978), 1449.
[20] AKHIEZER A., J. Phys., 1 (1939), 227.
[21] LAMBADE S.D., *The Nonlinear Elastic and Acoustic Properties of Some Solids*, Ph.D. Thesis, Nagpur University, India, 1997.
[22] SAHASRABUDHE G.G., LAMBADE S.D., J. Acoust. Soc. Am., 104 (1998).
[23] LAMBADE S.D., SAHASRABUDHE G.G., RAJAGOPALAN S., J. Phys. Chem. Solids, 57 (1996), 217.
[24] VERSHNEY D., KAURAV N., KINGE R., SINGH R.K., J. Phys.: Condens. Matter, 19 (2007), 236204.
[25] DU PLESSIS P. DE V., DE V., HOLDEN T.M., BUYERS W.J.L., JACKMAN J.A., MURRAY A.F., VAN DOORN C.F., J. Phys. C: Solid State Phys., 18 (1985), 2809.
[26] NEUENSCHWANDER J., BOPPART H., SCHOENES J., VOIT E., VOGT O., WACHTER P., *14th Journees des Actinides*, J. Schoenes (Ed.), Eidgenossiche Technische Hochschule, Zurich, 1984, 30.
[27] DU PLESSIS P. DE V., TILLWICK D.L., J. Appl. Phys., 50 (1979), 1834.
[28] DURAI S., BABU P., Bull. Matter. Sci., 28 (2005). 669.
[29] *AIP Handbook*, Academic Press, New York, 1981.
[30] CRC Data Series, CRC Press, Boca Raton, Fl, 1999.

Received 7 August 2008
Revised 12 June 2009

Materials Science-Poland, *Vol. 27*, *No. 4/1*, *2009*

Synthesis and characterization of nanoscale $Bi_2Cu_{0.1}V_{0.9}O_{5.35}$ powders by solution-based chemical methods

M. GUO[1], H. DENG[2], P. YANG[1*]

[1]Key Laboratory of Polar Materials and Devices, Department of Electronics, East China Normal University, Shanghai 200241, China

[2]Instrumental Analysis and Research Center, Institute of Materials, Shanghai University, 99 Shangda Rd, Shanghai 200444, China

Nanocrystalline $Bi_2Cu_{0.1}V_{0.9}O_{5.35}$ (BCVO) powders were synthesized by solution-based chemical methods. Materials have been characterized by the thermogravimetric analysis, X-ray diffraction, and scanning/transmission electron microscopy. The sintering temperatures to complete phase transition are above 330 °C, 320 °C and 470 °C for the primary powders obtained by the sol-gel technique, an ethylenediaminetetra acetate–citrate combustion gel route and a modified reversing titration co-precipitation method (RP), respectively, which were much lower than the 600 °C required by conventional solid state method (SS). The powders synthesized by EC with 2 wt. % of surfactant, polyethylene glycol PEG 4000 have rather a narrow size distribution, within 30–50 nm, and as the PEG 4000 content increases, they form agglomerates irregular in shapes. In RP the optimal concentration of PEG 4000 is about 5 wt. % and the average grain size of the sample is 20 nm. The modified reaction in homogeneous solutions can be controlled to produce uniform BCVO nanoparticles.

Key words: *ionic conduction; nanoscale powders; solution-based chemical methods; surfactant*

1. Introduction

$Bi_2Me_xV_{1-x}O_{5.5-3x/2}$ (BMVO) materials derived from the parent structure of ferroelectric bismuth vanadate $Bi_2VO_{5.5}$, where vanadium is partially replaced by different divalent or trivalent metal ions (Me), exhibit stable, high oxide-ion conductivity of the γ-phase at room temperature [1]. Potential applications have been developed for solid oxide fuel cells (SOFC), oxygen separation, oxygen sensing and oxidation membranes [2, 3]. The conductivity of BMVO is dependent on the characteristics of the material

*Corresponding author, e-mail: pxyang@ee.ecnu.edu.cn

[2, 4] such as particle size, morphology, purity, chemical composition, and phase, which are greatly affected by the preparation technique. The conventional way, namely diffusion-limited solid-state reaction by mixing oxide with repeatedly grinding/milling to synthesize the material, has some inherent disadvantages, including broad particle size distribution, chemical inhomogeneity, large particle size and introduction of impurities during milling/grinding, due to the high temperature required to obtain the target phase [1, 5, 6]. While the solution-based chemical methods such as sol-gel technique [7], co-precipitation [8], citrate combustion [9] and EDTA chelating [10] processes can provide homogeneously mixed reactants in atomic scale under relatively mild conditions.

On the other hand, owing to the difference in acidity of ions with different charges, the chemical reactivity of Bi^{3+} and V^{5+} source precursors is different, leading to low homogeneity of Bi–V oxide precursors. Good control over the properties of the precursor can overcome the above problem and nanocrystalline powders can thereby be obtained. The solution-based techniques show a great potential for the preparation of homogeneous mixed oxide gels.

Of all the BMVO materials, the highest conductivities have been exhibited by copper substituted bismuth vanadates $Bi_2Cu_xV_{1-x}O_{5.5-3x/2}$. It is reported that high-temperature tetragonal γ-phase is stable at room temperature for copper substitution of $0.07 \leq x \leq 0.20$ [11, 12]. The optimum conductivity is considered to be at $x = 0.1$, which corresponds to BCVO. The materials have been synthesized by conventional solid-state reaction method [11,12], which takes a long time and requires a relatively high temperature. This paper presents, for the first time, a systematic investigation into the synthesis of tetragonal nanocrystalline BCVO powders via solution-based methods, including modified sol-gel, ethylenediamine tetraacetate (EDTA)–citrate combustion gel and reversing titration precipitation. For comparison, BCVO powders were also prepared by a solid-state reaction at 600 °C. In addition, the adsorption of a surfactant such as polyethylene glycol (PEG) on the particle surface can prevent particle–particle aggregation due to steric hindrance effect [13–15], and therefore the effect of PEG on the BCVO was also investigated.

2. Experimental

$Bi(NO_3)_3 \cdot 5H_2O$ (AR), $Cu(NO_3)_3 \cdot 3H_2O$ (AR), NH_4VO_3 (AR), HNO_3 (65% w/w), ammonia, tetramethylammonium hydroxide (TMAH, 25% w/w aqueous solution, electronic grade), EDTA, polyethylene glycol PEG 4000 (average molecular weight equal to 4000) were used as supplied without further purification.

Firstly, a modified sol-gel technique (SG) was performed to synthesize BCVO. 20 mmol of $Bi(NO_3)_3 \cdot 5H_2O$ was dissolved in 10 cm^3 of 4 M HNO_3, and then 1 mmol of $Cu(NO_3)_3 \cdot 3H_2O$ was added into the solution. 9 mmol of NH_4VO_3 was dissolved into 20 cm^3 of 25% (w/w) aqueous solution of TMAH, which is a strong organic alkali,

instead of the conventional inorganic alkali. These two solutions were mixed and continuously stirred at room temperature for 0.5 h. The solution was quantitatively transferred to form 0.2 M green sol, and then the gel was formed overnight. The gel was dried completely at 80 °C and then milled. The powders were sintered in air at the given temperature in the range 300–600 °C for 4 h.

Secondly, the material was synthesized by the EDTA–citrate combustion gel method (EC). The same stoichiometric amounts of $Bi(NO_3)_3{\cdot}5H_2O$, $Cu(NO_3)_3{\cdot}3H_2O$ and NH_4VO_3 as above were dissolved in EDTA–$NH_3{\cdot}H_2O$ aqueous solution with continuously stirring at 60 °C, and then a proper amount of citric acid was added. 0 wt. %, 2 wt. %, 5 wt. % and 10 wt. % of PEG 4000 was added to the solutions. The solutions were concentrated at 80 °C to produce gels. The dark yellow fluffy products were obtained after the evaporation of water and then they were crushed. The samples were sintered in air at a given temperature in the range 300–600 °C for 4 h.

Thirdly, the material was synthesized by a modified reversing titration co-precipitation method (RP). $Bi(NO_3)_3{\cdot}5H_2O$ and $Cu(NO_3)_3{\cdot}3H_2O$ in the same molar ratio of 20:1 as above were dissolved in dilute nitric acid with different amounts of surfactant PEG 4000 (0, 2, 5 and 10 wt. %), NH_4VO_3 in stoichiometric amount was dissolved in 500 cm^3 of 1.26 M solution of ammonia, and then the mixed solution of $Bi(NO_3)_3$ and $Cu(NO_3)_3$ was added into NH_4VO_3 solution dropwise with mild stirring at 60 °C. The obtained precipitate was aged at 60 °C for 2 h, and then was washed with deionized water and subsequently with ethanol. The filtered samples were allowed to dry at 80 °C to get yellow material. The primary material was sintered in air at a given temperature in the range 300–600 °C for 4 h.

Finally, the material was synthesized by a conventional solid-state reaction method (SS) as comparison. A stoichiometric mixture of $Bi(NO_3)_3{\cdot}5H_2O$, $Cu(NO_3)_3{\cdot}3H_2O$ and NH_4VO_3 was milled with a mortar, and then dried at 80 °C. The mixture was sintered at 600 °C for 4 h.

Thermogravimetric analysis and differential thermal analysis (TG/DTA) of the powders were performed on a TGA 851e/SF/1100 thermogravimeter at the scan rate of 10 °C/min in air from ambient temperature to 850 °C. X-ray diffraction (XRD) analysis was carried out using a Rigaku D/max2200 diffractometer. Scanning electron microscopy (SEM) analysis was performed using a JEOL JSM-6700 scanning electron microscope. Transmission electron microscopy (TEM) analysis was performed using a JEOL-2000FX transmission electron microscope.

3. Results and discussion

The results of TGA analyses on the as-synthesized dry gels by SG are shown in Fig. 1. In the temperature range 25–120 °C, the mass of the sample decreased, which was consistent with the loss of water. The persistence of water/OH groups associated with oxide materials at high temperatures has been noted in another study [16]. Loss of water is attributed primarily to physisorbed water until approximately 120 °C.

Above this temperature, the total weight loss, of about 38 %, in the temperature range of 120–330 °C resulted from condensation of the surface hydroxyl group or evaporation of chemisorbed water and decomposition of the inorganic/organic composites such as the nitrates, the residual NH_4^+ and organic residues. There was a significant large exothermic peak centred at 330 °C in the DTA curve, corresponding the transition from α to γ phase [17]. In addition, there was no significant peak beyond 330 °C, indicating that the sintering temperature above 330 °C is possibly adequate for the as-synthesized dry gels to complete phase transition.

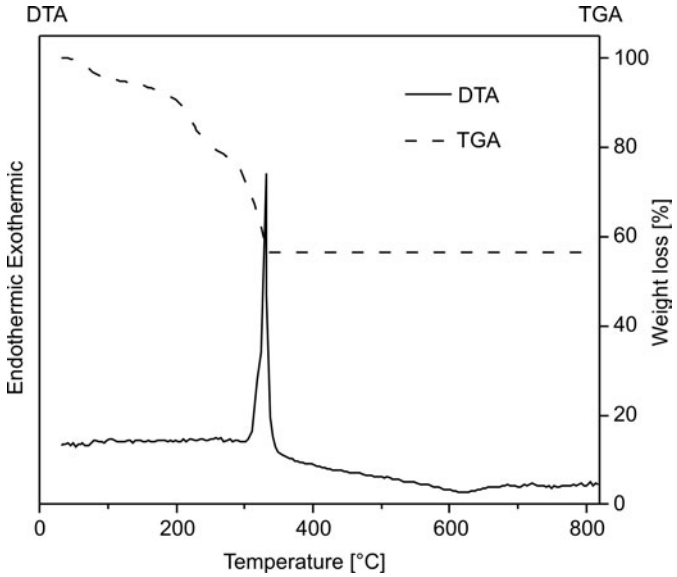

Fig. 1. TGA/DTA patterns of the as-synthesized dry gels prepared by SG

The XRD patterns of the samples obtained by SG after sintering at 300–600 °C for 4 h are shown in Fig. 2a. Phase transition is dependent on the sintering temperature. Tetragonal γ-phase of the parent compound $Bi_2VO_{5.5}$ was observed, indicating that it was stable at room temperature by the partial substitution of Cu for V ions [6]. In the sol-gel process, as evidenced from DTA/TGA patterns in Fig. 1, the crystallization of BCVO gel precursor started at 300 °C as seen in Fig. 2a. But at 300 °C, the phase of $BiVO_4$ also existed, as marked by a cross in Fig. 2a, and it vanished at 400 °C. The peaks of γ-phase $Bi_2VO_{5.5}$ peaks as marked by filled diamonds in Fig. 2a, which were sharp and distinct, indicate a higher degree of crystallinity of the sample. For comparison, the XRD pattern of the sample prepared by SS is shown in Fig. 2b. Some traces of impurity corresponding to $BiVO_4$ are observed after the sample was sintered at 600 °C, and is consistent with previous papers [6, 18]. This indicates that the sintering temperature in the SG process is 300 °C lower than that in conventional solid state methods, where the presence of BCVO phase was observed above 600 °C. We think

that the exothermic decomposition of the gel might provide enough heat to the crystallization of BCVO, and thus reduces the sintering temperature.

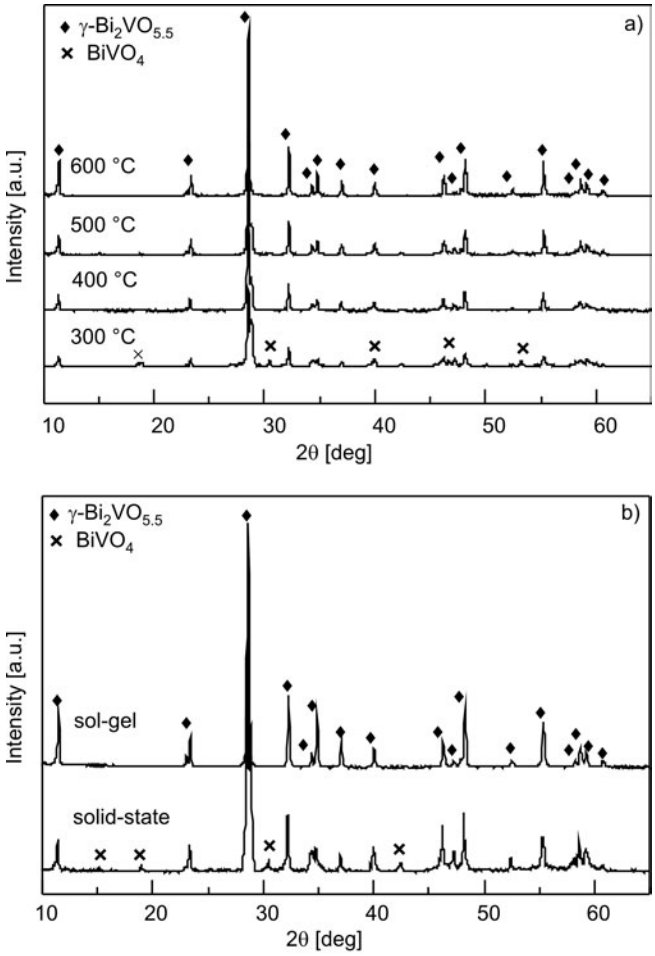

Fig. 2. XRD patterns of the samples prepared by SG after heating at 300–600 °C for 4 h (a) and XRD patterns of the samples prepared by SG and by SS after heating at 600 °C for 4 h (b)

On the other hand, the peak intensities in Fig. 2a increased with the sintering temperature. The average crystallite size of the BCVO powders after heating at 400 °C was about 50 nm at (103) reflection estimated by the Debye–Scherrer formula [17]. The calculated lattice parameters a and c, and cell volume V in powders were 0.3929 nm, 1.5487 nm and 0.23910 nm^3, respectively. These values are consistent with standard values of lattice parameters a = 0.3935 nm, c = 1.5476 nm, and V = 0.23968 nm^3.

The primary powders prepared by SG were brown-yellow, while the calcined powders were bright yellow, consistent with the colour of BCVO. Figure 3a shows the SEM image of the powders after heating at 600 °C.

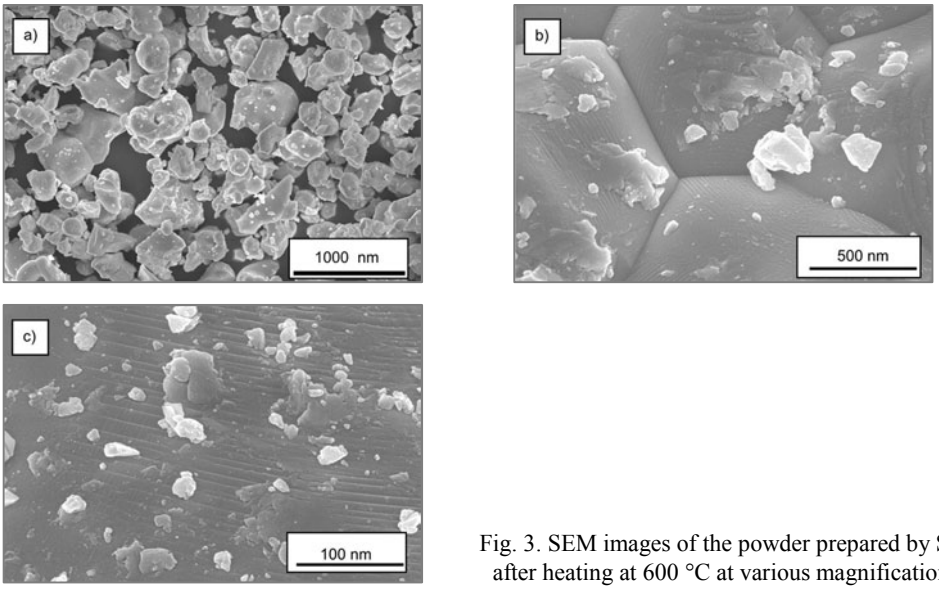

Fig. 3. SEM images of the powder prepared by SG after heating at 600 °C at various magnifications

The particles exhibit a range of sizes and the smallest one was about 200 nm. While the average crystallite size estimated from the XRD analysis of the material was about 50 nm, the actual particle sizes are significantly larger. The extent of aggregation of these particles requires further investigation. The particles have a hexagon-like appearance at the edges observed from the SEM image at high magnification in Fig. 3b. Furthermore, there is a small quantity of small particles adhering to the surface of the large grains in Fig. 3b, indicating the inhomogeneous distribution and the agglomeration of the small particles in the sample. At higher magnification, the terrace-like appearance in Fig. 3c is a possible evidence for a layered structure of the material.

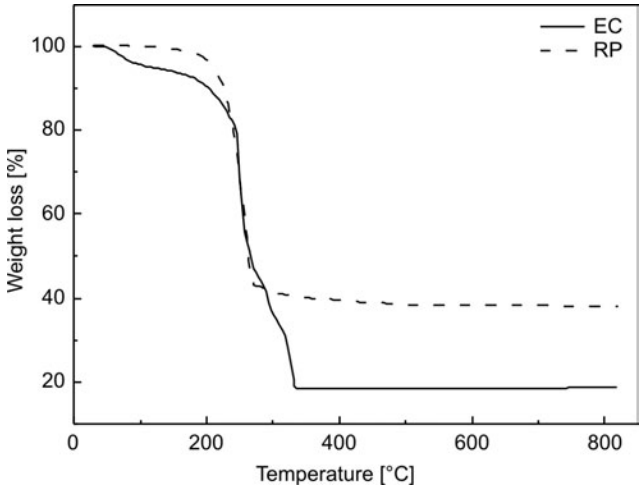

Fig. 4. TGA curves of the samples prepared by EC and RP with 5 wt. % of PEG 4000

The effect of surfactants was explored in order to reduce the particle–particle aggregation and thus reduce the grain size. EC and RP synthesis routes with various amounts of PEG 4000 were investigated. TGA analysis was performed on the primary products prepared by EC and RP with 5 wt. % of PEG 4000, and the results are shown in Fig. 4. Similar to that of the samples prepared by SG (Fig. 1), the weight loss in the temperature range 25–200 °C is attributed to loss of water. Significant weight losses between 200 and 320 °C for the sample fabricated by EC and between 200 and 270 °C for the sample synthesized by RP mainly result from the decomposition of inorganic/organic residues, as well as the decomposition of the surfactant. The total weight loss of the sample obtained by RP was lower than that by EC, indicating a lower content of organic molecules in primary powders obtained by RP. No weight loss occurred for the samples obtained by EC over 320 °C, suggesting that surfactant in the samples could be completely removed at this temperature and the sintering temperature above it is possibly adequate for the sample to complete phase transition. A slight weight loss of the sample made by RP in the temperature range 270–470 °C will be discussed later, together with the XRD results. The temperature of complete phase transition of BCVO fabricated by these three solution-based routes is significantly lower than that of the solid state reaction [19].

The XRD patterns of primary powders added with 0 wt. %, 2 wt. %, 5 wt. % and 10 wt. % of PEG 4000 are shown in Fig. 5. The powders were partially crystalline and the identification of peaks was very difficult due to the doublets of monoclinic and tetragonal $BiVO_4$. In addition, the crystallization was better for the sample with 2 wt. % PEG 4000 for EC and 5 wt. % PEG 4000 for RP compared with the samples with other amounts of PEG 4000 (Fig. 5). However, in order to determine the optimum content of PEG 4000, it is still necessary to examine, via electron microscope images, its effect on dispersions.

The primary samples prepared by EC with 2 wt. % of PEG 4000 were sintered in the temperature range 300–600 °C and their XRD analysis data are shown in Fig. 6. Tetragonal $Bi_2VO_{5.5}$, as marked by filled diamonds and the intermediate phase, $BiVO_4$, as marked by crosses in Fig. 6, were detected for the sample after heating at 300 °C, while the intermediate phase completely disappeared and only tetragonal $Bi_2VO_{5.5}$ was observed for the sample after heating at 400 °C. This is consistent with TGA analysis as shown in Fig. 4, where the mass of the samples was stable above 320 °C in EC. After heating at 500 °C, well-crystallized γ-phase was formed for the samples. When the sintering temperature increased to 600 °C, the peaks became sharper.

The primary samples prepared by RP with 5 wt. % of PEG 4000 were also heated in the temperature range 300–600 °C and the results of their XRD analyses are shown in Fig. 7. Two phases, tetragonal $Bi_2VO_{5.5}$ and the intermediate phase $BiVO_4$, were also observed for the sample after heating at 300 °C and 400 °C, while the intermediate phase completely vanished and only tetragonal $Bi_2VO_{5.5}$ existed at 500 °C. The change of phases from $BiVO_4$ to $Bi_2VO_{5.5}$ (i.e., $BiV_{0.5}O_{2.75}$) causes the

mass loss of the sample due to the evaporation of oxygen in order to maintain the electric charge neutrality, which might explain a slight weight loss seen in the TGA pattern in the temperature range of 270–470 °C (Fig. 4). Compared with XRD analysis of the sample obtained by EC, the required sintering temperature for phase transition increased for the sample obtained by RP, which is consistent with the TGA analysis shown in Fig. 4, where the mass of samples was stable above 320 °C for the EC samples, and above 470 °C for the RP samples. Similarly, peaks became sharper when the sintering temperature increased to 600 °C.

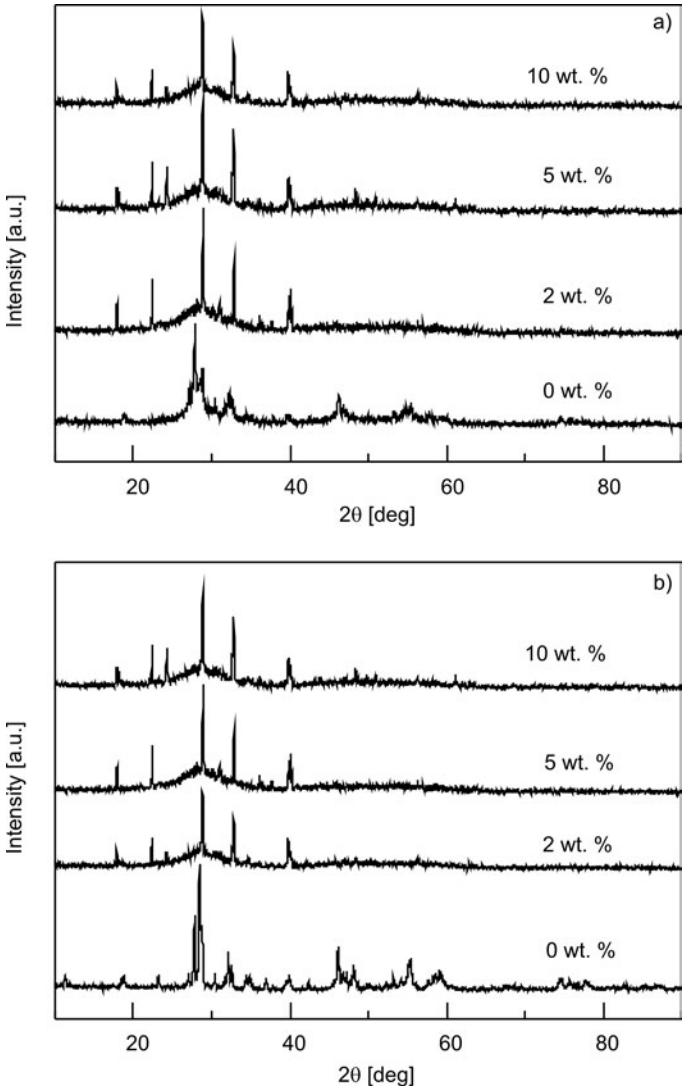

Fig. 5. XRD patterns of the samples with various contents of PEG 4000 prepared by EC (a) and by RP (b)

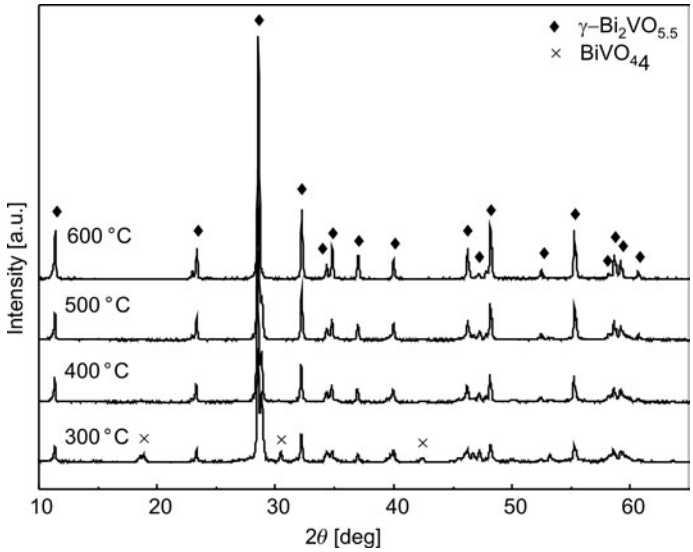

Fig. 6. XRD patterns of the samples prepared by EC with 2 wt. % of PEG 4000 after heating at 300–600 °C for 4 h

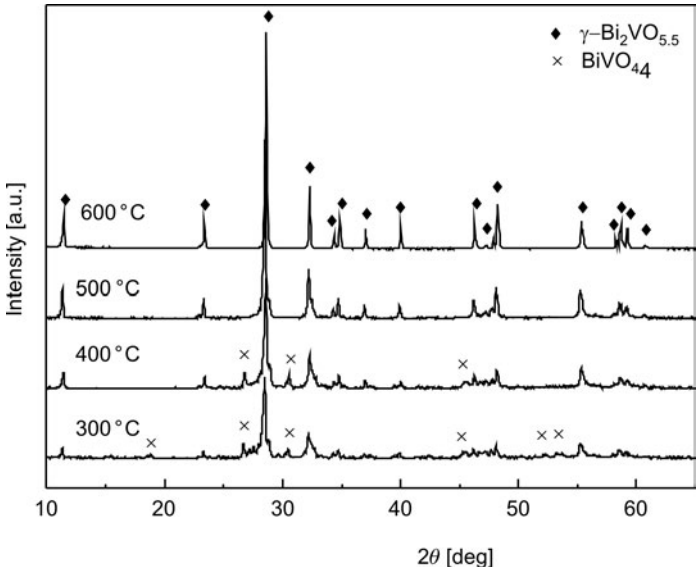

Fig. 7. XRD patterns of the samples prepared by RP with 5 wt. % of PEG 4000 after heating at 300–600 °C for 4 h

In order to investigate the morphology and the particle sizes of the samples with various amounts of PEG 4000 after heating at 500 °C prepared by EC and RP, TEM analyses were performed (Figs. 8 and 9). The particles with 2 wt. % of PEG 4000 have rather narrow size distribution with a slight accumulation phenomenon, and they are spherical. Their sizes are in the range of 30–50 nm (Fig. 8b). The highly agglomerated

products with 5 and 10 wt. % of PEG 4000 were dominated by nanoparticles with irregular shapes (Fig. 8c, d). This suggests that BCVO grains are less uniform and the sizes become larger when the concentration of PEG 4000 increases. The formation of aggregates comprising primary spherical nanoparticles could clearly be observed.

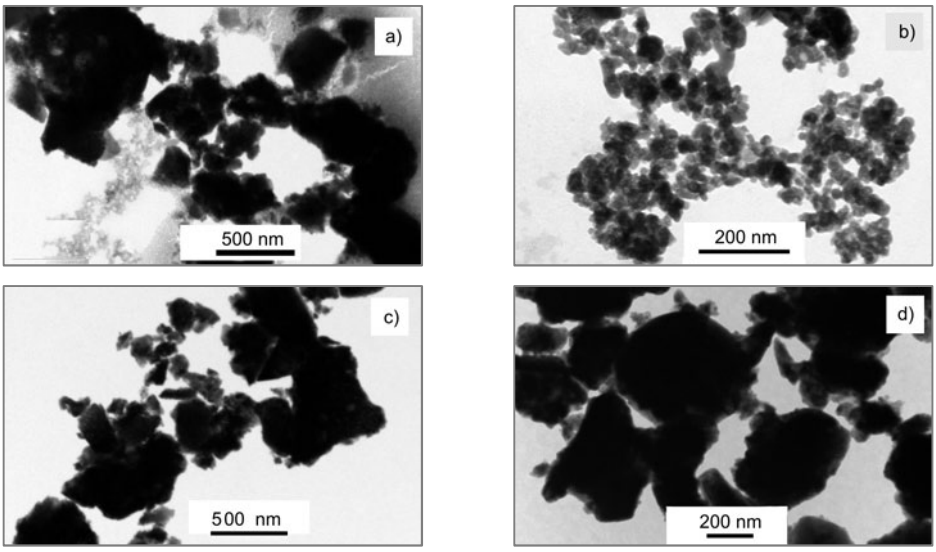

Fig. 8. TEM images of the powder prepared by EC after heating at 500 °C with various amounts of PEG 4000: a) 0 wt. %, b) 2 wt. %, c) 5 wt. %, d) 10 wt. %

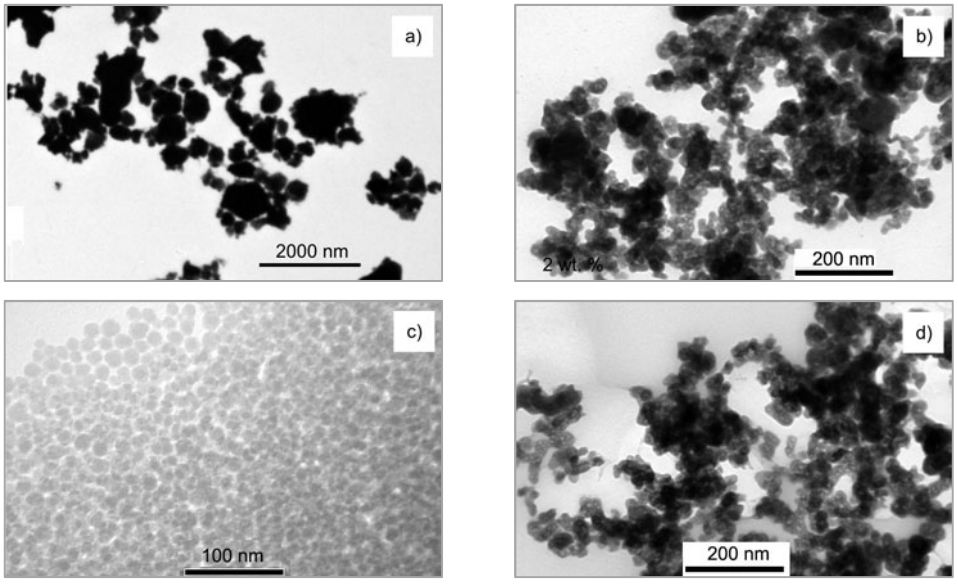

Fig. 9. TEM images of the powder prepared by RP after heating at 500 °C with various amounts of PEG 4000: a) 0 wt. %, b) 2 wt. %, c) 5 wt. %, d) 10 wt. %

However, the samples with 2, 5 and 10 wt. % of PEG 4000 prepared by RP at 500 °C were composed of uniform spherical nanoparticles, as shown in Fig. 9b–d, suggesting that the powders made by RP are much smaller than those made by EC. Adsorption of citrate species, in the EC case, on preferential crystal planes may easily lead to aggregation. The optimum concentration of PEG 4000 is about 5 wt. % in RP and the average grain size of the sample was 20 nm. Figures 9b, d show that the particles aggregated into some flocks, which could be attributed to the shortage and excess of PEG 4000 to coat the precursor with the increase of the nuclei when 2 and 10 wt. % of PEG 4000, respectively, were added. We also note that the morphology and the particle size of the samples with PEG 4000 prepared by SG have no obvious change compared with the primary pure material.

Monodispersed particles are favourable to be formed in solution when the rate of nucleation is much higher than that of the particle growth. The particles of the samples fabricated by SG have no interaction of steric hindrance without surfactant and tend to agglomerate, and therefore the final particles have large grain size, as shown in Fig. 3. In the EC and RP cases, PEG may be adsorbed preferably on the sol particles and keeps them separated in the solution with a polymeric long chain molecule to provide steric hindrance, slowing down the diffusion speed of solutes to the crystal surface of the as-formed nuclei, which ensure that the diffusion process becomes the rate-control step during the crystal growth. The modified reaction in homogeneous solutions can be controlled to produce the most highly uniform BCVO nanoparticles.

4. Conclusions

Nanocrystalline BCVO powders were prepared by the solution-based chemical methods. The sintering temperatures to complete phase transition are above 330 °C, 320 °C and 470 °C for the primary powders made by SG, EC and RP, respectively. Samples prepared by SG, EC and RP contain $BiVO_4$ and γ-$Bi_2VO_{5.5}$ after heating at 300–400 °C, and only γ-$Bi_2VO_{5.5}$ exists above 400–500 °C. The effects of surfactant PEG 4000 on the microstructures of the powders depend on the synthesis routes. The particles in powders obtained by EC with 2 wt. % of PEG 4000 have rather a narrow size distribution, within 30–50 nm, irregular shapes and, as the PEG 4000 content increases, they become more and more highly agglomerated. However, the optimum concentration of PEG 4000 is about 5 wt. % in RP and the average grain size of the sample is 20 nm. A shortage or excess of PEG 4000 can cause the particles to aggregate. In the EC and RP prepared samples, the diffusion process becomes the rate-control step during the crystal growth due to PEG slowing down the diffusion speed of solutes to the crystal surface of the as-formed nuclei. Uniform BCVO nanoparticles can be obtained by controlling the modified reaction in homogeneous solutions.

Acknowledgement

This work was supported by the National Natural Science Foundation of China (60677022), Science Foundation (Research Fund) for Excellent Youth Scholars of Shanghai Municipal Education Commission,

the Key Basic Research Program of Science and Technology Commission of Shanghai Municipality (07JC14018), the State Key Basic Research Program of China (2007CB924902), the Shanghai Leading Academic Discipline Project (B411) and the Ph.D Program Scholarship Fund of ECNU2008 (Project No. 20080051).

References

[1] LAZURE S., VERNOCHET C., VANNIER R.N., NOWOGROCKI G., MAIRESSE G., Solid State Ionics, 90 (1996), 117.
[2] STEIL M.C., FOULETIER J., KLEITZ M., LABRUNE P., J. Eur. Ceram. Soc., 19 (1999), 815.
[3] GOODENOUGH J.B., Nature, 404 (2000), 821.
[4] PRASAD K.V.R., VARMA K.B.R., J. Mater. Sci., 29 (1994), 2691.
[5] EVANS I.R., TAO S.W., IRVINE J.T.S., HOWARD J.A.K., Chem. Mater., 14 (2002), 3700.
[6] CHO H., SAKAI G., SHIMANOE K., Sens. Actuators B, 108 (2005), 335.
[7] PELL J.W., YING J.Y., LOYE H.C., Mater. Lett., 25 (1995), 117.
[8] BHATTACHARYA A.K., MALLICK K.K., THOMAS P.A., Solid State Commun., 91(1994), 357.
[9] ALIFANTI M., BAPS B., BLANGENOIS N., NAUD J., GRANGE P., DELMON B., Chem. Mater., 15 (2003), 395.
[10] WULLENS H., LEROY D., DEVILLERS M., Int. J. Inorg. Mater., 3 (2001), 309.
[11] ABRAHAM F., BOIVIN J.C., MAIRESSE G., NOWOGROCKI G., Solid State Ionics, 40–41 (1990), 934.
[12] ANNE M., BACMANN M., PERNOT E., ABRAHAM F., MAIRESSE G., STROBEL P., Physica B, 180–181 (1992), 621.
[13] CHEN Z., YAN Y., Phys. B, 392 (2007), 1.
[14] WANG X., WANG M., SONG H., DING B., Mater. Lett., 60 (2006), 2261.
[15] ABDULLAH M., OKUYAMA K., LENGGORO I.W., TAYA S., J. Non-Cryst. Solid., 351 (2005), 697.
[16] TOLEDO-ANTONIO J.A., GUTIÉRREZ-BAEZ R., SEBASTIAN P.J., VÁZQUEZ A.J., Solid State Chem., 174 (2003), 241.
[17] NIMAT R.K., BETTY C.A., PAWAR S.H., Appl. Surface Sci., 253 (2006), 2702.
[18] PAYDAR M.H., HADIAN A.M., SHIAMNOE K., YAMAZOE N., J. Eur. Ceram. Soc., 21 (2001), 1825.
[19] YAREMCHENKO A.A., AVDEEV M.V., KHARTON V., KOVALEVSKY A.Y., NAUMOVICH E.N., MARQUES F.M.B., Mater. Chem. Phys., 77 (2002), 552.

Received 22 August 2008
Revised 8 March 2009

Materials Science-Poland, *Vol. 27*, *No. 4/1*, *2009*

Synthesis of nanocrystalline rutile-phase titania at low temperatures

J. G. SANTOS[1], T. OGASAWARA[2], R. A. CORRÊA[1*]

[1]Instituto de Engenharia Nuclear IEN/CNEN Caixa Postal 68505, Cidade Universitária, Rio de Janeiro RJ - CEP: 21941-972, Brasil

[2]COPPE/PEMM, Universidade Federal do Rio de Janeiro, Brasil

Anatase and rutile are the predominant phases in titanium dioxide. In many cases, rutile stable phase is the desired product material, but at low temperatures methods of synthesis (aqueous route) produce metastable anatase as a major product that reverts to rutile only when heated up to 1000 °C. Calcination for obtaining rutile phase is the greatest energy demanding step for titanium dioxide production by the sulphate process, and is responsible for almost 60% of total energy consumption. In this work, an innovative technique involving a sonication pre-treatment in acid medium was developed to change particle reactivity and accelerate the anatase-to-rutile transformation. Scanning electron micrographs and surface area measurements confirmed the alteration in texture and porosity of the powders. Results indicate that it is possible to obtain 100% of rutile phase at temperatures as low as 430 °C.

Key words: *oxides; sonication; X-ray diffraction; transition temperature*

1. Introduction

Titanium dioxide (titania) is the most widely used white pigment in the world. It has no toxicity and is chemically stable, being used mainly to achieve or improve certain properties of commercial paints. It is also used in other industrial applications like filters, catalyst supports, ceramics, paper, food, cosmetics, or fibre manufacturing. Titania exists in three fundamental crystalline phases: tetragonal rutile, tetragonal anatase and orthorhombic brookite, but the latter is not commercially produced. Each phase shows different physical properties, such as refraction, chemical or photochemical reactivity, which allow its use in particular applications usually requiring a specific particle size.

*Corresponding author, e-mail: racorrea@ien.gov.br

Several works about the anatase–rutile transition, emphasizing the temperature of the process, have been discussed [1–5]. This transformation consists in changing from a metastable to a stable phase and occurs without a well-defined temperature, as in the case of reversible transformations in equilibrium processes. This phase transformation temperature can vary from 400 to 1200 °C, being influenced by many factors such as impurities, the method employed, the atmosphere in which the transformation occurs, unreliable stoichiometry, particle size etc. [4].

Rutile is thermodynamically stable at room temperature while anatase, for kinetic reasons, remains essentially metastable. Anatase–rutile transition is very slow at room temperature, being insufficiently useful for industrial purposes. Macroscopic change from anatase to rutile occurs at appreciable rates at temperatures higher than 800 °C [6, 7]. Nanometric particles of anatase enable processes to occur at appreciable rates at temperatures higher than 400 °C [1, 8, 9].

Reports on anatase–rutile transition, with emphasis on the temperature of the transformation process, are mostly found in patent texts [10, 11]. They provide the reader with information concerning the use of seeds, conditioners or promoters of the anatase–rutile transformation used to control calcination and to reduce the temperature of the process. Other works, using inorganic precursors, indicate the beginning of the anatase–rutile transition at 600 °C by addition transition promoters, conditioners and seeds before or during calcination [12, 13] and this temperature is further decreased to 400 °C when an alkoxide is used as a precursor [14]. Commercial production of TiO_2 pigment by sulphate process or derivatives, requires higher temperatures, due to the technical requirements of achieving the crystalline transformation, namely the solid state diffusion during calcination. Thus, anatase–rutile transition is influenced by the synthesis chosen to fabricate the amorphous precursor, and by impurities, addition of stabilizers, morphology and atmosphere of the system, and has no established temperature [2]. Nevertheless, attempts to reduce this temperature are important because high temperatures of calcination generate undesirable growth of primary particles that turns white titanium dioxide pigment slightly yellow, and promotes the formation of hard agglomerations, instead of the small particles that are necessary to improve pigment quality.

The objective of this work is to develop a process to obtain rutile titanium dioxide by calcination at low temperatures of a previously sonicated material. The role of sonication is to increase the number of defects on the surface of the powder in order to improve the kinetics and diffusion processes related to the anatase–rutile transitions.

2. Experimental

Hydrothermal treatment and sonication experiments were performed on hydrated TiO_2. This compound was obtained hydrometallurgically, by leaching an ilmenite solution through several solvent extraction stages, using di(2-ethylhexyl)phosphoric acid (DEHPA) as an agent to extract Ti^{4+} ions selectively. Titanium was re-extracted

from organic phase with ammonium fluoride yielding a titanium fluoride solution, which was precipitated with ammonium hydroxide at room temperature and pH ranging from 8 to 10, filtered under vacuum, suspended and reduced to pulp, and finally washed to remove fluorine traces. Separation and purification of titanium from ilmenite through conventional processes yields products of limited purity. Liquid–liquid extraction processes allow the attainment of products of elevated purity and minimize generation of liquid and solid rejects. As a result, all these studies are considered as pioneering efforts, due to the innovative use of hydrated TiO_2 as precursor.

Three types of samples of hydrated titanium dioxide were used in the experiments performed in this work:

Original powder 01 (OP1) – hydrated TiO_2 slowly precipitated with ammonium hydroxide.

Original powder 02 (OP2) – hydrated TiO_2 quickly precipitated with ammonium hydroxide. This powder was used only in adsorption experiments for determination of the Brunauer–Emmet–Teller (BET) parameters.

Hydrated TiO_2 powder quickly precipitated after addition of ammonium hydroxide to titanium sulphate solution.

The precipitated titanium hydroxide was calcined at 600, 700, 800, 940 and 970 °C for 3 h and at 980 °C for 4 h to determine the exact temperature of the anatase–rutile transformation. The same powder was also subjected to a hydrothermal treatment in the microwave system of Provecto Analitica – DGT 100 Plus Model. The influence of various solvents on the crystallization of TiO_2 and on the kinetics of anatase–rutile transition was also investigated.

Suspensions of amorphous TiO_2 were also submitted to high power sonication in acidic medium (HCl or HNO_3) for various durations and various acid concentrations (0.1 to 1.0 M). Sonications were performed in an ultrasonic bath Thornton – INPEC Eletronica S.A. 12D Model (25 kHz, 900 W).

The titania was analyzed by the X-ray diffraction (XRD) techniques to observe the progression with time of the anatase–rutile transformation. Diffraction patterns were obtained with a Rigaku model Miniflex diffractometer using CuK_α radiation (40 kV, 40 mA) and a graphite monochromator.

BET specific area measurements were performed with Micromeritics GEMINI 2375 equipment. Scanning electronic microscopy (SEM) for morphological and particle size analysis was performed with a Zeiss DMS 950 model using electron retro scattering.

3. Results and discussion

Several calcination experiments were performed in order to determine the anatase–rutile transition temperatures by analysis of the XRD of the samples obtained. Figure 1 shows the XRD patterns obtained for the anatase phase.

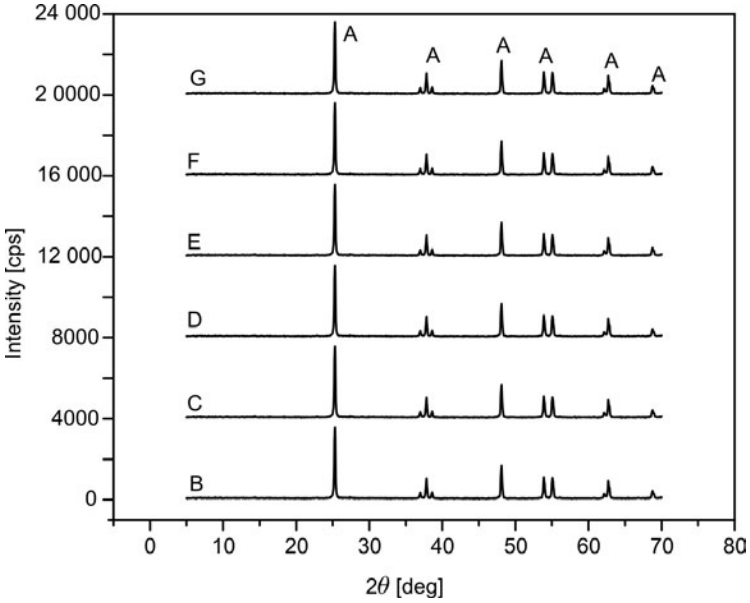

Fig. 1. XRD patterns of anatase (A). Calcinations
at 600 (B), 700 (C), 800 (D), 870 (E), 940 (F), and (G) 970 °C

XRD patterns for calcinations at 980 °C and for residence times ranging from 30 min to 4 h are shown in Fig. 2.

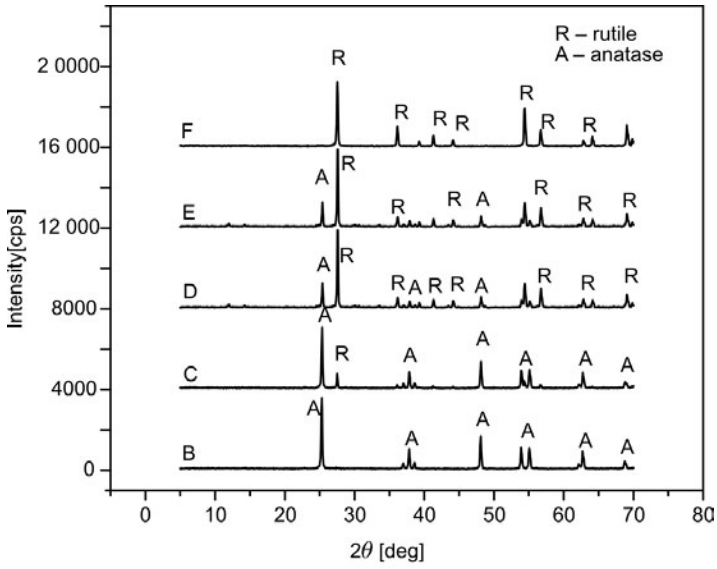

Fig. 2. XRD patterns of TiO_2. Calcinations
at 980 °C, 0.5 h (B), 1 h (C), 2 h (D), 3 h (F) and 4 h (G)

The hydroxide was also subjected to hydrothermal treatment in a microwave oven to investigate the effects of this type of synthesis on the kinetics of the anatase–rutile transformation. Water was used as a solvent.

Figure 3 shows the XRD patterns of the sample subjected to a hydrothermal synthesis in a microwave field, using water as solvent, and calcined to verify if the hydrothermal treatment would allow the formation of rutile in temperatures below those usually required by the anatase–rutile transformation. Although the diagrams indicate that this treatment can lead to increased reactivity, the transformation of anatase to rutile at low temperatures was not observed.

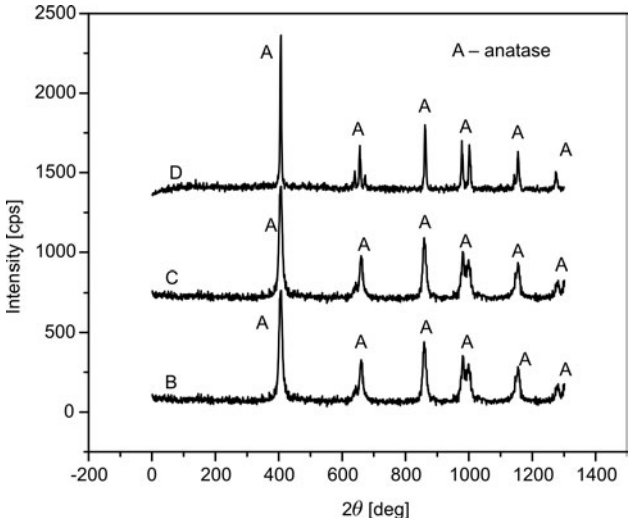

Fig. 3. XRD pattern. Hydrothermal synthesis of hydrated TiO_2 in microwaves in water; no calcinations (B), calcinations at 800 °C (C) and 960 °C (D)

The behaviour of the sample subjected to a hydrothermal synthesis using 1 M HCl as a solvent, instead of water, is shown in Fig. 4. The XRD patterns show that the powders became slightly more reactive than when treated in water, but not reactive enough to advance significantly the anatase conversion to rutile or even any important observable change in the transition phenomena.

Hydrothermal synthesis was also performed using precipitation of titanium fluoride with urea followed by hydrolysis of the latter, which provides OH^- ions during precipitation. The XRD patterns in Fig. 5 show the complete conversion of the product to rutile at 960 °C what indicates an increase in the rate of the transformation anatase –rutile. This observed increase, however, is not significant since the calcined material maintained an anatase structure both at 800 and at 900 °C.

The variation of the specific surface area BET with the calcination temperature is shown in Fig. 6 for the two main powders used in this research, labelled powder 1 and powder 2, respectively. It can be seen that the specific surface area of the original powder 02, which was quickly precipitated, reached larger values compared with

those for OP1. A severe decrease in the BET values is observed with the increase in the calcination temperature. At rutile conversion, the specific surface areas fall significantly, reaching values below 1m²/g.

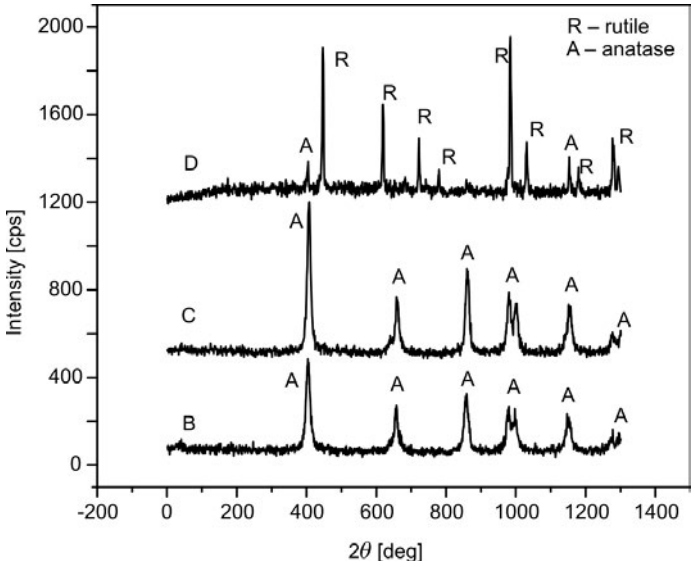

Fig. 4. XRD patterns. Hydrothermal synthesis in microwaves in 1 M HCl; no calcinations (B), calcinations at 800 °C (C) and 900 °C (D)

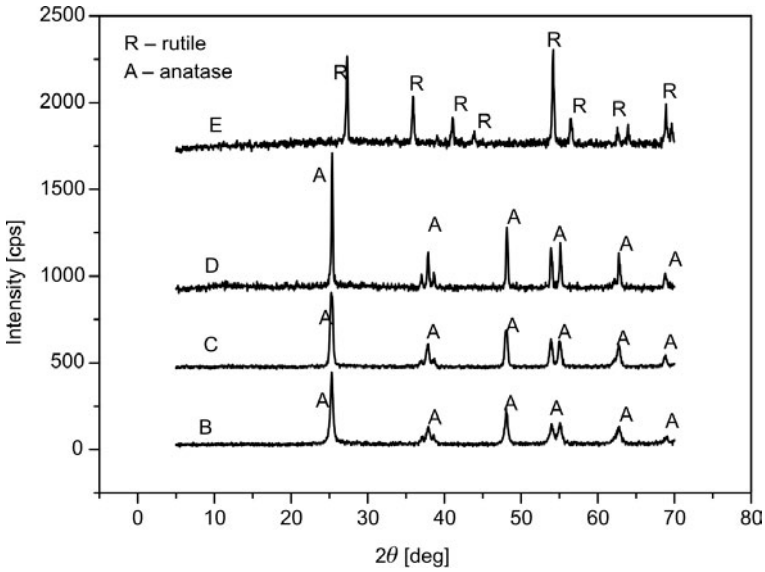

Fig. 5. XRD patterns. Hydrothermal synthesis in microwaves. Homogeneous precipitation in the presence of urea. Calcinations at 650 °C (B), 800 °C (C), 900 (D) and 960 °C (E)

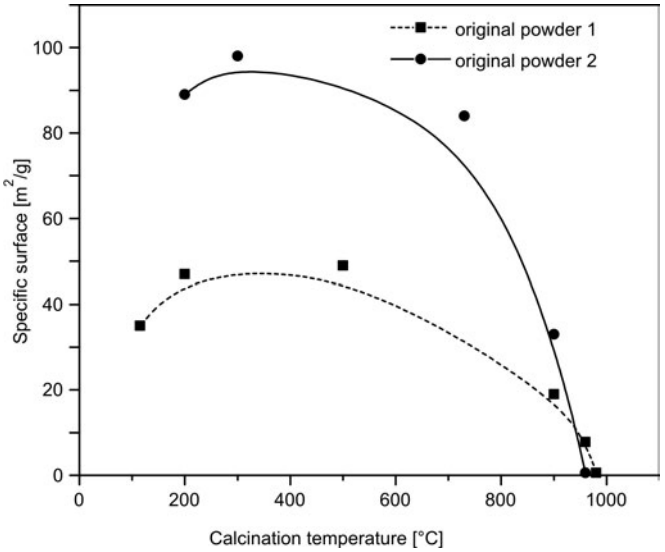

Fig. 6. Dependence of BET surface area on calcination temperature in hydrated TiO_2 without sonication

3.1. Sonication experiments

The influence of the calcination temperature on the rutile content for different periods of sonication, concentration, and types of solvents employed is shown in Fig. 7.

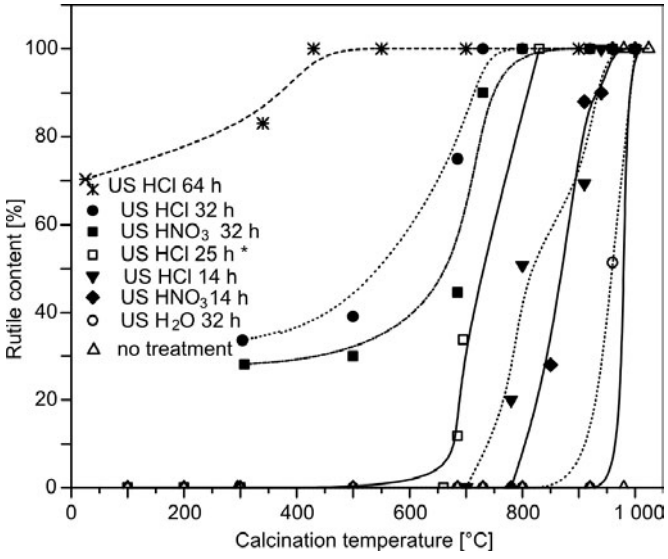

Fig. 7. Dependences of rutile content on calcination temperature; 0, 14, 32, and 64 h of sonication (US); solvents: HNO_3, HCl and water

The results clearly show the important effects of sonication on the kinetics of the anatase–rutile transformation. While materials that had not been sonicated were completely converted to rutile after calcination at around 1000 °C, materials that had been sonicated for 14 h have their transformation rate altered and complete conversion attained at calcinations near 900 °C and those sonicated for 32 h reached complete conversion at 730 °C. Materials sonicated for 64 h reached extensive conversion close to room temperature, which was complete after calcinations at 430 °C.

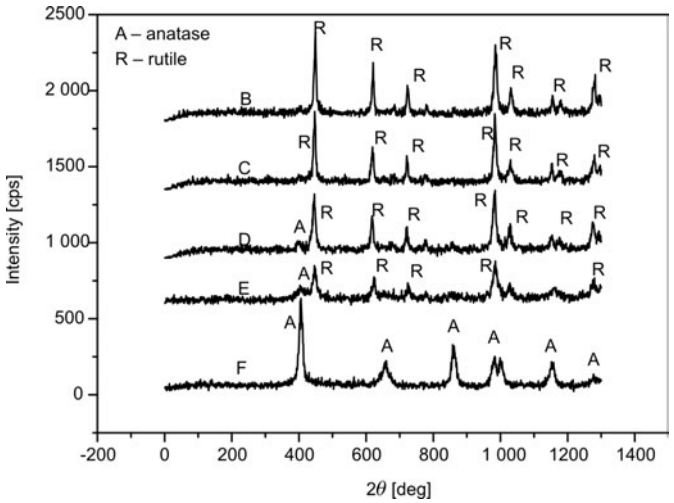

Fig. 8. XRD patterns. Sonicated titania, 64 h, 0.5 M HCl, calcinations at 510 °C (B), 430 °C (C), 340 °C (D), no calcinations (E); anatase not sonicated calcined at 500 °C (F)

XRD patterns of sonicated titania in 0.5 M HCl for 64 h and calcined at three different temperatures up to 510 °C are shown in Fig. 8. XRD diffractographs of not sonicated titania calcined at 530 °C (anatase) was also included for comparison. The findings are surprising and revealing. Analyses of these diagrams suggest nearly complete crystallization to rutile at room temperature making calcinations almost unnecessary.

3.2. Scanning electron microscopy

Scanning electronic micrographs of TiO_2 powder obtained as previously described and calcined at 980 °C for 3 h are shown in Fig. 9. The micrographs show some prismatic crystals, grown simultaneously to phase transition.

Figure 10 shows the electronic micrograph of amorphous hydrated TiO_2 sonicated for 32 h in 1M HCl solution and calcined at 730 °C. Its crystalline structure is a hundred percent single-crystalline rutile. Nevertheless, its texture remains porous, as indicated by BET surface area value – 28 m²/g. Highly porous structures with high concentration of defects favour diffusion in a solid state, which is the most important mode by which transformations evolve during calcinations.

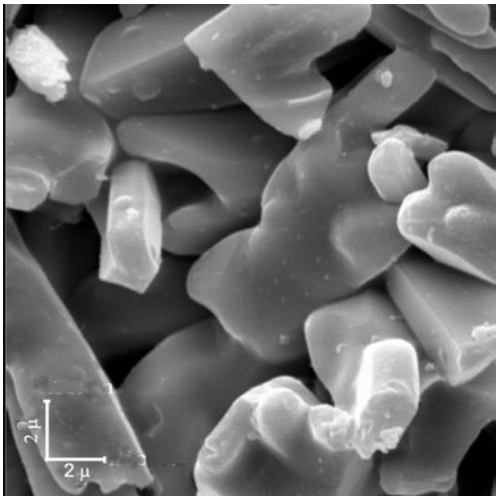

Fig. 9. Powder micrograph. Calcinations at 980 °C; rutile crystalline structure (3000×)

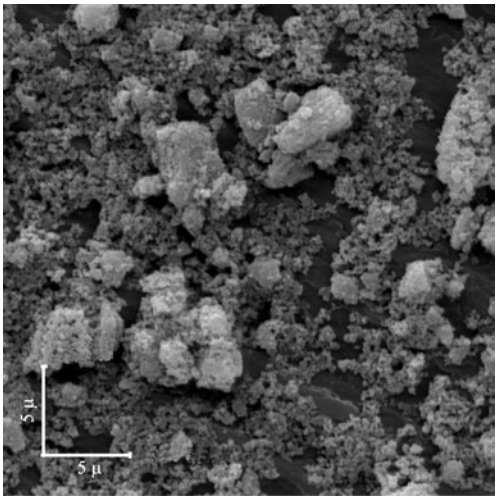

Fig. 10. SEM. Sonicated powder (rutile) for 32 h, 0.5 M HCl, calcination at 730 °C (3000×)

Primary particle sizes derived from the sonication treatment ranged between 13 and 18 nm, which are higher than those obtained by the sol–gel routes yielding particle sizes suitable for fast transformations at 600 °C [15]. The high density of surface defects generated by sonication plays a key role for increasing the kinetics of the transformation and for decreasing the transition temperature what agrees with the results of experiments reported by Gribb and Banfield [16].

4. Conclusions

In this work, a new technique was developed to increase the kinetics of the anatase–rutile transformation by incorporating sonication treatment before calcination. As a result, transformation to rutile phase occurs at great extent at room temperature, and complete transformation is achieved at a relatively reduced temperature of 430 °C. According to the results of this work, kinetics and diffusion processes related to the anatase–rutile transformation are enhanced, by increase in concentration of surface defects of the material, due to chemical-mechanical action of micro jets and shock waves generated by the pre-treatment proposed.

References

[1] HU Y., TSAI H.L., HUANG C.L., Mater. Sci. Eng., A344 (2003), 209.
[2] GENNAR F.G., PASQUEVICH D.M., J. Mater. Sci., 33 (1998), 1571.
[3] OKADA K., YAMAMOTO N., KAMESHIMA Y., and YASUMORI, A., J. Am. Cer. Soc. 84 (2001), 1591.
[4] KUMAR K.N.P, KEIZER K., BURGGRAAF A.J., J. Mater. Sci. Lett., 13 (1994), 59.
[5] ZHAO J., WANG Z., WANG L., YANG H., Zhao M., J. Mater. Sci. Lett., 17 (1998), 1867.

[6] KOLSMULSKI M., Adv. Coll. Int. Sci., 99 (2002), 255.
[7] ZHANG H., BANFIELD J.F., J. Phys. Chem. B, 104 (2000), 3481.
[8] GOUMA P.I., DUTTA P.K., MILLS M. J., Nanostr. Mater., 11 (1999), 1231.
[9] ZHANG Y.H., RELLER A., Mater. Sci. Eng. C, 19 (2002), 323.
[10] GOLDSCHMIDT V. M., U.S. Patent 1,348,129, 1920.
[11] HUGHES W., U.S. Patent 2253551, 1967.
[12] YOGANARASIMHAN S.R., RAO C.N.R., *Mechanism of Crystal Structure Transformation*, Trans. Faraday Soc., London, 1962.
[13] BLECHTA V., LAVICKA M., BLECHTA Z., J. Oil. Col. Chem. Assoc., 50 (1967), 495.
[14] HA P.S., YOUN H.J., JUNG H.S., HONG K.S., PARK Y.H., KO K.H., J. Coll. Int. Sci., 223 (2000), 16.
[15] LIU X.H., DING X.Z., J. Mater. Sci. Lett., 15 (1966), 1789.
[16] GRIBB A.A., BANFIELD J.F., Am. Miner., 82 (1997), 717.

Received 2 September 2008
Revised 22 April 2009

Materials Science-Poland, *Vol. 27*, *No. 4/1*, *2009*

Formation and stability of C–S–H (I) of various degrees of crystallinity in the $Ca(OH)_2$/CaO–Hi-Sil–H_2O system

K. BALTAKYS[1*], R. JAUBERTHIE[2]

[1]Department of Silicate Technology, Kaunas University of Technology, Radvilenu 19, LT – 50270 Kaunas, Lithuania

[2]Department of Civil Engineering, INSA, 20 Av. des Buttes de Coësmes, CS 14315, 35043 Rennes, France

The stability and crystal morphology of C–S–H (I) in the CaO/$Ca(OH)_2$–Hi-Sil–H_2O systems and a sequence of formation of the intermediary compound has been examined. Two series of samples, with different ratios of CaO to SiO_2 were used in the experimental tests. The molar ratio CaO/SiO_2 of primary mixtures was 1.0. Hydrothermal synthesis was carried out under the saturated steam pressure at temperatures of 90, 110, 130, 150 and 175 °C; the duration of isothermal curing was 2–72 h. It was determined that an increase of temperature significantly influences the stability, morphology and degree of crystallinity of C–S–H (I). It was found that C–S–H (I) is stable in the ranhe 90–130 °C. The overall morphology of C–S–H varies from the common fibrous type to irregular grains forming a reticular network. The compositions of intermediate products and of final products can be changed by adding calcium containing components ($Ca(OH)_2$, CaO). In the mixtures with $Ca(OH)_2$, an intermediate compound is C–S–H (I) and the final product is xonotlite. Meanwhile, in the mixtures with CaO, the main intermediate compounds are Z phase and C–S–H (I), and the main product is gyrolite.

Key words: *calcium silicate hydrates; C–S–H (I); xonotlite; gyrolite; X-ray diffraction*

1. Introduction

Calcium silicate hydrates (C–S–H) are an important group of silicate minerals with compositions varying over a large range of CaO/SiO_2 ratios (0.44–3.0) and crystallographic structures from amorphous to well-crystalline [1–8]. Calcium silicate hydrates are the prime candidates for heavy metal binding because of their abundance and appropriate structure [9–13]. Besides, these compounds are of great importance in cement chemistry, where C–S–H gels are the main reaction products and primary binding phases in Portland cement.

[*]Corresponding author, e-mail: kestutis.baltakys@ktu.lt

The conditions of formation and stability of various calcium silicate hydrates are governed by various parameters influencing the kinetics of the reaction and even the microstructure of the products, such as temperature, stirring, the presence of foreign ions and their concentrations [14–22].

The C–S–H (I) phase is a nearly amorphous gel with the specific surface exceeding 150 m^2/g. It is composed of a few elementary layers forming wrinkled foils whose thickness amounts to several nanometers. The substitution of aluminum in the octahedral or tetrahedral sheets of the C–S–H readily modifies the charge of the crystal lattice and might have a direct influence on the material macroscopic properties (cohesion, retention or release of pollutants, durability, etc.) [23, 24]. Hydrothermal treatment of lime–silica mixtures under saturated steam pressures below 250 °C usually gives ill-crystallized calcium silicate hydrates as an initial product, which reacts further to give crystalline calcium silicate hydrates. Mitsuda et al. [25] found that C–S–H (I) was always formed as an initial product of the crystalline phase. The authors presented the following reaction sequence in the temperature range 120–210 °C when the CaO/SiO_2 molar ratio was equal to 1:

C–S–H (crumpled foils) → C–S–H (mixture of crumpled foils and fibre aggregates) → xonotlite

These results for crystalline phases formed after C–S–H agreed with those reported by many authors [26–28].

It is well known that C–S–H (I) phase is thermodynamically unstable and shows a tendency to crystallize [29, 30]. It transforms to tobermorite but this processes is very slow, probably due to difficulties in nucleation. Elevated temperatures accelerate the transformation, high pressure seems to be even more efficient. In the majority of cases, the product of the transformation yields a mixture of C–S–H (I) and tobermorite [31]. Besides, C–S–H products exhibit similarities to the clay minerals in the crystal structure assembly. They comprise composite sheets made up of distorted calcium hydroxide sheets flanked on both sides by parallel rows of wollastonite type chains. The remaining calcium atoms are positioned in interlayer regions. A pH dependent surface charge is the result of silanol sites associated with the bridging silica tetrahedra or end chain tetrahedra [3, 32, 33].

According to the collected reference data, there are only a few published results (and even these are not comprehensive) about stability and crystal morphology of C–S–H (I) having different degrees of crystallinity. Besides, every year many companies cause a lot of environmental pollution in all countries of the world and this has become a really serious problem. Thus, these by-products are expedient to use as secondary raw materials. In particular, the compounds which have silicon and calcium components can be applied for the synthesis of calcium silicate hydrates.

The aim of this paper was to examine the stability and crystal morphology of C–S–H (I) in the $CaO/Ca(OH)_2$ and Hi-Sil mixtures as well as to analyze and explain the formation sequence of intermediary compounds.

2. Experimental

The following materials were used in this work: calcium hydroxide $Ca(OH)_2$ (of 98 % purity, a product of ACROS ORGANICS, Belgium), industrial CaO (loss of ignition 23%, Manufacturer Pigeon Chaux, Saint Pierre La Cour, France) and silica fume (Hi-Sil 255C-D obtained from PPG, amorphous silica > 87 %, crystalline silica < 0.01 %, Na_2SO_4 < 2 %, pH = 6.3, surface area – 180 m^2/g).

Two series of samples, with different ratios of CaO to SiO_2, were used in the experimental tests. The molar ratio CaO/SiO_2 of primary mixtures was 1.0. Hydrothermal synthesis was carried out under the saturated steam pressure at 90, 110, 130, 150 and 175 °C; the duration of isothermal curing was 2, 8, 24 or 72 hours. After synthesis, samples were removed from the teflon cells and transferred to an air conditioned chamber with relative humidity of 55% at 20 °C and sieved through a sieve with a 50 μm mesh.

The XRD data were collected with Philips PW 3710 X-ray diffractometer with the Bragg–Brentano geometry using Ni-filtered CuK_α radiation, operating with the voltage of 30 kV and emission current of 20 mA. The step-scan covered the angular range 2–60° (2θ) in steps of $2\theta = 0.02°$.

SEM (JEOL-JSM-6301F) of the samples was performed using an accelerating voltage of 9 kV and a working distance of 15 mm.

FTIR spectra were obtained with a Perkin Elmer spectrometer FTIR system spectrum X. Specimens were prepared by mixing 1 mg of the sample with 200 mg of KBr. The spectral analysis was performed in the range of 4000–400 cm^{-1} with a spectral resolution of 1 cm^{-1}.

3. Results and discussions

In the $Ca(OH)_2$–Hi-Sil–H_2O system, after 4 h at 90 °C C–S–H (I) (*d* spacing – 0.573, 0.304, 0.281, 0.210, 0.183 nm) and $CaCO_3$ (*d* spacing – 0.385, 0.304, 0.250, 0.229, 0.210, 0.191, 0.188 nm) formed (Fig. 1, curve 1).

The results of scanning electron microscopy were confirmed by the XRD data: amorphous, with no definite crystal structure aggregations typical of a low crystalline degree C–S–H (I) were identified in the products (Fig. 2a).

Upon extending the duration of synthesis to 8, 24 or 72 h, the same compounds (C–S–H (I) and $CaCO_3$) were obtained (Fig. 1). SEM analysis indicated that even after 72 h of isothermal curing at 90 °C, the crystal structure of the products remained practically unchanged (Fig. 2 b).

In order to determine the influence of temperature on the stability and crystal morphology of C–S–H (I), the synthesis was carried out at higher temperatures.

X-ray diffraction curves of the synthesized compounds show that similar amounts of C–S–H (I) (*d* spacing – 0.534, 0.304, 0.281, 0.210, 0.183 nm) and calcite (*d* spacing – 0.386, 0.304, 0.250, 0.229, 0.210, 0.192, 0.188 nm) were formed irrespective of the

temperature of synthesis (110, 130 °C) and its duration (4, 8, 24, 72 h), because the intensities of the main diffraction peaks are similar (Fig. 3, curve 1).

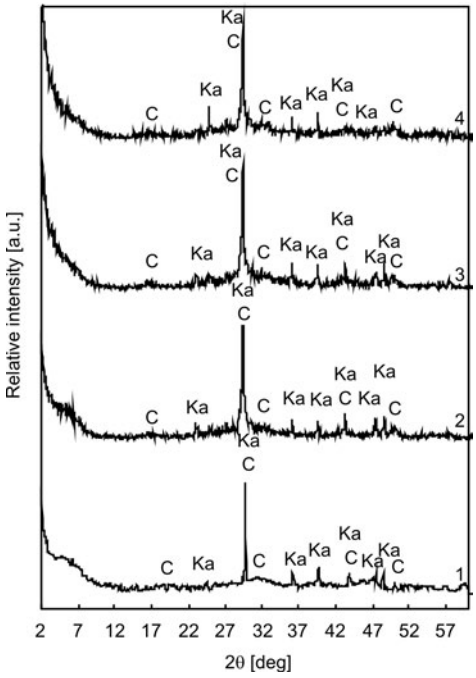

Fig. 1. X-ray diffraction patterns of products of the synthesis; the duration of the hydrothermal synthesis at 90 °C, h: 1 – 2, 2 – 8, 3 – 24, 4 – 72; C – C–S–H (I), Ka – calcite

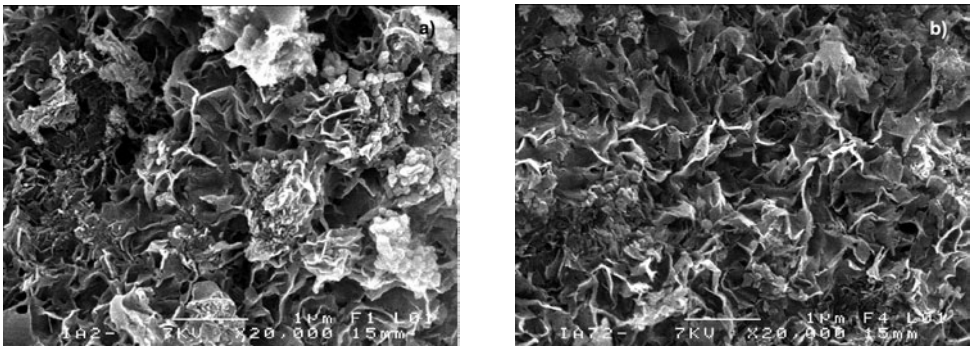

Fig. 2. SEM micrographs of the products of the synthesis; the duration of hydrotermal treatment at 90 °C was: a) 2 h, b) 72 h

The same reaction sequence was proved by SEM analysis. SEM data shows that the overall morphology of C–S–H can actually vary from the common fibrous type to irregular grains forming a reticular network (Fig. 4).

At the beginning of the reaction at 150 °C the same products dominated as at lower temperature (Fig. 5). The FTIR spectra showed typical bands of C–S–H (I): the band at ~970 cm^{-1} due to the Si–O stretching mode of nonbinding oxygens and the

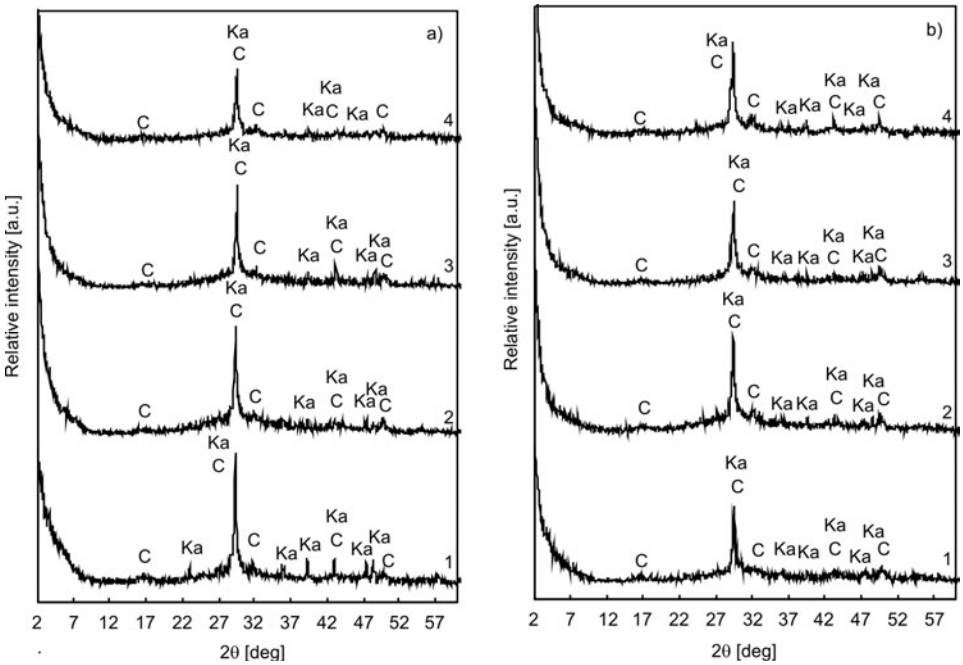

Fig. 3. X-ray diffraction patterns of the products of the synthesis; the duration of hydrothermal synthesis at 110 °C (a) and 130 °C (b), h: 1 – 4, 2 – 8, 3 – 24, 4 – 72; C – C–S–H (I), Ka – calcite

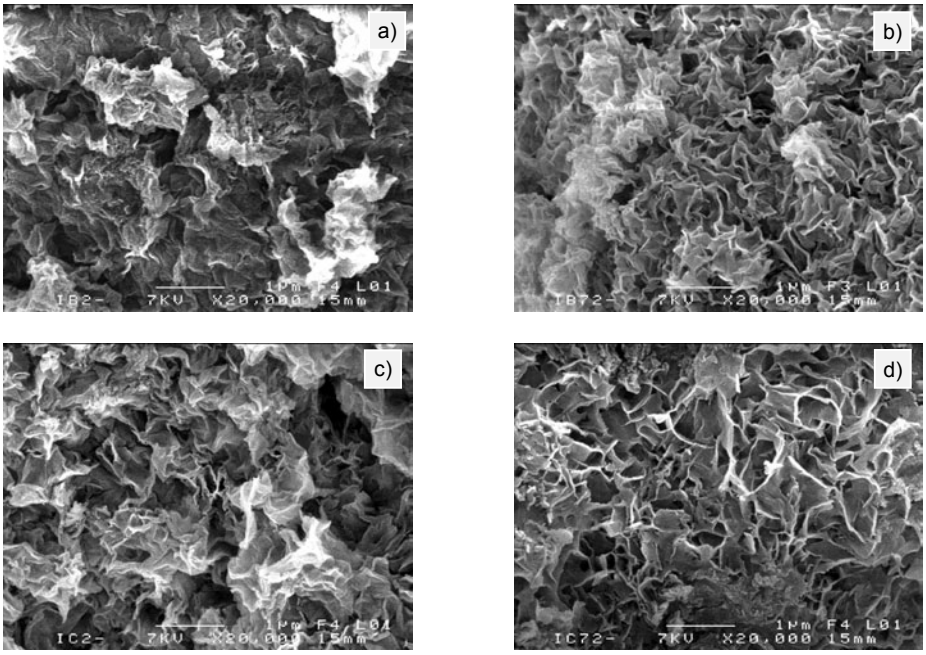

Fig. 4. SEM micrographs of the products of the synthesis. Duration of hydrotermal curing at 110 °C (a, b) and 130 °C (c, d): a) and c) – 2 h, b) and d) 72 h

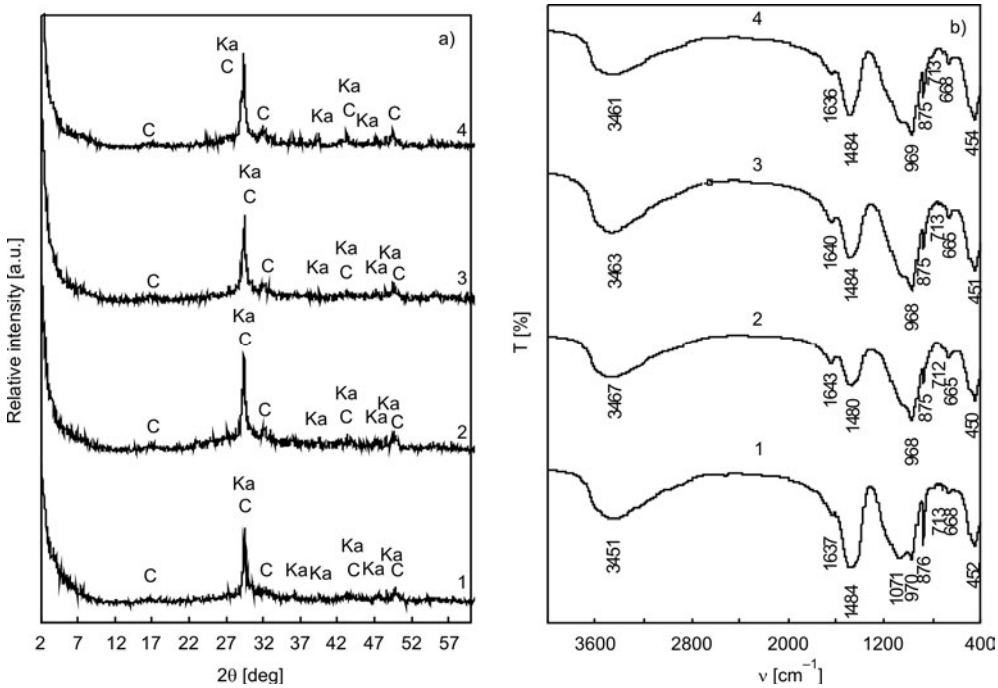

Fig. 5. XRD patterns (a) and FTIR spectra (b) of the products of the synthesis; the duration of the hydrothermal synthesis at 150 °C: 1 – 2 h, 2 – 8 h, 3 – 24 h, 4 – 72 h; C – C–S–H (I), Ka – calcite

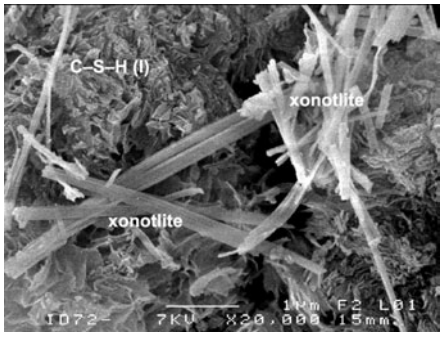

Fig. 6. SEM micrographs of the products of the synthesis; duration of hydrotermal curing at 150 °C was 72 h

band at ~668 cm^{-1} due to the Si–O–Si bonds. The broad band at ~3451 cm^{-1} was due to the stretching vibration of –OH groups in H_2O hydroxyls with a wide range of hydrogen bonding strength. Further water peak at about 1637 cm^{-1} confirmed $\delta(H_2O)$ stretching vibration. Moreover $\nu(CO_3^{2-})$ vibrations at 713, 876, 1484 cm^{-1} were found in the IR spectra (Fig. 5b).

It should be underlined that after 72 hours of isothermal curing unexpected results were obtained. The accumulation of two morphologous crystals can be seen in SEM micrographs: C–S–H (I) characteristic irregular shape crystals and long, needle/plate shape xonotlite crystals that are formed as on C–S–H (I) grains and in the interlayers between them (Fig. 6).

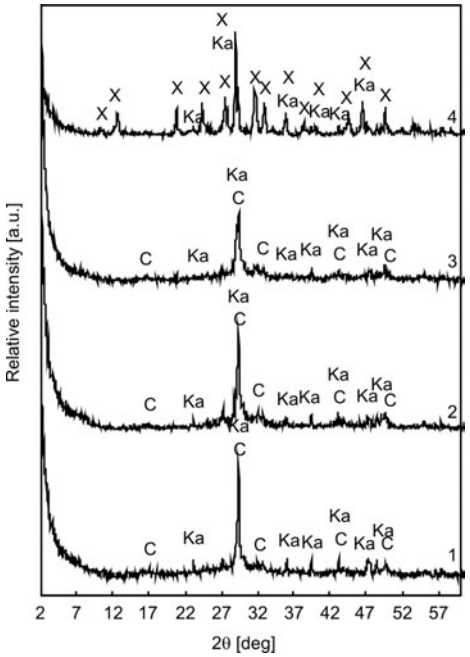

Fig. 7. X-ray diffraction patterns of the products of the synthesis; the duration of hydrothermal synthesis at 175 °C: 1 – 2 h, 2 – 8 h, 3 – 24 h, 4 – 72 h; C – C–S–H (I), X – xonotlite, Ka – calcite

The formation of xonotlite is confirmed by XRD studies only after 72 h at 175 °C: the main peak with *d* spacing – 0.703 nm, which is specific to xonotlite, was identified (Fig. 7, curve 4, *d* spacing – 0.703; 0.426; 0.364; 0.271; 0.250; 0.228 nm). This agrees with SEM data (Fig. 8).

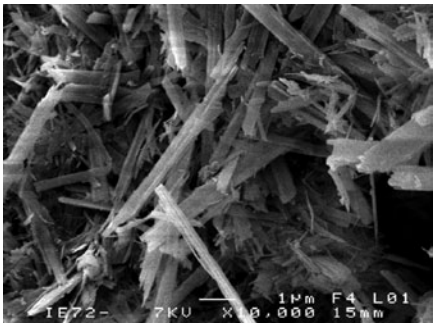

Fig. 8. SEM micrographs of the products of the synthesis; the duration of hydrotermal curing at 175 °C was 72 h

According to the obtained results, the reactions of new compound formations, in the mixture of CaO and Hi-Sil at 90–175 °C, occur in the following sequence:

$$\mathrm{Ca(OH)_2} + \text{Hi-Sil} + \mathrm{H_2O} \begin{matrix} \nearrow \mathrm{CaCO_3} \\ \searrow \mathrm{C-S-H\ gel} \end{matrix} \rightarrow \mathrm{C-S-H\ (I)} \rightarrow \text{xonotlite},\ \mathrm{CaCO_3}$$

It should be stressed that the mechanism of hydrothermal reactions and the sequence of the compounds formed in the CaO–Hi-Sil–H_2O mixture are quite different,

as another component containing Ca^{2+} was used. The data of XRD analysis showed that at 90 °C and 110 °C only one the products of the – C–S–H (I) (*d* spacing – 0.567, 0.304, 0.280, 0.209, 0.182 nm) and $CaCO_3$ (*d* spacing – 0.304, 0.249, 0.228, 0.209, 0.192, 0.188 nm) were formed (Fig. 9).

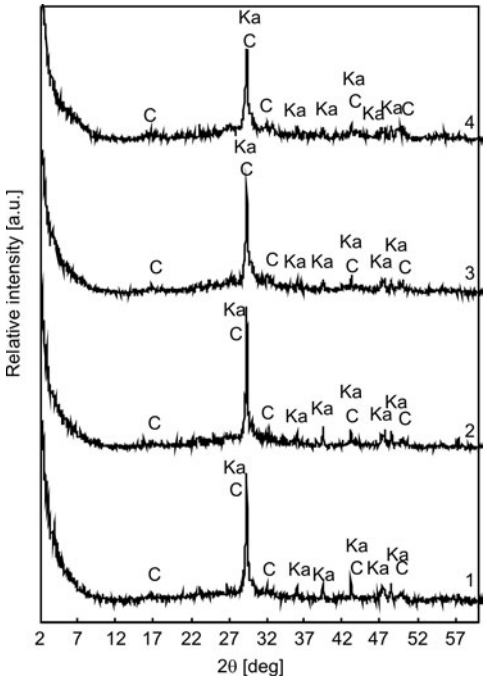

Fig. 9. X-ray diffraction patterns of the products of the synthesis; the duration of hydrothermal synthesis at 110 °C: 1 – 2 h, 2 – 8 h, 3 – 24 h, 4 – 72 h; C – C–S–H (I), Ka – calcite

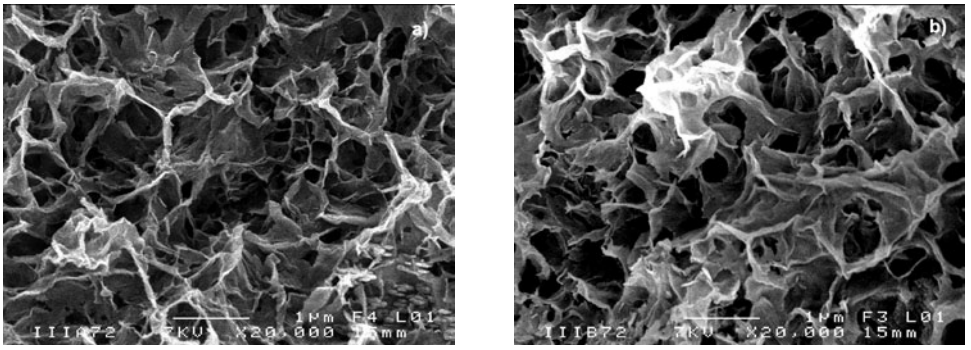

Fig. 10. SEM micrographs of the products of the synthesis; duration of hydrotermal curing at 90 °C (a) and 110 °C (b) was 72 h

Moreover, aggregations of the same crystal structure as in the $Ca(OH)_2$–Hi-Sil –H_2O mixture were identified after 72 h of isothermal curing at 90 and 110 °C (Fig. 10). It should be underlined that at 130 °C the degree of crystallinity of C–S–H (I) is higher than at 90 °C or 110 °C (Figs. 11, 12).

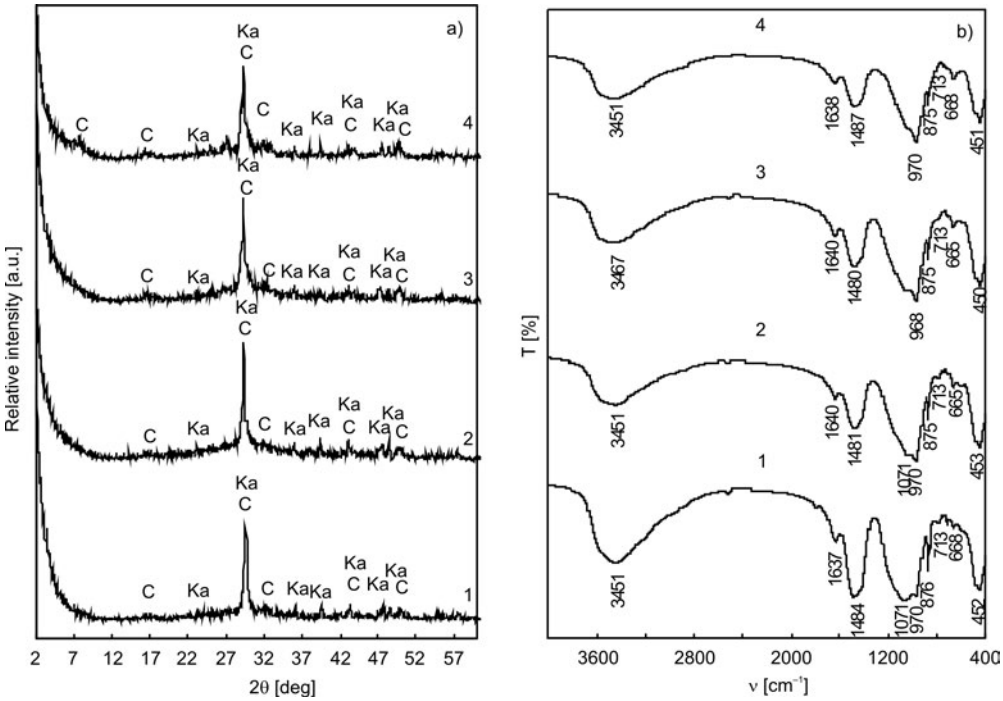

Fig. 11. X-ray diffraction patterns (a) and FT-IR spectra (b) of the products of the synthesis; the duration of the synthesis at 130 °C: 1 – 2 h, 2 – 8 h, 3 – 24 h, 4 – 72 h; C – C–S–H (I), Ka – calcite

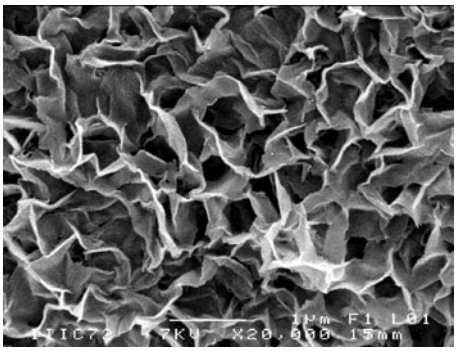

Fig. 12. SEM micrographs of the products of the synthesis; the duration of hydrotermal curing at 130 °C was 72 h

X-ray diffraction patterns show basic reflections characteristic of a semi-crystalline C–S–H (I) type calcium silicate hydrate already with larger *d* spacing – 1.2440; 0.304; 0.278; 0.183 nm (Fig. 11a, curve 4).

The data of SEM analysis showed that the overall morphology of C–S–H (I) varies from the common fibrous type to irregular plates (Fig. 12). Moreover, FTIR spectra of semi-crystalline compounds contain a characteristic set of bands at 3451, 1638, 1487, 970, 875, 668, 451 cm^{-1} (Fig. 11).

After 72 h of isothermal curing at 150 °C, unexpected results were also obtained: C–S–H (I) starts regrouping into low-base calcium silicate hydrate gyrolite gel

(*d* spacing – 2.230, 0.420, 0.304, 0.280, 0.210, 0.183 nm) and Z phase (*d* spacing – 1.522, 0.304, 0.280, 0.183 nm) (Fig. 13, curve 4). These results were confirmed by SEM analysis: gyrolite gel and Z phase tend to crystallize in clusters of plates, while C–S–H (I) forms fibrous material (Fig. 14).

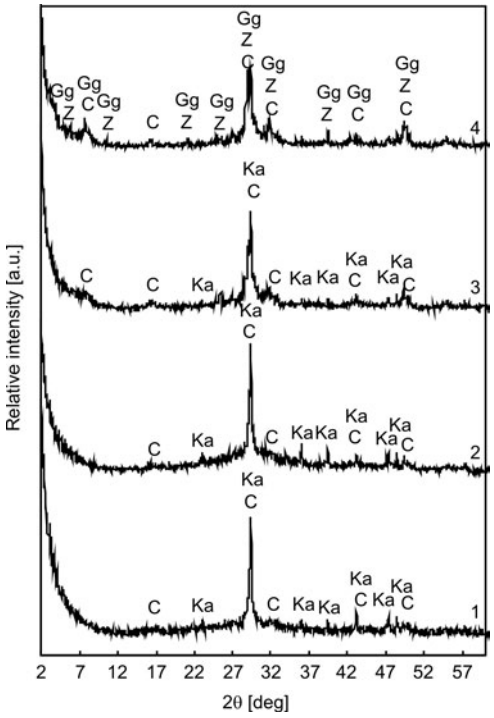

Fig. 13. X-ray diffraction patterns of the products of the synthesis; the duration of hydrothermal synthesis at 150 °C was: 1 – 2 h, 2 – 8 h, 3 – 24 h, 4 – 72 h; C – C–S–H (I), Ka – calcite, Gg – gyrolite gel, Z – Z phase

Fig. 14. SEM micrographs of the products of the synthesis; duration of hydrotermal curing at 150 °C was 72 h

As far as we know, this is the first evidence that C–S–H (I) is unstable in those mixtures for which the molar ratio (CaO/SiO_2) of the primary mixture is equal to 1.0. Besides, in CaO–Hi-Sil–H_2O mixtures this compound recrystallizes into calcium silicate hydrates when in $Ca(OH)_2$–Hi-Sil–H_2O system under the same conditions (72 h at 150 °C), xonotlite and calcite dominate in the products.

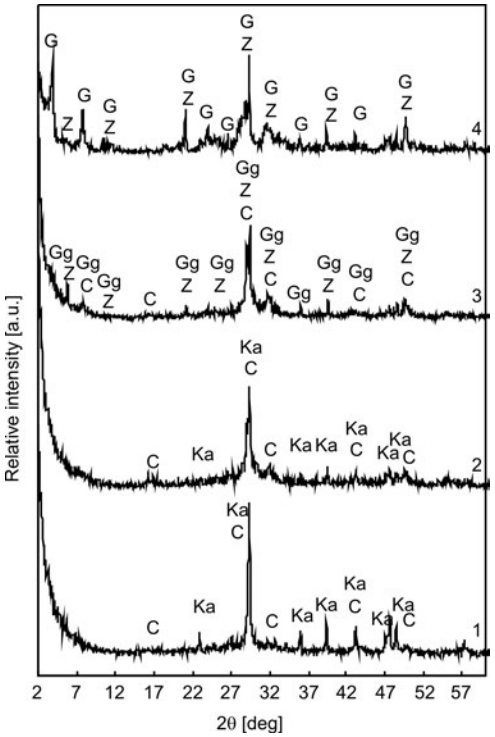

Fig. 15. X-ray diffraction patterns of the products of the synthesis; the duration of hydrothermal synthesis at 175 °C: 1 – 2 h, 2 – 8 h, 3 – 24 h, 4 – 72 h; C – C–S–H (I), Ka – calcite, Z – Z phase, Gg – gyrolite gel, G – gyrolite

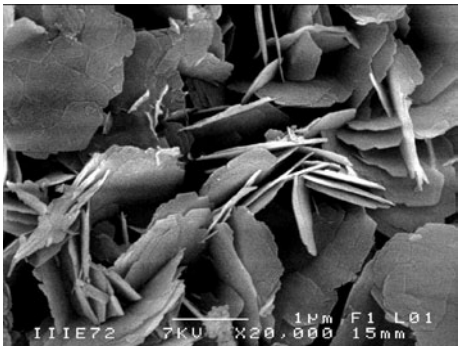

Fig. 16. SEM micrograph of the products of the synthesis; the duration of hydrotermal curing at 175 °C was 72 h

The data obtained at 175 °C proved that C–S–H (I) is a metastable compound, because after 24 h of synthesis, low base calcium silicate hydrates Z phase (*d* spacing – 1.501, 0.418, 0.303, 0.281, 0.184 nm) and gyrolite gel (*d* spacing – 2.232, 0.360, 0.303, 0.281, 0.248, 0.228, 0.209, 0.190, 0.184 nm) were prevalent (Fig. 15, curve 3). Furthermore, within 72 h of hydrothermal treatment, almost all the Z phase finishes transferring into gyrolite (Fig. 15, curve 4). These results were confirmed by SEM data: gyrolite crystallized into well-crystalline plates (Fig. 16).

Thus, in the CaO–Hi-Sil–H_2O system in the temperature range from 90 °C to 175 °C, xonotlite did not form even after 72 h of hydrothermal curing. The sequence of compounds to be formed during the synthesis is as follows:

$$\mathrm{CaO + Hi\text{-}Sil + H_2O} \nearrow \begin{matrix} \mathrm{CaCO_3} \\ \mathrm{C-S-H\ gel} \end{matrix} \searrow \rightarrow \mathrm{C-S-H(I),\ CaCO_3}$$

$$\rightarrow \begin{cases} \text{gyrolite gel} \\ \text{Z phase} \\ \mathrm{C-S-H\ (I)} \end{cases} \rightarrow \begin{cases} \text{gyrolite} \\ \text{Z phase} \end{cases}$$

The obtained results showed that the by-products can be used as secondary raw materials in the synthesis of calcium silicate hydrates. Meanwhile, the formation conditions and stability of aforementioned compounds depend on calcium containing component ($Ca(OH)_2$, CaO), which change the composition of intermediate and final products of the synthesis.

4. Conclusion

Increase in temperature significantly influences the stability, morphology and degree of crystalline of C–S–H (I) in the temperature range from 90 °C to 175 °C. It was found that in the $CaO/Ca(OH)_2$ and Hi-Sil mixtures when the molar ratio of the primary mixture CaO/SiO_2 equals 1.0, C–S–H (I) is stable in the temperature between 90 and 130 °C. The overall morphology of C–S–H varies from the common fibrous type to irregular grains forming a reticular network.

Calcium containing components ($Ca(OH)_2$, CaO) change the composition of intermediate and final products of the synthesis. In the mixtures with $Ca(OH)_2$, an intermediate compound is C–S–H (I) and the final product is xonotlite. Meanwhile, in the mixtures with CaO, the main intermediate compounds are Z phase and C–S–H (I), and the main product is gyrolite. In both mixtures, calcite prevails at the beginning of the synthesis and remains in the products in almost all conditions under investigation.

Acknowledgement

The authors express their thanks to Joseph Le Lannic, CMEBA Université de Rennes, for his assistance with scanning electron microscopy.

References

[1] TAYLOR H.F.W., ROY D.M., Proc. 7th Int. Symp. Chemistry of Cement, Paris, 1980, 1.
[2] ZHANG X., CHANG W., ZHANG T., ONG C.K., J. Am. Ceram. Soc., 83 (2000), 2600.
[3] RICHARDSON I.G., Cem. Concr. Res., 38 (2008), 137.
[4] CHEN J.J., THOMAS J.J., TAYLOR H.F.W., JENNINGS H.M., Cem. Concr. Res., 34 (2004), 1499.
[5] NONAT A., Cem. Concr. Res., 34 (2004), 1521.
[6] BLACK L., GARBEV K., BEUCHLE G., STEMMERMANN P., SCHILD D., Cem. Concr. Res., 36 (2006), 1023.
[7] HARTMANN A., BUHL J.-CH., BREUGEL K., Cem. Concr. Res., 37 (2007), 21.

[8] CONSTANTINIDES G., ULM F.J., J. Mech. Phys. Solids, 55 (2007), 64.
[9] HARFOUCHE M., WIELAND E., DÄHN R., FUJITA T., TITS J., KUNZ D., TSUKAMOTO M., J. Coll. Interface Sci., 303 (2006), 195.
[10] TITS J., WIELAND E., MÜLLER C.J., LANDESMAN C., BRADBURY M.H., J. Coll. Interface Sci., 300 (2006), 78.
[11] COLEMAN N.J., Separ. Purif. Techn., 48 (2006), 62.
[12] VIALLIS-TERRISSE H., NONAT A., PETIT J.C., J. Coll. Interface Sci., 244 (2001), 58.
[13] STUMM A., GARBEV K., BEUCHLE G., BLACK L., STEMMERMANN P., NUESCH R., Cem. Concr. Res., 35 (2005), 1665.
[14] ALLEN A.J., JEFFREY J.THOMAS J.J., Cem. Concr. Res., 37 (2007), 319.
[15] DEJONG M.J., ULM F.J., Cem. Concr. Res., 37 (2007), 1427.
[16] NOCUN-WCZELIK W., Cem. Concr. Res., 29 (1999), 1759.
[17] TSUJI M., KOMARNENI S., J. Mater. Res., 4 (1989), 698.
[18] AL-WAKEEL E.I., EL-KORASHY S.A., EL-HEMALY S.A., RIZK M.A., J. Mater. Sci., 36 (2001), 2405.
[19] GABROVSEK R., KURBUS B., MUELLER D., WEIKER W., Cem. Concr. Res., 2 (1993), 321.
[20] EL-KORASHY S.A., J. Ion Exchange, 15 (2004), 2.
[21] EL-KORASHY S.A., AL-WAKEEL E.I., EL-HEMALY S.A., RIZK M.A., Egypt J. Chem., 45 (2002), 723.
[22] MIYAKE M., IWAYA M., SUZUKI T., J. Am. Cer. Soc., 73 (1990), 3524.
[23] PELLENQ R.J.-M., DELVILLE A., VAN DAMME H., *Characterization of Porous Solids* IV, Royal Soc. Chem., London, 1997.
[24] FAUCON P., CHARPENTIER T., HENOCQ P., PETIT J.C., VIRLET J., ADENOT F., Proc. Scientific Basis for Nuclear Waste Management XXI Symposium, Materials Research Society (1997), 506.
[25] MITSUDA T., KOBAYAKAWA S., TORAYA H., 8th Int. Congress on the Chemistry of Cement, Rio de Janeiro, 1986, 160.
[26] JAUBERTHIE R., TEMIMI M., LAQUERBE M., Cem. Concr. Res., 26 (1996), 1335.
[27] SIAUCIUNAS R., BALTAKYS K., Cem. Concr. Res., 34 (2004), 2029.
[28] BALTAKYS K., SIAUCIUNAS R., J. Mater. Sci., 41 (2006), 4799.
[29] SUGIYAMA D., FUJITA T., Cem. Concr. Res., 36 (2006), 227.
[30] BABUSHKIN V.I., MATVEEV G.M., MCHEDLOW-PETROSSYAN O.P., *Thermodynamics of Silicates* (in Russian), Stroyizdat, Moscow, 1962.
[31] KURDOWSKI W., NGUYEN T.T., Proc. 9th ICCC, National Council for Cement and Building Materials, New Delhi, 1992, 591.
[32] POINTEAU I., PIRIOU B., FEDOROFF M., BARTES G.M., MARMIER N., FROMAGE F., J. Coll. Int. Sci., 236 (2001), 252.
[33] TERISSE V.H., NONAT A., PETIT C.J., J. Coll. Interface Sci., 244 (2001), 58.

Received 10 September 2008
Revised 26 February 2009

Materials Science-Poland, *Vol. 27*, *No. 4/1*, *2009*

Influence of gypsum additive on the formation of calcium silicate hydrates in mixtures with C/S = 0.83 or 1.0

K. BALTAKYS*

Department of Silicate Technology, Kaunas University of Technology,
Radvilenu 19, LT – 50270 Kaunas, Lithuania

The influence of gypsum additive on the formation of calcium silicate hydrates and on the formation of a sequence of intermediary compounds in the $CaO–SiO_2·nH_2O–H_2O$ system has been examined. The synthesis was carried out in unstirred suspensions. The molar ratios of primary mixtures were CaO/SiO_2 = 0.83, 1.0 and $SO_3/(SiO_2 + SO_3)$ = 0, 0.0125, 0.025. The durations of isothermal curing at 200 °C were 4, 8, 16 and 72 h. It was established that sulfate ions improve the synthesis of 1.13 nm tobermorite in the $CaO–SiO_2·nH_2O–H_2O$ system with CaO/SiO_2 = 0.83 at 200 °C. However, a larger amount of gypsum ($SO_3/(SiO_2 + SO_3)$ = 0.025) stimulates the formation not only of 1.13 nm tobermorite but also of $CaSO_4$ and xonotlite. In the $CaO–SiO_2·nH_2O–H_2O$ system with CaO/SiO_2 = 1.0, a small amount of sulfate ions prolong the persistence of intermediate compounds – 1.13 nm tobermorite and C–S–H (I). The products of synthesis were characterized by X-ray diffraction analysis, simultaneous thermal analysis and Fourier transform infrared spectroscopy.

Key words: *gyrolite; calcium sulfate; calcium silicate hydrate; X-ray diffraction*

1. Introduction

Significant amounts of sulfate impurities enter almost all carbonate rock. Moreover, large quantities of the by-product, gypsum, are produced by chemical industries and are currently being disposed by dumping into rivers, ponds or landfills. Due to increasing concern about environmental pollution, it is essential to utilize these wastes as building materials. Therefore, sulfate attack in concrete structures is among the major durability concerns in civil infrastructure systems. Proper modelling techniques can help us to understand the influence of severe environments on the properties of concrete, and improve the decision making process in every stage of construction and

*E-mail: kestutis.baltakys@ktu.lt

maintenance. It should be underlined that the study of the effect of salt (sulfate, chloride, etc.) on the durability of cement stone is highly relevant in countries with access to the sea, because they have constructions (jetties, quays, etc.) affected by sea water. The main hydration products and principal binding phases in all calcium silicate-based pastes and concrete are calcium silicate hydrate (C–S–H) gels. The composition and the degree of structural order of C–S–H phases depend on the nature of the system. For these reasons, some researchers studied the influence of gypsum additives on the synthesis of calcium silicate hydrate [1–12]. Most of them have found that the addition of gypsum accelerates the formation of calcium silicate hydrates [1–3, 5–8].

Krzheminskiy et al. [2, 3] indicated that at 175 °C, when the molar ratio of the primary mixture is CaO/SiO_2 = 0.5–1.0, small amounts (1–5%) of gypsum stimulate the reaction of CaO with C–S–H (I). Kuatbaev [7] has shown that gypsum has no influence on the solubility of quartz, but gypsum is more soluble than quartz and the solution contains a significant excess of anions. For this reason, SiO_4^{4-} is isomorphically replaced by SO_4^{2-}, and SO_3-substituted calcium silicate hydrates, more soluble than pure compounds, are formed. Grabko [8] found that gypsum additive in mixtures with a molar ratio CaO/SiO_2(C/S) = 0.8 primarily and significantly stimulates the formation of ellastadite. He indicates that calcium silicate hydrates start forming when all the volume of $CaSO_4$ has reacted. In this case, in the products α-C_2S hydrate prevails and during synthesis gradually recrystallizes into SO_3-substituted C–S–H (I), while in the pure system only C–S–H (I) is formed. Even 7% of gypsum can enter into the crystal structure of these compounds. However, after using a larger quantity of this additive, C–S–H (I) is metastable and regroups into 1.13 nm tobermorite. Vektaris et al. [9, 10] have also found that sulfate ions stimulate formation of calcium silicate hydrates. This process is more intensive in mixtures with the molar ratio CaO/SiO_2 equal to 0.8 than in equal to 1.0. Moreover, in the CaO–amorphous SiO_2–H_2O system, 5–10% of gypsum strongly affects the crystallization of C–S–H (I) into 1.13 nm tobermorite.

Other authors [4, 11, 12] indicate however that in lime–quartz–water mixtures under hydrothermal conditions at 175 °C gypsum has no influence on the solubility of lime, but somewhat changes the mineral composition of the final products. Besides, it was estimated that only 1.5% of sulfate ions can enter the calcium silicate hydrate crystal structure.

Thus, there are not much data (and none of it is comprehensive) about the sequence of the newly formed compounds and the influence of gypsum additives on it. The published papers describe the influence of alkaline metals [13–14], aluminium [15–18] and other elements [19–21] on the synthesis and properties of calcium silicate hydrates. Moreover, almost all of these tests were performed with quartz – less active form of SiO_2. There is little data about the effect of a more active form of SiO_2 (amorphous SiO_2) on the synthesis of calcium silicate hydrates or the sequence of the new compounds formed or the influence of additives on these processes.

The main objective of the present work was to examine the influence of gypsum additives on the formation of calcium silicate hydrates in the $CaO–SiO_2{\cdot}nH_2O–H_2O$ mixture with C/S = 0.83 or 1.0 as well as to analyze and explain the formation of a sequence of intermediary compounds.

2. Experimental

The following reagents were used as starting materials: fine-grained $SiO_2{\cdot}nH_2O$ (losses on ignition 21.43%, specific surface area S_a = 1560 m²/kg), calcium oxide (S_a = 548 m²/kg), $CaSO_4{\cdot}2H_2O$ (losses on ignition 23%).

The syntheses of calcium silicate hydrates were carried out in unstirred suspensions in vessels of stainless steel. The molar ratios of primary mixtures CaO/SiO_2 were 0.83, 1.0 and $SO_3/(SiO_2 + SO_3)$ = 0, 0.0125, 0.025. Dry primary mixtures were mixed with water to achieve a water/solid ratio of the suspension equal to 10.0. Hydrothermal synthesis was carried out under saturated steam pressure at 200 °C; the durations of isothermal curing were 4, 8, 16 and 72 h. The products of the syntheses were filtered, rinsed with ethyl alcohol to prevent carbonization, dried at 50 °C ± 5, and sieved through a sieve with a mesh size of 80 μm.

The X-ray powder diffraction (XRD) data were collected with a DRON–6 X-ray diffractometer equipped with the Bragg–Brentano geometry using Ni-filtered CuK_α radiation and a graphite monochromator operating under the voltage of 30 kV and an emission current of 20 mA. The step-scan covered the angular range 2–60° (2θ) in steps of $2\theta = 0.02°$.

Simultaneous thermal analyses (STA: differential scanning calorimetry – DSC and thermogravimetry – TG) were also employed for investigating the thermal stability and phase transformations of the synthesized products at the heating rate of 15 °C/min, the temperature ranged from 30 °C to 1000 °C under air atmosphere. The test was carried out on a STA 409 PC Luxx Netzsch instrument. Ceramic sample handlers and crucibles of Pt–Rh were used.

FTIR spectra were obtained with the aid of a Perkin Elmer FT–IR Spectrum X system. The specimens were prepared by mixing 1 mg of the sample with 200 mg of KBr. The spectral analysis was performed in the range of 4000–400 cm^{-1} with a spectral resolution of 1 cm^{-1}.

The specific surface area of the raw materials was determined by Blaine's method with an air permeability apparatus (Model 7201, Toni Technik Baustoffprufsysteme GmbH).

3. Results and discussion

In the $CaO–SiO_2{\cdot}nH_2O–H_2O$ system in which the molar ratio of the primary mixture of C/S = 0.83 at 200 °C, 1.13 nm tobermorite rapidly forms, because the key

components of this compound (*d* spacing – 1.137, 0.546, 0.306, 0.280, 0.207, 0.184 nm) and C–S–H (I) (*d* spacing – 0.306; 0.280; 0.184 nm) were identified after 4 h of isothermal curing (Fig. 1, curve 1).

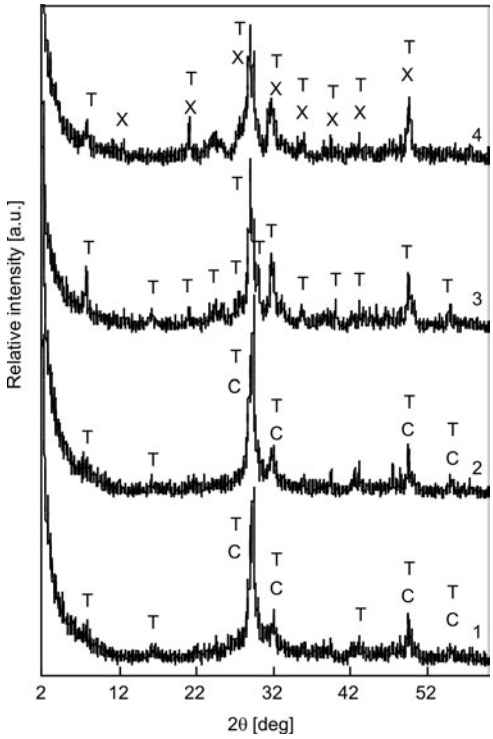

Fig. 1. X-ray diffraction patterns of the products of the syntheses; durations (h) of the hydrothermal syntheses at 200 °C: 1 – 4, 2 – 8, 3 – 16, 4 – 72; C – C–S–H (I), T – 1.13 nm tobermorite, X – xonotlite

After 16 h of synthesis 1.13 nm tobermorite has crystallised; its characteristic peaks increase (Fig. 1, curve 3). Upon continuing the synthesis, 1.13 nm tobermorite starts to transform into a higher-basicity compound – xonotlite (*d* spacing – 0.779, 0.421, 0.308, 0.282, 0.250, 0.234, 0.204, 0.184 nm) (Fig. 1, curve 4). Thus, at 200 °C 1.13 nm tobermorite is unstable, since after 72 h it starts recrystallising into xonotlite.

The analysis of the influence of gypsum additive on the formation of tobermorite at 200 °C, when the initial molar ratios $CaO/(SiO_2 + SO_3) = 0.83$ and $SO_3/(SiO_2 + SO_3) = 0.0125$ shows that during the first hours sulfate ions accelerate the synthesis of monobasic calcium silicate hydrates.

After 4 h of synthesis 1.13 nm tobermorite (*d* spacing – 1.139, 0.546, 0.307, 0.280, 0.184, 0.167 nm) and C–S–H (I) (*d* spacing – 0.546, 0.307, 0.280, 0.184, 0.167 nm) form in the products (Fig. 2, curve 1). Upon extending the duration of synthesis to 72 h, a higher degree of crystallinity 1.13 nm tobermorite forms in the products because the intensity of the basic peak, characteristic of tobermorite (*d* spacing – 1.13 nm) increases (Fig. 2). Thus, it was established that sulfate ions improve the synthesis of 1.13 nm tobermorite: after 72 h of hydrothermal treatment this compound remains stable, i.e. it does not transform into xonotlite, unlike a pure mixture.

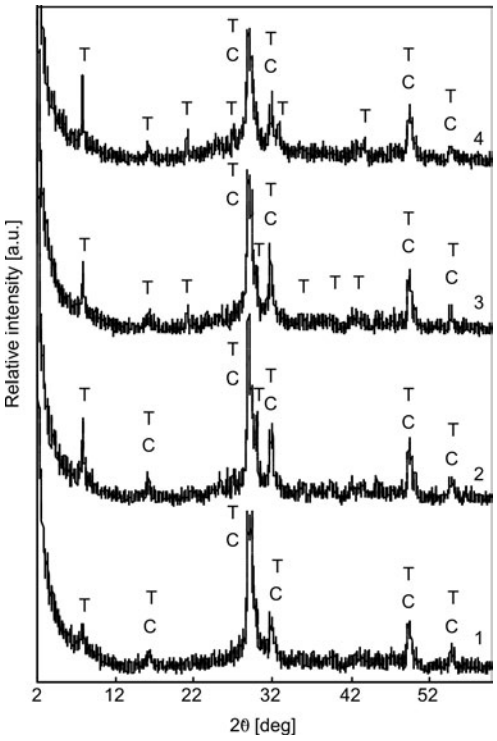

Fig. 2. X-ray diffraction patterns of the products of the syntheses when the molar ratios $CaO/(SiO_2 + SO_3)$ in the primary mixture equal 0.83 and $SO_3/(SiO_2 + SO_3)$ – 0.0125; durations (h) of hydrothermal syntheses at 200 °C: 1 – 4, 2 – 8, 3 – 16, 4 – 72; C – C–S–H (I), T – 1.13 nm tobermorite

Upon adding a larger amount of gypsum into the mixture ($CaO/(SiO_2 + SO_3)$ = 0.83 and $SO_3/(SiO_2 + SO_3)$ = 0.025), acceleration of the synthesis was noticed. However, after 4 h of hydrothermal treatment not only C–S–H (I) (*d* spacing – 0.307, 0.281, 0.184, 0.167 nm) and 1.13 nm tobermorite (*d* spacing – 1.142, 0.548, 0.307, 0.298, 0.281, 0.224, 0.200, 0.184, 0.167 nm) but also $CaSO_4$ (*d* spacing – 0.350, 0.175, 0.167 nm) formed (Fig. 3, curve 1).

The analysis of the DSC and FTIR results shows that during the first hours of synthesis a fair amount of C–S–H (I) is formed. This is represented by a clear exothermic effect at 851 °C in the thermal analysis curve (Fig. 4a, curve 1). Moreover, the absorption at 3474, 1639, 1492, 971, 674 and 449 cm^{-1} characteristic of C–S–H (I) and tobermorite were identified (Fig. 4b, curve 1).

Upon extending the synthesis to 8 h, the degree of crystallisnity of the formed tobermorite increases because the intensity of the peak of the *d* spacing – 1.13 nm grows in the X-ray diffraction pattern (Fig. 3, curve 2). In the meantime, the amount of $CaSO_4$ decreases, because the intensity of its main peak (*d* spacing – 0.350 nm) decreases. Similar results were obtained after 16 h of hydrothermal treatment (Fig. 3, curve 3). The presence of a low intensity absorption bands at 1201 cm^{-1} and 613 cm^{-1}, as observed in the spectrum, shows the formation of a new compound – xonotlite (Fig. 4b, curve 3).

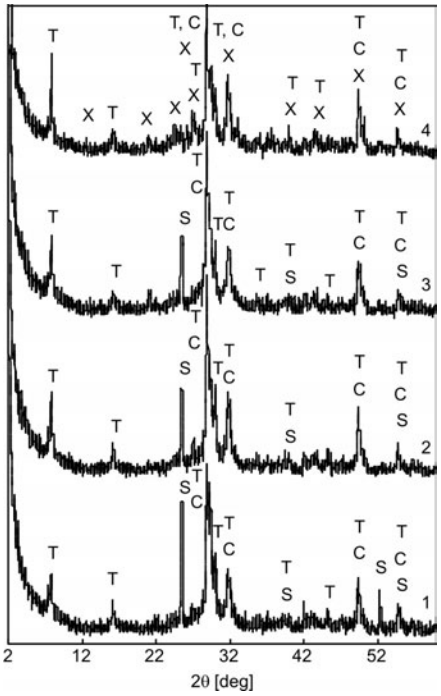

Fig. 3. X-ray diffraction patterns of the products of the syntheses when the molar ratios in the primary mixture $CaO/(SiO_2 + SO_3) = 0.83$ and $SO_3/(SiO_2 + SO_3) = 0.025$; duration (h) of hydrothermal syntheses at 200 °C: 1 – 4, 2 – 8, 3 – 16, 4 – 72; C – C–S – H (I), T – 1.13 nm tobermorite, X – xonotlite, S – $CaSO_4$

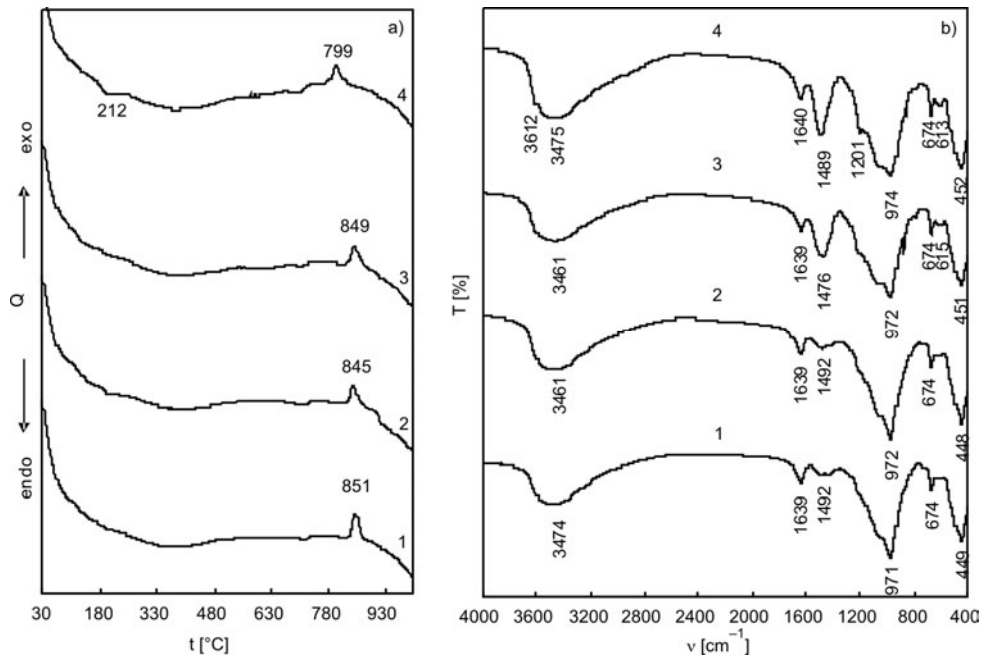

Fig. 4. DSC curves (a) and FTIR spectra (b) of the products of the syntheses when the molar ratios in the primary mixture $CaO/(SiO_2 + SO_3) = 0.83$ and $SO_3/(SiO_2 + SO_3) = 0.025$; durations of the hydrothermal syntheses at 200 °C: 1 – 4, 2 – 8, 3 – 16, 4 – 72

Upon extending the synthesis to 3 days, it was confirmed that all calcium sulfate reacted and a larger amount of 1.13 nm tobermorite was formed. In this case, the basic reflections of xonotlite (*d* spacing – 0.703, 0.423, 0.341, 0.329, 0.308, 0.281, 0.224, 0.207, 0.184, 0.167 nm) were identified in the X-ray diffraction pattern (Fig. 3, curve 4). These data are confirmed by the results of DSC analysis, because the DSC curve shows the endothermic effect at 212 °C, which is typical of tobermorite, and the exothermic effect at 799 °C – C–S–H (I) (Fig. 4a, curve 4). When C–S–H (I) recrystallizes into wollastonite, sulfate ions react as flux (alloying additive), because the exothermic peak, characteristic of formation of wollastonite, significantly shifts to lower temperatures. The FTIR spectrum exhibits absorption bands characteristic of xonotlite at 3612, 1201 and 613 cm^{-1} (Fig. 4b, curve 4).

One may assume that curing the mixture of CaO, amorphous SiO_2 and $CaSO_4$ at 200 °C under saturated steam pressure, leads to formation of tobermorite in the following sequence:

$$5Ca(OH)_2 + 6SiO_2 \cdot nH_2O + XCaSO_4 + nH_2O \rightarrow 5Ca(OH)_2 \cdot 6SiO_2 \cdot nH_2O \cdot XCaSO_4 \cdot pH_2O + (n-p)H_2O$$

$$5Ca(OH)_2 \cdot 6SiO_2 \cdot nH_2O \cdot XCaSO_4 \cdot pH_2O(C-S-H\ (I)) \rightarrow 5Ca(OH)_2 \cdot 6SiO_2 \cdot mCaSO_4 \cdot pH_2O(\text{tobermorite}) + (X-m)CaSO_4$$

In the second stage of the synthesis, the quantity of $(X - m)$ $CaSO_4$, which participates in the recrystallization of C–S–H (I) into tobermorite, is different. The main fact is the large quantity of sulfate ions in the C–S–H (I) structure, relative to tobermorite. Also, the addition of gypsum reduces the solubility of $Ca(OH)_2$ and provides better conditions of the synthesis for the formation of low-base calcium silicate hydrates.

Thus, the crystallization process of 1.13 nm tobermorite is concerned with the stability of the intermediary compound – C–S–H (I) with substituted sulfate ions. Meanwhile, a larger amount of gypsum ($SO_3/(SiO_2 + SO_3) = 0.025$) stimulates the formation of not only 1.13 nm tobermorite but also of $CaSO_4$ and xonotlite.

During hydrothermal exposure in the medium of saturated water vapour, tobermorite (*d* spacing – 1.133, 0.547, 0.305, 0.281, 0.250, 0.228, 0.210, 0.184 nm) and semicrystalline C–S–H (I) (*d* spacing – 0.547, 0.305, 0.281, 0.184 nm) form in the mixture of CaO and amorphous SiO_2, for which C/S = 1.0, after 4 h (Fig. 5a, curve 1). Upon adding an appropriate amount of sulfate ions when $CaO/(SiO_2 + SO_3) = 1.0$ and $SO_3/(SiO_2 + SO_3) = 0.0125$, C–S–H (I) (*d* spacing – 0.306, 0.281, 0.184 nm) and tobermorite gel form, because the diffraction peak with *d* spacing 1.13 nm is not clear and more uneven is identified in the XRD curve (Fig. 5b, curve 1).

Upon extending the duration of synthesis to 8 h, xonotlite (*d* spacing – 0.703, 0.426, 0.364, 0.324, 0.307, 0.284, 0.271, 0.250, 0.225, 0.209, 0.195, 0.184 nm) starts forming in the mixtures because the stoichiometric C/S ratio corresponds to the molar ratio of the primary mixture (C/S = 1.0) (Fig. 5a, curve 2). Further synthesis shows

that the amount of this compound in the products of synthesis increases, and after 72 h of isothermal curing it remains the only one in the pure mixtures (Fig. 5a, curve 4).

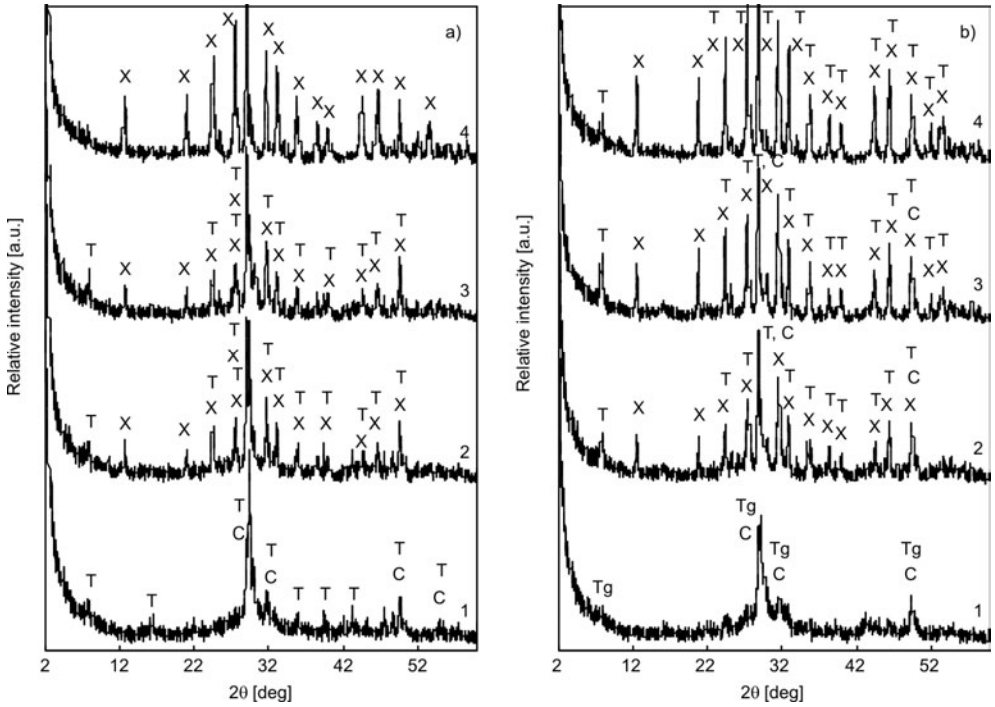

Fig. 5. X-ray diffraction patterns of the products of the syntheses when the molar ratios in the primary mixture $CaO/SiO_2 = 1.0$ (a) and $CaO/(SiO_2 + SO_3) = 1.0$, $SO_3/(SiO_2 + SO_3) = 0.0125$ (b); durations (h) of hydrothermal syntheses at 200 °C: 1 – 4, 2 – 8, 3 – 16, 4 – 72; C – C–S – H (I), Tg – tobermorite gel, T – 1.13 nm tobermorite, X – xonotlite

When the mixture contains sulfate ions, the transformation of intermediate compounds into xonotlite becomes more difficult. Even after 8, 16 and 72 h, apart from the main product, xonotlite, also 1.13 nm tobermorite and/or C–S–H (I) synthesize (Fig. 5b, curves 2–4). Upon addition of a larger amounts of gypsum to the mixture ($SO_3/(SiO_2 + SO_3) = 0.025$), a slow regrouping of intermediate compounds to xonotlite was noticed. After 4 h of hydrothermal treatment only C–S–H (I) (*d* spacing – 0,308, 0,284, 0,184 nm) forms (Fig. 6, curve 1). This is additionally confirmed by the FTIR analysis because the identified absorption bands at 3450, 1646, 1484, 973, 671, 454 cm^{-1} are characteristic of calcium silicate hydrate (Fig. 7b, curve 1). DSC analysis shows that C–S–H (I) transforms into wollastonite, which is characteristic of the exothermic effect at 840 °C (Fig. 7a, curve 1). When extending the synthesis up to 8 h, as expected, C–S–H (I) starts transforming into 1.13 nm tobermorite (*d* spacing – 1.136, 0.547, 0.365, 0.324, 0.308, 0.282, 0.272, 0.203, 0.195, 0.184 nm) and xonotlite (*d* spacing – 0.705, 0.427, 0.365, 0.324, 0.308, 0.282, 0.272, 0.203, 0.195, 0.184 nm). Calcium sulfate also forms in the products (*d* spacing – 0.350, 0.234 nm) (Fig. 6, curve 2).

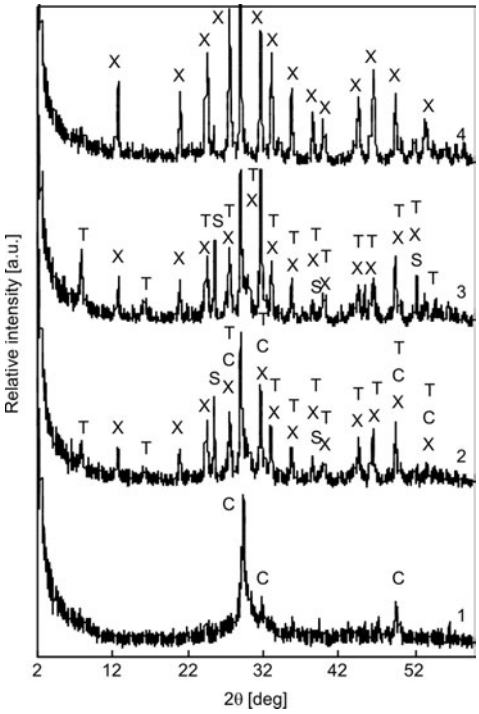

Fig. 6. X-ray diffraction patterns of the products of the syntheses when the in molar ratios in the primary mixture $CaO/(SiO_2 + SO_3) = 1.0$ and $SO_3/(SiO_2 + SO_3) = 0.025$; durations (h) of hydrothermal syntheses at 200 °C: 1 – 4, 2 – 8, 3 – 16, 4 – 72; C – C–S – H (I), T – 1.13 nm tobermorite, X – xonotlite, S – $CaSO_4$

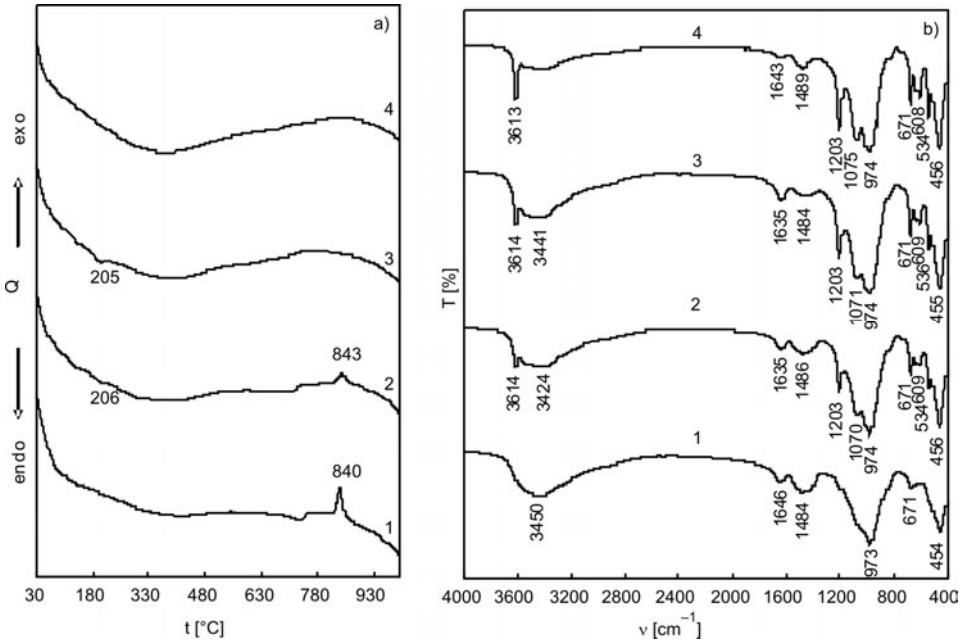

Fig. 7. DSC curves (a) and FTIR spectra (b) of the products of the syntheses when the molar ratios in the primary mixture $CaO/(SiO_2 + SO_3) = 1.0$ and $SO_3/(SiO_2 + SO_3) = 0.025$; durations (h) of hydrothermal syntheses at 200 °C: 1 – 4, 2 – 8, 3 – 16, 4 – 72

At the beginning of the synthesis all calcium sulfate penetrates into the crystal structure of semi-crystalline calcium silicate hydrates. Later on, these compounds re-crystallize into calcium silicate hydrates of more ordered structure. During this process the part of sulfate ions extrudes into solution which react with Ca^{2+} ions and form $CaSO_4$. The clear absorption band at ca. 3614 cm^{-1} testifies the crystallisation of xonotlite in the course of synthesis (Fig. 7b, curve 2). This narrow absorption band is obtained due to a clear OH position in the structure of crystal lattice as well as the shortage of hydrogen bonds.

Upon increasing the duration of crystallisation of calcium silicate hydrates (16 h), C–S–H (I) already regroups into 1.13 nm tobermorite and xonotlite. Besides, the amount of these compounds grows because much more intensive diffraction peaks (*d* spacing – 1.13 and 0.705 nm) are identified (Fig. 6, curve 3). The results of FT-IR analysis show increased intensities of absorption bands typical of these compounds (Fig. 7, b). The endothermic effect identified at a temperature of 205 °C, in the DSC curve proves the formation of 1.13 nm tobermorite and testifies to the fact that C–S–H (I) fully regroups into compounds with a higher degree of crystallinity, because exothermic effects typical of C–S–H (I) disappear in the temperature range 830–850 °C (Fig. 7a). After 72 h of isothermal curing, the only product that forms is xonotlite. These data were confirmed by the results of XRD, DSC and FTIR analyses (Figs. 6, 7).

Thus, in $CaO–SiO_2{\cdot}nH_2O–CaSO_4–H_2O$ system with the C/S molar ratio equal to 1.0, at 200 °C under saturated steam pressure, sulfate substitution retards crystallization of C–S–H (I) and tobermorite. For this reason, the transformation of intermediate compounds into xonotlite is more difficult as in a pure system. It is possible to assume that in the structure of calcium silicate hydrate, sulfate ions can be bound in such a way that S^{6+} always replaces ($Si^{4+} + 2H^+$) grou

4. Conclusions

Our results show that sulfate ions can be used to improve the synthesis of 1.13 nm tobermorite in the $CaO–SiO_2{\cdot}nH_2O–H_2O$ system with C/S = 0.83: after 72 h of hydrothermal treatment this compound remains stable, i.e. it does not transform into xonotlite, unlike a pure mixture. However, a larger amount of gypsum ($SO_3/(SiO_2 + SO_3)$ = 0.025) stimulates the formation not only of 1.13 nm tobermorite but also of $CaSO_4$ and xonotlite.

In the $CaO–SiO_2{\cdot}nH_2O–H_2O$ system with C/S = 1.0 at 200 °C, a small amount of sulfate ions prolongs the lifetime of intermediate compounds – 1.13 nm tobermorite and C–S–H (I). The transformation of intermediate compounds becomes increasingly more difficult as the number of sulfate ions increases: during the initial stage of synthesis, calcium sulfate penetrates into the crystal structure of semi-crystalline calcium silicate hydrates. In the later synthesis stages, these compounds re-crystallize into calcium silicate hydrates of more ordered structure. Some of the sulfate ions extrude into

solution during this re-crystallization process, thereby causing a reaction with Ca^{2+} ions which ultimately results in the formation of $CaSO_4$.

Acknowledgement

A. Baltusnikas , the Head of the X-ray diffraction analysis laboratory of KTU is gratefully acknowledged for carrying out X-ray analyses and for his constructive comments.

References

[1] SHAUMAN Z., The 2nd international Symposium on Science and Research in Silicate Chemistry, Brno, 1972, 25–39.
[2] KRZHEMINSKIJ S.A., *Hydrothermal treatment of silicate materials*, Stroyizdat, Moscow, Russia, 1974 (in Russian).
[3] KRZHEMINSKIJ S.A., KROJCHUK L.A., KOTIKOVA Z.P., BRUSNITSKAJA L.M., Collect. VNIISTROM Works, 24 (52) (1972), 15 (in Russian).
[4] BUDNIKOV P.P., KROJCHUK L.A., J. D. M. Mendeleev Chem. Soc., 13 2 (1986), 176 (in Russian).
[5] VERETINSKAJA I.A., [in:] *Calcium Silicate Hydrates and Their Application*, Kaunas, 1980, 41 (in Russian).
[6] SAKIYAMA M., MITSUDA T., Review of 31st General Meeting, The Cement Association of Japan, Tokyo, (1977), 35.
[7] KUATBAEV K.K., *Physical and Chemical Properties of Hardening and Durability Processes of Hydrothermally Treated Aliuminum Silicate and Silicate Materials*, PhD Thesis, Almaty (1982) (in Russian).
[8] GRABKO S.I., *Research of an Opportunity of Optimization of Technology Shale-Sand Hydrothermally Treated Concrete*, PhD Thesis, Tallinn (1975) (in Russian).
[9] VEKTARIS R., LESKAUSKAS B., SASNAUSKAS K., [In:] *Research of Building Materials*, Vilnius, 1987, 74–85 (in Russian).
[10] VEKTARIS R., *Compounds Formation in the $CaO–SiO_2–CaSO_4–H_2O$ System and Application of Products of Hydrothermal Synthesis*, PhD Thesis, KPI, Kaunas (1988) (in Russian).
[11] VINOGRADOV B.H., KROJCHUK L.A., J. Appl. Chem. USSR, 48 (1975), 28 (in Russian).
[12] BUDNIKOV P.P., KROJCHUK L.A., VINOGRADOV B.H., Dokl. Akad. Nauk SSSR., 173 (1967), 630 (in Russian).
[13] EL-KORASHY S.A., J. Ion Exchange, 15 (2004), 2.
[14] REINIK J., HEINMAA I., MIKKOLA J.P., KIRSO U., Fuel, 86 (2007), 669.
[15] SUN G.K., YOUNG J.F., KIRKPATRICK R.J., Cem. Concr. Res., 36 (2006), 18.
[16] MELLER N., HALL C., KYRITSIS K., GIRIAT G., Cem. Concr. Res., 37 (2007), 823.
[17] AL-WAKEEL E.I., EL-KORASHY S.A., EL-HEMALY S.A., RIZK M.A., J. Mater. Sci., 36 (2001), 2405.
[18] NOCUN-WCZELIK W., Cem. Concr. Res., 27 (1997), 83.
[19] TITS J., WIELAND E., MÜLLER C.J., LANDESMAN C., BRADBURY M.H., J. Coll. Interface. Sci., 300 (2006), 78.
[20] COLEMAN N.J., Separ. Purif. Tech., 48 (2006), 62.
[21] COLEMAN N.J., Mater. Res. Bull., 40 (2005), 2000.

Received 14 September 2008
Revised 10 June 2009

Materials Science-Poland, *Vol. 27*, *No. 4/1*, *2009*

Surface defects of investment castings of turbofan engine components made of IN713C nickel superalloy

H. MATYSIAK[1*], J. MICHALSKI[2], A. BALKOWIEC[3],
K. SIKORSKI[3], K. J. KURZYDŁOWSKI[3]

[1]Functional Materials Research Center, Warsaw University of Technology,
02-507 Warsaw, Wołoska 141, Poland

[2]Materials Engineers Group Sp. z o.o., 02-507 Warsaw, Wołoska 141, Poland

[3]Faculty of Materials Science and Engineering, Warsaw University of Technology,
02-507 Warsaw, Wołoska 141, Poland

The purpose of this study was to investigate typical casting defects occurring in investment cast turbofan engine parts made of IN713 C superalloy. SEM and EDS examinations were used to reveal that dross and non-metallic inclusions of a shell mould and crucible material are the most frequently occurring defects. A hypothesis is put forward with regard to the mechanisms of dross formation. EBSD studies were also carried out to reveal grain structure of the elements in question.

Key words: *IN713C; nickel based superalloy; investment casting; turbine blades*

1. Introduction

Investment casting of critical aircraft engine parts is a complex process [1] during which surface defects of castings of various origins may emerge. The surface defects of precision castings are important, particularly with regard to the high scale industrial production of airplane engine parts such as turbine blades, gas flow guide segments, blade outer air seals, etc. [2].

As these components are of crucial importance to flight safety, their functional reliability cannot be compromised by surface defects measuring no more than a few hundred of a millimeter (the critical, maximally-allowed defect size is 0.05 mm). In industrial practice, surface defects are detected via the fluorescent penetrant inspection (FPI). Detected defects are assessed with the naked eye, a magnifying glass or with a microscope. Defects are identified in accordance with the instructions given by customers. Those instructions are confidential, and may be different for each customer.

*Corresponding author, e-mail: hmatysia@inmat.pw.edu.pl

Defects are formed in the processes occurring at the interface between the liquid metal and the ceramic, as is evident from the locations where defects are found. As a result, reactions between liquid metal and a ceramic crucible shell may be of vital importance. In particular, this applies to the erosion of the crucible and the inner walls of the casting shell mould. An alloy charge may also be a source of impurities which are later "frozen" in the surface layer of the casting [1–5].

In order to ensure that the cast is of adequate quality, each stage of the casting process must be strictly monitored, taking into account the alloy chemistry , the shape of the cast, the configuration of the pouring-lip, as well as additional quality checks specific to particular products [2].

Thus efficient ways of improving the quality of the investment castings of airplane parts need to be identified, by systematic investigations into the formation of defects. The purpose of these investigations is to enhance technical guidelines for the manufacture of precision castings of critical airplane engine components.

2. Experimental

5-th and 7-th stage jet engine turbines were investigated. The turbines were made from IN 713C alloy. The chemical composition of the alloy was determined using an Arc-Met 930 arc spectrometer. Results are shown in Table 1.

Table 1. Chemical composition of IN713C [wt. %]

Material	C	Mn	Si	S	Cr	Mo	Nb+Ta	Ti	Al	Fe	Cu	Co	Ni
IN 713C	0.16	0.28	0.30	0.008	14.11	4.25	2.27	1.18	4.73	0.63	0.19	0.12	71.77
Norm PWA	max 0.2	max 0.35	max 0.35	max 0.015	13.00-15.00	3.50 5.50	1.00 3.00	0.75 1.25	5.50 6.50	Mac 1.00	Max 0.50	Max 1.00	Rest

During casting processes, typical ceramic shell moulds were used. The primary coat was based on Zircon (filler) and Ludox SK (binder). Casting processes were carried out under vacuum of 1.33 mbar at 1500 °C. The crucible was made from zirconia stabilized with magnesia. To determine melting time dependence of the gas content in the casting, three samples were taken. The microscope investigations were performed on the ingot material (sample marked as 0), on a sample with the cast material prepared in accordance with currently used technology (sample 1), and on the sample of the materials that had been kept in the melting chamber for 10 min longer (sample 2) than sample 1. The measurements of the gas content (O, N and H) in the castings were performed with the use of an ON-mat 8500nHmat 2500 made by Strohlein.

The surface defects were determined by FPI. Statistical tests were performed on the emergence of various types of defects (inclusions, dross, post cast, X-rays, hot tears). The statistics were compiled after defects had been identified in 250 turbines and van clusters (Fig. 1). The most common defects were inclusions.

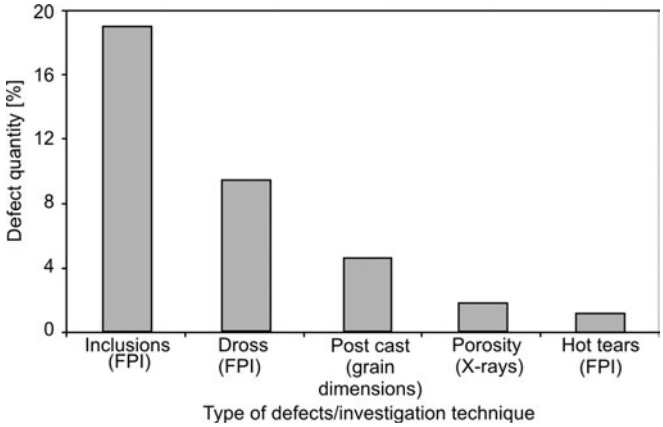

Fig. 1. Statistics of defect occurrences, compiled according to defect type and the method of testing

The cross-sections were prepared in the places were defects occurred. The cross sections were polished to 1 μm with diamond. Observations were performed with a Hitachi model S-3500 L SEM at an accelerating voltage of 15 kV. Samples were observed under secondary electron (SE) contrast in high vacuum mode. Examinations of chemical compositions in micro-regions were performed using a NORAN add-on for EDS analysis (energy-dispersive spectrometry). The grain size was quantitatively measured via the EBSD technique (by the HKL system).

3. Results and discussion

SEM and EDS investigations showed that few kinds of surface defects were present in the material: flow marks and non-metallic inclusions which are ceramic particles from the mould and crucible material and dross. Flow marks were investigated in two places, which are marked in Fig. 2 as imperfect and reference areas (grain size is a technical requirement). The results are shown in Figs. 3 and 4. The comparison of these two areas shows a difference in the grain size. In the flow marks area, the grain size is smaller than in the reference area.

EBSD images of the faulty and perfect sample were prepared using the concept of orientation maps. In the areas qualifying as reference areas, and in the imperfect areas, one observes the polycrystalline character of the microstructure. The results showed, however, a considerable difference in the grain sizes between these two areas. The grain size analysis (Table 2) reveals that areas qualifying as imperfect ones show three times smaller average grain sizes, measured in the directions perpendicular and parallel to the axes of the investigated turbine blades. EDS analysis of dross showed the presence of Mg and the main constituents of 713C. Mg is not present in the 713C alloy or in the shell mould (Fig. 5). The only source of magnesium is a crucible and it comes from ZrO_2 powder stabilized with 3% MgO.

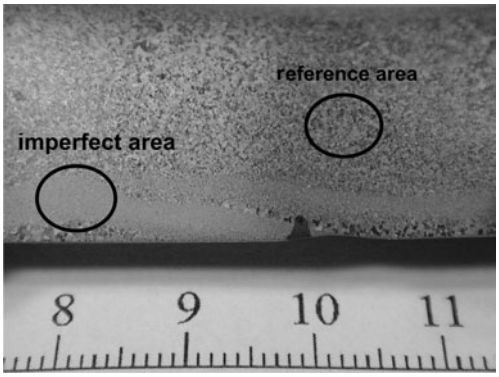

Fig. 2. Surface of a turbine blade after polishing and deep etching, revealed flow marks (imperfect area)

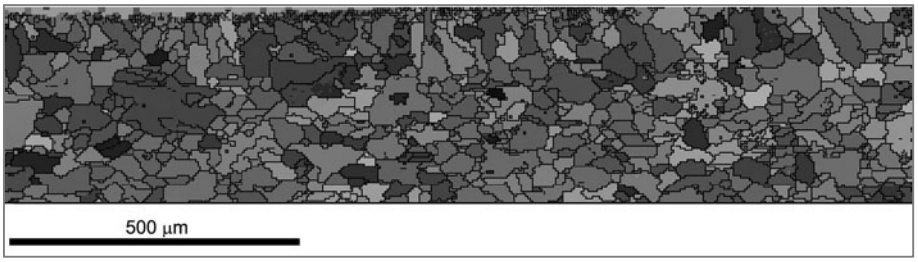

Fig. 3. Grain orientation map in the imperfect area. Turbine blade cross-section cut-out perpendicular to the blade axis – EBSD picture

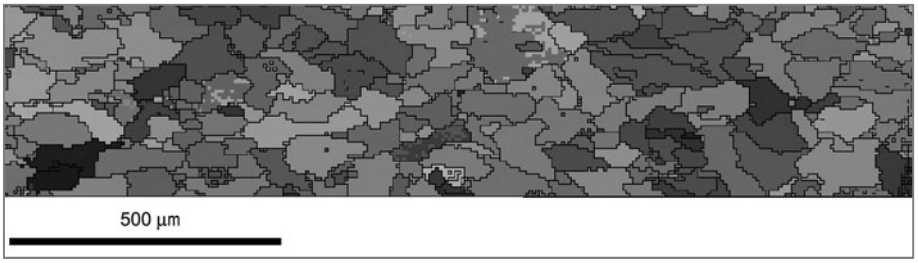

Fig. 4. Grain orientation map in the reference area. Turbine blade cross-section cut-out perpendicular to the blade axis – EBSD picture

Table 2. Average grain size d [μm] in the imperfect and reference area

Correct area on the cross-section perpendicular to the turbine blade axis	Defect area on the cross-section perpendicular to the turbine blade axis	Defect area on the cross-section parallel to the turbine blade axis
230	80	70

This suggests that during induction melting of the ingot and casting, Mg migrates into the alloy due to the chemical reaction or due to dissolution at the liquid alloy–crucible interface. Confirmation of this thesis was found in the analysis of skull formatted on the

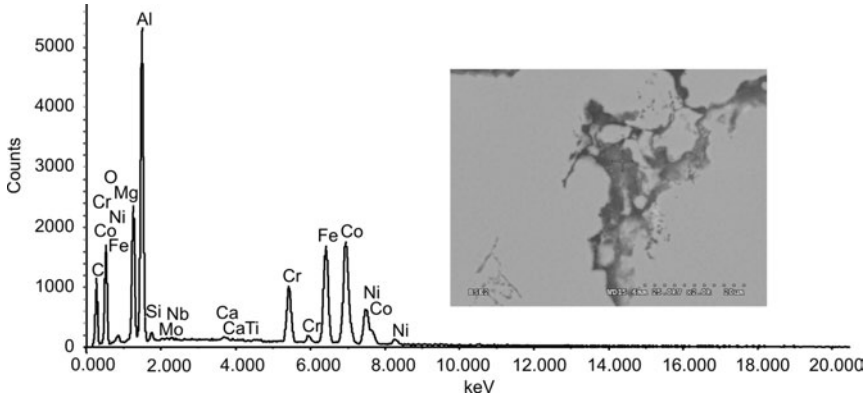

Fig. 5. EDS spectrum and the microstructure of the analysed dross type defect

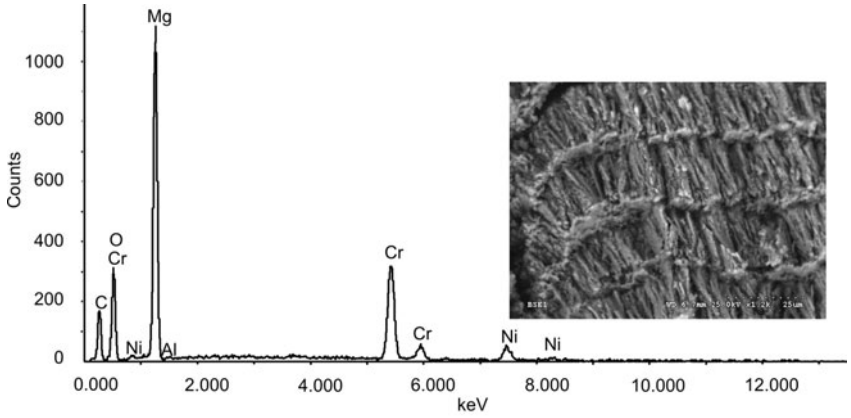

Fig. 6. EDS spectrum and the microstructure with marked spot analysis – skull formed on the surface of the crucible

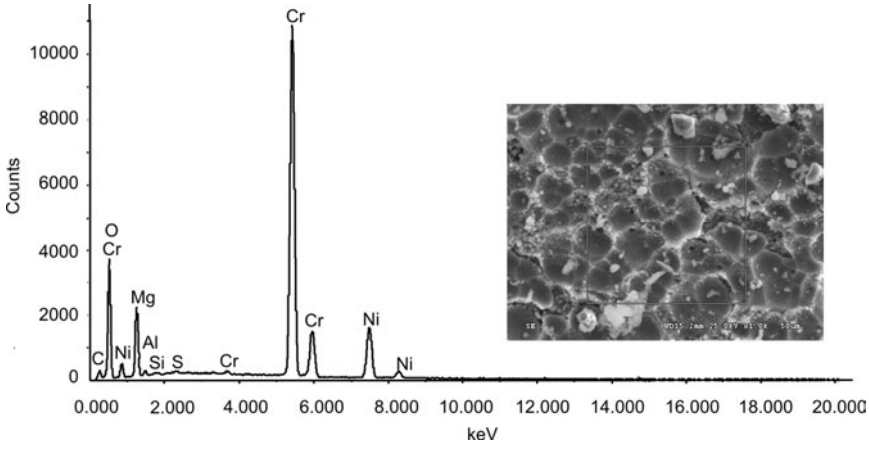

Fig. 7. EDS spectrum and the microstructure with marked spot analysis – contaminated layer removed from the wall of the casting furnace

surface of the crucible (Fig. 6) in which magnesium is the main component. There is a possibility that Mg gets into the liquid as the result of contact of the liquid surface with the gaseous atmosphere in the furnace. This is confirmed by the fact that magnesium is found in the contamination layer on the inner side of the furnace chamber walls (Fig. 7).

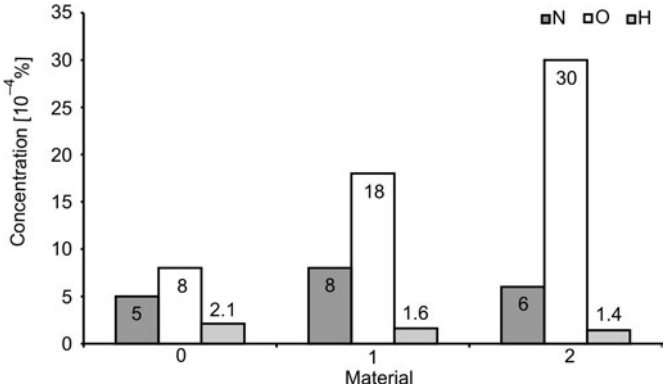

Fig. 8. Gas contents in the castings

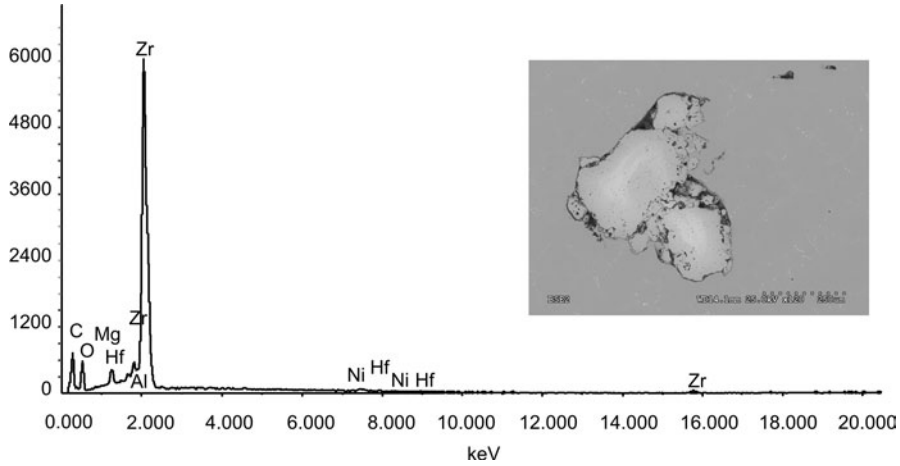

Fig. 9. Microstructure of the inclusion from the crucible material

During vacuum melting in zirconium oxide crucibles, the oxygen content in the castings increases considerably (Fig. 8). Alloy melting, according to theoretical predictions, results in at least a two-fold increase in the oxygen content of the casting. By extending the remelting time by 10 minutes, the oxygen content in the product was observed to be higher by a factor of almost four. At the same time the hydrogen and the nitrogen contents remained constant. The increase in the oxygen content of the castings, compared with the input material, proves evaporation, decomposition and erosion of the crucible material, into the liquid alloy. This is the result of the decom-

position of MgO (s) to Mg (g) and O_2 existing in furnace under special conditions (temperature and pressure). Calculations of thermodynamical stability will be published in a separate paper. A study of the reactivity of the alloy and the ceramic material of the crucible and mould in the sessile drop test is currently in progress.

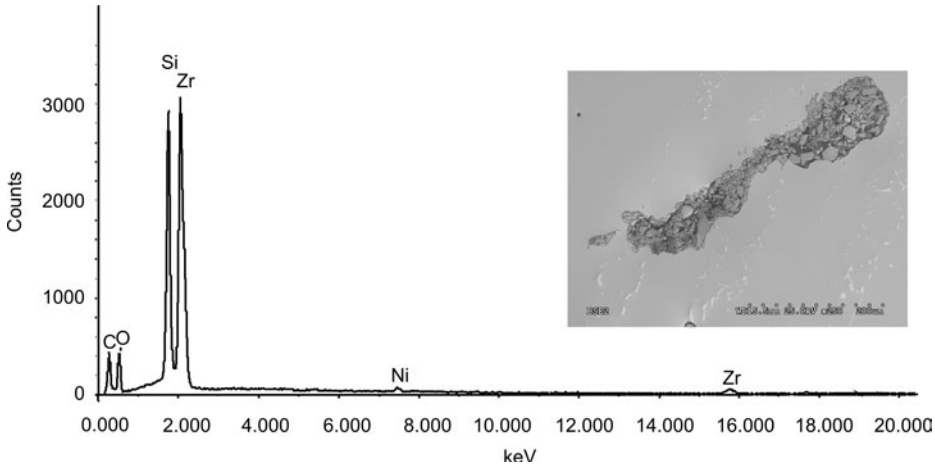

Fig. 10. Microstructure of the inclusion from the shell mould material – primary coat

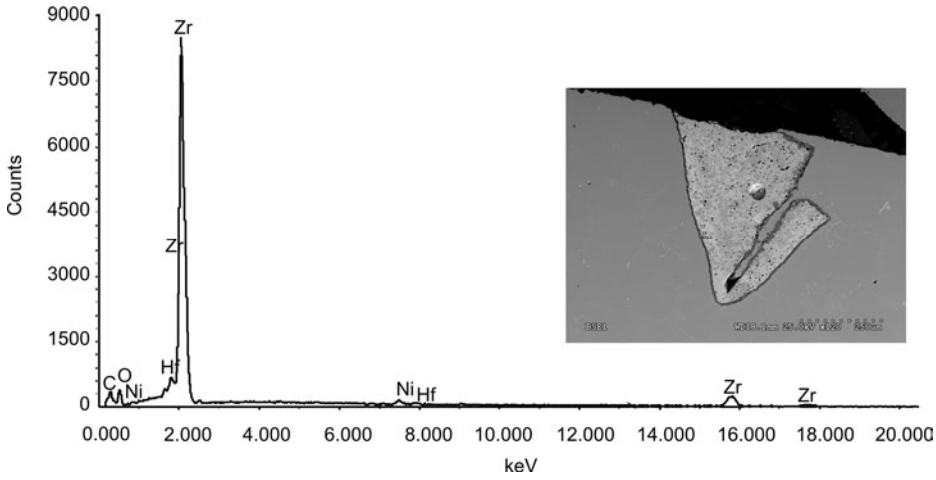

Fig. 11. Microstructure of the inclusion from the filter material

The morphology of the non-metallic inclusions originating from the materials of the shell mould and the casting crucible is presented in Figs. 9–11. The EDS investigations showed that the chemical composition of inclusions is the same as the chemical composition of crucible (Fig. 9), shell mould (Fig. 10) and filter (Fig. 11). The structure of inclusions explicitly shows that the direct cause of their occurrence are the phenomena of erosion and washing out of crucible inner walls, mould and filter by liquid alloy. Having this in mind, it is proposed that any modifications to the casting

process should address the following aspects: (i) crucible wedging and filling with charge material; (ii) the melting of ingot material; (iii) the dynamics of mould pouring; (iv) filtering and setting of the filter. Specific knowledge about these modifications is protected by WSK PZL Rzeszów S.A, and therefore will not be discussed in detail.

4. Conclusion

The examination of surface defects of precision castings of airplane parts was performed using FPI and lead to the conclusion that three types of defects occur: flow marks, non-metallic inclusions and drosses. Dross and nonmetallic inclusions, originating from mould and crucible material, are the most common faults. Non-metallic inclusions appear as a result of washing out the crucible mould and filter material. Dross formation is connected with MgO (which is a crucible ingredient) decomposition. MgO is not stable under the parameters of the casting process. The crucible material should be replaced with a different one, which would be stable under casting conditions. Mg diffusion into the melted alloy causes dross formation.

In the flow marks investigation, an immense difference in the grain size was revealed. These defects appear as a result of turbulent flow of liquid materials during pouring into the mould.

Acknowledgement

This work was done as a part of the commissioned research projects - PBZ/KBN/114/T08/2004 and PBZ-MNiSW-03/I/2007 financed by the Ministry of Science and Higher Education.

References

[1] BEELEY P.R., SMART R.F., CHAKRABORTY P.N., PANIGRAHI S.C., *Investment Casting*, The Institute of Materials, Cambridge, UK, 1995.

[2] THORNTON T., SIGH N.P., JAKSON J., *Inclusions And Dross During Alloy Melting For Investment Casting*, 52 Technical Conference and Equipment Expo 2004, Covington, KY USA, 14:1–14:7.

[3] SIMS C.T., STOLOFF N.S., HAGEL W.C., *Superalloys II*, Wiley, Canada, 1997.

[4] MIKUŁOWSKI B., *Stopy żaroodporne i żarowytrzymałe*, Wydawnictwo AGH, Kraków 1997.

[5] KURZ W., FISHER D.J., *Fundamentals of Solidification*, Trans Tech Publications Ltd., Switzerland, 2005.

Received 7 September 2008
Revised 6 January 2009

Contents

GUIDELINES FOR AUTHORS

Manuscripts can be sent by conventional mail or by e-mail. Submission of a manuscript to *Materials Science-Poland* implies that it is not being considered for the publication elsewhere, and the authors have a necessary authorization to publish the material contained in the paper. **The manuscripts should conform to the formal standards of the Journal which may be found in the first issue of each volume and on the web page.**

Authors are encouraged to submit electronic versions of the manuscript by e-mail, to the address of the Journal. A single PDF file should be sent, containing text, references, figures, tables etc. Alternatively, the authors can submit the manuscript by conventional mail, sending a CD with the PDF file mentioned above, to the Editor-in-Chief at his address given below.

Each submitted manuscript will be reviewed, the final decision concerning its acceptance resting with the editors. Upon acceptance, the corresponding author will be requested to submit the following material (via e-mail or by conventional mail, on CD)

- A DOC or RTF file containing the final version of the text, references, tables and figure captions. The content of the file should be identical with that of the hard copy, and should exactly match the version seen and accepted be the referee(s).
- File(s) in appropriate formats containing figures. The required formats of the drawings (plots, schemes of technological processes) must be vector files such as XLS, OPJ, cdr (Excel, Origin, CorelDraw) which may also be exported as EPS, EMF or WMF files. Drawings submitted in tiff or jpg formats (bitmaps, raster graphics), even if exported as EPS, EMF or WMF files, will not be accepted. **Bitmaps are acceptable only in the case of photographs**. The photographs (only in grayscale) should have the resolution not lower than 300 dpi (estimated for the size in which they are expected to be reproduced).
- A PDF file containing the complete manuscript (text, literature, tables, figures, etc). The file should be carefully checked as it will serve as a hard copy in case of doubts. **The contents of the PDF file should exactly match the material in other files.**

Irrespective of whether the final version is submitted by e-mail or by conventional mail, the authors should also send **via conventional mail** a signed copy of the Copyright Transfer Agreement (available on the web page of the Journal).

For detailed information consult the first issue of each volume or the web page of the Journal.

The mail should be addressed to:

Professor Juliusz Sworakowski
Editor-in-Chief, Materials Science-Poland
Politechnika Wrocławska, W-3
Wybrzeże Wyspiańskiego 27
50-370 Wrocław, Poland

Electronic correspondence should be sent to: MatSci@pwr.wroc.pl
Web page of Materials Science-Poland: www.MaterialsScience.pwr.wroc.pl

The Publisher reserves the right to make necessary alterations to the text. Each corresponding author will be supplied with one free copy of the journal. Orders for additional offprints can be placed with the Publisher.